

Miao Lin

**Regional gravity field recovery
using the point mass method**

München 2016

Verlag der Bayerischen Akademie der Wissenschaften
in Kommission beim Verlag C. H. Beck

ISSN 0065-5325

ISBN 978-3-7696-5169-0

Diese Arbeit ist gleichzeitig veröffentlicht in:
Wissenschaftliche Arbeiten der Fachrichtung Geodäsie und Geoinformatik der Leibniz Universität Hannover
ISSN 0174-1454, Nr. 319, Hannover 2015

Regional gravity field recovery
using the point mass method

Von der Fakultät für Bauingenieurwesen und Geodäsie
der Gottfried Wilhelm Leibniz Universität Hannover
zur Erlangung des Grades
Doktor-Ingenieur (Dr.-Ing.)
genehmigte Dissertation

von

M.Sc. Miao Lin
geboren am 08.05.1985 in Zhejiang, China

München 2016

Verlag der Bayerischen Akademie der Wissenschaften
in Kommission bei der C. H. Beck'schen Verlagsbuchhandlung München

Adresse der Deutschen Geodätischen Kommission:



Deutsche Geodätische Kommission

Alfons-Goppel-Straße 11 • D – 80 539 München

Telefon +49 – 89 – 23 031 1113 • Telefax +49 – 89 – 23 031 -1283 /- 1100

e-mail post@dgk.badw.de • <http://www.dgk.badw.de>

Prüfungskommission

Referent: Prof. Dr.-Ing. Jürgen Müller

1. Korreferent: Prof. Dr.-Ing. Jürgen Kusche

2. Korreferent: Prof. Dr.-Ing. Ingo Neumann

Tag der mündlichen Prüfung: 04.12.2014

© 2016 Deutsche Geodätische Kommission, München

Alle Rechte vorbehalten. Ohne Genehmigung der Herausgeber ist es auch nicht gestattet,
die Veröffentlichung oder Teile daraus auf photomechanischem Wege (Photokopie, Mikrokopie) zu vervielfältigen

ISSN 0065-5325

ISBN 978-3-7696-5169-0

Summary

The integral method and least-squares collocation (LSC), which work together with the remove-compute-restore technique, are state-of-the-art methods for computing accurate high-resolution regional gravity field models. However, both methods have some limitations. The integral method requires gridded gravity data as input for fast computations, which can introduce interpolation errors in the solution, and it is also not well suited for handling different types of input gravity field data. On the contrary, LSC can be applied for an optimal combination of heterogeneous observations, but a linear equation system must be solved, with the number of unknown parameters being equal to the number of observations. This prohibits it from being widely used in (real) cases with a large number of observations. Although the development of computer performance can partly solve the numerical problem of LSC, it is still of interest to seek for a method, which behaves as a compromise between the aforementioned two methods.

In this thesis, a parameterization method using radial basis functions (RBFs) is studied for regional gravity field modeling. On the one hand, this method is capable of dealing with different input data sets in comparison to the integral method. On the other hand, a linear equation system with a smaller number of unknown parameters is to be solved than for the case of LSC. The corresponding regional solution can be regarded as complementary to the integral method and LSC. The method mainly contains: (1) the design of the RBFs, including the choice of the spatial bandwidths of the RBFs and the horizontal positions of the RBFs; (2) the parameter determination.

In the first task, due to the space localization of the RBFs, the spatial bandwidths of the RBFs play the most important role for achieving a good approximation of the regional gravity field. An RBF's spatial bandwidth depends on its type, spectral bandwidth, and radial distance (i.e., depth below the reference sphere). The spectral bandwidth is defined by the minimum and maximum degree used in the series expansion of the RBF, resulting in a full RBF using all terms and a reduced RBF using only terms from a specified minimum degree to a maximum degree. In the context of this thesis, the type of the RBFs is chosen to be the point mass kernel (i.e., point mass RBFs). The spatial bandwidths of the RBFs then rely on the spectral bandwidths and depths. In this case, the design of the RBFs is equivalent to determine the RBF positions (i.e., horizontal positions and radial distances) and their spectral bandwidths. In practical applications, the positions of the RBFs are usually determined first. Then, the spectral bandwidths are properly selected, which further modifies the corresponding spatial bandwidths. For determining the RBF positions, two cases are studied: a fixed case and a free case. In the fixed case, all RBFs are located at the nodes of one or more grids. Obviously, the construction of the grids plays a crucial role, including the choice of the grid extent, grid spacing, grid depth, and grid formation. In contrary to the fixed case, the number and positions of the RBFs are unknown in the free case. A search process is developed to automatically select a number of point mass RBFs at reasonable positions by means of solving a series of small-scale nonlinear problems with bound constraints on the unknown parameters using an appropriate iteration algorithm to minimize the root-mean-square (RMS) of the differences between the predictions and observations.

The goal of the second task is to provide a stable estimate of the magnitudes of all searched point mass RBFs with known positions in the least-squares adjustment. Two solution schemes are proposed for estimating the magnitudes. In the first solution scheme, the full or reduced RBFs are used for assembling a linear equation system. Then, the magnitudes are estimated in a least-squares adjustment. In the second solution scheme, only the full RBFs are used for constructing the linear equation system. Additional constraints are taken into account in the least-squares adjustment. These constraints are derived from the relationship between the spherical harmonics and the point mass RBFs. To deal with the case of ill-posedness, Tikhonov regularization is applied, and the proper

regularization parameter is determined by either an empirical or a heuristic approach.

Several numerical tests using synthetic and real gravity data are carried out to test the developed point mass method. The “optimal” strategy for choosing appropriate model factors for the point mass method is derived from various numerical comparisons, so that a good gravity field solution in terms of RMS (or standard deviation) errors can be guaranteed. The solutions are validated against independent gravity field data or compared to the results computed by other methods. The numerical results show that the proposed point mass method is able to provide a good solution that is comparable to the solution of LSC if the model factors are chosen properly.

Keywords. Regional gravity field, radial basis functions, point mass method, least-squares, regularization

Zusammenfassung

Das Integralverfahren und die Kleinste-Quadrate-Kollokation (LSC) sind moderne und im Rahmen der Remove-Compute-Restore Technik aktuell genutzte Methoden zur Bestimmung genauer hochaufgelöster regionaler Schwerefeldmodelle. Aber beide Methoden haben ihre Einschränkungen. Das Integralverfahren benötigt als Eingangsdaten die Schwerewerte auf einem Gitter, so dass mögliche Interpolationsfehler die finale Lösung beeinflussen können. Außerdem ist die Methode für die Kombination unterschiedlicher Schwerefelddaten nicht sonderlich gut geeignet. Im Gegensatz dazu können die Daten mit LSC optimal kombiniert werden, da die Eingangsdaten ohne jegliche Interpolation verwendet werden. Ein wesentlicher Nachteil ist aber der hohe numerische Aufwand, denn es ist ein lineares Gleichungssystem mit genauso vielen Unbekannten wie Beobachtungen zu lösen. Da in realen Anwendungsfällen meist eine große Anzahl von Beobachtungen vorliegt, ist der LSC-Ansatz nicht sehr weit verbreitet, obwohl die heutige Rechenkapazität und Computertechnologie die numerischen Anforderungen zum Großteil erfüllen können.

In dieser Arbeit wird ein Ansatz zur regionalen Schwerefeldbestimmung mit Hilfe radialer Basisfunktionen (engl. radial basis functions, RBFs) vorgestellt. Auf der einen Seite ist dieses Verfahren, im Vergleich zum Integralverfahren, in der Lage, unterschiedliche Eingangsdatensätze zu verarbeiten, auf der anderen Seite weist das lineare System, das zu lösen ist, deutlich geringere Dimensionen auf. Die Methode der regionalen Lösung kann daher als Ergänzung zum Integralverfahren und zur LSC eingeordnet werden. Die Kernpunkte der Methode umfassen: (1) den Entwurf der RBFs, einschließlich der Wahl der räumlichen Bandbreiten und der horizontalen Positionen der RBFs sowie (2) die Parameterschätzung.

Die erste Aufgabe umfasst die Lokalisierung der RBFs. Dabei spielt die Bestimmung der räumlichen Bandbreiten die wichtigste Rolle, um eine gute Annäherung an das regionale Schwerefeld zu erreichen. Die räumliche Bandbreite einer RBF hängt im Wesentlichen von der Art, der spektralen Bandbreite sowie der radialen Entfernung der Basisfunktionen ab. Die spektrale Bandbreite wird über den minimalen und maximalen Grad in der Reihenentwicklung der Basisfunktion definiert. Dies führt einerseits zu vollen RBFs unter Nutzung aller Terme und andererseits zu reduzierten RBFs, bei denen nur ausgewählte Terme von einem minimalen Grad bis zu einem maximalen Grad genutzt werden. Als Typ werden im Rahmen dieser Arbeit RBFs mit Punktmassen-Kernen (Punktmassen-RBFs) gewählt. Somit hängen die räumlichen Bandbreiten der RBFs von der Wahl der spektralen Bandbreite und der radialen Entfernung ab. In diesem Fall ist das Entwerfen der RBFs äquivalent zur Bestimmung der RBF-Positionen (horizontale Positionen und radiale Abstände) und der spektralen Bandbreiten. In praktischen Anwendungen werden beide Faktoren nacheinander bestimmt. Meist werden die Positionen der RBFs unter Nutzung der vollen RBFs zuerst bestimmt. Dann werden die spektralen Bandbreiten geeignet ausgewählt, um die räumlichen Bandbreiten weiter verändern zu können. Für die RBF-Positionen werden zwei Fälle untersucht: ein fixierter Fall und ein freier Fall. Im fixierten Fall werden alle RBFs an den Knotenpunkten von einem oder mehreren Gittern fixiert. Offensichtlich spielt der Aufbau der Netze dabei eine entscheidende Rolle; dieser umfasst die Wahl der Gittergröße, des Gitterabstandes, der Gittertiefe und der Gitteranordnung. Im Gegensatz zum fixierten Fall sind Anzahl und Position der RBFs im freien Fall unbekannt. Es wurde ein automatisierter Suchprozess entwickelt, der die Anzahl der Punktmassen-RBFs auswählt und deren Positionen bestimmt. Dabei wird eine Reihe klein-skaliger nichtlinearer Probleme mit Randbedingungen für die Tiefen (d.h. radialen Abstände) oder die horizontalen Positionen gelöst. Dies geschieht unter Anwendung eines geeigneten Iterationsalgorithmus zur Minimierung der mittleren quadratischen Abweichung (root-mean-square, RMS) der Differenzen zwischen Vorhersagen und Beobachtungen.

Die zweite Aufgabe verfolgt das Ziel einer stabilen Schätzung der Amplitude aller gesuchten Punkt-

massen-RBFs mit bekannten Positionen unter Zuhilfenahme der Methode der kleinsten Quadrate. Es werden zwei Lösungsschemata zur Schätzung der Amplitude vorgeschlagen. Im ersten Lösungsschema werden volle oder reduzierte RBFs zum Aufbau des linearen Gleichungssystems genutzt. Die Amplituden der RBFs werden dann in einer Kleinste-Quadrate-Ausgleichung geschätzt. Das zweite Lösungsschema sieht vor, lediglich die vollen RBFs zum Aufbau des linearen Gleichungssystems zu verwenden. Zusätzliche Bedingungen werden im Zuge der Kleinste-Quadrate-Ausgleichung berücksichtigt. Die Bedingungen werden aus dem Verhältnis zwischen Kugelfunktionen und Punktmasse-RBFs abgeleitet. Im Falle schlecht gestellter Probleme wird die Tikhonov Regularisierung angewendet und der geeignete Regularisierungsparameter über einen deterministischen oder einen empirischen Ansatz bestimmt.

Unter Verwendung synthetischer und realer Schweredaten wird mittels mehrerer numerischer Tests die entwickelte Punktmassen-Methode getestet. Die "optimale" Strategie für die Auswahl geeigneter Modellfaktoren für die Punktmassen-Methode wird schließlich aus verschiedenen Zahlenvergleichen abgeleitet, so dass eine gute Schwerefeldlösung in Bezug auf RMS (oder Standardabweichung) gewährleistet werden kann. Die Lösungen werden entweder gegen unabhängige Schwerefelddaten validiert oder mit Ergebnissen anderer regionaler Methoden verglichen. Die Ergebnisse zeigen, dass die Punktmassen-Methode in der Lage ist, regionale Lösungen zu bestimmen, die mit LSC-Lösungen vergleichbar sind, sofern die Modellfaktoren geeignet gewählt werden.

Schlagwörter. Regionale Schwerefelder, Radiale Basisfunktionen, Punktmassen-Methode, Kleinste-Quadrate-Ausgleichung, Regularisierung

Abbreviations

BGI	Bureau Gravimétrique International
CA/NM	Central Alps/New Mexico
CHAMP	CHALLENGING Minisatellite Payload
DTM	Digital Terrain Model
EU/SA	Europe/South America
FIX-S	Solution of PM-FIX associated with a Single-grid Formation
FIX-T	Solution of PM-FIX associated with a Two-grid Formation
FRE-A	Solution of PM-FRE using Point Mass Search Model SMA
FRE-B	Solution of PM-FRE using Point Mass Search Model SMB
GBVP/GBVPs	Geodetic Boundary Value Problem/Geodetic Boundary Value Problems
GCV	Generalized Cross Validation
GN	Gauss-Newton Method
GNSS	Global Navigation Satellite System
GPS	Global Positioning System
GOCE	Gravity and steady-state Ocean Circulation Explorer
GRACE	Gravity Recovery And Climate Experiment
IAG	International Association of Geodesy
IGN	Institut Géographique National
L-BFGS	Limited-memory Broyden-Fletcher-Goldfarb-Shanno (BFGS) Method
L-BFGS-B	Bound-constrained Limited-memory BFGS Method
LM	Levenberg-Marquardt Method
LSC	Least-Squares Collocation
NLCG	Nonlinear Conjugate Gradient Method
PM-FIX	Point Mass Method with Fixed Positions
PM-FRE	Point Mass Method with Free Positions
RBF/RBFs	Radial Basis Function/Radial Basis Functions
RCR	Remove-Compute-Restore
RMS	Root-Mean-Square
RTM	Residual Terrain Model
SH	Spherical Harmonics
SHA	Spherical Harmonic Analysis
SHS	Spherical Harmonic Synthesis
SMA	Point Mass Search Model with only One Layer
SMB	Point Mass Search Model with more than One Layers
SRTM	Shuttle Radar Topography Mission
STD	Standard Deviation
STE	Stochastic Trace Estimation
SVD	Singular Value Decomposition
S1/S2	Solution of PM-FRE using Full/Reduced RBFs
TSVD	Truncated Singular Value Decomposition
VCE	Variance Component Estimation
2P/4P	Solution of PM-FRE using Radial-/All-direction Optimization
3D	Three-Dimensional

Contents

1	Introduction	1
1.1	Background	1
1.2	Research objectives	2
1.3	Thesis outline	2
2	Approximation of the regional gravity field	5
2.1	Fundamentals	5
2.1.1	The Earth's gravity field	5
2.1.2	The normal gravity field	6
2.1.3	Anomalous gravity field	7
2.2	Geodetic boundary value problem	9
2.3	Stokes's approach of the GBVP	10
2.4	Molodensky's approach of the GBVP	11
2.5	Spectral combination method	12
2.6	Least-squares collocation	14
2.7	Spherical harmonics and radial basis functions	18
2.7.1	Mathematical description	18
2.7.2	Comparison between SH and RBFs and their relationship	21
2.7.3	Spectral and spatial characteristics of RBFs: some examples	22
2.7.4	Remarks on RBFs	26
2.8	The remove-compute-restore technique and topographic effect	29
3	Regional gravity field modeling with the point mass method	31
3.1	Point masses and disturbing potential	31
3.2	Standard formulas for the point mass method	32
3.3	Least-squares estimation and regularization	37
3.3.1	Inverse problems and ill-posedness	37
3.3.2	Characteristics of inverse problems	38
3.3.3	Linear least-squares solution	40
3.3.4	Regularization	41
3.3.5	The choice of the regularization parameter	45
3.3.6	Nonlinear least-squares solution	49
3.4	Point mass method with fixed positions	57
3.4.1	Mathematical model	57
3.4.2	Grid setup	58
3.4.3	Grid formation	59
3.5	Point mass method with free positions	61
3.5.1	Mathematical model	61
3.5.2	Two-step point mass method and relevant model factors	64
3.5.3	Point mass search model	67
4	Numerical results	69
4.1	Tests with a small set of synthetic and real gravity data	69
4.1.1	Description of the data sets	70

4.1.2	Analysis of the results computed by PM-FIX	71
4.1.3	Analysis of the results computed by PM-FRE	83
4.1.4	A comparison between PM-FIX and PM-FRE	96
4.1.5	Summary and conclusions	98
4.2	Tests with a set of synthetic geoid heights with the same accuracy	99
4.2.1	Description of the data sets	100
4.2.2	Model setup	100
4.2.3	Determination of the regularization parameter	101
4.2.4	Results and discussion	102
4.2.5	Conclusions	104
4.3	Tests with a set of synthetic geoid heights with different accuracies	104
4.3.1	Data description	105
4.3.2	Solutions of PM-FRE	105
4.3.3	Conclusions	106
4.4	Tests with synthetic terrestrial and airborne gravity disturbances	107
4.4.1	Data description	107
4.4.2	Solution of PM-FRE using terrestrial data only	107
4.4.3	Solution of PM-FRE using both terrestrial and airborne data	110
4.4.4	Conclusions	112
4.5	Tests with a large-scale real data set in the Auvergne area	114
4.5.1	Data and preprocessing	114
4.5.2	Gravimetric solutions	115
4.5.3	Combined solutions	119
4.5.4	Conclusions	125
5	Summary and outlook	127
5.1	Summary	127
5.2	Outlook	129
	Bibliography	131
	Acknowledgement	139
	Curriculum Vitae	141

List of Figures

2.1	Normalized spectral and spatial characteristics of B^{PM} and B^{PK}	24
2.2	Normalized B^{PM} and B^{PK} at different depths	25
2.3	Normalized neighboring non-bandlimited B^{PM}	28
3.1	Normalized $D_{\Delta g} B^{\text{PM}}$ at different depths	34
3.2	Normalized degree variances $c_n^e(\Delta g, \Delta g)$ at different depths	35
3.3	Structural diagram of the RBFs	37
3.4	Examples for the TSVD and Tikhonov filter functions	44
3.5	Contour lines of the data misfits and the paths	55
3.6	Data misfits in terms of the number of iterations	56
3.7	Illustration of the point mass RBF locations	60
3.8	Computation procedure of the two-step method	65
3.9	Illustration of the point mass search models	68
4.1	Location of observations and control points	70
4.2	Location of 2767 Δg measurements, 153 Δg control points, and 20 GPS/leveling stations	71
4.3	Condition numbers for the CA test case	72
4.4	RMS errors for the CA test case as a function of grid depth and spectral bandwidths of the point mass RBFs associated with different grid spacings	75
4.5	RMS errors of Δg and ζ as a function of grid depth associated with different spectral bandwidths of the point mass RBFs in the case of $10' \times 10'$ grid spacing	76
4.6	RMS errors of Δg and ζ as a function of $N_{\text{min}} - 1$ associated with different grid depths in the case of $10' \times 10'$ grid spacing	76
4.7	Condition numbers for the NM test case	77
4.8	RMS and STD errors for the NM test case as a function of grid depth and spectral bandwidths of the point mass RBFs associated with different grid spacings	78
4.9	The choice of the “optimal” grid depth for the CA test case	80
4.10	The choice of the “optimal” grid depth for the NM test case	80
4.11	Square roots of the degree variances in terms of Δg and ζ for the CA test case (PM-FIX)	82
4.12	Square roots of the degree variances in terms of Δg and ζ for the NM test case (PM-FIX)	82
4.13	CA test case: different iteration algorithms	85
4.14	NM test case: different iteration algorithms	85
4.15	Empirical and analytical covariance functions of the observations	86
4.16	CA test case: RMS, STD, and RANGE for different model setups (1100 RBFs)	88
4.17	CA test case: RMS, STD, and RANGE for different model setups (1500 RBFs)	88
4.18	NM test case: RMS, STD, and RANGE for different model setups (700 RBFs)	89
4.19	CA test case: RMS, STD and RANGE for different model setups (1000 RBFs)	89
4.20	CA test case: data misfit and RMS differences	91
4.21	NM test case: data misfit and RMS differences	91
4.22	Square roots of the degree variances in terms of Δg and ζ for the CA test case (PM-FRE)	96
4.23	Square roots of the degree variances in terms of Δg and ζ for the NM test case (PM-FRE)	96
4.24	Simulated residual geoid heights over the test area	99
4.25	Empirical covariance function and the fitted analytical Tscherning-Rapp covariance function model for data set (a)	100

4.26	Histogram of the depths for the searched point mass RBFs	101
4.27	Distribution of 9801 data points for group (1) and 4264 points for group (2)	105
4.28	Errors of the modeled Δg at 11305 control points associated with different solutions .	106
4.29	Distribution of the input terrestrial, airborne gravity disturbances (δg), and of the terrestrial disturbing potentials (T) for the validation in the study areas of Europe and South America	107
4.30	Errors of the modeled disturbing potentials associated with two regional methods at the control points for both test cases	111
4.31	Errors of the modeled disturbing potentials at 8712 control points for the EU test case and 8640 control points for the SA test case	113
4.32	Location of Δg observations, Δg control points, and GPS/leveling points in the Auvergne area, France	114
4.33	Depth histogram and horizontal distribution for 10000 searched point mass RBFs . . .	117
4.34	Gravity anomaly errors at 1145 control points	118
4.35	Height anomaly errors at 75 GPS/leveling points (gravimetric)	118
4.36	Gravity anomaly models and quasigeoid models (gravimetric)	119
4.37	Height anomaly errors at 75 GPS/leveling points (combined)	121
4.38	Location of 36 GPS/leveling points for the development of the combined solutions and 39 points for the external validation	122
4.39	Height anomaly errors at 39 independent GPS/leveling points for I_{36} and II_{36}	123
4.40	Combined $1' \times 1'$ quasigeoid models	124
4.41	Differences between the gravimetric and the combined quasigeoid models	125

List of Tables

4.1	Model setup for investigating the effect of different area extension Δ	72
4.2	RMS Δg errors and RMS ζ errors for different Δ (20 km grid depth)	73
4.3	RMS Δg errors and RMS ζ errors for different Δ (40 km grid depth)	73
4.4	Model setup for investigating the effect of grid spacing, grid depth, and spectral bandwidths of the point mass RBFs	74
4.5	RMS errors of Δg and STD errors of ζ for different Δ (10 km grid depth)	77
4.6	RMS errors of Δg and STD errors of ζ for different Δ (20 km grid depth)	77
4.7	Model setup for investigating the performance of the empirical and the GCV approach	79
4.8	Model setup for comparing the unconstrained and constrained solutions	81
4.9	RMS errors associated with the unconstrained and constrained solutions for the CA test case (PM-FIX)	81
4.10	RMS errors of Δg and STD errors of ζ associated with the unconstrained and constrained solutions for the NM test case (PM-FIX)	81
4.11	Model setup for the numerical tests in Section 4.1.3.1	84
4.12	Model setup for the numerical tests in Section 4.1.3.2	87
4.13	Statistics of gravity solution errors for the CA test case	92
4.14	Statistics of gravity solution errors for the NM test case	92
4.15	Model setup for the numerical tests in Section 4.1.3.3	93
4.16	Errors of solutions associated with different values of N_{it}	94
4.17	Errors of solutions associated with different values of N_ε	94
4.18	RMS errors associated with the unconstrained and constrained solutions for the CA test case (PM-FRE)	95
4.19	RMS errors of Δg and STD errors of ζ associated with the unconstrained and constrained solutions for the NM test case (PM-FRE)	95
4.20	Statistics of Δg and ζ errors associated with different solutions for the CA test case.	97
4.21	Statistics of Δg and ζ errors associated with different solutions for the NM test case.	97
4.22	Mode setup for the numerical tests in Section 4.2	101
4.23	Regularization parameters obtained by three approaches	102
4.24	Statistics of the modeled gravity anomaly errors for test case (a)	103
4.25	Statistics of the modeled gravity anomaly errors for test case (b)	103
4.26	Statistics of the modeled gravity anomaly errors for test case (c)	103
4.27	Statistics of the modeled Δg errors at 11305 control points for different solutions	105
4.28	Square roots of estimated variance components for the two data groups	106
4.29	Statistics of global model-derived and residuals δg	108
4.30	RMS of the fit to observed δg and true T for different numbers of point mass RBFs.	108
4.31	RMS of the fit to observed δg and true T for different values of N_{\min}	109
4.32	Model setup for the numerical test cases in Section 4.4.2.3	110
4.33	Statistics of the residual disturbing potentials T at the control points computed from two methods for the two test cases	110
4.34	RMS of the fit to observed terrestrial δg^T and airborne δg^A , as well as to true T for different solutions	112
4.35	Statistics of the gravity and height anomalies	115
4.36	Model setup for the numerical tests in the Auvergne area	116

4.37	Statistics of the differences between the predicted and observed values at the control points (gravimetric)	117
4.38	Statistics of the differences for Method I	121
4.39	Statistics of the differences between the predicted and observed values at the control points (combined)	122
4.40	Statistics of the differences at GPS/leveling points for different combined solutions . .	123

1 Introduction

1.1 Background

In geodesy, one of the major tasks is the determination of the Earth's gravity field, which provides a fundamental contribution to geodetic, oceanographic, and geophysical applications. The highest accuracy and resolution demands in the field of geodesy are coming from Global Navigation Satellite System (GNSS) positioning and the determination of gravity field related heights. In this context, the geoid and quasigeoid are of major interest, as they serve as a height reference surface for the orthometric and normal heights, respectively, such that ellipsoidal heights measured by GNSS can be directly transformed into gravity field related heights. Furthermore, a geoid or quasigeoid model with sufficient accuracy is also necessary for the realization of a global height reference as well as for the derivation of the ocean circulation based on accurate sea surface heights measured by altimeter satellites. In addition, the knowledge of the gravity field also gives insight into the Earth's interior, such as crustal density variations, Moho undulations, rift basins, and lithospheric structure.

With the advent of dedicated gravity satellite missions, e.g., CHALLENGING Minisatellite Payload (CHAMP), Gravity Recovery And Climate Experiment (GRACE) as well as Gravity field and steady-state Ocean Circulation Explorer (GOCE), the accuracy of the global gravity field is highly improved, in particular at long and medium wavelengths. For the GOCE mission (Drinkwater et al., 2003), the target accuracy is 1 – 2 cm for the geoid and 1 mGal for gravity anomalies, at a resolution of about 100 km. Due to the global support of spherical harmonics, which are conventionally applied for representing the global gravity field, and due to the fact that the real gravity field exhibits strong signal variations in selected regions, in particular in the higher frequency part of the gravity field spectrum, the regional features can not sufficiently be taken into account by a global solution. Alternatively, regional gravity field modeling is applied to extract more information from the satellite data in the region of interest (e.g., Eicker et al., 2014). In addition to satellite data, dense (near) surface gravity observations (e.g., terrestrial, marine, airborne, and altimeter data) are also available in some regions, and hence the regional gravity field modeling aims at merging the satellite and (near) surface data in an optimal way (e.g., Denker, 2013).

To benefit from the dramatic improvements of the long-wavelength global gravity field components, the remove-compute-restore (RCR) technique (Forsberg, 1984) is frequently used in regional gravity field modeling. A global field is subtracted from the observations before gravity field modeling to remove the long-wavelength signal and reduce edge effects, and finally is restored to the computed residual field. A number of different methods exist to approximate the anomalous gravity potential. A review of the properties of various methods can be found, e.g., in Tscherning (1981). In addition to the traditional integral formulae (e.g., Stokes's integral) and least-squares collocation (LSC) (e.g., Heiskanen and Moritz, 1967; Moritz, 1980), radial basis functions (RBFs) have been used extensively for the regional parameterization of the gravity field in recent years. Some examples are the point mass kernel (e.g., Dampney, 1969; Needham, 1970; Heikkinen, 1981; Barthelmes, 1986; Cordell, 1992; Vermeer, 1995; Antunes et al., 2003), radial multipoles (e.g., Marchenko, 1998; Marchenko et al., 2001), spherical wavelets (Schmidt et al., 2007; Bentel et al., 2013; Naeimi, 2013), spherical spline functions (e.g., Eicker, 2008; Eicker et al., 2014), and Poisson wavelets (e.g., Klees and Wittwer, 2007; Klees et al., 2008; Tenzer and Klees, 2008; Wittwer, 2009; Panet et al., 2010). As the radial basis functions are space localizing, it is expected that a proper model setup within the parameterization will play a crucial role for a good representation of the regional gravity field.

1.2 Research objectives

The goal of the research presented in this thesis is to develop a parameterization method for the approximation of regional gravity field using RBFs. This method works in the framework of the RCR technique, and the calculated regional gravity field solutions are considered as independent solutions in comparison to the ones computed from the integral method and LSC.

The method mainly includes: (1) the design of the RBFs (i.e., model setup) based on data distribution and signal content. It comprises the choice of the spatial bandwidths and horizontal positions of the RBFs. The spatial bandwidth of an RBF is defined as the spherical angle where the basis function is half its maximum (Wittwer, 2009), describing the approximation characteristics of the RBF. It depends on the RBF's type, spectral bandwidth, and radial distance (i.e., depth below the reference sphere); (2) the estimation of the unknown RBF coefficients. The type of the RBFs is pre-selected in the context of this thesis, i.e., point mass RBFs are taken. And therefore, the main emphasis is on the choice of the spectral bandwidths of the RBFs, the radial distances of the RBFs as well as their horizontal positions. An RBF's spectral bandwidth is defined by the minimum and maximum degree used in the series expansion of the basis function, leading to a non-bandlimited (i.e., full) or a bandlimited (i.e., reduced) RBF (Section 2.7.3). When the spectral bandwidths are also fixed, the spatial bandwidths of the RBFs are then determined by their radial distances. In this case (the type and spectral bandwidths of the RBFs are fixed), the design of the RBFs is equivalent to determine the three-dimensional (3D) positions of the RBFs.

For the determination of the 3D positions of the RBFs, two cases are studied. In the first case, the RBFs are defined to be at the grid points, and hence the design of the grids is very important. Several model factors related to the grid have to be carefully chosen for achieving a good approximation. They are the grid extent, grid spacing, grid depth, and grid formation. The effect caused by these factors on the regional solution will be discussed. In contrary to the first case, the RBFs are considered as free in the second case. This means that the number and positions of the RBFs to be used for the modeling are unknown. In this case, we aim at developing a search process to find a set of RBFs at reasonable positions.

After fixing the RBFs (i.e., the type, spectral bandwidths, number, and positions), a linear equation system is generated and to be solved in the least-squares sense for estimating the coefficients of the RBFs. A stable parameterization process considering Tikhonov regularization is to be developed, which is capable of handling the ill-posedness.

In addition, the issue of data combination is also to be considered in the pursued method due to the availability of more than one data sets in some regions of interest.

1.3 Thesis outline

The content of this thesis is divided into five chapters. Besides the current chapter with the introduction, the remaining parts are organized as follows.

In Chapter 2 several methods for regional gravity field modeling are reviewed. The fundamental concepts of potential theory are summarized at first. Then the geodetic boundary value problem is outlined, and the corresponding approaches for solving the boundary value problem are briefly described. Furthermore, the spectral combination approach is introduced. In addition to integral method, LSC and parameterization method using RBFs are the other two commonly used approaches for the approximation of the regional gravity field. This chapter ends with the description of the RCR technique and the topography reduction; both are frequently applied for practical computations.

The principle of the point mass method and the computation procedures are described in detail in Chapter 3. The relation between the point masses and the disturbing potential is explained at first. Functional and stochastic models to be used in the regional gravity field analysis are then presented,

resulting in the observation equations to be used for the approximation process. Afterwards, the least-squares solution of the observation equations in both linear and nonlinear cases, as well as the regularization process for obtaining a stable solution, are introduced. According to the way of determining the positions of the point mass RBFs, two point mass approaches with fixed and free positions are described; both are to be tested for the regional computations in Chapter 4. The latter approach represents the main contribution of this thesis.

Chapter 4 addresses the numerical tests. Five tests using synthetic and real data are conducted to test the proposed point mass approaches. The aim of the first three numerical tests is to find the “optimal” strategies for the two regional approaches to obtain a good representation of the gravity field through the investigations on the effect caused by different model setups and the comparisons with traditional approaches. The inter-comparisons between the two point mass approaches are also carried out. The best performing point mass approach considering the derived “optimal” strategy is then applied to the remaining two numerical tests to verify its applicability.

Finally, the contributions of this thesis are summarized, and recommendations concerning challenges that still need to be investigated as well as future research topics are given in Chapter 5.

2 Approximation of the regional gravity field

In this chapter, the tools that are necessary for the approximation of the regional gravity field are reviewed. First of all, the fundamental concepts of potential theory are summarized as they present the basic setting for the modeling. In Section 2.2, the geodetic boundary value problem (GBVP) is outlined, and the corresponding approaches for solving the GBVP, i.e., the Stokes's approach and the Molodetsky's approach, are briefly described in Section 2.3 and 2.4, respectively. Furthermore, the spectral combination method, which is able to combine different data sets by spectral weights, is introduced in Section 2.5. The introduction of LSC in Section 2.6 provides a different view for regional gravity field modeling. In addition to the integral method and LSC, the parameterization method using RBFs is discussed in detail in Section 2.7. The spherical harmonics (SH), which are suitable for representing the global gravity field, are also included for the purpose of comparison. Finally, the RCR technique and the topography reduction are shortly reviewed in Section 2.8; they are frequently used in the practical regional gravity field computations.

2.1 Fundamentals

2.1.1 The Earth's gravity field

A particle with the mass m rotating with the Earth is affected by two forces, the gravitational force \mathbf{F}_b caused by the attraction from the Earth and the centrifugal force \mathbf{F}_c caused by the Earth's rotation. According to the definition in Heiskanen and Moritz (1967), $\mathbf{F}_g = \mathbf{F}_b + \mathbf{F}_c$ is called the force of gravity of the particle. The force of gravity \mathbf{F}_g and the gravity acceleration \mathbf{g} is connected by the particle mass m , satisfying Newton's second law of motion: $\mathbf{F}_g = m\mathbf{g}$. Accordingly, the gravity acceleration (or gravity) vector \mathbf{g} is also the resultant of the gravitational acceleration \mathbf{b} and the centrifugal acceleration \mathbf{c} :

$$\mathbf{g} = \mathbf{b} + \mathbf{c}. \quad (2.1)$$

The direction of \mathbf{g} is the same as the one of the plumb line (or vertical) and its magnitude $g = \|\mathbf{g}\|$ is often called gravity.

According to Newton's law of gravitation, the gravitational acceleration \mathbf{b} at an arbitrary point i with position vector \mathbf{r}_i is a function of mass densities and mass distribution inside the Earth and is given by

$$\mathbf{b}_i = \mathbf{b}(\mathbf{r}_i) = G \iiint_{\Omega} \frac{\rho(\mathbf{r})}{\|\mathbf{r} - \mathbf{r}_i\|^3} (\mathbf{r} - \mathbf{r}_i) d\Omega, \quad (2.2)$$

in which G is the gravitational constant with the value of $(6.67384 \pm 0.00080) \times 10^{-11} \text{ m}^3\text{kg}^{-1}\text{s}^{-2}$ (recommended by CODATA 2010; Mohr et al., 2012), $\rho(\mathbf{r})$ is the density of the Earth as a function of the position vector \mathbf{r} , and $d\Omega$ is the volume element of the Earth Ω . In the Earth-fixed rectangular coordinate system (e.g., Cartesian x -, y -, z -system) the position vector \mathbf{r} , \mathbf{r}_i , and the Euclidean distance $\|\mathbf{r} - \mathbf{r}_i\|$ are expressed as

$$\begin{cases} \mathbf{r} = (x, y, z)^T & \text{and} & \mathbf{r}_i = (x_i, y_i, z_i)^T \\ \|\mathbf{r} - \mathbf{r}_i\| = \sqrt{(x - x_i)^2 + (y - y_i)^2 + (z - z_i)^2} \end{cases}, \quad (2.3)$$

and the expression of the centrifugal acceleration \mathbf{c}_i is given by (Torge and Müller, 2012)

$$\mathbf{c}_i = \mathbf{c}(\mathbf{p}_i) = \omega^2 \mathbf{p}_i \quad \text{with} \quad \mathbf{p}_i = (x_i, y_i, 0)^T \quad \text{and} \quad p_i = \|\mathbf{p}_i\| = \sqrt{x_i^2 + y_i^2}, \quad (2.4)$$

where ω is the angular velocity of the Earth's rotation, \mathbf{p}_i is the distance vector from the rotation axis and has the same direction as \mathbf{c}_i .

As the gravity is a conservative force field, it can be derived as the gradient of a scalar potential (i.e., gravity potential W_i) according to

$$\mathbf{g}_i = \text{grad}W_i. \quad (2.5)$$

The gravity potential W_i of the Earth can be determined by

$$W_i = V_i + C_i = G \iiint_{\Omega} \frac{\rho(\mathbf{r})}{\|\mathbf{r} - \mathbf{r}_i\|} d\Omega + \frac{1}{2} \omega^2 p_i^2, \quad (2.6)$$

where V_i is the gravitational potential that vanishes at infinity, C_i is the centrifugal potential, which is an analytical function. Obviously, the variations of W_i are mainly dependent on V_i . Applying the Laplace operator $\Delta = \frac{\partial^2}{\partial x^2} + \frac{\partial^2}{\partial y^2} + \frac{\partial^2}{\partial z^2}$, a differential operator that represents the sum of the second partial derivatives with respect to the three Cartesian coordinates, to W_i in Eq. (2.6), yields (Heiskanen and Moritz, 1967)

$$\Delta W_i = \Delta V_i + \Delta C_i = \begin{cases} -4\pi G\rho + 2\omega^2 & \text{for point } i \text{ inside } \Omega \quad (\text{Poisson}) \\ 0 + 2\omega^2 & \text{for point } i \text{ outside } \Omega \quad (\text{Laplace}) \end{cases}. \quad (2.7)$$

Any continuous functions, having continuous first and second derivatives and fulfilling Laplace's equation, are called harmonic functions (Torge and Müller, 2012). Thus, the gravitational potential outside of the Earth masses is a harmonic function, whereas inside of those masses it is not harmonic, but satisfies Poisson's equation. The centrifugal potential is not harmonic. The solution of $\Delta V_i = 0$ in the spherical polar coordinate system, i.e., $\mathbf{r} = (\vartheta, \lambda, r)$, can be expressed by spherical harmonic expansions in the following way (Heiskanen and Moritz, 1967)

$$V_i = V(\vartheta_i, \lambda_i, r_i) = \frac{GM}{a} \sum_{n=0}^{\infty} \left(\frac{a}{r_i}\right)^{n+1} \sum_{m=0}^n \left(\bar{C}_{nm} \cos m\lambda_i + \bar{S}_{nm} \sin m\lambda_i\right) \bar{P}_{nm}(\cos \vartheta_i), \quad (2.8)$$

where ϑ_i , λ_i , and r_i are the colatitude, longitude, and radial distance of the computation point i , GM is the product of the gravitational constant G and the total mass M of the Earth, a is typically set to be the semi-major axis of a reference ellipsoid, n and m are integers denoted as the degree and order of the expansion, \bar{P}_{nm} are the fully normalized associated Legendre functions of the first kind, and \bar{C}_{nm} , \bar{S}_{nm} are the normalized spherical harmonic coefficients. For more details about the spherical harmonic expansions, one can refer to the textbooks, e.g., Heiskanen and Moritz (1967), Torge and Müller (2012). In the remaining of this thesis, only the harmonic case will be of further interest.

2.1.2 The normal gravity field

For the determination of the external gravity field W , the normal gravity field U is introduced as a reference system, which represents the normal figure of the Earth. On the one hand, the normal gravity field should provide a reasonably good agreement with the real field. On the other hand, it should possess a simple formation (Torge and Müller, 2012). Based on these considerations, the normal gravity field may be referred to the rotational ellipsoid by considering it to be a level ellipsoid (Torge

and Müller, 2012). If the given parameters of the level ellipsoid (i.e., semi-major axis a^N , flattening f^N , total mass M^N of the ellipsoid, and rotational angular velocity ω^N) are those values that correspond to the real Earth, then this yields the optimal approximation to the geometry of the geoid and to the external gravity field. The latest two frequently used level ellipsoids in geodetic community are GRS80 (Moritz, 2000) and WGS84 (NIMA, 1997). Furthermore, with the availability of very accurate satellite gravity field models from the recent satellite missions (e.g., CHAMP, GRACE, and GOCE), it is also worth to employ a global geopotential model up to a certain degree as a normal gravity field.

Corresponding to the real gravity potential W_i in Eq. (2.6), the normal gravity potential U_i is composed of the normal gravitational potential V_i^N and the centrifugal potential C_i^N :

$$U_i = V_i^N + C_i^N. \quad (2.9)$$

Analogue to Eq. (2.5), the associated normal gravity vector is given by

$$\boldsymbol{\gamma}_i = \text{grad}U_i. \quad (2.10)$$

The direction of $\boldsymbol{\gamma}$ is the same as the one of the normal plumb line. Its magnitude $\gamma = \|\boldsymbol{\gamma}\|$ is the normal gravity.

The normal gravitational potential of the level ellipsoid can be formulated by the ellipsoidal harmonics, or in terms of spherical harmonics (Heiskanen and Moritz, 1967). Considering a complete spherical harmonic expansion of the normal gravitational potential as well as the centrifugal potential expressed in spherical polar coordinates according to Eqs (2.6), (2.8), and (2.9), yields

$$\begin{aligned} U_i &= U(\vartheta_i, \lambda_i, r_i) = V^N(\vartheta_i, \lambda_i, r_i) + C^N(\vartheta_i, \lambda_i, r_i) \\ &= \frac{GM^N}{a^N} \sum_{n=0}^{\infty} \left(\frac{a^N}{r_i}\right)^{n+1} \sum_{m=0}^n \left(\bar{C}_{nm}^N \cos m\lambda_i + \bar{S}_{nm}^N \sin m\lambda_i\right) \bar{P}_{nm}(\cos \vartheta_i) + \frac{1}{2} \left(\omega^N r_i \sin \vartheta_i\right)^2. \end{aligned} \quad (2.11)$$

Because of the symmetry of the level ellipsoid with respect to the rotational axis, there will be only zonal terms (i.e., $m = 0$), and because of the symmetry with respect to the equatorial plane, there will be only even zonal harmonics (i.e., $n = \text{even}$ and $m = 0$) in the gravitational part of Eq. (2.11) (Heiskanen and Moritz, 1967). An expansion up to degree $n = 10$ is usually sufficient for practical computations (Denker, 2013).

2.1.3 Anomalous gravity field

The small difference between the actual gravity potential W and the normal gravity potential U is called the anomalous potential, or disturbing potential T . For an arbitrary point i outside of the Earth's surface, the disturbing potential is obtained according to

$$T_i = W_i - U_i. \quad (2.12)$$

Assuming that the centrifugal parts in both W_i and U_i are identical, see e.g., Eqs (2.6) and (2.11), the disturbing potential T_i is then expressed as the difference between the actual V_i and the normal gravitational potential V_i^N :

$$T_i = V_i - V_i^N, \quad (2.13)$$

and hence T_i is a harmonic function too, satisfying $\Delta T_i = 0$. With regard to Eqs (2.8) and (2.11), the disturbing potential can be expanded in spherical harmonics:

$$T_i = T(\vartheta_i, \lambda_i, r_i) = \frac{GM}{a} \sum_{n=0}^{\infty} \left(\frac{a}{r_i}\right)^{n+1} \sum_{m=0}^n \left(\Delta \bar{C}_{nm} \cos m\lambda_i + \Delta \bar{S}_{nm} \sin m\lambda_i \right) \bar{P}_{nm}(\cos \vartheta_i) \quad (2.14)$$

with the Stokes coefficients $\Delta \bar{C}_{nm} = \bar{C}_{nm} - \left(\frac{GM^N}{GM}\right) \left(\frac{a^N}{a}\right)^n \bar{C}_{nm}^N$, $\Delta \bar{S}_{nm} = \bar{S}_{nm} - \left(\frac{GM^N}{GM}\right) \left(\frac{a^N}{a}\right)^n \bar{S}_{nm}^N = \bar{S}_{nm}$ for $\bar{S}_{nm}^N = 0$. The different values of GM , a in V and GM^N , a^N in V^N lead to a rescaling of the coefficients of the normal potential. The summation of Eq. (2.14) starts at degree $n = 0$ to account for possible differences in the quantities of GM and GM^N (Denker, 2013).

The gravity disturbance vector is defined as the difference between the actual gravity and the normal gravity vectors, which are evaluated at the same point. It is consequently a one-point function related to the same point in space. Corresponding to the disturbing potential T_i , the gravity disturbance vector $\delta \mathbf{g}_i$ is given by

$$\delta \mathbf{g}_i = \mathbf{g}_i - \boldsymbol{\gamma}_i = \text{grad} W_i - \text{grad} U_i = \text{grad} T_i, \quad (2.15)$$

while the scalar gravity disturbance is written as

$$\delta g_i = g_i - \gamma_i. \quad (2.16)$$

The vector of gravity anomaly is defined as the difference between the actual gravity on the Earth's surface and the normal gravity on the telluroid:

$$\Delta \mathbf{g}_i = \mathbf{g}_i - \boldsymbol{\gamma}_{i'} = \delta \mathbf{g}_i + (\boldsymbol{\gamma}_i - \boldsymbol{\gamma}_{i'}) = \text{grad} T_i + (\text{grad} U_i - \text{grad} U_{i'}), \quad (2.17)$$

where the point i is located on the Earth's surface, and the point i' is the projected point on the telluroid through the normal gravity vector $\boldsymbol{\gamma}$. Thus, the gravity anomalies are two-point functions, i.e., related to the points on the Earth's surface and the telluroid. On the basis of Eq. (2.17), the scalar equations of the gravity anomaly vector $\Delta \mathbf{g}_i$ can be expressed as

$$\Delta g_i = g_i - \gamma_{i'}, \quad (2.18a)$$

$$\xi_i = \Phi_i - \phi_{i'}, \quad (2.18b)$$

$$\eta_i = (\Lambda_i - \lambda_{i'}) \cos \phi_{i'}, \quad (2.18c)$$

where Δg_i represents the magnitude of the gravity anomaly vector, ξ_i and η_i denote the north-south and east-west components of the deflection of the vertical, (Φ_i, Λ_i) are the astronomical latitude and longitude, and $(\phi_{i'}, \lambda_{i'})$ are the geodetic latitude and longitude.

The distance between the point i on the geoid and the projected point i' on the ellipsoid is called geoid undulation or geoid height N . It can be computed by the Bruns formula (Heiskanen and Moritz, 1967)

$$N_i = \frac{T_{i(\text{geoid})}}{\gamma_{i'(\text{ellipsoid})}}, \quad (2.19)$$

and similarly, for the height anomaly

$$\zeta_i = \frac{T_{i(\text{surface})}}{\gamma_{i'(\text{telluroid})}}, \quad (2.20)$$

where $T_{i(\text{geoid})}$ and $T_{i(\text{surface})}$ are the disturbing potentials on the geoid and the Earth's surface, $\gamma_{i'(\text{ellipsoid})}$ and $\gamma_{i'(\text{telluroid})}$ are the normal gravity on the ellipsoid and the telluroid, respectively. For more details about these definitions, one can refer to, e.g., Heiskanen and Moritz (1967), Torge and Müller (2012), and Denker (2013).

Finally, on the basis of Eqs (2.15)–(2.20), the relationships between the disturbing potential T and the above-mentioned gravity field quantities in spherical approximations are summarized as follows (Heiskanen and Moritz, 1967):

$$\delta g = -\frac{\partial T}{\partial r}, \quad (2.21a)$$

$$\Delta g = -\frac{\partial T}{\partial r} - \frac{2T}{r}, \quad (2.21b)$$

$$\xi = -\frac{1}{\gamma r} \frac{\partial T}{\partial \phi}, \quad (2.21c)$$

$$\eta = -\frac{1}{\gamma r \cos \phi} \frac{\partial T}{\partial \lambda}, \quad (2.21d)$$

$$N = \frac{T}{\gamma}, \quad \text{or} \quad \zeta = \frac{T}{\gamma}. \quad (2.21e)$$

Eq. (2.21b) is called the fundamental equation of physical geodesy; however, it might be replaced by Eq. (2.21a) in the future because of the development of the Global Navigation Satellite System (GNSS) technique (Hofmann and Moritz, 2005). It is also worth to emphasize that the spherical approximations in Eq. (2.21) do not imply that the boundary is replaced by a sphere. Here, ellipsoid terms have just been omitted.

2.2 Geodetic boundary value problem

The geodetic boundary value problem (GBVP) comprises the determination of the Earth's physical surface or the geoid, as well as the exterior gravity potential W from the observations on or close to the Earth's surface (Torge and Müller, 2012). Because of the insufficient knowledge of the Earth's density structures, the direct determination of W is not possible, and it can only be computed indirectly from the boundary data by solving a GBVP. The given boundary data usually are linear or nonlinear functionals of the gravity potential, leading to the gravimetric GBVP. An example of a linear functional is the gravity potential itself, e.g., the potential (differences), while an example of a nonlinear functional is the gravity disturbance that is defined as the magnitude of the gradient of the gravity potential.

Depending on the geometry of the boundary surface, it is appropriate to divide the gravimetric GBVP into fixed and free formulations (Heck, 1997). The boundary surface is assumed to be known (e.g., fixed by the coordinate vectors from GNSS technique) for the fixed gravimetric GBVP, and therefore the only remaining unknown is the potential function W . Contrary to the fixed case, the information on the geometry of the boundary surface is either incomplete or missing entirely for the free gravimetric GBVP, resulting in Molodensky's boundary value problem (Molodenskii et al., 1962), i.e., the classical free gravimetric GBVP. It can further be subdivided into the vectorial free GBVP, where the position of the boundary is completely unknown, leading to four unknowns (i.e., potential W and three-dimensional coordinates), and the scalar free GBVP, where the horizontal positions are known, resulting in only two unknowns (i.e., vertical coordinate and potential) (Heck, 1997). The well-known Stokes's and Molodensky's GBVPs can both be considered as scalar free problems as the horizontal coordinates of gravity data were traditionally based on the geodetic network, mostly allowing a transformation to the Earth-fixed system with sufficient accuracy. The main difference between the two problems is that the gravity data for Stokes's problem are located at the geoid while the data for Molodensky's problem are at the Earth's surface (Denker, 2013). The employment of the normal gravity potential U for approximating the gravity potential W leads to the linearized GBVP,

in which the primary unknown to be solved is the disturbing potential T . Accordingly, the scalar free gravimetric GBVP is transformed into the fixed GBVP with ellipsoid and telluroid serving as the boundary surfaces for Stokes's and Molodensky's problem, respectively (Moritz, 1980; Denker, 2013). Once T is known, all relevant gravity field quantities can be calculated according to Eqs (2.21a)–(2.21e).

2.3 Stokes's approach of the GBVP

The Stokes's classical GBVP aims at the determination of the geoid from gravity anomalies on the geoid. This corresponds to a boundary value problem of the third kind (Robin problem) of potential theory (Jekeli, 2009). After linearization of Stokes's GBVP by approximating the geoid by an ellipsoid, the Stokes's approach to this GBVP is based on the partial differential equation $\Delta T(\vartheta, \lambda, r) = 0$ with the spherically approximated boundary condition

$$\Delta g(\vartheta, \lambda, r_g) = -\left. \frac{\partial T(\vartheta, \lambda, r)}{\partial r} \right|_{r=r_g} - \frac{2T(\vartheta, \lambda, r_g)}{r}, \quad (2.22)$$

in which $\Delta g(\vartheta, \lambda, r_g)$ means the gravity anomaly on the geoid. After spherical and constant radius approximation, the solution of Stokes's GBVP is then given by the Stokes formula (or Stokes integrals) (Heiskanen and Moritz, 1967)

$$T(\vartheta, \lambda, r_g) = \frac{R}{4\pi} \iint_{\sigma} \Delta g(\vartheta', \lambda', r_g') S(\psi) d\sigma \quad (2.23)$$

with the mean radius R of the Earth and the Stokes function (or Stokes kernel)

$$\begin{aligned} S(\psi) &= \sum_{n=2}^{\infty} \frac{2n+1}{n-1} P_n(\cos \psi) \\ &= \frac{1}{\sin(\psi/2)} - 6 \sin \frac{\psi}{2} + 1 - 5 \cos \psi - 3 \cos \psi \ln \left(\sin \frac{\psi}{2} + \sin^2 \frac{\psi}{2} \right), \end{aligned} \quad (2.24)$$

where ψ is the spherical distance and P_n are the Legendre polynomials.

The existence of topography and atmosphere violates the boundary condition. Therefore, it is necessary to remove the masses above the geoid to fulfill this condition. The calculation of the geoid within the framework of Stokes's GBVP has two important consequences (Denker, 2013): (1) the gravity values must refer to the geoid; (2) there must be no masses outside the geoid.

In order to obtain the gravity anomalies at the geoid, the masses outside the geoid can either be removed completely or moved inside the geoid. This changes the shape of the level surface and the geoid, leading to the cogeoid. Furthermore, it is also advantageous to preserve the total mass of the Earth. Therefore, Helmert's second condensation method is usually applied, in which the masses outside the geoid are condensed onto a layer on the geoid. It is an extreme case of an isostatic reduction according to the Pratt-Hayford system as the depth of compensation D goes to zero (Heiskanen and Moritz, 1967). The removal and condensation of the topographic masses require the knowledge of the mass densities between the geoid and the Earth's surface. Due to the lack of the density information for the whole topography, a constant density (e.g., 2.67 g/cm³) is usually assumed to be the real one, introducing an error into the corresponding solutions. An investigation on the topographic mass density variation effect on the geoid for the Stokes's problem can be found in, e.g., Huang et al. (2001) and Huang (2002). In general, the entire procedure for the computation of the geoid using Helmert's second condensation method can be described as follows (Heiskanen and Moritz, 1967; Denker, 2013):

- ① The masses above the geoid are removed by subtracting the attraction effect A_P from the gravity value at the surface point P .
- ② The gravity station is lowered from the point P to the corresponding point P' on the geoid using the free-air correction F or harmonic downward continuation.
- ③ The topographic masses are condensed on the geoid, and the attraction effect $A_{P'}^c$ at P' is restored.
- ④ The indirect effect $\delta T_{P'}^{\text{ind}}$ on the potential due to the shifting of the topographic masses is computed at P' .
- ⑤ The indirect effect $\delta g_{P'}^{\text{ind}}$ on gravity, which reduces gravity from the geoid to the cogeoid, is taken into account at P' , yielding the gravity anomaly on the cogeoid as $\Delta g_{P'}^c = g_P - A_P + F + A_{P'}^c + \delta g_{P'}^{\text{ind}} - \gamma_Q$. The point Q is the projected point on the reference ellipsoid with respect to the point P' on the geoid.
- ⑥ The disturbing potential $T_{P'}^c$ for the cogeoid is computed by applying the Stokes's operator to $\Delta g_{P'}^c$.
- ⑦ The disturbing potential $T_{P'}$ for the geoid is computed by adding the indirect affect $\delta T_{P'}^{\text{ind}}$ to $T_{P'}^c$, yielding $T_{P'} = T_{P'}^c + \delta T_{P'}^{\text{ind}}$.
- ⑧ Finally, the geoid height is obtained from the Bruns formula: $N_{P'} = \frac{T_{P'}}{\gamma_Q}$.

In the case of $\delta A = A_{P'}^c - A_P \approx c$ and $\delta g_{P'}^{\text{ind}} \approx 0$, the gravity anomaly at the cogeoid becomes $\Delta g_{P'}^c \approx g_P + F + c - \gamma_Q \approx \Delta g_P + c = \Delta g_{\text{Faye}}$ (i.e., Faye anomalies) (Forsberg and Tscherning, 1997), where c is the classical terrain correction. For further discussion on this matter one can refer to, e.g., Sideris (1994) and Forsberg and Tscherning (1997). Recently, some practical examples of national geoid or quasigeoid computations are the models for Canada (Huang and Veronneau, 2013), China (Li, 2012), and USA (Wang et al., 2012).

2.4 Molodensky's approach of the GBVP

In order to avoid the removal and condensation of the topographic masses, which are necessary for Stokes's GBVP, Molodensky's GBVP is based on gravity observations on the Earth's surface. Within the linearization process, the scalar free GBVP is transformed into the fixed one by approximating the Earth's surface by means of the telluroid, serving as the boundary surface, to which the boundary conditions as well as the boundary data refer. The solution of Molodensky's GBVP can be obtained by making use of the following boundary condition in spherical approximation

$$\Delta g(\vartheta, \lambda, r_t) = -\left. \frac{\partial T(\vartheta, \lambda, r)}{\partial r} \right|_{r=r_t} - \frac{2T(\vartheta, \lambda, r_t)}{r}, \quad (2.25)$$

in which $\Delta g(\vartheta, \lambda, r_t)$ is the gravity anomaly on the Earth's surface. An efficient solution is provided by the method of analytical continuation (Moritz, 1980; Sideris, 1987; Hofmann and Moritz, 2005), in which the gravity anomalies Δg , given on the Earth's surface, are analytically continued to a normal level surface passing through the given computation point P (so-called "point level"), leading to the analytical continued gravity anomalies

$$\Delta g' = \sum_{n=0}^{\infty} g_n, \quad (2.26)$$

where g_n are analytical continuation terms. As $\Delta g'$ refer to the normal surface passing through point P , the Stokes formula can be applied to determine the disturbing potential T at P , yielding

$$T(\vartheta, \lambda, r_t) = \frac{R}{4\pi} \iint_{\sigma} \Delta g(\vartheta', \lambda', r_t') S(\psi) d\sigma + \sum_{n=1}^{\infty} \frac{R}{4\pi} \iint_{\sigma} g_n S(\psi) d\sigma. \quad (2.27)$$

According to Eq. (2.27), the main contribution to the Molodensky's solution is from the Stokes term while the further analytical continuation terms consider that the data are not given on a level surface. Since g_n terms depend on the computation point P , a new set of g_n values have to be computed for every new computation point. It is rather impractical. Therefore, a two-step procedure is suggested (Sideris, 1987; Forsberg and Tscherning, 1997), in which the surface gravity anomalies are first analytically continued to the geoid as Δg^0 , then the Stokes formula is used to compute the harmonically continued disturbing potential T^0 , and finally T^0 is analytically continued back to the telluroid.

Furthermore, the first order solution of Eq. (2.27) is known as the gradient solution (Moritz, 1980), which can be formulated by

$$T \approx \frac{R}{4\pi} \iint_{\sigma} (\Delta g + g_1) S(\psi) d\sigma \approx \frac{R}{4\pi} \iint_{\sigma} (\Delta g + c) S(\psi) d\sigma = \frac{R}{4\pi} \iint_{\sigma} \Delta g_{\text{Faye}} S(\psi) d\sigma. \quad (2.28)$$

It only holds in the linear approximation for gravity anomaly Δg that is linearly dependent on the elevation. It is also worth mentioning that the Faye anomalies play an important role in the first order solution of Molodensky's problem as well as in the solution of Stokes's problem (see also Section 2.3). For more details about Molodensky's GBVP, see e.g., Moritz (1980) and Heck (1997).

2.5 Spectral combination method

The spectral combination method is based on the Laplace surface harmonics derived from different data sets, which are then combined by employing different spectral weights. This method was initially developed to combine a global geopotential model and terrestrial gravity data in an optimal way for the purpose of geoid/quasigeoid computations. It was promoted mainly by Sjöberg (1980, 1981, 2003) and Wenzel (1981, 1982), while the basic idea already being outlined in Moritz (1976).

In the light of Eq. (2.14), the disturbing potential T can be expressed as

$$T(\vartheta, \lambda, r) = \sum_{n=0}^{\infty} T_n(\vartheta, \lambda, r) \quad (2.29)$$

with the Laplace surface harmonics of the disturbing potential

$$T_n(\vartheta, \lambda, r) = \sum_{m=0}^n \left(\frac{GM}{a} \right) \left(\frac{a}{r} \right)^{n+1} \left(\Delta \bar{C}_{nm} \cos m\lambda + \Delta \bar{S}_{nm} \sin m\lambda \right) \bar{P}_{nm}(\cos \vartheta) \quad (2.30)$$

referring to the radius r . Similar to Eq. (2.29), the gravity anomaly $\Delta g(\vartheta, \lambda, r)$ can also be given as a summation of a series of gravity anomaly surface harmonics $\Delta g_n(\vartheta, \lambda, r)$. According to Eq. (2.21b), the relation between $T_n(\vartheta, \lambda, r)$ and $\Delta g_n(\vartheta, \lambda, r)$ is given as (Heiskanen and Moritz, 1967)

$$T_n(\vartheta, \lambda, r) = \frac{r}{n-1} \Delta g_n(\vartheta, \lambda, r) = \frac{r}{4\pi} \frac{2n+1}{n-1} \iint_{\sigma} \Delta g(\vartheta', \lambda', r') P_n(\cos \psi) d\sigma. \quad (2.31)$$

In the following derivations, the spherical and constant radius approximation is applied, assuming that the observations are given on the sphere with a radius $r = R$. Only two data sets are considered, one for the global geopotential model and the other for the terrestrial gravity anomaly. The combined disturbing potential surface spherical harmonics are computed as a weighted mean in the form of

$$\hat{T}_n(\vartheta, \lambda, R) = w_n^M T_n^M(\vartheta, \lambda, R) + w_n^G T_n^G(\vartheta, \lambda, R), \quad (2.32)$$

where T_n^M and T_n^G are the surface spherical harmonics from a global geopotential model and the terrestrial gravity data, w_n^M and w_n^G are the spectral weights corresponding to T_n^M and T_n^G , which can either be determined empirically, e.g., as filter coefficients (Haagmans et al., 2003), or within the framework of least-squares adjustment or least-squares collocation solution (Kern, 2004). In the least-squares approach, the solution takes into account the error estimates of T_n^M and T_n^G , and gives the following spectral weights to the gravity components (Denker, 2013)

$$w_n^G = \frac{\sigma_n^2(\varepsilon_{TM}, R)}{\sigma_n^2(\varepsilon_{TM}, R) + \sigma_n^2(\varepsilon_{TG}, R)} \quad (2.33)$$

with the error degree variances

$$\sigma_n^2(\varepsilon_{TM}, R) = \left(\frac{GM}{a}\right)^2 \left(\frac{a}{R}\right)^{2n+2} \sum_{m=0}^n (\delta\bar{S}_{nm}^2 + \delta\bar{C}_{nm}^2) \quad (2.34)$$

for the global geopotential model, and

$$\begin{aligned} \sigma_n^2(\varepsilon_{TG}, R) &= \left(\frac{R}{n-1}\right)^2 \sigma_n^2(\varepsilon_{\Delta g^G}, R) \\ &= \left(\frac{R}{n-1}\right)^2 \frac{2n+1}{2} \int_0^\pi Cov(\varepsilon_{\Delta g^G}, \varepsilon'_{\Delta g^G}, \psi, R) P_n(\cos \psi) \sin \psi d\psi \end{aligned} \quad (2.35)$$

for the terrestrial gravity data. $\delta\bar{C}_{nm}$ and $\delta\bar{S}_{nm}$ are the standard deviations of the Stokes coefficients $\Delta\bar{C}_{nm}$ and $\Delta\bar{S}_{nm}$, and $\sigma_n^2(\varepsilon_{\Delta g^G}, R)$ are the error degree variances of terrestrial gravity anomalies, which are derived from the error covariance function $Cov(\varepsilon_{\Delta g^G}, \varepsilon'_{\Delta g^G}, \psi, R)$. The weights w_n^M can be obtained from the following relation

$$s_n = w_n^M + w_n^G, \quad (2.36)$$

in which s_n is usually set to be 1.0 (Denker, 2013). Inserting Eq. (2.36) in the form $w_n^M = 1.0 - w_n^G$ into Eq. (2.32) yields the following combined disturbing potential surface harmonics:

$$\begin{aligned} \hat{T}_n(\vartheta, \lambda, R) &= (1.0 - w_n^G) T_n^M(\vartheta, \lambda, R) + w_n^G T_n^G(\vartheta, \lambda, R) \\ &= T_n^M(\vartheta, \lambda, R) + w_n^G [T_n^G(\vartheta, \lambda, R) - T_n^M(\vartheta, \lambda, R)]. \end{aligned} \quad (2.37)$$

On the right-hand side of Eq. (2.37), the first term is a component from a global geopotential model, and the second term corresponds to the differences between the terrestrial gravity anomalies and the global model values. Inserting Eq. (2.37) into Eq. (2.29) and summing up from degree 2 to ∞ , the final disturbing potential is computed according to

$$\begin{aligned}
T(\vartheta, \lambda, R) &= \sum_{n=2}^{\infty} \hat{T}_n(\vartheta, \lambda, R) \\
&= \sum_{n=2}^{\infty} T_n^M(\vartheta, \lambda, R) + \sum_{n=2}^{\infty} w_n^G [T_n^G(\vartheta, \lambda, R) - T_n^M(\vartheta, \lambda, R)] \\
&= T^M(\vartheta, \lambda, R) + T^G(\vartheta, \lambda, R)
\end{aligned} \tag{2.38}$$

with T^M and T^G being the contributions from the global geopotential model and the terrestrial gravity data, respectively. According to Eq. (2.31) with $r = R$, T^G can be formulated as

$$T^G(\vartheta, \lambda, R) = \frac{R}{4\pi} \iint_{\sigma} [\Delta g(\vartheta', \lambda', R) - \Delta g^M(\vartheta', \lambda', R)] W(\psi, R) d\sigma \tag{2.39}$$

with the (modified Stokes) kernel

$$W(\psi, R) = \sum_{n=2}^{\infty} w_n^G \frac{2n+1}{n-1} P_n(\cos \psi). \tag{2.40}$$

In Eq. (2.39), Δg are the terrestrial gravity anomalies and Δg^M are the model anomalies. Regarding Eqs (2.38)–(2.40), the spectral combination method results in a remove-compute-restore procedure, in which the residual gravity anomalies are used to compute the residual disturbing potentials, and finally the disturbing potentials from the global model are added. The difference between the combination method and Stokes formula is dependent on the choice of w_n^G . In the case of $w_n^G = 1.0$ for degree $n \in [2, \infty)$, the method is equivalent to Stokes formula with $W(\psi, R) = S(\psi)$, i.e., see Eqs (2.24) and (2.40). All contributions are from the terrestrial gravity data. If $w_n^G = 0$ for degree $2 \leq n \leq n_{\max}$ and $w_n^G = 1.0$ for degree $n > n_{\max}$, the long-wavelength contributions ($2 \leq n \leq n_{\max}$) are from the global geopotential model, while the short-wavelength contributions ($n > n_{\max}$) are provided by the terrestrial gravity data. Therefore, the spectral weights allow to control which degrees are taken from the geopotential model and which from the terrestrial gravity data, resulting in an optimal spectral combination of two data sets. Some examples for European quasigeoid modelings by using the spectral combination method can be found in Denker (1998), Denker et al. (2009), and Denker (2013).

2.6 Least-squares collocation

In physical geodesy, the least-squares collocation (LSC) can be considered as a combination of least-squares adjustment and least-squares prediction (Moritz, 1978), providing an optimal combination of geodetic observations of different kinds, such as classical angle and distance measurements, astronomical observations, gravity measurements, and satellite data, to obtain the geometry of the Earth's surface and the exterior gravitational potential. For the derivation of LSC, there are two fundamentally different viewpoints with correspondingly different mathematical/physical concepts and ideas. The first one is the deterministic approach, and the second one is called the stochastic-probabilistic approach. Both approaches as well as a compromise of the two approaches (called spatio-statistical approach) are discussed and compared in detail in Kotsakis and Sideris (1999) and Kotsakis (2000). For further information about the mathematical foundations of LSC, one can refer to Moritz (1980).

Suppose for an unknown function f in a reproducing kernel Hilbert space, its approximation \hat{f} can be determined from the observations, which are linear functionals of f . For gravity field modeling, the unknown function is disturbing potential T , and the observations are, e.g., gravity anomalies Δg ,

gravity disturbances δg , etc. Considering n observations l_i with random and systematic errors, the basic observation equation for LSC is given as

$$l_i = L_i(T) + A_i X + e_i, \quad (2.41)$$

or, in matrix notation

$$\mathbf{l} = \mathbf{L}(T) + \mathbf{A}\mathbf{X} + \mathbf{e} = \mathbf{t} + \mathbf{A}\mathbf{X} + \mathbf{e}. \quad (2.42)$$

The vectors \mathbf{l} and \mathbf{e} comprise n measurements and corresponding random errors, respectively. \mathbf{L} is the vector of linear operators with respect to the disturbing potential, resulting in the signal vector $\mathbf{L}(T)$ or \mathbf{t} . The vector \mathbf{X} comprises m systematic parameters, and \mathbf{A} is known as an $n \times m$ matrix with $m < n$. In general, $\mathbf{A}\mathbf{X}$ may, for example, express the effect of a datum-shift or a bias and tilt in the observations (Tscherning, 2013). According to the minimum principle for least-squares collocation (Moritz, 1980):

$$\mathbf{e}^T \mathbf{C}_{ee}^{-1} \mathbf{e} + \mathbf{s}^T \mathbf{C}_{ss}^{-1} \mathbf{s} = \text{minimum} \quad (2.43)$$

with \mathbf{C}_{ss} the auto-covariance matrix of the signal vector \mathbf{s} and \mathbf{C}_{ee} the error covariance matrix of the vector \mathbf{e} of the measuring error, the best linear estimates of $\hat{\mathbf{X}}$ and $\hat{\mathbf{s}}$ are given as

$$\hat{\mathbf{X}} = \left(\mathbf{A}^T \mathbf{C}_{ll}^{-1} \mathbf{A} \right)^{-1} \mathbf{A}^T \mathbf{C}_{ll}^{-1} \mathbf{l}, \quad (2.44a)$$

$$\hat{\mathbf{s}} = \mathbf{C}_{st} \mathbf{C}_{ll}^{-1} \left(\mathbf{l} - \mathbf{A} \hat{\mathbf{X}} \right), \quad \text{with } \mathbf{C}_{ll} = \mathbf{C}_{tt} + \mathbf{C}_{ee}, \quad (2.44b)$$

where \mathbf{C}_{tt} and \mathbf{C}_{st} are the auto- and cross-covariance matrices related to the signals \mathbf{t} at the observation points and \mathbf{s} at the prediction points. In most cases of practical applications, the systematic part is not taken into account, leaving only the random part in the observations. As a consequence, Eq. (2.44a) is no longer required, and Eq. (2.44b) becomes

$$\hat{\mathbf{s}} = \mathbf{C}_{st} \mathbf{C}_{ll}^{-1} \mathbf{l} \quad \text{with } \mathbf{C}_{ll} = \mathbf{C}_{tt} + \mathbf{C}_{ee}. \quad (2.45)$$

Furthermore, in the case that the observations are assumed to be error-free, the corresponding LSC solution is

$$\hat{\mathbf{s}} = \mathbf{C}_{st} \mathbf{C}_{ll}^{-1} \mathbf{l} \quad \text{with } \mathbf{C}_{ll} = \mathbf{C}_{tt}. \quad (2.46)$$

Accordingly, the three LSC models depending on the errors in the observations are summarized as follows:

- ① **LSC with random and systematic errors.** The observation equation is given in Eq. (2.42), and the corresponding solution is given in Eq. (2.44).
- ② **LSC with only random errors.** The observation equation is given in Eq. (2.42) but with $\mathbf{A} = \mathbf{0}$, and the corresponding solution is given in Eq. (2.45).
- ③ **LSC without errors.** The observation equation is given in Eq. (2.42) but with both $\mathbf{A} = \mathbf{0}$ and $\mathbf{e} = \mathbf{0}$, and the corresponding solution is given in Eq. (2.46).

In the context of this thesis, only the latter two models are used for the gravity field computations. Model ② is usually utilized in the practical applications as the gravity measurements always contain measurement errors. Model ③ is only employed in the test cases with synthetic data. The LSC solution given in Eq. (2.45) (called the standard LSC solution in the following) can be considered as being equivalent to Tikhonov regularization with signal constraints, where the regularization parameter equals 1 (Bouman, 1998), i.e., see the second term of the left-hand side of Eq. (2.43). Often, the standard LSC can provide stable solutions for ill-posed problems. However, the amount of smoothing

provided by the noise covariance matrix \mathbf{C}_{ee} is not enough in some cases, then an additional regularization parameter α has to be introduced into Eq. (2.45), leading to the regularized LSC solution (Marchenko et al., 2001):

$$\hat{\mathbf{s}} = \mathbf{C}_{st}\mathbf{C}_{ll}^{-1}\mathbf{l} \quad \text{with} \quad \mathbf{C}_{ll} = \mathbf{C}_{tt} + \alpha\mathbf{C}_{ee} \quad (2.47)$$

in accordance with the minimum principle (Marchenko et al., 2001)

$$\mathbf{e}^T\mathbf{C}_{ee}^{-1}\mathbf{e} + \alpha\mathbf{s}^T\mathbf{C}_{ss}^{-1}\mathbf{s} = \text{minimum}. \quad (2.48)$$

If $\alpha = 1$, Eq. (2.48) equals to Eq. (2.43), and Eq. (2.47) is the same as Eq. (2.45). The regularization parameter α is determined based on the following formula solved from the so-called misclosure principle (Ameti, 2006):

$$\alpha = 1 + \sqrt{1 + \frac{\text{trace}(\mathbf{C}_{tt}\mathbf{C}_{ee})}{\text{trace}(\mathbf{C}_{ee}\mathbf{C}_{ee})}}. \quad (2.49)$$

Suppose that (1) only one data type is used; (2) the noise covariance matrix can be represented as $\mathbf{C}_{ee} = \sigma_e^2\mathbf{I}$, where σ_e^2 is the variance of the noise, and \mathbf{I} is the identity matrix; (3) the auto-covariance matrix can be approximately written as $\mathbf{C}_{tt} = \sigma_t^2\mathbf{I}$, where σ_t^2 is the variance of the signals, then Eq. (2.49) can be approximated as (Marchenko and Tartachynska, 2003)

$$\alpha = 1 + \sqrt{1 + \frac{\sigma_t^2}{\sigma_e^2}}. \quad (2.50)$$

It should be noted that Eq. (2.50) only provides a possible upper limit of α . More approaches for the determination of the regularization parameter α in LSC are described in Ameti (2006).

The application of LSC requires the determinations of \mathbf{C}_{st} and \mathbf{C}_{tt} , see e.g., Eq. (2.47). In this context, the covariance function of the disturbing potential $C_{TT}(P, Q)$ is typically chosen as the basic covariance function from which all other required covariance functions are derived by the law of covariance propagation, considering the harmonicity of T and the analytical relations between T and its functionals. For two gravity functions f and g , which are related to T by the linear operators L_f^P and L_g^Q for points P and Q , the required covariance function is obtained by the following equation

$$C_{fg}(P, Q) = L_f^P L_g^Q C_{TT}(P, Q). \quad (2.51)$$

The (spatial) homogeneous and isotropic covariance function of the disturbing potential is defined as

$$C_{TT}(P, Q) = C_{TT}(\psi_{PQ}) = M\{T_P, T_Q\}, \quad (2.52)$$

where $M\{\cdot\}$ is the averaging operator, and hence $M\{T_P, T_Q\}$ can be interpreted as averaging first over a circle with a radius ψ_{PQ} , keeping point P fixed and letting point Q move along the circle, then varying P over the whole sphere. Following the derivations in Heiskanen and Moritz (1967), the covariance function of the disturbing potential can be expanded into a series of spherical harmonics as

$$C_{TT}(P, Q) = \sum_{n=2}^{\infty} c_n(T, T) \left(\frac{R_E^2}{r_P r_Q} \right)^{n+1} P_n(\cos \psi_{PQ}), \quad (2.53)$$

in which R_E is the mean radius of the Earth, $c_n(T, T)$ is the degree variance of the disturbing potential, which is related to the Stokes coefficients $\Delta\bar{C}_{nm}$ and $\Delta\bar{S}_{nm}$ of T by (Heiskanen and Moritz, 1967)

$$c_n(T, T) = \sum_{m=0}^n \left(\Delta \bar{C}_{nm}^2 + \Delta \bar{S}_{nm}^2 \right). \quad (2.54)$$

In practice, the covariance function can not be precisely determined, as the knowledge of the disturbing potential function is limited. For instance, the degree variances $c_n(T, T)$ are often not available for $n > N$ with N being the maximum degree of the current global geopotential models, e.g., $N = 2190$ for EGM2008 model (Pavlis et al., 2012). An analytical model is usually employed to fill the missing part. The degree variance model of Tscherning and Rapp (1974), which results in closed formulas for all covariance functions, is widely used. Its expression in terms of the disturbing potential is given as

$$c_n^{TR}(T, T) = \frac{A}{(n-1)(n-2)(n+B)}, \quad (2.55)$$

where A is a constant in units of $(\text{m/s})^4$, B is an integer that is typically set to be a small value (e.g., $B = 4$) if a gravity model has been subtracted from the input data. As result, a complete covariance function in terms of the disturbing potential for practical applications is given as

$$C_{TT}(P, Q) = \sum_{n=2}^N c_n(T, T) \left(\frac{R_E^2}{r_{PrQ}} \right)^{n+1} P_n(\cos \psi_{PQ}) + \sum_{n=N+1}^{\infty} c_n^{TR}(T, T) \left(\frac{R_B^2}{r_{PrQ}} \right)^{n+1} P_n(\cos \psi_{PQ}), \quad (2.56)$$

where R_B is the radius of the Bjerhammar sphere. For the residual disturbing potential, Eq. (2.56) can be replaced by

$$C_{TT}(P, Q) = a \sum_{n=2}^N \sigma_n^2(T, T) \left(\frac{R_E^2}{r_{PrQ}} \right)^{n+1} P_n(\cos \psi_{PQ}) + \sum_{n=N+1}^{\infty} c_n^{TR}(T, T) \left(\frac{R_B^2}{r_{PrQ}} \right)^{n+1} P_n(\cos \psi_{PQ}) \quad (2.57)$$

with a being a scaling factor, $\sigma_n^2(T, T)$ being the error degree variance of the disturbing potential, see also Eq. (2.34).

For regional gravity field modeling, a covariance function is determined by the available gravity functionals within the area of interest. In the case where the input data are gravity anomalies, the auto- and cross-covariance functions $C_{\Delta g \Delta g}$ and $C_{T \Delta g}$ is obtained on the basis of Eq. (2.51), yielding

$$C_{\Delta g \Delta g}(P, Q) = \sum_{n=2}^{\infty} c_n(\Delta g, \Delta g) \left(\frac{R_E^2}{r_{PrQ}} \right)^{n+1} P_n(\cos \psi_{PQ}) \quad (2.58a)$$

$$C_{T \Delta g}(P, Q) = \sum_{n=2}^{\infty} c_n(T, \Delta g) \left(\frac{R_E^2}{r_{PrQ}} \right)^{n+1} P_n(\cos \psi_{PQ}) \quad (2.58b)$$

with

$$c_n(\Delta g, \Delta g) = \frac{(n-1)^2}{r_{PrQ}} c_n(T, T), \quad (2.58c)$$

$$c_n(T, \Delta g) = \frac{(n-1)}{r_Q} c_n(T, T). \quad (2.58d)$$

It should be noted that Eqs (2.58a)–(2.58d) are based on C_{TT} given in Eq. (2.53). In practice, C_{TT} should be used in the form of Eq. (2.56) or (2.57), and similar expressions for $C_{\Delta g \Delta g}$ and $C_{T \Delta g}$ can be obtained by certain derivations. The parameters a , A , and R_B are estimated iteratively when fitting the covariance function (e.g., $C_{\Delta g \Delta g}$) to the empirically derived model (Knudsen, 1987). For

more details about the computation of the empirical covariance function, see also Goad et al. (1984).

Compared to the integral method for regional gravity field modeling (see Sections 2.3–2.5), LSC can handle all gravity functionals of the disturbing potential as input or output data, including the associated error estimates (Moritz, 1980). The data can be located at arbitrary points with different heights, and hence no gridding is required. However, a system of linear equations with the number of unknowns being the same as the number of observations has to be solved in LSC. For the case with tens thousands of observations or even more, the high computational burden might become a significant problem. In addition, numerical instabilities may be caused by identical points or points at a short distance, making \mathbf{C}_{ll} singular. Consequently, duplicate points should be excluded from the input data before the computations.

2.7 Spherical harmonics and radial basis functions

In the following, spherical harmonics (SH), which are frequently used for representing the global gravity field, are introduced; they are the eigenfunctions of the Laplace operator Δ and represent a set of basis functions with global support. Most of the existing global geopotential models are formulated in terms of spherical harmonic coefficients, such as EGM2008, GOCO03s (Mayer-Gürr et al., 2012), etc. However, their applicability to the approximation of the regional gravity field is regarded as less appropriate (e.g., Schmidt et al., 2007; Eicker, 2008). Alternatively, the concept of radial basis functions (RBFs) that have space localizing characteristics is introduced as they act as an essential tool for regional gravity field modeling. In Section 2.7.1, the mathematical descriptions of both SH and RBFs for the representation of gravity field are given. A brief comparison between SH and RBFs, as well as their relationship, are then presented in Section 2.7.2. In Section 2.7.3, the spectral and spatial characteristics of two selected RBFs are investigated as examples. Finally, some remarks on the regional gravity field modeling using RBFs are summarized.

2.7.1 Mathematical description

Let Ω_R be a sphere with the radius R , the position vector \mathbf{r} is defined as

$$\mathbf{r} = (\phi, \lambda, r)^T \quad \text{with} \quad \|\mathbf{r}\| = r \geq R, \quad (2.59)$$

where ϕ, λ are the geocentric latitude and longitude, r is the radial distance from the origin.

The space of all square integrable functions f on the sphere Ω_R is called $L^2(\Omega_R)$, which is a Hilbert space satisfying the inner product (Schmidt et al., 2007; Eicker, 2008; Naeimi, 2013)

$$\langle f, g \rangle_{L^2(\Omega_R)} = \frac{1}{4\pi R^2} \iint_{\Omega_R} f(\phi, \lambda, R) g(\phi, \lambda, R) d\Omega_R \quad (2.60)$$

with $f, g \in L^2(\Omega_R)$, $\iint_{\Omega_R} = \int_{\phi=0}^{\phi=\pi} \int_{\lambda=0}^{\lambda=2\pi}$, and $d\Omega_R = R^2 \cos \phi d\phi d\lambda$. Defining the L^2 norm by $\|f\| = \sqrt{\langle f, f \rangle_{L^2(\Omega_R)}}$, the space $L^2(\Omega_R)$ consists of all functions such that $\|f\| < \infty$.

For any function $f \in L^2(\Omega_R)$, it can be expanded into a series of spherical harmonics as (Schmidt et al., 2007)

$$f(\phi, \lambda, R) = \sum_{n=0}^{\infty} \sum_{m=-n}^n \bar{c}_{nm} \bar{Y}_{nm}(\phi, \lambda), \quad (2.61)$$

where \bar{c}_{nm} are the spherical harmonic coefficients. The basis functions \bar{Y}_{nm} are called surface spherical harmonics of degree n and order m , forming a complete orthogonal basis of $L^2(\Omega_R)$.

According to the orthogonality property of \bar{Y}_{nm} on the sphere Ω_R :

$$\begin{cases} \frac{1}{4\pi R^2} \iint_{\Omega_R} \bar{Y}_{nm}(\phi, \lambda) \bar{Y}_{n'm'}(\phi, \lambda) d\Omega_R = 0 & \text{if } n \neq n' \text{ or } m \neq m' \\ \frac{1}{4\pi R^2} \iint_{\Omega_R} \bar{Y}_{nm}(\phi, \lambda) \bar{Y}_{n'm'}(\phi, \lambda) d\Omega_R = 1 & \text{if } n = n' \text{ and } m = m' \end{cases}, \quad (2.62)$$

the coefficients \bar{c}_{nm} can consequently be determined by

$$\bar{c}_{nm} = \frac{1}{4\pi R^2} \iint_{\Omega_R} f(\phi, \lambda, R) \bar{Y}_{nm}(\phi, \lambda) d\Omega_R. \quad (2.63)$$

Eqs (2.61) and (2.63) are known as the spherical harmonic synthesis (SHS) and spherical harmonic analysis (SHA), respectively. SHS can be considered as a forward process as the coefficients \bar{c}_{nm} are known. SHA is an inverse process, where the coefficients are usually estimated by using the numerical integrals or the least-squares adjustment based on the functions on the sphere. More computational details about the SHA can be found in Colombo (1981). The expansion of a function in spherical harmonics in Eq. (2.61) can also be interpreted as the Fourier expression on the sphere, with each degree and order associated with a certain frequency. Accordingly, the power spectrum of the function f is defined by the whole set of degree variances $c_n = \sum_{m=-n}^n \bar{c}_{nm}^2$, see also Eq. (2.54). According to Parseval's theorem, the norm of the function f in the L^2 sense is given as

$$\|f\|^2 = \frac{1}{4\pi R^2} \iint_{\Omega_R} f(\phi, \lambda, R)^2 d\Omega_R = \sum_{n=0}^{\infty} \sum_{m=-n}^n \bar{c}_{nm}^2 = \sum_{n=0}^{\infty} c_n, \quad (2.64)$$

indicating that the set of spherical harmonic basis functions $\bar{Y}_{nm}(\phi, \lambda)$ constitutes a complete orthogonal set on the sphere Ω_R .

The above specifications of spherical harmonics have been performed on the sphere Ω_R . In the following, the spherical harmonic expansion will be adapted to describe the disturbing potential of the Earth in the exterior of Ω_R with R being the mean radius of the Earth. According to Eq. (2.61), the disturbing potential outside of this sphere can be expressed as

$$T(\phi, \lambda, r) = \frac{GM}{R} \sum_{n=2}^{\infty} \sum_{m=-n}^n \left(\frac{R}{r}\right)^{n+1} \bar{c}_{nm} \bar{Y}_{nm}(\phi, \lambda) \quad (2.65a)$$

with

$$\bar{c}_{nm} = \begin{cases} \Delta \bar{C}_{nm} & \text{for } m \geq 0 \\ \Delta \bar{S}_{n|m|} & \text{for } m < 0 \end{cases}, \quad (2.65b)$$

$$\bar{Y}_{nm}(\phi, \lambda) = \begin{cases} \bar{P}_{nm}(\sin \phi) \cos(m\lambda) & \text{for } m \geq 0 \\ \bar{P}_{n|m|}(\sin \phi) \sin(|m|\lambda) & \text{for } m < 0 \end{cases}. \quad (2.65c)$$

Analogue to Eq. (2.63), the Stokes coefficients \bar{c}_{nm} can be determined by

$$\bar{c}_{nm} = \frac{1}{4\pi R^2} \frac{R}{GM} \iint_{\Omega_R} T(\phi, \lambda, r) \left(\frac{r}{R}\right)^{n+1} \bar{Y}_{nm}(\phi, \lambda) d\Omega_R. \quad (2.66)$$

For the disturbing potential, the norm of a function as introduced in Eq. (2.64) can be approximated by an empirical model known as Kaula's rule of thumb (Kaula, 1966):

$$\|T\|^2 = \sum_{n=0}^{\infty} c_n \approx \sum_{n=0}^{\infty} (2n+1) \frac{10^{-10}}{n^4} \quad (2.67)$$

or the Tscherning-Rapp model as shown in Eq. (2.55). Kaula's rule of thumb is considered as a priori information of the Stokes coefficients \bar{c}_{nm} and is widely used for the regularization of global gravity field modeling using spherical harmonics. The Tscherning-Rapp model is usually employed for the computation of the covariance function of the disturbing potential in LSC, see also Section 2.6.

Inserting Eq. (2.66) into (2.65a), yields

$$\begin{aligned} T(\phi_i, \lambda_i, r_i) &= \frac{1}{4\pi R^2} \iint_{\Omega_R} T(\phi_k, \lambda_k, r_k) \sum_{n=0}^{\infty} \sum_{m=-n}^n \left(\frac{r_k}{r_i}\right)^{n+1} \bar{Y}_{nm}(\phi_k, \lambda_k) \bar{Y}_{nm}(\phi_i, \lambda_i) d\Omega_R \\ &= \frac{1}{4\pi R^2} \iint_{\Omega_R} T(\phi_k, \lambda_k, r_k) \sum_{n=0}^{\infty} \left(\frac{r_k}{r_i}\right)^{n+1} (2n+1) P_n(\cos \psi_{ik}) d\Omega_R \end{aligned} \quad (2.68)$$

in accordance with the addition theorem given by (Heiskanen and Moritz, 1967)

$$P_n(\cos \psi_{ik}) = \frac{1}{2n+1} \sum_{m=-n}^n \bar{Y}_{nm}(\phi_k, \lambda_k) \bar{Y}_{nm}(\phi_i, \lambda_i). \quad (2.69)$$

Here ψ_{ik} is the spherical distance between points i and k and is calculated by

$$\cos \psi_{ik} = \sin \phi_i \sin \phi_k + \cos \phi_i \cos \phi_k \cos(\lambda_i - \lambda_k). \quad (2.70)$$

Now, let

$$H(\mathbf{r}_i, \mathbf{r}_k) = \frac{1}{4\pi R^2} \sum_{n=0}^{\infty} \left(\frac{r_k}{r_i}\right)^{n+1} (2n+1) P_n(\cos \psi_{ik}), \quad (2.71)$$

then Eq. (2.68) becomes

$$T(\mathbf{r}_i) = \langle T(\mathbf{r}_k), H(\mathbf{r}_i, \mathbf{r}_k) \rangle_{L^2(\Omega_R)}, \quad (2.72)$$

showing the reproducing kernel property of $H(\mathbf{r}_i, \mathbf{r}_k)$. In Schmidt et al. (2007), a "two-point" function $B(\mathbf{r}_i, \mathbf{r}_k)$, which allows the computation of the function $T(\mathbf{r}_i)$ mainly from the signal values around \mathbf{r}_i , was preferred for local or regional gravity modeling. Therefore, the inner product in Eq. (2.72) is replaced by a series expansion of radial basis functions for representing $T(\mathbf{r}_i)$, resulting in

$$T(\mathbf{r}_i) = \sum_{k=1}^{\infty} \beta_k B(\mathbf{r}_i, \mathbf{r}_k). \quad (2.73)$$

Here \mathbf{r}_i and \mathbf{r}_k are the position vectors of the i -th computation point and the center of the k -th radial basis function, respectively, β_k is the scaling coefficient. The radial basis function $B(\mathbf{r}_i, \mathbf{r}_k)$ is defined by the Legendre series (Schmidt et al., 2007; Klees et al., 2008):

$$B(\mathbf{r}_i, \mathbf{r}_k) = \frac{1}{4\pi R^2} \sum_{n=0}^{\infty} \left(\frac{r_k}{r_i}\right)^{n+1} (2n+1) b_n P_n(\cos \psi_{ik}). \quad (2.74)$$

The shape coefficients (or Legendre coefficients) b_n define the type of the function; in the case where $b_n = 1$, $B(\mathbf{r}_i, \mathbf{r}_k)$ is equivalent to $H(\mathbf{r}_i, \mathbf{r}_k)$. Some examples of the RBFs with different shape coefficients will be addressed in Section 2.7.3. Combining Eqs (2.73) and (2.74), yields

$$T(\phi_i, \lambda_i, r_i) = \frac{1}{4\pi R^2} \sum_{k=1}^{\infty} \beta_k \sum_{n=0}^{\infty} \left(\frac{r_k}{r_i}\right)^{n+1} (2n+1) b_n P_n(\cos \psi_{ik}), \quad (2.75)$$

which is analogue to Eq. (2.65). As the term $1/4\pi R^2$ in the above equation is a constant, it can be incorporated into the scaling coefficients, leading to (Eicker, 2008; Naeimi, 2013)

$$T(\phi_i, \lambda_i, r_i) = \sum_{k=1}^{\infty} \beta_k \sum_{n=0}^{\infty} \left(\frac{r_k}{r_i}\right)^{n+1} (2n+1) b_n P_n(\cos \psi_{ik}) \quad (2.76)$$

2.7.2 Comparison between SH and RBFs and their relationship

In Section 2.7.1, the mathematical models of both spherical harmonics and radial basis functions for representing the disturbing potential have been introduced. A brief comparison between them will now be given to show why RBFs are more suitable for regional gravity field modeling.

A gravity function can be localized in the space as well as in the frequency domain. Spherical harmonics are ideal frequency localizing basis functions, as every degree n and order m can be associated with one single frequency. Consequently, it is easy to allow the spectral analysis of the global gravity field based on the geopotential models, which are represented in terms of SH. However, they do not have any localizing features in the space domain at all. Since SH are globally supported basis functions, each spherical harmonic is significantly different from zero almost over the whole sphere. Thus, the represented gravity field values on the complete sphere will be affected by the changes in one coefficient. The changes in the represented field of one specific area will also affect the whole set of spherical harmonic coefficients. Therefore, the calculation of the gravity field value at one single point needs all coefficients of the global model while global and homogeneous data are required for the determination of each coefficient. In most of the regional cases, only the data in the area of interest are available, and the given data are always inhomogeneous. Furthermore, SH are only capable of representing bandlimited signals in practice. Therefore, SH are not well suited for computing a regional gravity field model with high accuracy and high resolution.

In contrast to SH, the Dirac functions are ideal space localizing functions and exhibit no localizing in the frequency domain. They are zero everywhere except at only one single point in the space domain, but contain every frequency with equal weight. As a consequence, infinite Dirac functions are needed to model a continuous signal. This is impossible in practice. The radial basis functions provide a good compromise between space and frequency localization. According to Eq. (2.76), the RBFs are the functions that only depend on the spherical distances between the evaluation points and the points at which the RBFs are located; they decrease rapidly with the distances from their origins, meaning that the corresponding scaling coefficients mainly benefit from the data around them. Hence, the RBFs can be regarded as quasi space localizing functions. In regional gravity field modeling with irregular input data, it is also possible to adapt the RBFs to the input data to represent the signals as much as possible but only with a small number of RBFs (e.g., Barthelmes, 1986; Klees et al., 2008). The RBFs can be distinguished into non-bandlimited and bandlimited functions; the former functions contain full frequencies, while only the frequencies between the degree N_{\min} and N_{\max} are nonzero for the latter functions. Some related examples will be presented in Section 2.7.3.

Because of the perfect frequency localization of SH, if an RBF solution can be transformed into an equivalent set of spherical harmonic coefficients, the corresponding spectrum can be easily analyzed. In the following, the relationship between SH and RBFs will be investigated.

Regarding Eqs (2.65), (2.69), and (2.76) and rearranging the order of summation, yields

$$T(\phi_i, \lambda_i, r_i) = \sum_{n=2}^{\infty} \sum_{m=-n}^n \frac{GM}{R} \left(\frac{R}{r_i}\right)^{n+1} \bar{c}_{nm} \bar{Y}_{nm}(\phi_i, \lambda_i), \quad (2.77a)$$

$$T(\phi_i, \lambda_i, r_i) = \sum_{n=0}^{\infty} \sum_{m=-n}^n \sum_{k=1}^{\infty} \beta_k \left(\frac{r_k}{r_i}\right)^{n+1} b_n \bar{Y}_{nm}(\phi_k, \lambda_k) \bar{Y}_{nm}(\phi_i, \lambda_i). \quad (2.77b)$$

Comparing Eq. (2.77a) to (2.77b), the Stokes coefficients \bar{c}_{nm} can be obtained by

$$\bar{c}_{nm} = \frac{R}{GM} \sum_{k=1}^{\infty} \left(\frac{r_k}{R}\right)^{n+1} \beta_k b_n \bar{Y}_{nm}(\phi_k, \lambda_k). \quad (2.78)$$

Eq. (2.78) shows that \bar{c}_{nm} can be directly computed from the estimated scaling coefficients β_k and the given shape coefficients b_n . In an ideal case, an infinite number of RBFs that are homogeneously distributed over the whole sphere of the Earth are required. However, the number of RBFs is always finite in practical regional applications. Therefore, the transformed Stokes coefficients are only suited for the spectral analysis of the regional solutions computed by using the RBFs.

2.7.3 Spectral and spatial characteristics of RBFs: some examples

The spectral characteristics of RBFs is determined by the chosen shape coefficients b_n , which act as the degree-dependent weighting for the Legendre polynomials P_n , resulting in different basis function kernels (i.e., different types of RBFs). In recent years, various RBFs with different kernels have been employed and compared for regional gravity field modeling (e.g., Schmidt et al., 2007; Eicker, 2008; Klees et al., 2008; Tenzer and Klees, 2008; Wittwer, 2009; Bentel et al., 2013; Naeimi, 2013; Eicker et al., 2014). The behavior of RBFs in the space domain is more complicated. Besides the basis function kernels, it is also affected by the radial distances of the RBFs. In addition, both spectral and spatial characteristics depend on the spectral bandwidths of the RBFs (i.e., the range of degrees for nonzero shape coefficients). In this section, two simple RBFs are selected for the investigations. The first one is the RBF with the point mass kernel and the second one is associated with the Poisson kernel (Klees et al., 2008; Wittwer, 2009). Both RBFs can be expressed in analytical form, indicating that they are well suited for constructing a regional model with high accuracy and high resolution. For more details about other RBFs, see the above given references.

Eq. (2.76) describes a general form of the disturbing potential in the formation of RBFs. One can rewrite it for practical applications as follows:

$$T(\phi_i, \lambda_i, r_i) = \sum_{k=1}^K \beta_k B(\mathbf{r}_i, \mathbf{r}_k), \quad (2.79a)$$

where

$$B(\mathbf{r}_i, \mathbf{r}_k) = \sum_{n=0}^{\infty} \left(\frac{r_k}{r_i}\right)^{n+1} (2n+1) b_n P_n(\cos \psi_{ik}), \quad (2.79b)$$

and

$$\begin{cases} b_n \neq 0 & \text{for } N_{\min} \leq n \leq N_{\max} \\ b_n = 0 & \text{otherwise} \end{cases}. \quad (2.79c)$$

Here K is the number of RBFs, N_{\min} and N_{\max} are the minimum and maximum degrees between

which the shape coefficients are nonzero. If $N_{\min} = 0$ and $N_{\max} = \infty$, $B(\mathbf{r}_i, \mathbf{r}_k)$ are non-bandlimited. Otherwise, the bandlimited RBFs are provided. Accordingly, the mathematical models for the RBFs with the point mass kernel and the Poisson kernel are described as follows.

RBFs with the point mass kernel

The analytical expression of the RBFs with the point mass kernel is given as (e.g., Heiskanen and Moritz, 1967; Klees et al., 2008; Tenzer and Klees, 2008; Wittwer, 2009)

$$B^{\text{PM}}(\mathbf{r}_i, \mathbf{r}_k) = \frac{1}{\ell_{ik}} = \frac{1}{\sqrt{r_i^2 + r_k^2 - 2r_i r_k \cos \psi_{ik}}} = \sum_{n=0}^{\infty} \frac{1}{r_k} \left(\frac{r_k}{r_i}\right)^{n+1} P_n(\cos \psi_{ik}), \quad (2.80)$$

which is the reciprocal distance between the computation point i and the center of the k -th RBF.

Comparing Eq. (2.80) to Eqs (2.79b) and (2.79c), yields

$$\begin{cases} b_n^{\text{PM}} = \frac{1}{r_k(2n+1)} & \text{for } N_{\min} \leq n \leq N_{\max} \\ b_n^{\text{PM}} = 0 & \text{otherwise} \end{cases}, \quad (2.81)$$

leading to

$$\begin{cases} B^{\text{PM}}(\mathbf{r}_i, \mathbf{r}_k) = \text{Eq. (2.80)} & \text{for } N_{\min} = 0 \text{ and } N_{\max} = \infty \text{ (Case 1)} \\ B^{\text{PM}}(\mathbf{r}_i, \mathbf{r}_k) = \sum_0^{N_{\max}} \frac{1}{r_k} \left(\frac{r_k}{r_i}\right)^{n+1} P_n(\cos \psi_{ik}) & \text{for } N_{\min} = 0 \text{ and } N_{\max} \neq \infty \text{ (Case 2)} \\ B^{\text{PM}}(\mathbf{r}_i, \mathbf{r}_k) = \sum_{N_{\min}}^{\infty} \frac{1}{r_k} \left(\frac{r_k}{r_i}\right)^{n+1} P_n(\cos \psi_{ik}) & \text{for } N_{\min} > 0 \text{ and } N_{\max} = \infty \text{ (Case 3)} \\ B^{\text{PM}}(\mathbf{r}_i, \mathbf{r}_k) = \sum_{N_{\min}}^{N_{\max}} \frac{1}{r_k} \left(\frac{r_k}{r_i}\right)^{n+1} P_n(\cos \psi_{ik}) & \text{for } N_{\min} > 0 \text{ and } N_{\max} \neq \infty \text{ (Case 4)} \end{cases}. \quad (2.82)$$

RBFs with the Poisson kernel

The analytical RBFs with the Poisson kernel is expressed as (e.g., Heiskanen and Moritz, 1967; Klees et al., 2008; Tenzer and Klees, 2008; Wittwer, 2009)

$$B^{\text{PK}}(\mathbf{r}_i, \mathbf{r}_k) = \frac{r_k (r_i^2 - r_k^2)}{\ell_{ik}^3} = \sum_{n=0}^{\infty} (2n+1) \left(\frac{r_k}{r_i}\right)^{n+1} P_n(\cos \psi_{ik}). \quad (2.83)$$

Comparing Eq. (2.83) to Eqs (2.79b) and (2.79c), yields

$$\begin{cases} b_n^{\text{PK}} = 1 & \text{for } N_{\min} \leq n \leq N_{\max} \\ b_n^{\text{PK}} = 0 & \text{otherwise} \end{cases}, \quad (2.84)$$

leading to

$$\begin{cases} B^{\text{PK}}(\mathbf{r}_i, \mathbf{r}_k) = \text{Eq. (2.83)} & \text{for } N_{\min} = 0 \text{ and } N_{\max} = \infty \text{ (Case 1)} \\ B^{\text{PK}}(\mathbf{r}_i, \mathbf{r}_k) = \sum_0^{N_{\max}} (2n+1) \left(\frac{r_k}{r_i}\right)^{n+1} P_n(\cos \psi_{ik}) & \text{for } N_{\min} = 0 \text{ and } N_{\max} \neq \infty \text{ (Case 2)} \\ B^{\text{PK}}(\mathbf{r}_i, \mathbf{r}_k) = \sum_{N_{\min}}^{\infty} (2n+1) \left(\frac{r_k}{r_i}\right)^{n+1} P_n(\cos \psi_{ik}) & \text{for } N_{\min} > 0 \text{ and } N_{\max} = \infty \text{ (Case 3)} \\ B^{\text{PK}}(\mathbf{r}_i, \mathbf{r}_k) = \sum_{N_{\min}}^{N_{\max}} (2n+1) \left(\frac{r_k}{r_i}\right)^{n+1} P_n(\cos \psi_{ik}) & \text{for } N_{\min} > 0 \text{ and } N_{\max} \neq \infty \text{ (Case 4)} \end{cases}. \quad (2.85)$$

As can be seen from Eqs (2.81) and (2.84), the shape coefficient b_n^{PM} for the point mass kernel is

a function of degree n . High-frequency contents are damped with increasing degrees. However, all frequencies have the same weight for the shape coefficient b_n^{PK} , which is independent on the degree. Four cases of RBFs are given in both Eqs (2.82) and (2.85) with different choices of N_{\min} and N_{\max} . In Case 1, full frequencies are contained in RBFs, resulting in non-bandlimited functions. The RBFs are bandlimited in the other three cases as only parts of the frequencies are considered. The frequencies above N_{\max} are neglected in Case 2, acting as a low-pass filtering. In Case 3, the frequencies below N_{\min} are removed, and hence it can be regarded as a high-pass filtering. Analogue to the band-pass filtering, only the frequencies between N_{\min} and N_{\max} are kept in the RBFs for Case 4. Assuming that an evaluation point is located on a sphere with $R = 6371$ km and the RBFs are located at the depth of 50 km with respect to the sphere, several examples of the behavior of the two RBFs in both frequency and space domain are illustrated in Fig. 2.1.

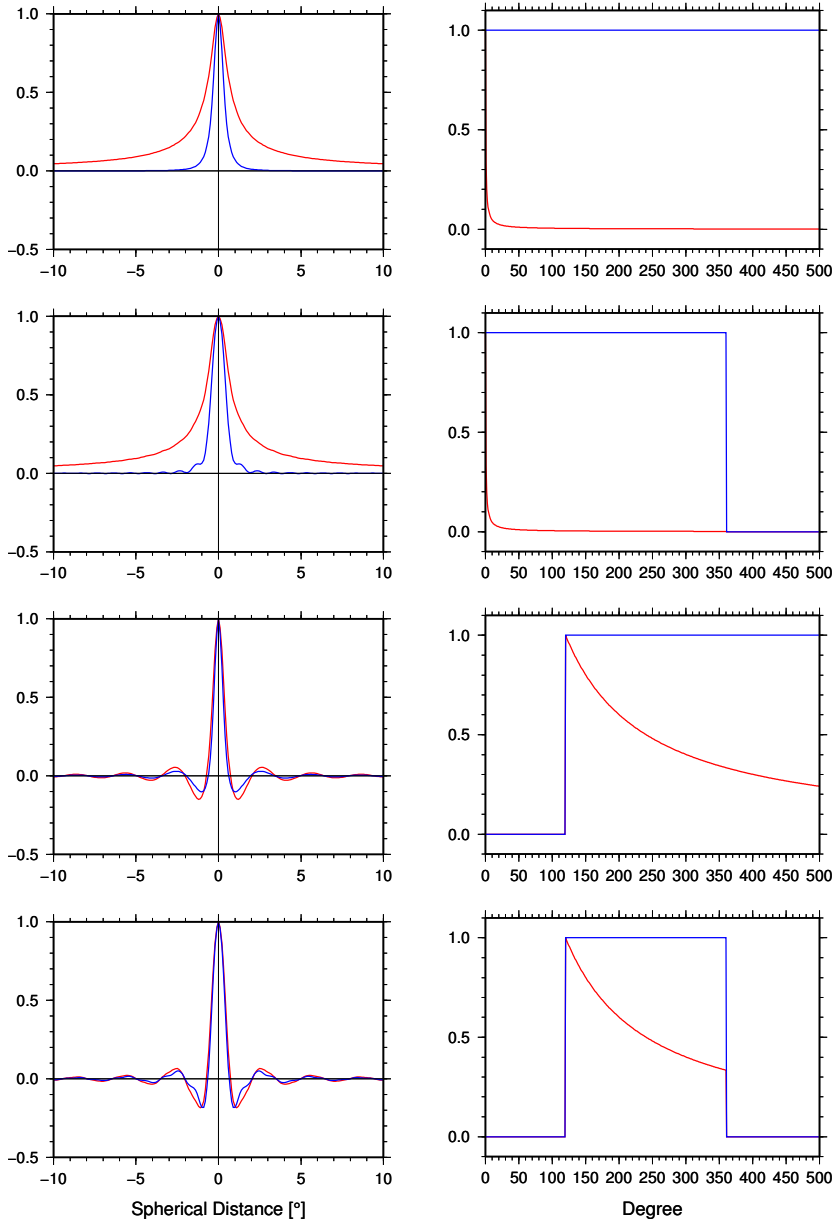


Figure 2.1: Normalized spectral and spatial characteristics of B^{PM} and B^{PK} . For each row, the *left* one is in the space domain and the *right* one is in the frequency domain. *Red lines:* for B^{PM} ; *blue lines:* for B^{PK} . *Row 1:* $N_{\min} = 0$ and $N_{\max} = \infty$; *row 2:* $N_{\min} = 0$ and $N_{\max} = 360$; *row 3:* $N_{\min} = 120$ and $N_{\max} = \infty$; *row 4:* $N_{\min} = 120$ and $N_{\max} = 360$.

From Fig. 2.1, it is easy to see that the RBF with the Poisson kernel has a stronger space localizing than the RBFs with the point mass kernel. The reason is due to the shape coefficients of different kinds. The removal of high frequencies from the kernels can make the shape of the RBFs wider (see row 2), resulting in less strong space localizing; the corresponding RBFs are suited for gravity field modeling using satellite data only. The shape of the RBFs becomes much narrower when neglecting the low frequencies (see row 3). Such RBFs can be employed in the case where residual terrestrial gravity data without the long-wavelength components are used as input. For the residual terrestrial data with the removal of both the long- and short-wavelength components, the RBFs as shown in row 4 may be a good choice.

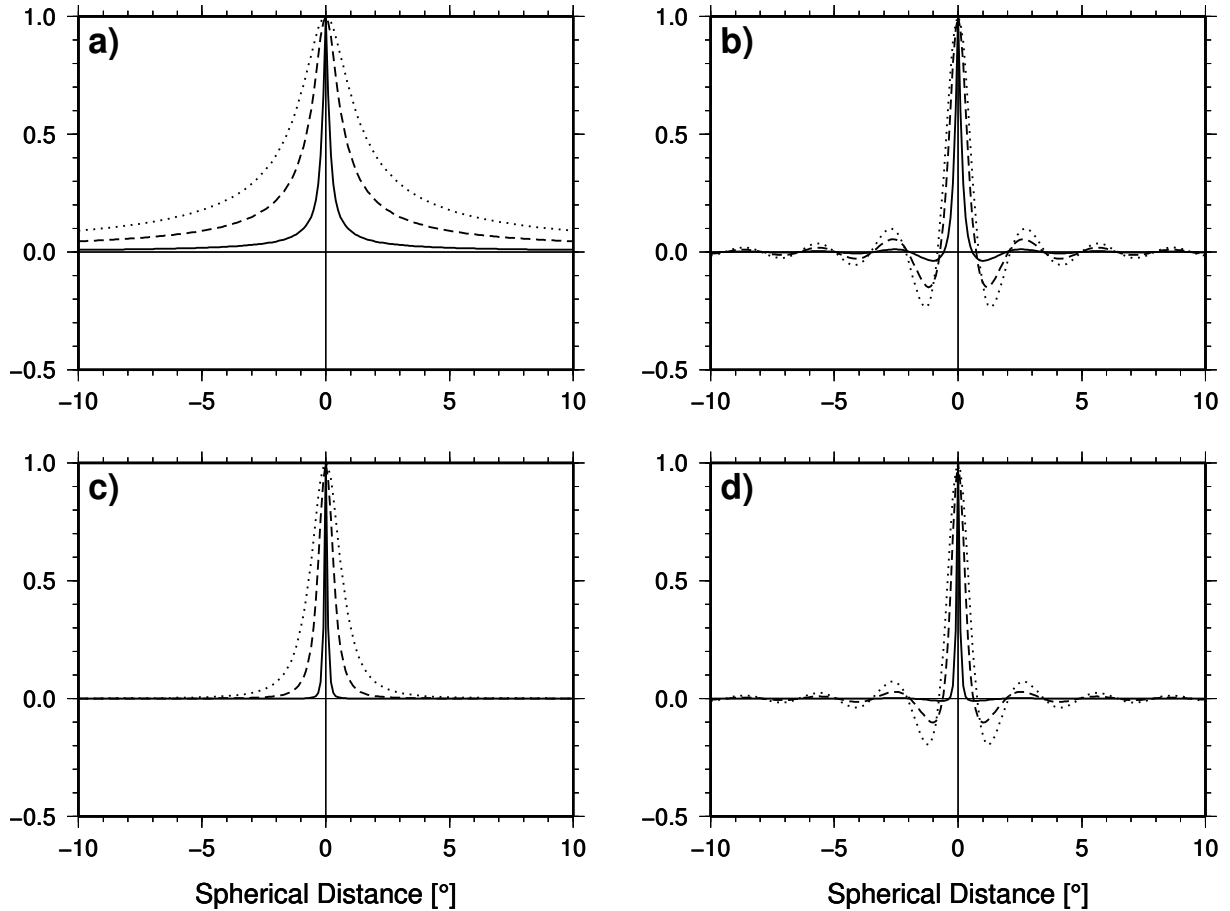


Figure 2.2: Normalized B^{PM} and B^{PK} at a depth of 10 km (*solid lines*), 50 km (*dashed lines*), and 100 km (*dotted lines*); **a)** for B^{PM} with $N_{\min} = 0$ and $N_{\max} = \infty$; **b)** for B^{PM} with $N_{\min} = 120$ and $N_{\max} = \infty$; **c)** for B^{PK} with $N_{\min} = 0$ and $N_{\max} = \infty$; **d)** for B^{PK} with $N_{\min} = 120$ and $N_{\max} = \infty$.

Another factor that can affect the shape of the basis function is the radial distance of the function, or equivalently, the depth with respect to the reference sphere. If the depths of RBFs with different kernels are chosen properly, similar shape of RBFs can be obtained, leading to similar solutions (Tenzer and Klees, 2008). In the following, several examples about the effect of the depths on the shape of the RBFs are shown in Fig. 2.2. Three depths referred to $R = 6371$ km are used for the two selected RBFs. Moreover, non-bandlimited and bandlimited cases are also included.

As can be seen from Fig. 2.2, the deeper the basis functions are, the less strong space localizing the functions become. As a consequence, the RBFs should be located at shallow depths for representing short-wavelength gravity signals, and the long-wavelength signals are mainly recovered by deep RBFs.

When the low frequencies are removed from the functions, the shape of the functions becomes much narrower in the cases of the depths of 50 km and 100 km, whereas the shape remains nearly the same in the case of the depth of 10 km. This indicates that the RBFs at shallow depths are dominated by short-wavelength contributions, while the ones at deep depths are dominated by long-wavelength contributions. As the basis function with the Poisson kernel has a stronger space localizing than the one with the point mass kernel, the former function is expected to be located at a deeper depth such that it can provide a similar shape to the one of the latter function.

2.7.4 Remarks on RBFs

As shown in Section 2.7.3, the spectral and spatial characteristics of a single RBF are dependent on the choices of the shape coefficients, spectral bandwidths, and radial distances. Often, more than one RBFs are used for representing the regional gravity field, and hence the proper choice of the horizontal positions of the RBFs is also of importance. Accordingly, four factors have to be determined in regional gravity field modeling using RBFs. They are: (1) the shape coefficients; (2) the spectral bandwidths of the RBFs; (3) the radial distances of the RBFs; and (4) the horizontal positions of the RBFs. In the following, the four factors are classified into two categories; both are discussed in detail.

1) The choice of the spatial bandwidths of the RBFs

According to Wittwer (2009), the spatial bandwidth of one RBF is considered as the function's half-width $\psi_{0.5}$, which is defined as the spherical distance where the function attains half of its maximum value. The larger the spatial bandwidth is, the less strong space localizing the RBF has and vice versa. In the light of Eqs (2.79b) and (2.79c), the spatial bandwidth is determined by three factors: (1) the shape coefficients b_n (i.e., the type of RBF); (2) the spectral bandwidth of the RBF, depending on the minimum degree N_{\min} and the maximum degree N_{\max} for nonzero shape coefficients; and (3) the radial distance r_k of the RBF, or the depth $d_k = R - r_k$ below the reference sphere with a radius of R . The effect of the above three factors on the spatial bandwidths of the RBFs has been discussed in Section 2.7.3.

The proper choice of the spatial bandwidth is of biggest importance. Otherwise, RBFs will not have the optimal approximation characteristics. A spatial bandwidth, which is too small, might lead to a good fit of the data to the model and a well-conditioned normal equation system, but to a poor fit at independent control points. Too large spatial bandwidth will result in numerical instabilities as the significant support of neighboring RBFs at one observation point overlaps too much, which leads to similar columns in the design matrix. Such a spatial bandwidth can provide a smooth solution; however, possible leakage will occur as the RBFs are not able to represent the high-frequency signal content contained in the observations.

As concluded in Tenzer and Klees (2008), similar regional gravity field solutions can be computed when using different kinds of RBFs with proper spatial bandwidths. Thus, the RBF type is usually determined before the computations. Bentel et al. (2013) compared different RBFs and their performance using simulated regional gravity data. They showed that the kernel's spatial behavior is much more important for a good regional modeling than the kernel's spectral behavior. Accordingly, the spectral bandwidths of the RBFs are also fixed before the computations. If the input data are residuals with the removal of the long-wavelength contributions, which are derived from a geopotential model up to degree $n = n_{\max}$, the RBFs with $N_{\min} \geq 0$ and $N_{\max} = \infty$ are usually used. In this case, Klees et al. (2008) suggested setting $N_{\min} = n_{\max} + 1$, assuming that there are not enough signals below degree $n_{\max} + 1$ contained in the residuals, or that the input data are represented by a spherical harmonic expansion up to degree n_{\max} and a finite number of RBFs. However, they also pointed out that $N_{\min} = 0$ works fine through numerous numerical experiments with terrestrial gravity data. An explanation was given that the shallow RBFs make the contribution of low-degree Legendre

coefficients negligible. Regarding the non-perfect spectral localizing property of the RBFs and the existence of long-wavelength errors in the residuals, we prefer to choose $0 \leq N_{\min} \leq n_{\max} + 1$ while the value of N_{\min} being dependent on the particular applications. After fixing the type and spectral bandwidths of the RBFs, the choice of optimal spatial bandwidths of the RBFs for regional gravity field modeling is equivalent to the determination of optimal depths of the RBFs. Often, the RBFs are located at gridded or scattered points at a constant depth, which is selected by “trial-and-error” or based on empirically found relations with the data spacing or the gravity anomaly covariance function (e.g., Dampney, 1969; Hardy and Göpfert, 1975; Heikkinen, 1981; Sünkel, 1981; Vermeer, 1995); all RBFs have the same spatial bandwidths in this case. Sometimes, several grids at various depths are used (e.g., Reilly and Herbrechtsmeier, 1978; Heikkinen, 1981; Vermeer, 1983, 1984; Ihde et al., 1998; Chen, 2006), and sometimes, each RBF is placed below one data point at a depth, which is proportional to the distance to the nearest neighboring data point (e.g., Cordell, 1992). Additionally, some advanced strategies involve the generalized cross validation (GCV) technique (e.g., Klees et al., 2008), the adaptation of the RBFs’ depths to the local signal covariance function (e.g., Marchenko et al., 2001), and the direct determination of the depths as well as the scaling coefficients by solving a nonlinear problem (e.g., Barthelmes, 1986; Lehmann, 1993; Claessens et al., 2001).

2) *The choice of the horizontal positions of the RBFs*

The choice of the horizontal positions of the RBFs addresses the issue of how many RBFs are to be used for the modeling. This is important as the number of used RBFs defines the resolution of the gravity field solution. In addition, the chosen horizontal positions should be adapted to the input data to achieve a reasonable solution. There are three possible cases for choosing the horizontal positions:

- ① RBFs are placed on one or more grids.
- ② RBFs are placed on scattered points.
- ③ RBFs are placed on both gridded and scattered points.

In the first case, the RBFs are to be distributed as homogeneously as possible on the surface of a sphere inside the Earth. Therefore, a grid is designed, and the RBFs are placed on the nodes of the grid. Four factors are needed for designing a grid: (1) the grid type; (2) the grid extent; (3) the grid spacing; and (4) the grid depth. The horizontal positions of the RBFs are determined by the first three factors, and the last one is related to the spatial bandwidth. Several kinds of grids on the sphere, such as geographical grid, Driscoll-Healy grid, Reuter grid, triangle center grid, triangle vertex grid, and recursive quasi random grid are summarized and compared in Eicker (2008), suggesting that the Reuter grid and the triangle vertex grid are very well suited as nodal point patterns for RBFs. In this context, only the geographical grid will be used due to its simplicity, and due to the fact that the selected research areas for numerical tests are at medium latitudes. For the areas at high latitudes, the geographical grid should be avoided. The grid extent is usually set to be as large as the data area. If the model area is smaller than the data area, such a choice is satisfactory. However, if the model area is the same as the data area, a larger extent may be preferred such that the edge effect caused by the lack of data outside the model area could be reduced. It should be pointed out that the larger the grid extent than the data area is, the serious the numerical instabilities become. A study about the choice of the grid extent is given in Naeimi (2013). The grid spacing should be carefully chosen to avoid under- and over-parameterization. It also has a high correlation with the grid depth (i.e., spatial bandwidth). Fig. 2.3 shows two examples of three neighboring non-bandlimited RBFs B^{PM} with a grid spacing of 2° at different depths. It can be found that if the grid depth is too deep (see Fig. 2.3b), the neighboring RBFs overlap too much in comparison with the case of a shallow grid (see Fig. 2.3a). This will lead to numerical instabilities. To overcome this problem, we can make the

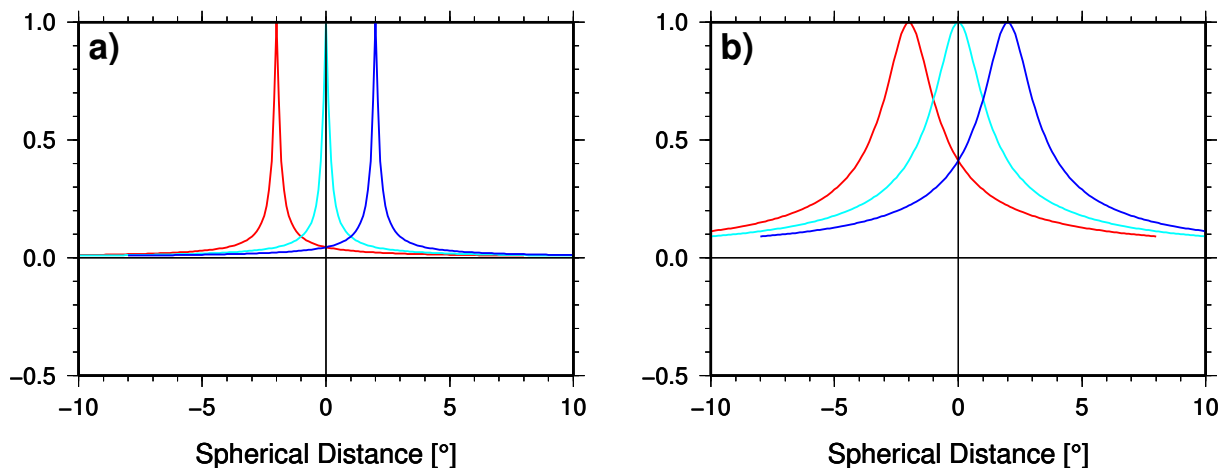


Figure 2.3: Normalized neighboring non-bandlimited B^{PM} with a grid spacing of 2° ; a) grid at a depth of 10 km; b) grid at a depth of 100 km.

grid depth shallower or make the grid spacing larger such that the overlaps between the functions become smaller. Often, one of the two factors (i.e., grid spacing and grid depth) is fixed at first, and then the other one is determined by experimenting with various choices and comparing obtained solutions. Furthermore, the grid spacing should be related to the signal content of the input data. A dense grid is required for the area with rough structures, and a coarse grid is sufficient for smooth signals. However, the signal content is not fully taken into account when employing only one grid for the modeling as all RBFs have the same spatial bandwidths. A hierarchical arrangement of the RBFs by placing them on two or more grids seems to be more reasonable. The deep grid always has a large spacing and extent and is used for modeling the low-frequency signals. The high-frequency signals shall be represented by the grid situated at a shallow depth, of which the spacing and extent is smaller. When the grids are chosen, the number of RBFs is known too. It is also worth mentioning that the effect of data distribution on the choice of the grid spacing is significant. In principle, the grids are well suited for the case with regular data. For the case with irregular data, a relatively coarser grid is advisable to reduce the danger of over-parameterization.

In the second case, the RBF center locations are selected based on the signal content of the input data. Least-squares collocation can be considered as an approach, in which there is one RBF under each observation at an optimal depth, resulting in the high numerical complexity. In practice, it is not necessary to place the RBFs below every data point. The efficient way is to construct a set of RBFs iteratively by adding one RBF at each time. Cordell (1992) designed an algorithm for using the point masses. At each time, one point mass is chosen under the data point with the largest absolute (residual) value at a depth derived from the distance to the nearest neighboring data point, and then the magnitude of the point mass is computed individually. Barthelmes (1986) proposed a similar point mass approach; however, it requires solving a nonlinear problem with four unknowns per point mass, i.e., the 3D position and the magnitude of the point mass. Marchenko et al. (2001) also developed an approach with the use of radial multipoles. The sequential multipole analysis is applied to determine the horizontal position, the order, and the depth of the multipole at each time. The latter two parameters are fixed by using the covariance function of the observations in the vicinity of the data point corresponding to the multipole. Comparing to the approaches using the RBFs on grids, the approaches using scattered RBFs are more flexible and require fewer RBFs for a good approximation; however, they are also more complicated.

An approach that is a compromise between the first and second case is proposed by Klees and Wittwer (2007) and Klees et al. (2008). A coarse grid of RBFs at a depth, which is determined by

the GCV technique, is used to model the smooth signals over the research area. If the approximation quality is not satisfactory, the local refinement is carried out by placing one RBF below the data point with the largest absolute residual value iteratively. A joint least-squares solution is finally computed when all RBFs are fixed. A good approximation can be obtained by this approach with a relatively small number of RBFs.

2.8 The remove-compute-restore technique and topographic effect

In practice, the approximation of regional gravity field is usually based on discrete observations over the area of interest and its surroundings. This always leads to two problems (Denker, 2013): (1) the long-wavelength gravity signals (i.e., longer than the extent of the research area) can not be properly represented by available observations due to the limited data coverage; (2) the representation of very-short-wavelength gravity information is not proper because of the discrete data points, leading to aliasing effects. The employment of a global geopotential model can remedy the first problem well, and the second problem can be counteracted by using a digital terrain model (DTM) to obtain the very-high-frequency gravity signals. As a consequence, the long- and short-wavelength gravity signals are provided by a global geopotential model and a DTM, while the medium-wavelength signals are derived from the discrete residual gravity observations. This computation procedure is called the remove-compute-restore (RCR) technique. It usually can be implemented in three steps:

- ① The short- and long-wavelength information is first removed from the observations, which are described as linear functionals L of the disturbing potential T , resulting in the residual observations:

$$L_{obs}(T^{Res}) = L_{obs}(T) - L_{obs}(T^M) - L_{obs}(T^T), \quad (2.86)$$

where $L_{obs}(T)$ and $L_{obs}(T^{Res})$ are the original and residual observations, $L_{obs}(T^M)$ and $L_{obs}(T^T)$ are the contributions from a global geopotential model and a DTM.

- ② The residual observations are then transformed into other gravity field quantities by applying a proper gravity field modeling technique, e.g., integral method, LSC, or parameterization method using RBFs, yielding

$$L_{obs}(T^{Res}) \xrightarrow{\text{Modeling Technique}} L_{pre}(\hat{T}^{Res}). \quad (2.87)$$

- ③ Finally, the contributions of the global geopotential model and the topography are restored again, leading to the final predictions:

$$L_{pre}(\hat{T}) = L_{pre}(\hat{T}^{Res}) + L_{pre}(\hat{T}^M) + L_{pre}(\hat{T}^T). \quad (2.88)$$

The removal of the short- and long-wavelength gravity information in Step ① can be regarded as a band-pass filtering, resulting in the residual observations with smaller values and smoother structures than the original observations; such residuals can facilitate the field transformation in Step ②. The RCR technique is now a standard procedure for the computation of regional gravity field models; some recent examples can be found in numerous literature, e.g., Denker et al. (2009), Forsberg (2010), Li (2012), Wang et al. (2012), Denker (2013), and Huang and Veronneau (2013).

When using the RCR technique for practical applications, the most suitable global geopotential model for the research area is often chosen to be the one with which the resulting residuals exhibit the smoothest structures. The high-degree geopotential models are preferred as they can provide gravity information as much as possible, and hence make the residuals as smooth as possible. The ultra-high-degree EGM2008 model, which includes coefficients up to degree $n_{\max} = 2190$, corresponding to a

resolution of $5'$ or about 9 km, is a good choice for the reduction of original gravity data. Regarding the areas with high-quality data included in EGM2008, only the short-wavelength gravity signals are necessary to be added by means of terrestrial gravity and terrain data. However, in areas where only poor data were available for EGM2008, the situation may be quite different. In this case, large errors might be introduced into the residuals as the contributions from the EGM2008 model are inaccurate. Therefore, further investigations are needed for the optimal use of EGM2008 in regional gravity field modeling (Forsberg, 2010). Often, the maximum degree of the global geopotential model for data reduction is chosen to be 360, corresponding to a resolution of $30'$ or about 55 km.

After subtracting the contribution of a global geopotential model from the original observations, the terrain reduction is required to remove the very-short-wavelength gravity information. In Forsberg and Tscherning (1981, 1997) and Forsberg (1984), different terrain reduction schemes and the associated advantages and disadvantages are discussed in detail. As the subtracted contribution of a global model also contains the global topographic effect, the residual terrain model (RTM) reduction (Forsberg, 1984) is widely used. It is based on a reference topography surface, which is usually obtained by applying a moving average or other filtering (e.g., a Gaussian filtering) to the given high resolution DTM, and then only the differences between the actual and the reference topography are utilized in the reduction process. If the reference surface is a sufficiently long-wavelength surface, the RTM reduction may be approximated by a Bouguer reduction to the reference level (Forsberg, 1984). Apparently, the resolution R_{rt} of the reference topography should be chosen appropriately. If R_{rt} is too large, one more part of the effect of the topography, which is also included in the geopotential model, is subtracted from the observations again, leading to the so-called “double accounting” of the topography. Some very-short-wavelength signals caused by the topography still remain in the residuals if R_{rt} is too small. Although the numerical studies in Forsberg (2010) showed that the “double accounting” of the topography does not matter in practice, the selection of R_{rt} is based on the maximum degree n_{max} of the reference global geopotential model in this thesis, resulting in

$$R_{rt} = \frac{180}{n_{max}} \times 60 \quad (2.89)$$

in units of arc-minutes, or

$$R_{rt} \approx \frac{20000}{n_{max}} \quad (2.90)$$

in units of km. Assuming that the contribution from a global geopotential model up to degree $n_{max} = 360$ is removed, the corresponding resolution of the reference topography is chosen to be $30'$ or about 55 km. If $n_{max} = 200$, then $R_{rt} = 54'$ or $R_{rt} \approx 100$ km. For more details about the RTM reduction, see the references mentioned above.

In principle, the RCR technique can be applied in combination with all methods for gravity field modeling described in this chapter, such as the integral method, LSC, and parameterization method using RBFs. In the context of this thesis, all numerical computations are carried out with the use of the RCR technique, in which the RTM reduction is applied.

3 Regional gravity field modeling with the point mass method

In the previous chapter, we have introduced several methods for regional gravity field modeling, e.g., integral method, LSC, and parameterization method using RBFs. The point mass method, which is equivalent to the method using the RBFs with the point mass kernel, will be applied for computation of the regional gravity field in this thesis. Correspondingly, the principle of the point mass method and the computation procedures will be described in detail in this chapter. In Section 3.1, the relation between the point masses and the disturbing potential is discussed. A set of standard formulas of the point mass method for representing different gravity field quantities are presented in Section 3.2. These formulas are the basis for constructing the observation equations. Since only the least-squares case is considered in this thesis, the computation procedures for solving a linear or nonlinear equation system, as well as the regularization process that aims at stabilizing the solution, are then introduced in Section 3.3. In the next two sections, the details of the point mass methods with fixed and free positions are described. Both approaches will be applied for the numerical computations in Chapter 4.

3.1 Point masses and disturbing potential

According to Newton's law of gravitation, the disturbing potential T can be obtained according to

$$T = G \int_M \frac{dM}{\ell}, \quad (3.1)$$

where dM is the mass element, ℓ is the distance between the mass element and the computation point. If an anomalous mass distribution is known, the disturbing potential T at any point on and outside of the Earth's surface can be fully described by Eq. (3.1). However, a complete knowledge of the anomalous mass distribution is not possible in practice. A practicable way is to determine the anomalous masses based on the observed gravity field quantities first, and then to represent the disturbing potential by using estimated anomalous masses. The first process can be considered as a gravimetric inverse problem, and the second process is called forward modeling. A given disturbing potential can be generated by different anomalous mass distributions, the non-uniqueness of the inverse problem is inevitable. In geodetic applications, the only quantity of interest is often the gravity field itself, and not the internal density structure of the Earth. Accordingly, an anomalous mass model (including the mass magnitudes and mass distribution) that agrees well with the parameters of the gravity field can always be chosen in these applications. Then, all gravity field quantities that are uniquely determined by the gravity field can be computed by this model. Now, there arises an issue of how to construct such an anomalous mass model. In the context of this thesis, we work within the framework of the Runge-Krarup theorem (Krarup, 1969; Moritz, 1980):

Any harmonic function Φ , regular outside the Earth's surface, may be uniformly approximated by the harmonic functions ϕ , regular outside an arbitrary given sphere S inside the Earth, in the sense that for any given $\epsilon > 0$, the relation $|\Phi - \phi| < \epsilon$ holds everywhere outside and on any closed surface completely surrounding the Earth's surface.

The number ϵ may be arbitrarily small, and the surrounding surface may be arbitrarily close to the Earth's surface. As a consequence, the task of finding an anomalous mass model that will generate

the true disturbance potential T is simplified to find a set of anomalous masses, which will represent the disturbing potential T' in the space outside of a given surface S that encloses all of the anomalous masses to assure that T' can be taken as an approximation of T at points on and outside of the Earth's surface. It follows that the anomalous mass positions as well as their masses are the key factors for a good approximation of the gravity field. Imagining that there are infinitely many small spheres (intersect or not) inside the surface S , each of which has a certain positive or negative anomalous density, the use of all spheres for gravity field modeling can be replaced by using their center points with the same masses as the spheres, as the gravity potential caused by a spherically symmetric body at the point outside of this body is the same as if all masses were concentrated in the center. This leads to the point mass method for gravity field modeling in the geodetic literature, e.g., Needham (1970), Heikkinen (1981), Barthelmes (1986), Vermeer (1995), and Antunes et al. (2003), or to the equivalent source method in geophysics for the interpolation of gravity anomalies, e.g., Dampney (1969) and Cordell (1992). Herein, the approximation problem is reduced to the determination of a set of point masses at proper positions. In practical applications, the number of point masses is always finite. Assuming K point masses enclosed by a given spherical surface S inside the topographic masses, the disturbing potential T at point i exterior to the Earth's surface is given as

$$T(\phi_i, \lambda_i, r_i) = G \sum_{k=1}^K \frac{m_k}{\ell_{ik}} = \sum_{k=1}^K \frac{\beta_k}{\ell_{ik}} = \sum_{k=1}^K \beta_k B^{\text{PM}}(\mathbf{r}_i, \mathbf{r}_k) \quad (3.2)$$

in accordance with Eqs (2.79) and (2.80). In the above equation, m_k is the mass for the k -th point mass, $\beta_k = Gm_k$ is called the magnitude of the k -th point mass in this thesis, and $1/\ell_{ik}$ represents the reciprocal distance between the computation point and the point mass, being equivalent to the non-bandlimited RBFs with the point mass kernel $B^{\text{PM}}(\mathbf{r}_i, \mathbf{r}_k)$, see Case 1 in Eq. (2.82). Obviously, the point mass method given in Eq. (3.2) only represents one of the four cases of the parameterization method using $B^{\text{PM}}(\mathbf{r}_i, \mathbf{r}_k)$. No matter which $B^{\text{PM}}(\mathbf{r}_i, \mathbf{r}_k)$ is used, the corresponding method is always called the point mass method in the remaining of this thesis. Spherical approximation is applied for practical computations using the point mass method, where the mean Earth radius $R = 6371$ km is used for the reference sphere (Moritz, 1980).

3.2 Standard formulas for the point mass method

Eq. (3.2) is regarded as the fundamental observation equation for the point mass method. Unfortunately, the disturbing potential is always not available from the terrestrial gravity measurements. Instead, the commonly available observations are the linear functionals of the disturbing potential. Some examples of them are the gravity anomalies Δg from terrestrial or shipborne gravimetry, the gravity disturbances δg from airborne gravimetry, the deviations between the sea surface and the reference ellipsoid (here we consider them roughly as the geoid heights N) from satellite altimetry, and the height anomalies ζ , which are obtained as the differences between GPS (Global Positioning System) ellipsoidal heights and leveled normal heights. Using the relationships in spherical approximation, which are given in Eqs (2.21a), (2.21b), and (2.21e), the functional models between the point masses and related gravity field quantities are given as follows:

$$\Delta g(\phi_i, \lambda_i, r_i) = \sum_{k=1}^K \beta_k D_{\Delta g} B^{\text{PM}}(\mathbf{r}_i, \mathbf{r}_k), \quad (3.3a)$$

$$\delta g(\phi_i, \lambda_i, r_i) = \sum_{k=1}^K \beta_k D_{\delta g} B^{\text{PM}}(\mathbf{r}_i, \mathbf{r}_k), \quad (3.3b)$$

$$N/\zeta(\phi_i, \lambda_i, r_i) = \sum_{k=1}^K \beta_k D_{N/\zeta} B^{\text{PM}}(\mathbf{r}_i, \mathbf{r}_k), \quad (3.3c)$$

with the RBFs in the form of

$$\begin{cases} D_{\Delta g} B^{\text{PM}}(\mathbf{r}_i, \mathbf{r}_k) = \left(\frac{r_i - r_k \cos \psi_{ik}}{\ell_{ik}^3} - \frac{2}{\ell_{ik} r_i} \right) = \sum_{n=0}^{\infty} \frac{n-1}{r_k r_i} \left(\frac{r_k}{r_i} \right)^{n+1} P_n(\cos \psi_{ik}), \\ D_{\delta g} B^{\text{PM}}(\mathbf{r}_i, \mathbf{r}_k) = \left(\frac{r_i - r_k \cos \psi_{ik}}{\ell_{ik}^3} \right) = \sum_{n=0}^{\infty} \frac{n+1}{r_k r_i} \left(\frac{r_k}{r_i} \right)^{n+1} P_n(\cos \psi_{ik}), \\ D_{N/\zeta} B^{\text{PM}}(\mathbf{r}_i, \mathbf{r}_k) = \frac{1}{\gamma_i'} \left(\frac{1}{\ell_{ik}} \right) = \sum_{n=0}^{\infty} \frac{1}{\gamma_i' r_k} \left(\frac{r_k}{r_i} \right)^{n+1} P_n(\cos \psi_{ik}). \end{cases} \quad (3.3d)$$

In the above equations, $D_{\Delta g}$, $D_{\delta g}$, and $D_{N/\zeta}$ are the gravity anomaly operator, the gravity disturbance operator, and the geoid height/height anomaly operator, respectively.

In Section 2.8, we mentioned that all numerical computations are carried out in the framework of the RCR technique in the context of this thesis. This means that the residual observations, which are obtained after the contributions of a global geopotential model complete to degree n_{max} and of the topography computed from a DTM have been subtracted, are used as input. The resulting residuals are almost bandlimited, and hence it is reasonable to modify the non-bandlimited RBFs given in Eq. (3.3d) to make the spectral bandwidths of the input data and the RBFs compatible. Considering Eq. (2.81), the functional models in Eq. (3.3) are rewritten as

$$\Delta g(\phi_i, \lambda_i, r_i) = \sum_{k=1}^K \beta_k \sum_{n=N_{\text{min}}}^{N_{\text{max}}} \frac{n-1}{r_k r_i} \left(\frac{r_k}{r_i} \right)^{n+1} P_n(\cos \psi_{ik}), \quad (3.4a)$$

$$\delta g(\phi_i, \lambda_i, r_i) = \sum_{k=1}^K \beta_k \sum_{n=N_{\text{min}}}^{N_{\text{max}}} \frac{n+1}{r_k r_i} \left(\frac{r_k}{r_i} \right)^{n+1} P_n(\cos \psi_{ik}), \quad (3.4b)$$

$$N/\zeta(\phi_i, \lambda_i, r_i) = \sum_{k=1}^K \beta_k \sum_{n=N_{\text{min}}}^{N_{\text{max}}} \frac{1}{\gamma_i' r_k} \left(\frac{r_k}{r_i} \right)^{n+1} P_n(\cos \psi_{ik}). \quad (3.4c)$$

In principle, N_{max} should be chosen based on the resolution of the used DTM as there are no very high frequencies in the residuals. In this case, the RBFs are computed by summing a series expansion up to a rather high degree. Regarding the computational complexity, N_{max} is often set to be ∞ in practice, so that we can make use of the analytical expressions of the RBFs as given in Eq. (3.3d). However, the above treatment of N_{max} may introduce additional errors into the solution. According to numerous experiments, the spatial bandwidths of the RBFs with the point mass kernel for $N_{\text{max}} \geq 2160$ look close to the case of $N_{\text{max}} = \infty$. In practical applications, the resolution of the DTM is usually higher than $1'$, which is equivalent to the degree 10800. Therefore, the additional errors caused by using $N_{\text{max}} = \infty$ can often be neglected and will not be discussed in this thesis. In the light of the discussion in Section 2.7.4, $0 \leq N_{\text{min}} \leq n_{\text{max}} + 1$ is selected. Combing Eq. (3.3d) and Eqs (3.4a)–(3.4c), yields

$$\Delta g(\phi_i, \lambda_i, r_i) = \sum_{k=1}^K \beta_k \underbrace{\left[\left(\frac{r_i - r_k \cos \psi_{ik}}{\ell_{ik}^3} - \frac{2}{\ell_{ik} r_i} \right) - \sum_{n=0}^{N_{\text{min}}-1} \frac{n-1}{r_k r_i} \left(\frac{r_k}{r_i} \right)^{n+1} P_n(\cos \psi_{ik}) \right]}_{D_{\Delta g} B^{\text{PM}}(\mathbf{r}_i, \mathbf{r}_k)}, \quad (3.5a)$$

$$\delta g(\phi_i, \lambda_i, r_i) = \sum_{k=1}^K \beta_k \underbrace{\left[\left(\frac{r_i - r_k \cos \psi_{ik}}{\ell_{ik}^3} \right) - \sum_{n=0}^{N_{\text{min}}-1} \frac{n+1}{r_k r_i} \left(\frac{r_k}{r_i} \right)^{n+1} P_n(\cos \psi_{ik}) \right]}_{D_{\delta g} B^{\text{PM}}(\mathbf{r}_i, \mathbf{r}_k)}, \quad (3.5b)$$

$$N/\zeta(\phi_i, \lambda_i, r_i) = \sum_{k=1}^K \beta_k \underbrace{\left[\frac{1}{\gamma_{i'}} \left(\frac{1}{\ell_{ik}} \right) - \sum_{n=0}^{N_{\min}-1} \frac{1}{\gamma_{i'} r_k} \left(\frac{r_k}{r_i} \right)^{n+1} P_n(\cos \psi_{ik}) \right]}_{D_{N/\zeta} B^{\text{PM}}(\mathbf{r}_i, \mathbf{r}_k)}. \quad (3.5c)$$

Accordingly, a general formula for the point mass representation of any linear functional $l_i = L_i T$ is given as

$$l(\phi_i, \lambda_i, r_i) = \sum_{k=1}^K \beta_k \underbrace{\left\{ L_i \left(\frac{1}{\ell_{ik}} \right) - \sum_{n=0}^{N_{\min}-1} L_i \left[\frac{1}{r_k} \left(\frac{r_k}{r_i} \right)^{n+1} P_n(\cos \psi_{ik}) \right] \right\}}_{D_l B^{\text{PM}}(\mathbf{r}_i, \mathbf{r}_k)}. \quad (3.6)$$

In the following, the term $D_l B^{\text{PM}}(\mathbf{r}_i, \mathbf{r}_k)$ in Eq. (3.6) will be named as the full point mass RBF with respect to the observation l in the case of $N_{\min} = 0$. When $N_{\min} > 0$, it is called the reduced point mass RBF. In comparison to the full point mass RBFs, the larger the truncation degree $N_{\min} - 1$ is, the more computation time is needed for the reduced RBFs. It should be noted that the choice of the truncation degree may also depend on the types of the input and output data, in particular the latter one. Fig. 3.1 shows the full and reduced point mass RBFs $D_{\Delta g} B^{\text{PM}}$ with respect to the gravity anomalies at different depths using Eq. (3.5a). The other parameters for this example are the same as the ones for Fig. 2.2. Comparing Figs 3.1a and 3.1b to Figs 2.2a and 2.2b, it can be seen that the RBFs $D_{\Delta g} B^{\text{PM}}$ have much stronger space localizing characteristics than the B^{PM} with respect to the disturbing potential at each depth. The spatial bandwidths of $D_{\Delta g} B^{\text{PM}}$ are less dependent on the depths of the RBFs as well as on the removal of low frequencies from the RBFs. Consequently, it can be expected that, if the input is the residual gravity anomaly and the output is the geoid height or height anomaly, the use of the reduced point mass RBFs seems to be necessary. If the input and the output are interchanged, the full point mass RBFs may also work fine. This issue will be further investigated by the numerical tests in Chapter 4.

Concerning Eqs (2.78) and (2.81) in the case when K point mass RBFs are used for regional gravity field modeling, it is easy to transform the estimated point mass RBFs into the equivalent Stokes coefficients according to

$$\begin{cases} \bar{c}_{nm}^e = \sum_{k=1}^K \left(\frac{r_k}{R} \right)^n \frac{\beta_k}{(2n+1)GM} \bar{Y}_{nm}(\phi_k, \lambda_k) & \text{for } N_{\min} \leq n \leq N_{\max} \\ \bar{c}_{nm}^e = 0 & \text{otherwise} \end{cases}. \quad (3.7)$$

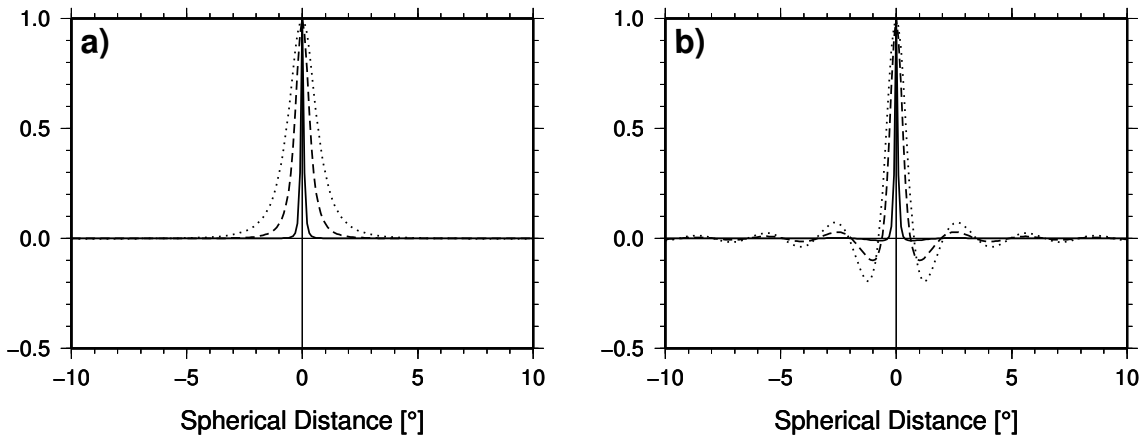


Figure 3.1: Normalized $D_{\Delta g} B^{\text{PM}}$ at a depth of 10 km (solid lines), 50 km (dashed lines), and 100 km (dotted lines); a) the full RBFs with $N_{\min} = 0$; b) the reduced RBFs with $N_{\min} = 120$.

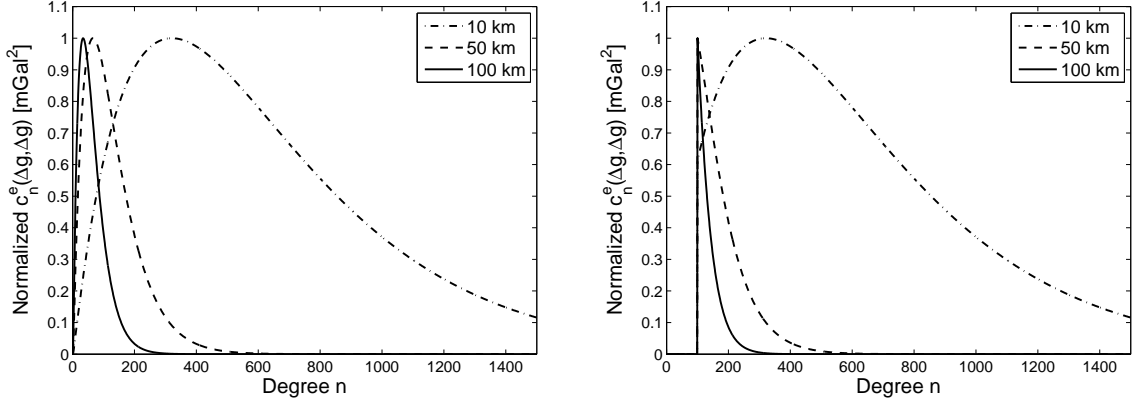


Figure 3.2: Normalized degree variances $c_n^e(\Delta g, \Delta g)$ derived from a single full point mass RBF (left, $N_{\min} = 0$) and a single reduced RBF (left, $N_{\min} = 100$) at different depths.

On the basis of Eqs (2.65b), (2.54), (2.58c), and (2.69), the degree variances for the gravity anomaly derived from the equivalent Stokes coefficients are given by

$$\begin{cases} c_n^e(\Delta g, \Delta g) = \frac{(n-1)^2}{(2n+1)(GM)^2 r_P r_Q} \sum_{k=1}^K \sum_{j=1}^K \left(\frac{r_k}{R}\right)^n \left(\frac{r_j}{R}\right)^n \beta_k \beta_j P_n(\cos \psi_{kj}) & \text{for } N_{\min} \leq n \leq N_{\max} \\ c_n^e(\Delta g, \Delta g) = 0 & \text{otherwise} \end{cases}, \quad (3.8)$$

in which r_P and r_Q are the radial distances of the observation points P and Q , respectively. For the full point mass RBFs, i.e., $N_{\min} = 0$ in Eqs (3.5) and (3.6), the equivalent Stokes coefficients \bar{c}_{nm}^e and the degree variances $c_n^e(\Delta g, \Delta g)$ are nonzero for all degrees. For the reduced RBFs (i.e., $N_{\min} > 0$), \bar{c}_{nm}^e and $c_n^e(\Delta g, \Delta g)$ are equal to 0 for $n < N_{\min}$.

Suppose that only a single point mass RBF k is at a depth of d km below a sphere with a radius of $R = 6371$ km on which all observations are located, Eq. (3.8) is then simplified as

$$\begin{cases} c_n^e(\Delta g, \Delta g) = \frac{(n-1)^2}{(2n+1)(GMR)^2} \left(\frac{r_k}{R}\right)^{2n} \beta_k^2 & \text{for } N_{\min} \leq n \leq N_{\max} \\ c_n^e(\Delta g, \Delta g) = 0 & \text{otherwise} \end{cases} \quad (3.9)$$

with $r_k = R - d$. From Eq. (3.9) it follows that the spectrum of a single point mass RBF also depends on its depth. As an example, a single full point mass RBF and a single reduced RBF with $N_{\min} = 100$ at the depths of $d = 10, 50,$ and 100 km are studied. The corresponding normalized degree variances $c_n^e(\Delta g, \Delta g)$ are illustrated in Fig. 3.2. The spectrum of a point mass RBF at a shallow depth (e.g., at a depth of 10 km) covers a wide range of frequencies. Its power is mainly concentrated in the high-frequency part. The spectrum derived from the point mass RBF at a deep depth (e.g., at a depth of 50 or 100 km) has a narrow shape, only concentrating in the low-frequency part. Accordingly, a deep point mass RBF mainly contributes to the low-frequency signals, while the RBF at a shallow depth is capable of representing the high-frequency signals. Comparing to the smooth edges of the spectrum associated with the full point mass RBFs (Fig. 3.2, left panel), there are sharp edges in the spectrum obtained from the reduced RBFs (Fig. 3.2, right panel), and the signals below the degree $n = 100$ are not recovered for all three cases with different depths. The reduced RBF at a deep depth only has a minor contribution to the gravity anomaly solution as most power of its spectrum is cut. The contribution from the RBF at a shallow depth is significant. Such properties of the reduced point mass RBFs are quite suitable for regional gravity field computations with the use of the RCR technique, as one assumes that the low-frequency signals are mainly provided by a global geopotential

model.

Previously, we have proposed a scheme to deal with the case of residual input by truncating the full point mass RBFs (i.e., reduced RBFs). The resulting RBFs will be used to construct an observation equation system. Alternatively, another scheme will be introduced by adding constraints to the observation equation system, which is constructed by the full point mass RBFs.

At first, we consider that the input gravity data contain full frequencies. In this case, it is reasonable to use the full point mass RBFs for the modeling. As a result, the equivalent Stokes coefficients \bar{c}_{nm}^e are nonzero for all degrees, see Eq. (3.7). There are no Stokes coefficients \bar{c}_{nm} for $n = 0, 1$ in the spherical harmonic expansions of the input gravity field quantities, see the example of the disturbing potential given in Eq. (2.65a). Therefore, it appears to be necessary to set the relevant equivalent Stokes coefficients to be 0, leading to

$$\begin{cases} \Delta \bar{C}_{00}^e = \sum_{k=1}^K \frac{\beta_k}{GM} = 0 \\ \Delta \bar{C}_{10}^e = \sum_{k=1}^K \left(\frac{r_k}{R}\right) \frac{\beta_k}{3GM} \sin \phi_k = 0 \\ \Delta \bar{C}_{11}^e = \sum_{k=1}^K \left(\frac{r_k}{R}\right) \frac{\beta_k}{3GM} \cos \phi_k \cos \lambda_k = 0 \\ \Delta \bar{S}_{11}^e = \sum_{k=1}^K \left(\frac{r_k}{R}\right) \frac{\beta_k}{3GM} \cos \phi_k \sin \lambda_k = 0 \end{cases} \quad (3.10)$$

The above four formulas will be used as constraints when estimating the magnitudes of the full point mass RBFs in the least-squares sense. Similarly, if the input gravity data are the residuals with the removal of the long-wavelength components derived from a global geopotential model up to degree $n = n_{\max}$, a set of constraints is given as

$$\begin{cases} \Delta \bar{C}_{nm}^e = \sum_{k=1}^K \left(\frac{r_k}{R}\right)^n \frac{\beta_k}{(2n+1)GM} \bar{P}_{nm}(\sin \phi_k) \cos(m\lambda_k) = 0 & \text{for } 0 \leq n \leq n' \text{ and } 0 \leq m \leq n \\ \Delta \bar{S}_{nm}^e = \sum_{k=1}^K \left(\frac{r_k}{R}\right)^n \frac{\beta_k}{(2n+1)GM} \bar{P}_{nm}(\sin \phi_k) \sin(m\lambda_k) = 0 & \text{for } 0 < n \leq n' \text{ and } 0 < m \leq n \end{cases}, \quad (3.11)$$

resulting in $(n' + 1)^2$ additional equations. Assuming that the residual input data do not contain enough long-wavelength signals below degree n_{\max} , n' can be equal to or smaller than n_{\max} . On the one hand, the chosen n' should be capable of providing a good solution. On the other hand, n' is preferred to be as small as possible so that high computational burden can be avoided.

As discussed in Section 2.7.4, the spatial bandwidths and the horizontal positions of the RBFs serve as two important aspects for obtaining a good regional gravity field solution. Thus, it is necessary to choose them appropriately. For a good choice of each aspect, several factors need to be defined properly. Fig. 3.3 shows the structure of the RBFs. We can see that the simultaneous determination of both spatial bandwidths and horizontal positions of the RBFs for optimal regional gravity field modeling is not possible as too many factors need to be determined (see the green boxes in Fig. 3.3). A practicable way is to fix some of them to reduce the degree of complexity of the model while keeping the other factors free. The extreme case is to fix both spatial bandwidths and horizontal positions of the RBFs before parameter estimation. Since the point mass method is used for the modeling in this thesis, the shape coefficients of the RBFs are always fixed. The spectral bandwidths of the point mass RBFs are usually defined based on the spectrum of the input data. As a consequence, the remaining free factors are the radial distances of the point mass RBFs and their horizontal positions, or equivalently, are their 3D positions. According to the strategy for determining the RBF positions, the point mass method can simply be divided into two groups:

- Point mass method with fixed positions (PM-FIX),
- Point mass method with free positions (PM-FRE).

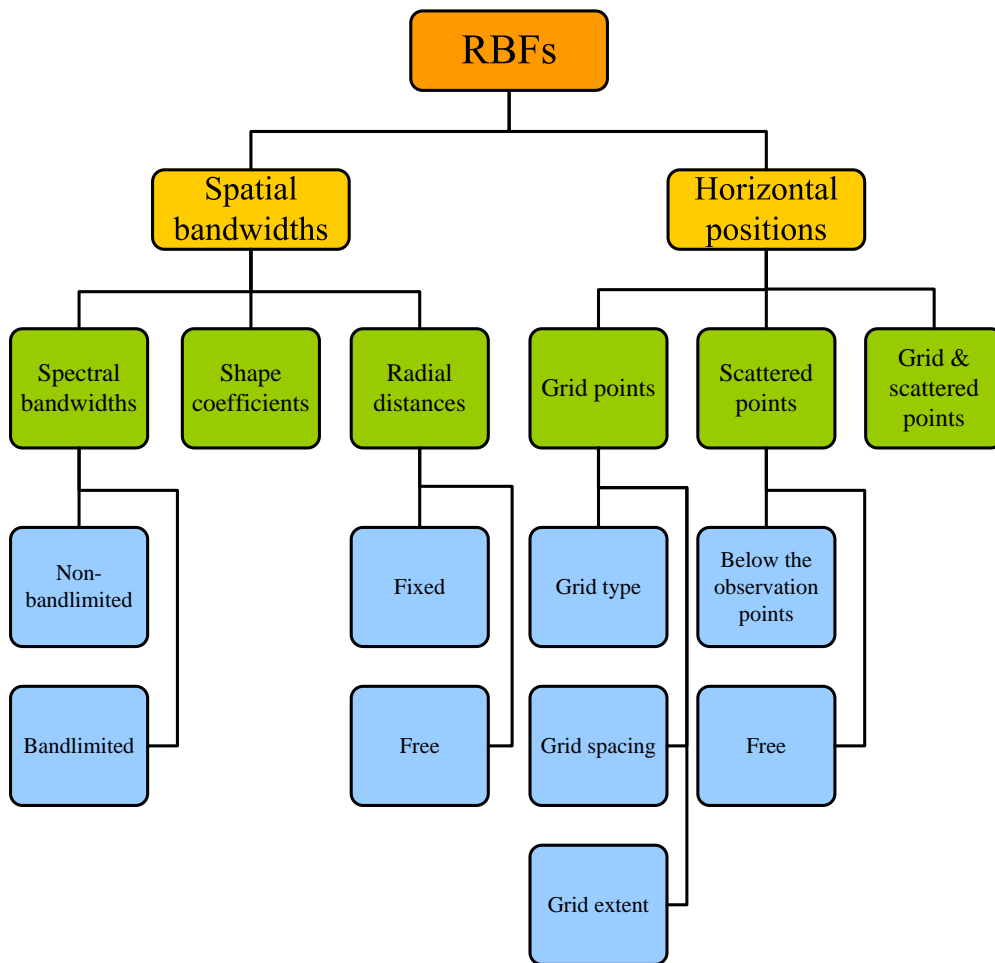


Figure 3.3: Structural diagram of the RBFs.

Both methods will be discussed in this thesis, where the latter one is the main contribution. Before introducing the two methods, we prefer to review the estimation principle first, which will be applied for estimating the unknown parameters in the two methods.

3.3 Least-squares estimation and regularization

3.3.1 Inverse problems and ill-posedness

Most inverse problems describe the continuous physical world and take the form of Fredholm integral equations of the first kind. These problems arise in many disciplines such as geophysics, medical physics, image and signal processing, astrophysics, and geodesy. The general form of this integral equation is given by

$$\int_{\Omega} K(s_i, t) x(t) dt = l(s_i), \tag{3.12}$$

where $K(s_i, t)$ is a smoothing kernel, describing the process, $l(s_i)$ is the measured data as a function of the time or position s_i , and Ω is the domain of integration. The purpose of the inverse problem is to find the model $x(t)$ at the time or position t based on the given l . Given the model x , to compute the data l is consequently called the forward modeling. In practical computations, the continuous system given by Eq. (3.12) needs to be discretized. There are two approaches: (1) the continuous system is discretized with a number of model parameters K that is smaller than the number of observations I , leading to an overdetermined system; (2) the system is discretized with $K > I$, resulting in an

underdetermined system. In gravity field modeling, the first approach is considered. When the kernel $K(s_i, t)$ is linear with respect to the model $x(t)$, the integral equation in Eq. (3.12) can be rewritten in matrix-vector notation after discretization:

$$\mathbf{A}\mathbf{x} = \mathbf{l}, \quad (3.13)$$

where $\mathbf{A}: X \rightarrow L$ is a linear operator mapping the unknown vector space X to the observation vector space L with $\mathbf{x} \in X$ and $\mathbf{l} \in L$. Comparing Eq. (3.13) to Eq. (3.12), the matrix \mathbf{A} is constructed from the kernel $K(s_i, t)$, the vectors \mathbf{x} and \mathbf{l} are related to the model $x(t)$ and the data $l(s_i)$, respectively.

According to the definitions in Hadamard (1923), the inverse problem is regarded as “well-posed” only in the case that it satisfies the following three requirements:

- \mathbf{A} is surjective so that Eq. (3.13) is solvable for all $\mathbf{l} \in L$ (**existence**).
- \mathbf{A} is injective so that Eq. (3.13) has only one solution $\mathbf{x} \in X$ (**uniqueness**).
- \mathbf{A}^{-1} exists but also is continuous with respect to the data so that a small change in the data also leads to a small change in the model (**stability**).

As soon as any one of the above requirements is violated, the problem is then said to be “ill-posed” or “improperly posed”. In the field of geodesy, since the model parameters are often not subject to direct observations, one frequently has to deal with the inverse problem. Inverse problem is usually ill-posed as very often at least one of the conditions mentioned above is not satisfied. A typical inverse problem for the non-uniqueness is the determination of the mass distribution in the interior of the Earth from the exterior gravity field observations, as infinitely many mass distributions can produce the same exterior gravity field. In gravity field modeling using spherical harmonics or radial basis functions, the issue of **existence** and **uniqueness** can properly be resolved by introducing additional requirements to the solutions. For example, the solution $\hat{\mathbf{x}}$ computed by minimizing $\|\mathbf{l} - \mathbf{A}\mathbf{x}\|^2$ in the least-squares sense can be considered as the best approximation to the exact solution \mathbf{x} if minimal variance of the data misfit is desired. In the context of this thesis, further investigation on the ill-posedness is due to the lack of **stability**; such an ill-posed problem can be solved by employing a so-called regularization, which will be discussed later. In regional gravity field modeling using the point mass RBFs, the missing stability might be caused by the following factors:

- In the case of using airborne gravity data for the calculation of gravity field functionals on the Earth’s surface, the downward continuation causes an ill-posed problem, as the data errors and unmodeled signals are strongly amplified especially in the high-frequency part of the spectrum.
- Irregular data distribution or data gaps, which often occur in the case when using terrestrial gravity data for the modeling, lead to numerical instabilities.
- Very-deep or closely located point mass RBFs, which result in similar columns in the design matrix, cause numerical instabilities.

3.3.2 Characteristics of inverse problems

Most inverse problems have common characteristics. A powerful tool to identify the instability of an inverse problem expressed by Eq. (3.13) is to examine the spectral behavior of the linear operator (or the design matrix) $\mathbf{A} \in \mathbb{R}^{I \times K}$ by the Singular Value Decomposition (SVD) (e.g., Golub and van Loan, 1996; Hansen, 1997), yielding

$$\mathbf{A} = \mathbf{U}\mathbf{\Sigma}\mathbf{V}^T = \sum_{i=1}^K \mathbf{u}_i \sigma_i \mathbf{v}_i^T \quad \text{with} \quad \mathbf{\Sigma} = \begin{pmatrix} \mathbf{\Sigma}_K \\ 0 \end{pmatrix}, \quad (3.14)$$

where $\mathbf{U} = (\mathbf{u}_1, \dots, \mathbf{u}_I) \in \mathbb{R}^{I \times I}$ is an orthogonal matrix that spans the data space, satisfying $\mathbf{U}^T \mathbf{U} = \mathbf{U} \mathbf{U}^T = \mathbf{I}$, $\mathbf{V} = (\mathbf{v}_1, \dots, \mathbf{v}_K) \in \mathbb{R}^{K \times K}$ is an orthogonal matrix that spans the model space, satisfying $\mathbf{V}^T \mathbf{V} = \mathbf{V} \mathbf{V}^T = \mathbf{I}$. The orthogonal vectors \mathbf{u}_i and \mathbf{v}_i are the corresponding left and right singular vectors, satisfying the following relations

$$\begin{cases} \mathbf{u}_i^T \mathbf{u}_i = \mathbf{v}_i^T \mathbf{v}_i = 1 \\ \mathbf{A} \mathbf{v}_i = \sigma_i \mathbf{u}_i \\ \mathbf{A}^T \mathbf{u}_i = \sigma_i \mathbf{v}_i \end{cases} . \quad (3.15)$$

The matrix $\mathbf{\Sigma} \in \mathbb{R}^{I \times K}$ contains a diagonal matrix $\mathbf{\Sigma}_K = \text{diag}(\sigma_1, \dots, \sigma_K)$ with the singular values σ_i , which are arranged in decreasing order such that

$$\sigma_1 \geq \sigma_2 \geq \dots \geq \sigma_K > 0. \quad (3.16)$$

The condition number for the design matrix \mathbf{A} is equal to the ratio σ_1/σ_K (e.g., Hansen, 2008). If the singular values of \mathbf{A} descend too fast, the linear system in the form of Eq. (3.13) is considered as ill-posed, resulting in a large condition number. The matrix \mathbf{A} is then said to be ‘‘ill-conditioned’’. In the extreme case such that one or more singular values equal zero, the matrix \mathbf{A} does not have full column rank and is said to be ‘‘rank deficient’’.

The singular values σ_i of the design matrix \mathbf{A} can be connected to the eigenvalues λ_i of the normal matrix by the relation $\mathbf{N} = \mathbf{A}^T \mathbf{A} = \mathbf{V} \mathbf{\Sigma}^2 \mathbf{V}^T = \mathbf{V} \mathbf{\Lambda} \mathbf{V}^T$ with $\mathbf{\Lambda} = \text{diag}(\lambda_1, \dots, \lambda_K) = \text{diag}(\sigma_1^2, \dots, \sigma_K^2)$. The condition number of \mathbf{N} is consequently equal to the ratio σ_1^2/σ_K^2 . Although it is very difficult to prove in general, the large singular values are associated with smooth singular vectors, and the small singular values are associated with oscillatory vectors (Hansen, 2008). It can also be interpreted in such a way that smooth singular vectors are associated with low frequencies and oscillatory singular vectors correspond to high frequencies. Considering Eq. (3.14), the mapping $\mathbf{A} \mathbf{x}$ of a vector \mathbf{x} can be described by

$$\mathbf{A} \mathbf{x} = \sum_{i=1}^K \sigma_i (\mathbf{v}_i^T \mathbf{x}) \mathbf{u}_i = \mathbf{l}. \quad (3.17)$$

Here the high-frequency components of \mathbf{x} are more damped during the mapping process due to the multiplication with small singular values σ_i . Therefore, the smoothness of the mapping is guaranteed by the smoothing property of the matrix \mathbf{A} . On the other hand, when solving for \mathbf{x} from the equation system in Eq. (3.17), the solution is given by

$$\hat{\mathbf{x}} = \sum_{i=1}^K \frac{\mathbf{u}_i^T \mathbf{l}}{\sigma_i} \mathbf{v}_i. \quad (3.18)$$

It becomes obvious that the high frequencies of the observations \mathbf{l} are amplified by large factor $1/\sigma_i$ with increasing i , requiring that the observations must not be arbitrarily rough as the terms $\mathbf{u}_i^T \mathbf{l}$ have to decay faster than the singular values σ_i to achieve the convergence of the solution $\hat{\mathbf{x}}$. This requirement is described as the discrete Picard condition in Hansen (2008). However, if errors exist in the observations the Picard condition might be violated. For example, the white noise is of equal magnitude for all frequencies, and its effect on the solution becomes more severe when i increases. In this case, the inverse problem is unstable.

3.3.3 Linear least-squares solution

In the following, the process for estimating the unknown gravity field parameters from a linear equation system will be described. It represents a standard Gauss-Markov model, which is based on the assumptions that the observation errors have an expectation of zero, and that the covariance matrix of the observations is known a priori. The functional model and stochastic model then read (Koch, 1999):

$$\mathbf{l} - \mathbf{e} = \mathbf{A}\mathbf{x} \quad \text{with} \quad E(\mathbf{e}) = \mathbf{0} \quad \text{and} \quad D(\mathbf{e}) = D(\mathbf{l}) = \sigma_e^2 \mathbf{P}_e^{-1}. \quad (3.19)$$

Here \mathbf{l} is the $I \times 1$ vector containing observed gravity field quantities, \mathbf{e} is the $I \times 1$ vector of random observation errors, $D(\mathbf{e}) = D(\mathbf{l}) = \sigma_e^2 \mathbf{P}_e^{-1}$ represents the $I \times I$ covariance matrix of \mathbf{e} with \mathbf{P}_e the weight matrix of the observations and σ_e^2 the corresponding positive variance factor, and \mathbf{x} is the $K \times 1$ vector of unknown gravity field parameters, such as the Stokes coefficients for spherical harmonics or the magnitudes for the point mass method. The $I \times K$ design matrix \mathbf{A} describes the functional relation between \mathbf{x} and \mathbf{l} . For the sake of simplicity, $D(\mathbf{e})$ is denoted as \mathbf{D}_e in the following.

The objective function, which needs to be minimized in the least-squares adjustment, is given as the weighted square sum of the residuals

$$\Phi(\mathbf{x}) = \frac{1}{\sigma_e^2} (\mathbf{l} - \mathbf{A}\mathbf{x})^T \mathbf{P}_e (\mathbf{l} - \mathbf{A}\mathbf{x}) = \|(\mathbf{l} - \mathbf{A}\mathbf{x})\|_{\mathbf{D}_e^{-1}}^2. \quad (3.20)$$

The minimum of $\Phi(\mathbf{x})$ can be achieved by differentiating with respect to \mathbf{x} and forcing it to zero, i.e., $\partial\Phi(\mathbf{x})/\partial\mathbf{x} = 0$. This results in a system of normal equations

$$\mathbf{N}\mathbf{x} = \mathbf{y}, \quad (3.21)$$

in which $\mathbf{N} = \mathbf{A}^T \mathbf{P}_e \mathbf{A}$ and $\mathbf{y} = \mathbf{A}^T \mathbf{P}_e \mathbf{l}$. The estimation of the unknown gravity field parameters by means of least-squares adjustment is consequently the solution of the normal equation system, yielding

$$\hat{\mathbf{x}} = \mathbf{N}^{-1} \mathbf{y} = (\mathbf{A}^T \mathbf{P}_e \mathbf{A})^{-1} (\mathbf{A}^T \mathbf{P}_e \mathbf{l}). \quad (3.22)$$

More details about the least-squares method can be found in textbooks, e.g., Koch (1999). In order to assess the quality of estimated parameters $\hat{\mathbf{x}}$, the covariance matrix $D(\hat{\mathbf{x}})$ can be derived by applying the law of variance propagation to Eq. (3.22) under consideration of Eq. (3.19), yielding

$$D(\hat{\mathbf{x}}) = \hat{\sigma}_e^2 \mathbf{N}^{-1} \quad (3.23a)$$

with

$$\hat{\sigma}_e^2 = \frac{1}{I - K} (\mathbf{l} - \mathbf{A}\hat{\mathbf{x}})^T \mathbf{P}_e (\mathbf{l} - \mathbf{A}\hat{\mathbf{x}}). \quad (3.23b)$$

Besides the internal validation by calculating the covariance matrix $D(\hat{\mathbf{x}})$, the external validation is frequently used in regional gravity field computations. Assuming \mathbf{q} is an $N \times 1$ vector that contains independent gravity field quantities, the predictions $\hat{\mathbf{q}}$ can be connected to the estimated parameters $\hat{\mathbf{x}}$ via the $N \times K$ design matrix \mathbf{B} according to

$$\hat{\mathbf{q}} = \mathbf{B}\hat{\mathbf{x}}, \quad (3.24)$$

and the vector of residuals is then given as

$$\hat{\boldsymbol{\epsilon}} = \mathbf{q} - \hat{\mathbf{q}}. \quad (3.25)$$

The relevant statistical values can then be obtained according to $\hat{\boldsymbol{\epsilon}}$, such as

$$\begin{cases} Mean(\hat{\boldsymbol{\epsilon}}) = \frac{1}{N} \sum_{n=1}^N \hat{\epsilon}_n \\ RMS(\hat{\boldsymbol{\epsilon}}) = \sqrt{\frac{1}{N} \sum_{n=1}^N \hat{\epsilon}_n^2} \\ STD(\hat{\boldsymbol{\epsilon}}) = \sqrt{\frac{1}{N-1} \sum_{n=1}^N [\hat{\epsilon}_n - Mean(\hat{\boldsymbol{\epsilon}})]^2} \end{cases}, \quad (3.26)$$

in which $Mean(\hat{\boldsymbol{\epsilon}})$, $RMS(\hat{\boldsymbol{\epsilon}})$, and $STD(\hat{\boldsymbol{\epsilon}})$ are the mean, root-mean-square, and standard deviation of the residuals, respectively. In the context of this thesis, the external validation is the main tool for assessing the quality of the regional gravity field solutions. Often, a good gravity field solution is defined as the one with a small RMS when comparing the predictions to independent observations, assuming that those control data are accurate enough. In some cases with significant systematic errors, which can be removed by the post-processing approach (e.g., in the case of geoid/quasigeoid modeling), the solution with a small STD is considered as good.

3.3.4 Regularization

In Section 3.3.2, we have analyzed the spectral characteristics of the inverse problem by using SVD. The singular vectors, corresponding to very small singular values, are found to be the causes for ill-posedness. From this point of view, the direct way to stabilize the problem is to discard some small singular values as well as their corresponding singular vectors by adding a filter to the standard SVD solution as shown in Eq. (3.18), yielding

$$\hat{\mathbf{x}} = \sum_{i=1}^K f_i \frac{\mathbf{u}_i^T \mathbf{1}}{\sigma_i} \mathbf{v}_i \quad (3.27a)$$

with

$$f_i = \begin{cases} 1 & \text{for } i \leq K' \\ 0 & \text{for } i > K' \end{cases}. \quad (3.27b)$$

The process using Eq. (3.27) is called the Truncated Singular Value Decomposition (TSVD) (e.g., Hansen, 1987; Xu, 1998; Hansen, 2008). The solution is obtained from the first $K' \leq K$ singular values and related singular vectors, and the rest are ignored. Alternatives to TSVD for solving the ill-posed problem are, e.g., Tikhonov regularization (Tikhonov, 1963) and iterative regularization methods (e.g., Bouman, 1998; Hansen, 2008), etc. An overview on a variety of regularization methods can be found in, e.g., Hansen (1997), Bouman (1998), and Hansen (2008). In this thesis, only the Tikhonov regularization will be applied as it has been widely used in regional gravity field modeling using RBFs (e.g., Eicker, 2008; Klees et al., 2008; Alberts, 2009; Wittwer, 2009; Naeimi, 2013). And hence, it will now be described in more detail.

Tikhonov regularization

Comparing to TSVD, no decomposition of the design matrix or the normal matrix is required for Tikhonov regularization. The fundamental idea of this procedure is to minimize the objective function in Eq. (3.20) considering a priori assumption about the size and smoothness of the desired solution.

This assumption can be described by adding a penalty term $\|\boldsymbol{\mu}\|_{\mathbf{D}_\mu}^2$ that describes the norm of a priori information $\boldsymbol{\mu}$ given as linear functionals $\mathbf{L}\mathbf{x}$ of the unknown parameters \mathbf{x} to the objective function. From the Bayesian point of view, it is equivalent to adding an additional observation equation system in the form of

$$\boldsymbol{\mu} - \mathbf{e}_\mu = \mathbf{L}\mathbf{x} \quad \text{with} \quad E(\mathbf{e}_\mu) = 0 \quad \text{and} \quad \mathbf{D}_\mu = \sigma_\mu^2 \mathbf{P}_\mu^{-1} \quad (3.28)$$

to the main observation equation system given in Eq. (3.19) (e.g., Koch and Kusche, 2002; Eicker, 2008). Here σ_μ^2 is the unknown variance factor of $\boldsymbol{\mu}$, and \mathbf{P}_μ is the corresponding weight matrix. Concerning $E(\boldsymbol{\mu}) = 0$, the objective function for the Tikhonov regularization based on the Bayesian approach is equivalent to (Eicker, 2008)

$$\Phi_\alpha(\mathbf{x}) = \left[\begin{pmatrix} \mathbf{1} \\ 0 \end{pmatrix} - \begin{pmatrix} \mathbf{A} \\ \mathbf{L} \end{pmatrix} \mathbf{x} \right]^T \bar{\mathbf{D}}^{-1} \left[\begin{pmatrix} \mathbf{1} \\ 0 \end{pmatrix} - \begin{pmatrix} \mathbf{A} \\ \mathbf{L} \end{pmatrix} \mathbf{x} \right] \quad (3.29a)$$

with the inverse of the extended covariance function

$$\bar{\mathbf{D}}^{-1} = \frac{1}{\sigma_e^2} \begin{pmatrix} \mathbf{P}_e & 0 \\ 0 & \frac{\sigma_e^2}{\sigma_\mu^2} \mathbf{P}_\mu \end{pmatrix}. \quad (3.29b)$$

Let $\partial\Phi_\alpha(\mathbf{x})/\partial\mathbf{x} = 0$, the regularized normal equation system then reads:

$$\left(\mathbf{A}^T \mathbf{P}_e \mathbf{A} + \alpha \mathbf{L}^T \mathbf{P}_\mu \mathbf{L} \right) \mathbf{x} = \mathbf{A}^T \mathbf{P}_e \mathbf{1}, \quad (3.30)$$

where $\alpha = \sigma_e^2/\sigma_\mu^2$ is the regularization parameter, which can be interpreted as a noise-to-signal ratio if $\boldsymbol{\mu}$ represents the signals. Thus, it is expected that a large α is needed for the data with large noise in the same study case. An important alternative of the objective function in Eq. (3.29) is given as

$$\Phi_\alpha(\mathbf{x}) = (\mathbf{1} - \mathbf{A}\mathbf{x})^T \mathbf{P}_e (\mathbf{1} - \mathbf{A}\mathbf{x}) + \alpha \mathbf{x}^T \mathbf{L}^T \mathbf{P}_\mu \mathbf{L} \mathbf{x} = \|\mathbf{1} - \mathbf{A}\mathbf{x}\|_{\mathbf{P}_e}^2 + \alpha \|\mathbf{L}\mathbf{x}\|_{\mathbf{P}_\mu}^2. \quad (3.31)$$

It represents the general form of the objective function for the Tikhonov regularization in the Bayesian sense. \mathbf{L} is a linear operator that is used for the determination of certain solutions to be constrained. It should be defined depending on the particular applications. In the case of $\mathbf{L} = \mathbf{I}$, the smoothness constraints are only applied for the unknown parameter vector \mathbf{x} itself not for its functionals. \mathbf{P}_μ is often set to be the identity matrix in regional gravity field modeling. A more familiar formulation of Eq. (3.31) for geodesists is formulated as

$$\Phi_\alpha(\mathbf{x}) = (\mathbf{1} - \mathbf{A}\mathbf{x})^T \mathbf{P}_e (\mathbf{1} - \mathbf{A}\mathbf{x}) + \alpha \mathbf{x}^T \mathbf{R} \mathbf{x} = \|\mathbf{1} - \mathbf{A}\mathbf{x}\|_{\mathbf{P}_e}^2 + \alpha \|\mathbf{x}\|_{\mathbf{R}}^2, \quad (3.32)$$

in which $\mathbf{R} = \mathbf{L}^T \mathbf{P}_\mu \mathbf{L}$ is known as the regularization matrix with the dimension of $K \times K$. From Eq. (3.32) it is clear that both the choices of the regularization matrix and the regularization parameter play an important role in obtaining an optimal solution. Related studies about the choice of \mathbf{R} for spherical harmonic solutions can be found in, e.g., Kusche and Klees (2002) and Ditmar et al. (2003), and for solutions of RBFs in, e.g., Eicker (2008), Alberts (2009), and Eicker et al. (2014). Often, \mathbf{R} is simply chosen as the identity matrix \mathbf{I} . Then, Tikhonov regularization is known as ordinary ridge regression in statistics and is also called the standard Tikhonov regularization. The objective function in Eq. (3.32) is then rewritten according to

$$\begin{aligned} \Phi_\alpha(\mathbf{x}) &= (\mathbf{1} - \mathbf{A}\mathbf{x})^T \mathbf{P}_e (\mathbf{1} - \mathbf{A}\mathbf{x}) + \alpha \mathbf{x}^T \mathbf{x} \\ &= \|\mathbf{1} - \mathbf{A}\mathbf{x}\|_{\mathbf{P}_e}^2 + \alpha \|\mathbf{x}\|_{\mathbf{I}}^2 = \Phi_d + \alpha \Phi_m, \end{aligned} \quad (3.33)$$

resulting in the regularized solution

$$\hat{\mathbf{x}}_\alpha = \left(\mathbf{A}^T \mathbf{P}_e \mathbf{A} + \alpha \mathbf{I} \right)^{-1} \mathbf{A}^T \mathbf{P}_e \mathbf{l}. \quad (3.34)$$

If the identity matrix \mathbf{I} is replaced by the matrix \mathbf{R} , Eq. (3.34) becomes the solution for the objective function in Eq. (3.32). From Eq. (3.33), the objective function $\Phi_\alpha(\mathbf{x})$ is divided into two parts, i.e., the data misfit function Φ_d and the model function Φ_m . The choice of the regularization parameter α becomes a crucial task as it determines how well the solution should fit the data. When α is large, the solution fits less well to the data. In this case, much information contained in the data is lost. If α is very small, the solution starts to fit noise. An optimal α should be chosen in such a way that the solution fits the data as well as possible while the data noise should be damped as strongly as necessary. This issue will be discussed in Section 3.3.5 in more detail.

Analysis of the Tikhonov regularization

In order to understand the basic properties of the standard Tikhonov regularization, the SVD is employed again for the analysis in the following. The normal equation corresponding to the solution in Eq. (3.34) is given as

$$\left(\mathbf{A}^T \mathbf{P}_e \mathbf{A} + \alpha \mathbf{I} \right) \mathbf{x} = \mathbf{A}^T \mathbf{P}_e \mathbf{l}. \quad (3.35)$$

Inserting Eq. (3.14) into the above equation under consideration of $\mathbf{P}_e = \mathbf{I}$, yields

$$\left(\mathbf{A}^T \mathbf{A} + \alpha \mathbf{I} \right) \mathbf{x} = \left(\mathbf{V} \boldsymbol{\Sigma}^2 \mathbf{V}^T + \alpha \mathbf{V} \mathbf{V}^T \right) \mathbf{x} = \mathbf{V} \left(\boldsymbol{\Sigma}^2 + \alpha \mathbf{I} \right) \mathbf{V}^T \mathbf{x} = \mathbf{V} \boldsymbol{\Sigma} \mathbf{U}^T \mathbf{l}. \quad (3.36)$$

Multiplying both sides with \mathbf{V}^T gives

$$\left(\boldsymbol{\Sigma}^2 + \alpha \mathbf{I} \right) \mathbf{V}^T \mathbf{x} = \boldsymbol{\Sigma} \mathbf{U}^T \mathbf{l}, \quad (3.37)$$

and the solution is computed according to

$$\hat{\mathbf{x}}_\alpha = \mathbf{V} \left(\boldsymbol{\Sigma}^2 + \alpha \mathbf{I} \right)^{-1} \boldsymbol{\Sigma} \mathbf{U}^T \mathbf{l} = \mathbf{V} \boldsymbol{\Sigma}^{-1} \left(\boldsymbol{\Sigma}^2 + \alpha \mathbf{I} \right)^{-1} \boldsymbol{\Sigma}^2 \mathbf{U}^T \mathbf{l}. \quad (3.38)$$

Let $\left(\boldsymbol{\Sigma}^2 + \alpha \mathbf{I} \right)^{-1} \boldsymbol{\Sigma}^2 = \mathbf{F}$, Eq. (3.38) can be reformulated as

$$\hat{\mathbf{x}}_\alpha = \mathbf{V} \boldsymbol{\Sigma}^{-1} \mathbf{F} \mathbf{U}^T \mathbf{l} = \sum_{i=1}^K f_i \frac{\mathbf{u}_i^T \mathbf{l}}{\sigma_i} \mathbf{v}_i \quad (3.39a)$$

with the Tikhonov filter function

$$f_i = \frac{\sigma_i^2}{\sigma_i^2 + \alpha}. \quad (3.39b)$$

The left panel of Fig. 3.4 shows the Tikhonov filter functions for three regularization parameters α . It follows that the filter function penalizes the singular vectors, which are associated with the singular values $\sigma_i^2 \ll \alpha$. As a result, the singular vectors associated with small singular values have nearly no contribution to the regularized solution, leading to a stable solution. Comparing the TSVD to the standard Tikhonov regularization, i.e., see Eqs (3.27) and (3.39), the main difference between them is the filter function. The right panel of Fig. 3.4 shows one example of the TSVD filter function and the Tikhonov filter function. It demonstrates that the TSVD filter function acts as an exact low-pass filter and the Tikhonov filter function can be considered as a quasi low-pass filter with a smooth transition zone.

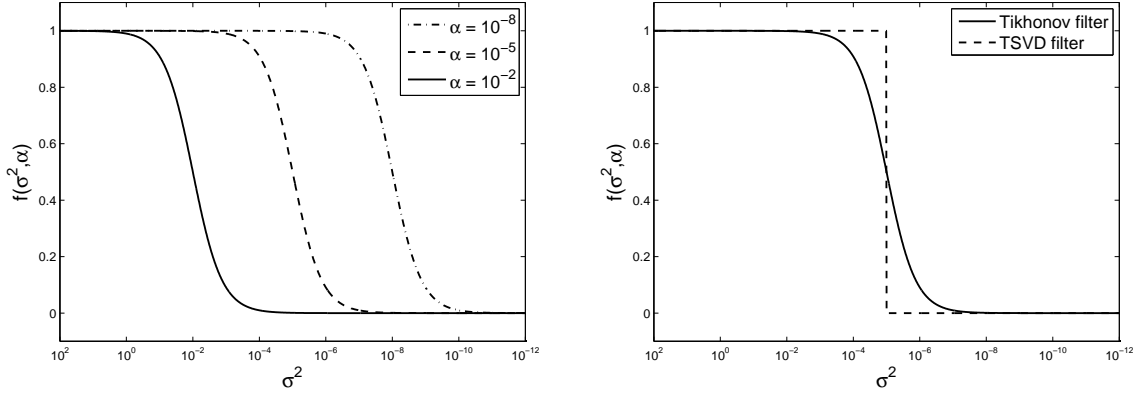


Figure 3.4: Examples for the TSVD and Tikhonov filter functions. *Left:* the Tikhonov filter functions for three regularization parameters $\alpha = 10^{-8}, 10^{-5}, 10^{-2}$; *right:* one TSVD filter function truncated at $\sigma^2 = 10^{-5}$ and one Tikhonov filter function for $\alpha = 10^{-5}$.

Relationship between the Tikhonov regularization and the least-squares collocation

In the following the relationship between the Tikhonov regularization and the least-squares collocation (see also Section 2.6) will be briefly discussed. Eq. (2.45) for the prediction of a signal vector \mathbf{s} based on a set of noisy observations \mathbf{l} is reformulated with tiny changes:

$$\hat{\mathbf{s}} = \mathbf{C}_{st} (\mathbf{C}_{tt} + \mathbf{C}_{ee})^{-1} \mathbf{l} \quad \text{with} \quad \mathbf{C}_{ee} = \sigma_e^2 \mathbf{P}_e^{-1} = \sigma_e^2 \mathbf{I}. \quad (3.40)$$

According to the following relations:

$$\mathbf{A}\mathbf{x} = \mathbf{t}, \quad (3.41a)$$

$$\mathbf{B}\mathbf{x} = \mathbf{s}, \quad (3.41b)$$

the auto-covariance matrix \mathbf{C}_{tt} and the cross-covariance matrix \mathbf{C}_{st} can be obtained as

$$\mathbf{C}_{tt} = \mathbf{A}\mathbf{C}_{xx}\mathbf{A}^T, \quad (3.42a)$$

$$\mathbf{C}_{st} = \mathbf{B}\mathbf{C}_{xx}\mathbf{A}^T, \quad (3.42b)$$

in which \mathbf{C}_{xx} is the covariance matrix of the unknown parameters \mathbf{x} . Inserting Eq. (3.42) into Eq. (3.40), yields (Rummel et al., 1979; Bouman, 1998)

$$\begin{aligned} \hat{\mathbf{s}} &= \mathbf{B}\mathbf{C}_{xx}\mathbf{A}^T (\mathbf{A}\mathbf{C}_{xx}\mathbf{A}^T + \sigma_e^2 \mathbf{I})^{-1} \mathbf{l} = \mathbf{B} (\mathbf{A}^T \sigma_e^{-2} \mathbf{A} + \mathbf{C}_{xx}^{-1})^{-1} \mathbf{A}^T \sigma_e^{-2} \mathbf{l} \\ &= \mathbf{B} (\mathbf{A}^T \mathbf{A} + \sigma_e^2 \mathbf{C}_{xx}^{-1})^{-1} \mathbf{A}^T \mathbf{l}. \end{aligned} \quad (3.43)$$

The same predictions as given in Eq. (3.43) can be computed by the least-squares adjustment considering the Tikhonov regularization:

$$\hat{\mathbf{s}} = \mathbf{B}\hat{\mathbf{x}} = \mathbf{B} (\mathbf{A}^T \mathbf{A} + \alpha \mathbf{R})^{-1} \mathbf{A}^T \mathbf{l}. \quad (3.44)$$

Comparing Eq. (3.43) to (3.44), LSC can be regarded as a special case of the Tikhonov regularization approach with the use of a regularization matrix $\mathbf{R} = \sigma_e^2 \mathbf{C}_{xx}^{-1}$ while taking the regularization parameter $\alpha = 1$. For the regularized LSC given by Eq. (2.47), a general form of Eq. (3.43) is given as (Rummel et al., 1979)

$$\hat{\mathbf{s}} = \mathbf{B} \left(\mathbf{A}^T \mathbf{A} + \alpha \sigma_e^2 \mathbf{C}_{xx}^{-1} \right)^{-1} \mathbf{A}^T \mathbf{l}. \quad (3.45)$$

For standard Tikhonov regularization, the use of an identity matrix \mathbf{I} instead of \mathbf{R} seems to be a less appropriate choice than the use of $\sigma_e^2 \mathbf{C}_{xx}^{-1}$ in LSC.

3.3.5 The choice of the regularization parameter

The crucial task for obtaining a stable solution when using the standard Tikhonov regularization is how to choose a proper regularization parameter α , as it controls the trade-off between the degree of the data fit and the degree of the smoothness of the solution. In practice, several criteria are used to choose a proper α , each of them may be suited better for specific problems. An overview of some approaches for the choice of the regularization parameter is given in Hansen (1997) and Bouman (1998). In this thesis, the regularization parameter is determined by one of the following three approaches:

- Minimizing the RMS of the differences between predicted and observed values at a set of control points, assuming that the observed values are accurate enough, see e.g., Tenzer and Klees (2008).
- Generalized cross validation (GCV), see e.g., Golub et al. (1979), Hansen (1997), Bouman (1998), Kusche and Klees (2002), Ditmar et al. (2003), and Hansen (2008).
- Variance component estimation (VCE), see e.g., Koch and Kusche (2002).

The first approach is empirical, and the latter two are the heuristic approaches, which do not depend on the additional control values, but only on the input data.

Empirical approach

The empirical approach aims at choosing a regularization parameter α with which a minimal RMS of the differences between the predictions and the observations at the given control points can be achieved. Often, a set of n candidates α_i , which are arranged in the order such that $\alpha_1 > \alpha_2 > \dots > \alpha_n \geq 0$ have to be pre-selected. Starting from α_1 , this approach can be described mathematically as

$$RMS(\alpha_i) = \sqrt{\frac{1}{N} \|\mathbf{B}\hat{\mathbf{x}}_{\alpha_i} - \mathbf{q}\|^2} \quad \text{with } i = 1, 2, \dots, n, \quad (3.46)$$

where N is the number of control points, \mathbf{q} is an $N \times 1$ vector containing the observed control values, \mathbf{B} is the $N \times K$ design matrix, and $\hat{\mathbf{x}}_{\alpha_i}$ is the $K \times 1$ estimated parameter vector computed by Eq. (3.34) with $\alpha = \alpha_i$. This approach is easy to implement, and the solution is reliable in the case when the control points are accurate enough and homogeneously distributed. If control points are absent or are distributed inhomogeneously, the related solution might be less reliable.

Generalized cross validation

The generalized cross validation for finding a proper regularization parameter was first proposed by Golub et al. (1979). It is based on the leave-one-out idea:

The solution vector $\hat{\mathbf{x}}_{\alpha_i}^{(k)}$, which depends on the given regularization parameter α_i , is computed by Eq. (3.34) without the observation l_k . It is then used to predict the “missing” observation $\hat{l}_k = \left(\mathbf{A}\hat{\mathbf{x}}_{\alpha_i}^{(k)} \right)_k$. A well-selected regularization parameter is expected to result in a small difference between the predicted \hat{l}_k and the observed value l_k . Repeating this procedure step by step until all observations have been tested, a proper choice of the regularization parameter should lead to a small mean square error of all possible differences $l_k - \hat{l}_k$.

This idea is quite similar to the empirical approach but without requiring external control values. Assuming uncorrelated observations of equal weight (i.e., $\mathbf{P}_e = \mathbf{I}$), the ordinary cross validation function $CV(\alpha_i)$ is given by

$$CV(\alpha_i) = \frac{1}{I} \sum_{k=1}^I [(\mathbf{A}\hat{\mathbf{x}}_{\alpha_i}^{(k)})_k - \mathbf{l}_k]^2 = \frac{1}{I} \sum_{k=1}^I \frac{[(\mathbf{A}\hat{\mathbf{x}}_{\alpha_i})_k - \mathbf{l}_k]^2}{(1 - Q_{kk}^{\alpha_i})^2}, \quad (3.47)$$

where $Q_{kk}^{\alpha_i}$ are the main diagonal elements of the influence matrix \mathbf{Q}^{α_i} , which is defined by

$$\mathbf{A}\hat{\mathbf{x}}_{\alpha_i} = \mathbf{Q}^{\alpha_i}\mathbf{l}. \quad (3.48)$$

For the derivation of the second expression in Eq. (3.47), see Golub and van Loan (1996). The generalized cross validation function $GCV(\alpha_i)$ is generated when the weights $(1 - Q_{kk}^{\alpha_i})$ are replaced by their average value $tr(\mathbf{I} - \mathbf{Q}^{\alpha_i})/I$:

$$GCV(\alpha_i) = \sum_{k=1}^I \frac{I [(\mathbf{A}\hat{\mathbf{x}}_{\alpha_i})_k - \mathbf{l}_k]^2}{[tr(\mathbf{I} - \mathbf{Q}^{\alpha_i})]^2} = \frac{I \|\mathbf{A}\hat{\mathbf{x}}_{\alpha_i} - \mathbf{l}\|^2}{[I - tr(\mathbf{Q}^{\alpha_i})]^2}. \quad (3.49)$$

For a non-identity noise covariance matrix $\mathbf{D}_e = \sigma_e^2 \mathbf{P}_e^{-1}$, the GCV function reads:

$$GCV(\alpha_i) = \frac{I \|\mathbf{A}\hat{\mathbf{x}}_{\alpha_i} - \mathbf{l}\|_{\mathbf{P}_e}^2}{[I - tr(\mathbf{Q}^{\alpha_i})]^2} \quad (3.50a)$$

with

$$\mathbf{Q}^{\alpha_i} = \mathbf{A} (\mathbf{A}^T \mathbf{P}_e \mathbf{A} + \alpha_i \mathbf{R})^{-1} \mathbf{A}^T \mathbf{P}_e. \quad (3.50b)$$

The optimal regularization parameter is the one corresponding to the minimum of the GCV function. Thus, our goal is to find the minimal $GCV(\alpha_i)$ by testing n candidates arranged in decreasing order. It should be mentioned that the selection of the candidates plays an important role in both the empirical approach and the GCV approach. If the computational burden is acceptable, a reliable way is to select them based on the Tikhonov filter function given in Eq. (3.39b). In practical applications, the computation of $tr(\mathbf{Q}^{\alpha_i})$ is quite time-consuming in the case of a large-scale problem, as it requires the inverse of a large regularized normal matrix. Alternatively, the stochastic trace estimation proposed by Koch and Kusche (2002) is widely used, which will be described in detail in the following.

Variance component estimation

In Section 3.3.4, we mentioned that the Tikhonov regularization can be interpreted as considering a priori information in the Bayesian sense and that the regularization parameter is obtained as the ratio between two variance factors, see Eqs (3.28)–(3.31). In the same context, if different kinds of observations are used as input, the determination of proper relative weights of the observations is essential to achieve an accurate result. For both tasks, the variance component estimation (e.g., Koch and Kusche, 2002) can be applied. Assuming there are p observation groups, the functional model and the stochastic model for each group are given as

$$\mathbf{l}_i - \mathbf{e}_i = \mathbf{A}_i \mathbf{x} \quad \text{with} \quad E(\mathbf{e}_i) = 0 \quad \text{and} \quad D(\mathbf{e}_i) = D(\mathbf{l}_i) = \sigma_i^2 \mathbf{P}_i^{-1} \quad (3.51)$$

with σ_i^2 for $i \in \{1, 2, \dots, p\}$ being the variance component (or variance factor) of the observation group i . If the observations are combined with a priori information $\boldsymbol{\mu}$ as given in Eq. (3.28) under

consideration of both $\mathbf{L} = \mathbf{I}$ and $E(\boldsymbol{\mu}) = 0$, the least-squares solution $\hat{\mathbf{x}}$ can be obtained by solving a combined normal equation

$$\mathbf{N}\mathbf{x} = \mathbf{y} \quad (3.52a)$$

with

$$\mathbf{N} = \frac{1}{\sigma_1^2} \mathbf{A}_1^T \mathbf{P}_1 \mathbf{A}_1 + \dots + \frac{1}{\sigma_p^2} \mathbf{A}_p^T \mathbf{P}_p \mathbf{A}_p + \frac{1}{\sigma_\mu^2} \mathbf{P}_\mu, \quad (3.52b)$$

$$\mathbf{y} = \frac{1}{\sigma_1^2} \mathbf{A}_1^T \mathbf{P}_1 \mathbf{l}_1 + \dots + \frac{1}{\sigma_p^2} \mathbf{A}_p^T \mathbf{P}_p \mathbf{l}_p. \quad (3.52c)$$

Multiplying both sides of Eq. (3.52a) with σ_1^2 and taking $\omega_i = \sigma_1^2/\sigma_i^2$ and $\alpha = \sigma_1^2/\sigma_\mu^2$, a new form of the normal equation is given as

$$\left(\mathbf{A}_1^T \mathbf{P}_1 \mathbf{A}_1 + \dots + \omega_p \mathbf{A}_p^T \mathbf{P}_p \mathbf{A}_p + \alpha \mathbf{P}_\mu \right) \mathbf{x} = \mathbf{A}_1^T \mathbf{P}_1 \mathbf{l}_1 + \dots + \omega_p \mathbf{A}_p^T \mathbf{P}_p \mathbf{l}_p, \quad (3.53)$$

where the ratio ω_i stands for the relative weight of the observation group i with respect to group 1. The unknown variance components σ_i^2 and σ_μ^2 are estimated iteratively according to

$$\hat{\sigma}_i^2 = \frac{\hat{\mathbf{e}}_i^T \mathbf{P}_i \hat{\mathbf{e}}_i}{r_i} = \frac{(\mathbf{A}_i \hat{\mathbf{x}} - \mathbf{l}_i)^T \mathbf{P}_i (\mathbf{A}_i \hat{\mathbf{x}} - \mathbf{l}_i)}{r_i}, \quad (3.54a)$$

$$\hat{\sigma}_\mu^2 = \frac{\hat{\mathbf{e}}_\mu^T \mathbf{P}_\mu \hat{\mathbf{e}}_\mu}{r_\mu} = \frac{\hat{\mathbf{x}}^T \mathbf{P}_\mu \hat{\mathbf{x}}}{r_\mu}, \quad (3.54b)$$

where r_i and r_μ are the partial redundancies, i.e., the contributions of the observation group i and the a priori information $\boldsymbol{\mu}$ to the overall redundancy I . The partial redundancies are computed by (Koch and Kusche, 2002)

$$r_i = I_i - \text{tr} \left(\frac{1}{\sigma_i^2} \mathbf{A}_i^T \mathbf{P}_i \mathbf{A}_i \mathbf{N}^{-1} \right), \quad (3.55a)$$

$$r_\mu = K - \text{tr} \left(\frac{1}{\sigma_\mu^2} \mathbf{P}_\mu \mathbf{N}^{-1} \right), \quad (3.55b)$$

where I_i denotes the number of observations in group i , satisfying $\sum_{i=1}^p I_i = I$. Concerning $\mathbf{P}_i = \mathbf{G}_i \mathbf{G}_i^T$ and $\mathbf{P}_\mu = \mathbf{G}_\mu \mathbf{G}_\mu^T$, where \mathbf{G}_i and \mathbf{G}_μ are the regular lower triangular matrices, and using the relation $\text{tr}(AB) = \text{tr}(BA)$, Eq. (3.55) can be transformed into

$$r_i = I_i - \frac{1}{\sigma_i^2} \text{tr} \left(\underbrace{\mathbf{G}_i^T \mathbf{A}_i \mathbf{N}^{-1} \mathbf{A}_i^T \mathbf{G}_i}_{\mathcal{T}_i} \right), \quad (3.56a)$$

$$r_\mu = K - \frac{1}{\sigma_\mu^2} \text{tr} \left(\underbrace{\mathbf{G}_\mu^T \mathbf{N}^{-1} \mathbf{G}_\mu}_{\mathcal{T}_\mu} \right). \quad (3.56b)$$

The computation of the traces \mathcal{T}_i and \mathcal{T}_μ to obtain the partial redundancies in Eq. (3.56) requires the inverse of the combined normal matrix \mathbf{N} , which may be too time-consuming for the case of a large number of unknown parameters. The stochastic trace estimation (STE) (Hutchinson, 1990; Koch and Kusche, 2002) is introduced to improve the numerical efficiency. We use the theorem by Hutchinson (1990): $E(\mathbf{u}^T \mathbf{B} \mathbf{u}) = \text{tr}(\mathbf{B})$, where \mathbf{B} is a symmetric matrix and \mathbf{u} is a random vector with $E(\mathbf{u}) = 0$

and $D(\mathbf{u}) = \mathbf{I}$. If the vector \mathbf{u} contains independent samples of the values $+1$ and -1 with equal probability, then $\mathbf{u}^T \mathbf{B} \mathbf{u}$ is an unbiased estimator of $tr(\mathbf{B})$ with minimum variance. Accordingly, the calculation of an unbiased estimate of the trace \mathcal{T}_i in Eq. (3.56a) is equivalent to

$$\mathcal{T}_i = \mathbf{u}^T \mathbf{G}_i^T \mathbf{A}_i \mathbf{N}^{-1} \mathbf{A}_i^T \mathbf{G}_i \mathbf{u}. \quad (3.57)$$

The computation procedure of \mathcal{T}_i by STE can be setup as follows:

- ① Generate a random vector \mathbf{u} .
- ② Solve the linear equation system $\mathbf{N} \boldsymbol{\beta}_i = \mathbf{A}_i^T \mathbf{G}_i \mathbf{u}$, yielding $\boldsymbol{\beta}_i = \mathbf{N}^{-1} \mathbf{A}_i^T \mathbf{G}_i \mathbf{u}$.
- ③ Compute $\mathcal{T}_i = \mathbf{u}^T \mathbf{G}_i^T \mathbf{A}_i \boldsymbol{\beta}_i$.

Often, the trace should be the mean of several results obtained by using different vectors \mathbf{u} of independent samples. Golub and von Matt (1997) recommended just one sample vector \mathbf{u} to compute the trace. Their recommendation was successfully applied for geopotential determination from satellite data in Koch and Kusche (2002). And therefore, this recommendation is also followed here. In the STE procedure for calculating the trace, the direct inverse of the normal matrix is replaced by solving a linear equation system; this can significantly improve the numerical efficiency, especially for large-scale problems.

The STE procedure can also be used to compute the traces in Eq. (3.56b) and Eq. (3.50). If there is only one kind of observations, Eq. (3.56) can be simplified as

$$r_1 = I - K + \frac{1}{\sigma_\mu^2} tr(\mathbf{G}_\mu^T \mathbf{N}^{-1} \mathbf{G}_\mu), \quad (3.58a)$$

$$r_\mu = K - \frac{1}{\sigma_\mu^2} tr(\mathbf{G}_\mu^T \mathbf{N}^{-1} \mathbf{G}_\mu). \quad (3.58b)$$

In comparison to Eq. (3.56), only the trace \mathcal{T}_μ needs to be computed in this case. Concerning Eqs (3.56) and (3.58), a new form of the GCV function suited for practical computations is obtained according to (see also Eq. (3.50); Koch and Kusche, 2002)

$$GCV(\alpha_i) = \frac{I(\mathbf{A} \hat{\mathbf{x}}_{\alpha_i} - \mathbf{l})^T \mathbf{P}_e (\mathbf{A} \hat{\mathbf{x}}_{\alpha_i} - \mathbf{l})}{\left[I - K + \alpha_i \cdot tr(\mathbf{G}_\mu^T \mathbf{N}^{-1} \mathbf{G}_\mu) \right]^2} \quad (3.59a)$$

with

$$\bar{\mathbf{N}} = \mathbf{A}^T \mathbf{P}_e \mathbf{A} + \alpha_i \mathbf{R}, \quad \mathbf{R} = \mathbf{G}_\mu \mathbf{G}_\mu^T. \quad (3.59b)$$

Finally, the computation procedure of VCE is summarized as follows:

- ① Fix the weight matrix \mathbf{P}_i for $i \in \{1, 2, \dots, p\}$ and \mathbf{P}_μ ; they are usually set to be \mathbf{I} . Then, give initial values of the variance components (i.e., σ_i^2 and σ_μ^2).
- ② Construct the normal equation system by calculating the combined normal matrix \mathbf{N} and the right-hand side \mathbf{y} based on the given variance components, see Eq. (3.52).
- ③ Solve the normal equation system constructed at ②, see Eq. (3.52) or Eq. (3.53), resulting in the solution $\hat{\mathbf{x}}$.
- ④ Compute the variance components by using STE, see Eqs (3.54)–(3.58).

- ⑤ Compare the newly estimated variance components to the old ones. If the criterion for convergence is satisfied, go to ⑥. Otherwise, replace the old variance components with the new ones, and then go to ②.
- ⑥ Stop the whole procedure. The estimated parameters $\hat{\mathbf{x}}$ based on the current variance components are considered as the final solution. The resulting variance components can be interpreted as a posteriori information of the observation groups.

3.3.6 Nonlinear least-squares solution

Previously, we have reviewed the least-squares solution of a linear equation system and the regularization process for obtaining a stable estimate of the gravity field parameters. In some cases, the functional model that describes the relation between the observations and unknown parameters is not linear, leading to a nonlinear equation system. As an example of the point mass method, besides the magnitudes, if the 3D positions (i.e., horizontal positions and radial distances) or only the radial distances of the point mass RBFs are also unknown, the problem is nonlinear. In the following, the least-squares solution of a nonlinear equation system will be described.

Similar to the linear case, a nonlinear equation system can be simply described as

$$\mathbf{l} - \mathbf{e} = F(\mathbf{m}), \quad (3.60)$$

where F represents the forward modeling operator and \mathbf{m} is the $M \times 1$ model parameter vector. The definitions of the other variables in the above equation are as in Eq. (3.19). The relation between the number of model parameters M and the number of observations I satisfies $M \leq I$.

The least-squares solution of the nonlinear equation system is obtained by minimizing an objective function under consideration of Tikhonov regularization, defined by

$$\begin{aligned} \Phi_\alpha(\mathbf{m}) &= [\mathbf{l} - F(\mathbf{m})]^T \mathbf{P}_e [\mathbf{l} - F(\mathbf{m})] + \alpha \mathbf{m}^T \mathbf{R} \mathbf{m} \\ &= \|\mathbf{l} - F(\mathbf{m})\|_{\mathbf{P}_e}^2 + \alpha \|\mathbf{m}\|_{\mathbf{R}}^2 \end{aligned} \quad (3.61)$$

with given α , \mathbf{P}_e , and \mathbf{R} . To minimize the objective function Φ_α , it is common to apply linearization and iteration. Four nonlinear iteration algorithms are considered for minimizing Φ_α with respect to \mathbf{m} in the context of this thesis: the Levenberg-Marquardt method, the nonlinear conjugate gradient method, the limited-memory Broyden-Fletcher-Goldfarb-Shanno (BFGS) method, and the bound-constrained limited-memory BFGS method. They are labeled as LM, NLCG, L-BFGS, and L-BFGS-B, respectively. The first three algorithms are unconstrained optimization algorithms, and the last one is capable of handling the simple bound constraints on the model parameters. Each algorithm generates a sequence of models $\mathbf{m}_0, \mathbf{m}_1, \dots, \mathbf{m}_\ell$ and aims at reaching $\Phi_\alpha(\mathbf{m}_\ell) \rightarrow \min_{\mathbf{m}} \Phi_\alpha(\mathbf{m})$ as $\ell \rightarrow \infty$.

Before introducing the above four algorithms, a set of notations will be explained first. The gradient and the Hessian of the objective function are the $M \times 1$ vector \mathbf{g} and $M \times M$ symmetric matrix \mathbf{H} , defined by

$$g^j(\mathbf{m}) = \frac{\partial \Phi_\alpha(\mathbf{m})}{\partial m_j} \quad \text{and} \quad (3.62a)$$

$$H^{jk}(\mathbf{m}) = \frac{\partial^2 \Phi_\alpha(\mathbf{m})}{\partial m_j \partial m_k} \quad \text{with } j, k = 1, \dots, M, \quad (3.62b)$$

where m_j is the j -th element in \mathbf{m} , $g^j(\mathbf{m})$ is the j -th element in \mathbf{g} , and $H^{jk}(\mathbf{m})$ is an element of \mathbf{H} corresponding to row j and column k .

Let \mathbf{J} denote the $I \times M$ Jacobian matrix of the residual vector $\mathbf{l} - F(\mathbf{m})$, yielding

$$J^{ik}(\mathbf{m}) = \frac{\partial [l_i - F^i(\mathbf{m})]}{\partial m_k} = -\frac{\partial F^i(\mathbf{m})}{\partial m_k} \quad \text{with } i = 1, \dots, I \quad \text{and } k = 1, \dots, M. \quad (3.63)$$

According to Eqs (3.61) and (3.62), yields

$$\mathbf{g}(\mathbf{m}) = 2\mathbf{J}(\mathbf{m})^T \mathbf{P}_e [\mathbf{l} - F(\mathbf{m})] + 2\alpha\mathbf{R}\mathbf{m}, \quad (3.64a)$$

$$\begin{aligned} \mathbf{H}(\mathbf{m}) &= 2\mathbf{J}(\mathbf{m})^T \mathbf{P}_e \mathbf{J}(\mathbf{m}) + 2\alpha\mathbf{R} + 2\frac{\partial \mathbf{J}(\mathbf{m})^T}{\partial \mathbf{m}} \mathbf{P}_e [\mathbf{l} - F(\mathbf{m})] \\ &= 2\mathbf{J}(\mathbf{m})^T \mathbf{P}_e \mathbf{J}(\mathbf{m}) + 2\alpha\mathbf{R} - 2\sum_i^M q^i \mathbf{B}_i(\mathbf{m}), \end{aligned} \quad (3.64b)$$

in which $\mathbf{q} = \mathbf{P}_e [\mathbf{l} - F(\mathbf{m})]$ and \mathbf{B}_i is the Hessian of F^i .

An approximate objective function is defined based on the linearization of the forward function F . For linearization about a reference model \mathbf{m}_{ref} , yields

$$\tilde{F}(\mathbf{m}, \mathbf{m}_{ref}) = F(\mathbf{m}_{ref}) - \mathbf{J}(\mathbf{m}_{ref})(\mathbf{m} - \mathbf{m}_{ref}), \quad (3.65a)$$

$$\tilde{\Phi}_\alpha(\mathbf{m}, \mathbf{m}_{ref}) = [\mathbf{l} - \tilde{F}(\mathbf{m}, \mathbf{m}_{ref})]^T \mathbf{P}_e [\mathbf{l} - \tilde{F}(\mathbf{m}, \mathbf{m}_{ref})] + \alpha\mathbf{m}^T \mathbf{R}\mathbf{m}. \quad (3.65b)$$

The gradient and Hessian of $\tilde{\Phi}_\alpha$ are obtained according to

$$\tilde{\mathbf{g}}(\mathbf{m}, \mathbf{m}_{ref}) = 2\mathbf{J}(\mathbf{m}_{ref})^T \mathbf{P}_e [\mathbf{l} - \tilde{F}(\mathbf{m}, \mathbf{m}_{ref})] + 2\alpha\mathbf{R}\mathbf{m}, \quad (3.66a)$$

$$\tilde{\mathbf{H}}(\mathbf{m}_{ref}) = 2\mathbf{J}(\mathbf{m}_{ref})^T \mathbf{P}_e \mathbf{J}(\mathbf{m}_{ref}) + 2\alpha\mathbf{R}. \quad (3.66b)$$

In this case, $\tilde{\Phi}_\alpha$ is quadratic in \mathbf{m} , $\tilde{\mathbf{g}}$ is linear in \mathbf{m} , and $\tilde{\mathbf{H}}$ is independent of \mathbf{m} . Accordingly, we generate the following important relations:

$$\tilde{\Phi}_\alpha(\mathbf{m}, \mathbf{m}_{ref}) = \Phi_\alpha(\mathbf{m}_{ref}) + \tilde{\mathbf{g}}(\mathbf{m}_{ref})^T (\mathbf{m} - \mathbf{m}_{ref}) + \frac{1}{2} (\mathbf{m} - \mathbf{m}_{ref})^T \tilde{\mathbf{H}}(\mathbf{m}_{ref}) (\mathbf{m} - \mathbf{m}_{ref}), \quad (3.67a)$$

$$\tilde{\mathbf{g}}(\mathbf{m}, \mathbf{m}_{ref}) = \mathbf{g}(\mathbf{m}_{ref}) + \tilde{\mathbf{H}}(\mathbf{m}_{ref})(\mathbf{m} - \mathbf{m}_{ref}). \quad (3.67b)$$

Thus, $\tilde{F}(\mathbf{m}_{ref}) = F(\mathbf{m}_{ref})$, $\tilde{\Phi}(\mathbf{m}_{ref}) = \Phi(\mathbf{m}_{ref})$, and $\tilde{\mathbf{g}}(\mathbf{m}_{ref}) = \mathbf{g}(\mathbf{m}_{ref})$, but $\tilde{\mathbf{H}}(\mathbf{m}_{ref})$ is only an approximation to $\mathbf{H}(\mathbf{m}_{ref})$ obtained by neglecting the last term in Eq. (3.64b).

Gauss-Newton and Levenberg-Marquardt

Given an initial model \mathbf{m}_0 , one can describe the Gauss-Newton (GN) method as recursive minimization of $\tilde{\Phi}_\alpha$ given in Eq. (3.67a), leading to the following model sequence:

$$\tilde{\Phi}_\alpha(\mathbf{m}_{\ell+1}, \mathbf{m}_\ell) = \min_{\mathbf{m}} \tilde{\Phi}_\alpha(\mathbf{m}, \mathbf{m}_\ell) \quad \text{with } \ell = 0, 1, 2, \dots \quad (3.68)$$

A consequence of Eq. (3.68) is that the gradient vector $\tilde{\mathbf{g}}(\mathbf{m}_{\ell+1}, \mathbf{m}_\ell)$ in Eq. (3.67b) is equal to zero, resulting in the following relation:

$$-\mathbf{g}_\ell = \tilde{\mathbf{H}}_\ell(\mathbf{m}_{\ell+1} - \mathbf{m}_\ell) \quad (3.69)$$

with the abbreviations

$$\mathbf{g}(\mathbf{m}_\ell) \equiv \mathbf{g}_\ell, \quad \tilde{\mathbf{H}}(\mathbf{m}_\ell) \equiv \tilde{\mathbf{H}}_\ell.$$

Suppose that $\tilde{\mathbf{H}}_\ell$ is nonsingular, the solution of the GN method iterates as

$$\mathbf{m}_{\ell+1} = \mathbf{m}_\ell - \underbrace{\tilde{\mathbf{H}}_\ell^{-1} \mathbf{g}_\ell}_{\mathbf{p}_\ell}, \quad (3.70)$$

where \mathbf{p}_ℓ is the search direction. In order to deal with the case where $\tilde{\mathbf{H}}_\ell$ is poorly conditioned, Levenberg (1944) and Marquardt (1963) proposed a modification of the GN method in which the model increment at each iteration is damped to prevent unproductive movements through the solution space. This makes the new method compromise between the GN method and the gradient descent method (i.e., $\mathbf{p}_\ell = -\mathbf{g}_\ell$). Instead of Eq. (3.70), the solution of the Levenberg-Marquardt (LM) method is in the form of

$$\mathbf{m}_{\ell+1} = \mathbf{m}_\ell - \underbrace{\left(\tilde{\mathbf{H}}_\ell + \lambda_\ell \mathbf{D}_\ell^T \mathbf{D}_\ell \right)^{-1} \mathbf{g}_\ell}_{\mathbf{p}_\ell}, \quad (3.71)$$

where λ_ℓ is a positive damping factor and \mathbf{D}_ℓ is a diagonal matrix consisting of positive diagonal entries, which takes into account the scaling of the problem. Sometimes, the $\mathbf{D}_\ell^T \mathbf{D}_\ell$ is chosen as the diagonal of $\tilde{\mathbf{H}}_\ell$ (e.g., Nocedal and Wright, 2006).

Since no stabilizing term of the objective function in Eq. (3.61) is considered for all computations in the context of this thesis, the subproblem of the LM method for iteration ℓ is equivalent to minimize the objective function Ψ along the search direction \mathbf{p}_ℓ :

$$\Psi(\mathbf{p}_\ell) = \|\mathbf{r}_\ell - \mathbf{J}_\ell \mathbf{p}_\ell\|_{\mathbf{P}_e}^2 \quad \text{considering} \quad \|\mathbf{D}_\ell \mathbf{p}_\ell\|^2 \leq \Delta_\ell, \quad (3.72)$$

where $\mathbf{r}_\ell = \mathbf{1} - F(\mathbf{m}_\ell)$ is the residual vector, $\mathbf{J}_\ell \equiv \mathbf{J}(\mathbf{m}_\ell)$ is the Jacobian matrix, and $\Delta_\ell > 0$ is the trust region radius. In this case, the LM method can easily be implemented by the robust and efficient software package **MINPACK** (Moré et al., 1980). For the ℓ -th iteration of the LM method in **MINPACK**, it works as follows (Moré, 1978):

- ① Given $\Delta_\ell > 0$, find $\lambda_\ell \geq 0$ such that if

$$\left(\tilde{\mathbf{H}}_\ell + \lambda_\ell \mathbf{D}_\ell^T \mathbf{D}_\ell \right) \mathbf{p}_\ell = -\mathbf{g}_\ell,$$

then either $\lambda_\ell = 0$ and $\|\mathbf{D}_\ell \mathbf{p}_\ell\|^2 \leq \Delta_\ell$, or $\lambda_\ell > 0$ and $\|\mathbf{D}_\ell \mathbf{p}_\ell\|^2 = \Delta_\ell$.

- ② If $\|\Phi_\alpha(\mathbf{m}_\ell + \mathbf{p}_\ell)\|^2 < \|\Phi_\alpha(\mathbf{m}_\ell)\|^2$, set $\mathbf{m}_{\ell+1} = \mathbf{m}_\ell + \mathbf{p}_\ell$ and evaluate $\mathbf{J}_{\ell+1}$; otherwise, set $\mathbf{m}_{\ell+1} = \mathbf{m}_\ell$ and $\mathbf{J}_{\ell+1} = \mathbf{J}_\ell$.
- ③ Choose $\Delta_{\ell+1}$ and $\mathbf{D}_{\ell+1}$.

It has to be mentioned that both GN and LM methods require the storing and manipulating of the dense Hessian at each iteration. It is prohibitive when the number of model parameters is very large. For more details about the LM method see, e.g., Moré (1978) and Nocedal and Wright (2006).

Nonlinear conjugate gradient

In contrary to the GN and LM methods, which work in the framework of linearized inversion, the nonlinear conjugate gradient (NLCG) method directly solves the objective function Φ_α . The corresponding model sequence is determined by a sequence of line searches along the computed search directions until it reaches the minimum of the objective function Φ_α :

$\mathbf{m}_0 = \text{given},$

$$\Phi_\alpha(\mathbf{m}_\ell + \lambda_\ell \mathbf{p}_\ell) = \min_\lambda \Phi_\alpha(\mathbf{m}_\ell + \lambda \mathbf{p}_\ell), \quad (3.73)$$

$$\mathbf{m}_{\ell+1} = \mathbf{m}_\ell + \lambda_\ell \mathbf{p}_\ell \quad \text{with } \ell = 0, 1, 2, \dots,$$

in which λ_ℓ is the step length obtained by means of a one-dimensional search. A positive λ_ℓ will be accepted if it satisfies the Wolfe conditions (e.g., Nocedal and Wright, 2006):

$$\Phi_\alpha(\mathbf{m}_\ell + \lambda_\ell \mathbf{p}_\ell) \leq \Phi_\alpha(\mathbf{m}_\ell) + \sigma_1 \lambda_\ell \mathbf{g}(\mathbf{m}_\ell)^\top \mathbf{p}_\ell, \quad (3.74a)$$

$$\mathbf{g}(\mathbf{m}_\ell + \lambda_\ell \mathbf{p}_\ell)^\top \mathbf{p}_\ell \geq \sigma_2 \mathbf{g}(\mathbf{m}_\ell)^\top \mathbf{p}_\ell, \quad (3.74b)$$

where $0 < \sigma_1 < \sigma_2 < 1$. Eq. (3.74a) ensures that the objective function is reduced sufficiently, and Eq. (3.74b) prevents the steps from being too small. The search direction iterates as

$$\mathbf{p}_\ell = \begin{cases} -\mathbf{g}_\ell & \text{for } \ell = 0 \\ -\mathbf{g}_\ell + \beta_\ell \mathbf{p}_{\ell-1} & \text{for } \ell > 0 \end{cases}, \quad (3.75)$$

in which β_ℓ is a scalar. It is chosen such that the method reduces to the linear conjugate gradient method in the case when the objective function is quadratic and λ_ℓ is the exact one-dimensional minimizer (Gilbert and Nocedal, 1992). The well-known formulas for β_ℓ are called the Fletcher-Reeves (FR), Polak-Ribière (PR), and Hestenes-Stiefel (HS) formulas, and are given by (e.g., Nocedal and Wright, 2006)

$$\beta_\ell^{\text{FR}} = \frac{\mathbf{g}_\ell^\top \mathbf{g}_\ell}{\mathbf{g}_{\ell-1}^\top \mathbf{g}_{\ell-1}}, \quad (3.76a)$$

$$\beta_\ell^{\text{PR}} = \frac{\mathbf{g}_\ell^\top (\mathbf{g}_\ell - \mathbf{g}_{\ell-1})}{\mathbf{g}_{\ell-1}^\top \mathbf{g}_{\ell-1}}, \quad (3.76b)$$

$$\beta_\ell^{\text{HS}} = \frac{\mathbf{g}_\ell^\top (\mathbf{g}_\ell - \mathbf{g}_{\ell-1})}{(\mathbf{g}_\ell - \mathbf{g}_{\ell-1})^\top \mathbf{p}_{\ell-1}}. \quad (3.76c)$$

In the light of Eqs (3.73)–(3.76), the ℓ -th iteration of the NLCG method works as follows:

- ① Calculate the gradient \mathbf{g}_ℓ based on estimated \mathbf{m}_ℓ , then compute β_ℓ according to one of the formulas given in Eq. (3.76).
- ② Update the search direction \mathbf{p}_ℓ according to Eq. (3.75).
- ③ Perform a line search iteration to find the λ_ℓ , which results in the minimum of the objective function $\Phi_\alpha(\mathbf{m}_\ell + \lambda \mathbf{p}_\ell)$, see also the second formula in Eq. (3.73).
- ④ Update the model parameters $\mathbf{m}_{\ell+1}$ by using the third formula in Eq. (3.73).

In this thesis, the NLCG method is implemented using the software package **CG+**, and the PR formula is employed for the computation. For more theoretical details about this method see, e.g., Gilbert and Nocedal (1992), Nocedal (1992), and Nocedal and Wright (2006).

L-BFGS and L-BFGS-B

The quasi-Newton (QN) methods require only the gradient of the objective function at each iteration. By measuring the changes in gradients, they construct a model of the objective function that is good enough to produce superlinear convergence. The most popular QN method is the BFGS method, named after its discoverers Broyden, Fletcher, Goldfarb, and Shanno. In this method, the solution to the problem is updated as follows (e.g., Nocedal and Wright, 2006):

$$\mathbf{m}_{\ell+1} = \mathbf{m}_{\ell} + \lambda_{\ell} \mathbf{p}_{\ell} \quad \text{with} \quad \mathbf{p}_{\ell} = -\mathbf{B}_{\ell} \mathbf{g}_{\ell}, \quad (3.77)$$

where λ_{ℓ} is chosen to satisfy the Wolfe conditions given by Eq. (3.74), and \mathbf{B}_{ℓ} is the approximation of the inverse Hessian, which is updated at each iteration through the formula

$$\mathbf{B}_{\ell+1} = \mathbf{V}_{\ell}^{\text{T}} \mathbf{B}_{\ell} \mathbf{V}_{\ell} + \rho_{\ell} \mathbf{s}_{\ell} \mathbf{s}_{\ell}^{\text{T}}, \quad (3.78a)$$

where

$$\mathbf{s}_{\ell} = \mathbf{m}_{\ell+1} - \mathbf{m}_{\ell}, \quad \mathbf{y}_{\ell} = \mathbf{g}_{\ell+1} - \mathbf{g}_{\ell}, \quad \rho_{\ell} = \frac{1}{\mathbf{y}_{\ell}^{\text{T}} \mathbf{s}_{\ell}}, \quad \mathbf{V}_{\ell} = \mathbf{I} - \rho_{\ell} \mathbf{y}_{\ell} \mathbf{s}_{\ell}^{\text{T}}. \quad (3.78b)$$

The approximate inverse Hessian \mathbf{B}_{ℓ} is dense with the dimension of $M \times M$. In the case of a large-scale problem, the storage and manipulation of \mathbf{B}_{ℓ} are prohibitive. Nocedal (1980) proposed a technique that partially solves the storage problem caused by the BFGS update. Instead of using Eq. (3.78), $\mathbf{B}_{\ell+1}$ is updated implicitly by the vector pairs $\{\mathbf{s}_i, \mathbf{y}_i\}$ from the previous k iterations (usually, $3 \leq k \leq 7$). This implies that when the number of iterations is smaller than k , we have a usual BFGS update, and when it is larger than k , we have a limited-memory BFGS (L-BFGS) update. The updated matrix $\mathbf{B}_{\ell+1}$ is obtained by the following formulas:

For $\ell + 1 \leq k$, we have a BFGS update:

$$\begin{aligned} \mathbf{B}_{\ell+1} &= \mathbf{V}_{\ell}^{\text{T}} \mathbf{V}_{\ell-1}^{\text{T}} \cdots \mathbf{V}_0^{\text{T}} \mathbf{B}_{\ell+1}^0 \mathbf{V}_0 \cdots \mathbf{V}_{\ell-1} \mathbf{V}_{\ell} \\ &\quad + \mathbf{V}_{\ell}^{\text{T}} \cdots \mathbf{V}_1^{\text{T}} \rho_0 \mathbf{s}_0 \mathbf{s}_0^{\text{T}} \mathbf{V}_1 \cdots \mathbf{V}_{\ell} \\ &\quad \vdots \\ &\quad + \mathbf{V}_{\ell}^{\text{T}} \rho_{\ell-1} \mathbf{s}_{\ell-1} \mathbf{s}_{\ell-1}^{\text{T}} \mathbf{V}_{\ell} \\ &\quad + \rho_{\ell} \mathbf{s}_{\ell} \mathbf{s}_{\ell}^{\text{T}}, \end{aligned} \quad (3.79a)$$

and for $\ell + 1 > k$, we have an L-BFGS update:

$$\begin{aligned} \mathbf{B}_{\ell+1} &= \mathbf{V}_{\ell}^{\text{T}} \mathbf{V}_{\ell-1}^{\text{T}} \cdots \mathbf{V}_{\ell-k+1}^{\text{T}} \mathbf{B}_{\ell+1}^0 \mathbf{V}_{\ell-k+1} \cdots \mathbf{V}_{\ell-1} \mathbf{V}_{\ell} \\ &\quad + \mathbf{V}_{\ell}^{\text{T}} \cdots \mathbf{V}_{\ell-k+2}^{\text{T}} \rho_{\ell-k+1} \mathbf{s}_{\ell-k+1} \mathbf{s}_{\ell-k+1}^{\text{T}} \mathbf{V}_{\ell-k+2} \cdots \mathbf{V}_{\ell} \\ &\quad \vdots \\ &\quad + \mathbf{V}_{\ell}^{\text{T}} \rho_{\ell-1} \mathbf{s}_{\ell-1} \mathbf{s}_{\ell-1}^{\text{T}} \mathbf{V}_{\ell} \\ &\quad + \rho_{\ell} \mathbf{s}_{\ell} \mathbf{s}_{\ell}^{\text{T}}. \end{aligned} \quad (3.79b)$$

On the basis of Eq. (3.79), a two-loop recursion scheme is applied to compute the product $\mathbf{B}_{\ell+1} \mathbf{g}_{\ell+1}$ efficiently (Nocedal, 1980; Nocedal and Wright, 2006). Furthermore, this recursion allows the initial matrix $\mathbf{B}_{\ell+1}^0$ to be chosen freely and to vary between iterations. Nocedal and Wright (2006) proposed

an effective and practical method for choosing $\mathbf{B}_{\ell+1}^0$ at iteration $\ell + 1$:

$$\mathbf{B}_{\ell+1}^0 = \gamma_{\ell+1} \mathbf{B}_0 \quad \text{with} \quad \gamma_{\ell+1} = \frac{\mathbf{y}_\ell^T \mathbf{s}_\ell}{\mathbf{y}_\ell^T \mathbf{y}_\ell}. \quad (3.80)$$

According to the above descriptions, the solver of the L-BFGS method works as follows:

- ① Choose k , \mathbf{m}_0 , σ_1 , σ_2 , and a symmetric and positive definite initial matrix \mathbf{B}_0 (usually $\mathbf{B}_0 = \mathbf{I}$). Set $\ell = 0$.
- ② Compute \mathbf{p}_ℓ and $\mathbf{m}_{\ell+1}$ based on Eq. (3.77) where the step length λ_ℓ meets the Wolfe conditions given in Eq. (3.74).
- ③ Define a symmetric and positive definite matrix $\mathbf{B}_{\ell+1}^0$ based on Eq. (3.80).
- ④ Calculate $\mathbf{B}_{\ell+1}$ for iteration $\ell + 1$ according to estimated $\mathbf{B}_{\ell+1}^0$. If $\ell + 1 \leq k$, update $\mathbf{B}_{\ell+1}^0$ $\ell + 1$ times using the vector pairs $\{\mathbf{s}_i, \mathbf{y}_i\}$ for $i = 0, 1, \dots, \ell$ based on Eq. (3.79a). Otherwise, update $\mathbf{B}_{\ell+1}^0$ k times using the vector pairs $\{\mathbf{s}_i, \mathbf{y}_i\}$ for $i = \ell - k + 1, \ell - k + 2, \dots, \ell$ based on Eq. (3.79b).
- ⑤ Set $\ell = \ell + 1$ and go to ② until the convergence is reached.

For σ_1 and σ_2 , we set $\sigma_1 = 10^{-4}$ and $\sigma_2 = 0.9$ as proposed by Liu and Nocedal (1989). More details about the L-BFGS method can be found in, e.g., Nocedal (1980), Liu and Nocedal (1989), and Nocedal and Wright (2006).

The L-BFGS-B method is an extension of the L-BFGS method capable of handling simple bounds on the model parameters. It is to minimize the objective function Φ_α considering the bound constraints

$$\mathbf{m}_{\min} \leq \mathbf{m} \leq \mathbf{m}_{\max}, \quad (3.81)$$

where \mathbf{m}_{\min} and \mathbf{m}_{\max} are the vectors consisting of the lower and upper bounds on the model parameters \mathbf{m} . The L-BFGS-B method is described in detail in Byrd et al. (1995) and is briefly introduced as follows (Zhu et al., 1997). At iteration ℓ , a limited-memory BFGS approximation to the inverse Hessian \mathbf{B}_ℓ is updated. The limited-memory matrix is used to define a quadratic model of the objective function. By means of the line search method, the search direction is then computed using a two-stage approach: first, the gradient projection method is used to identify a set of active model parameters, i.e., the parameters that will be held at their bounds; then the quadratic model is approximately minimized with respect to the free model parameters. The search direction is defined to be the vector leading the current iteration to this approximate minimizer. Finally, a line search is performed along the search direction using the subroutine described in Moré and Thuente (1994).

In this thesis, the L-BFGS and L-BFGS-B methods are implemented based on the software packages **L-BFGS** and **L-BFGS-B** (Zhu et al., 1997). Several successful applications of the two algorithms in geophysics and hydraulic engineering can be found in Guitton and Symes (2003), Ding et al. (2004), Brossier et al. (2009), and Asnaashari et al. (2013).

Comparisons of the algorithms: a synthetic example

In the following, a synthetic example for gravity inversion as given in Pujol (2007) is used to analyze the performance of the four nonlinear iteration algorithms, i.e., LM, NLCG, L-BFGS, and L-BFGS-B. The inversion problem is described as follows.

Consider a buried homogeneous sphere of a radius R with the center at (x_o, y_o, z_o) . The vertical component of the gravitational attraction at a point (x_i, y_i, z_i) caused by the sphere is given by

$$g(x_i, y_i, z_i) = \frac{4\pi}{3} \frac{\mathcal{G}\rho R^3(z_o - z_i)}{[(x_i - x_o)^2 + (y_i - y_o)^2 + (z_i - z_o)^2]^{3/2}} \quad (3.82)$$

with \mathcal{G} the gravitational constant, ρ the density contrast, which is the difference between the densities of the sphere and the surrounding medium. For the distance in km, density in g/cm^3 , and gravity in mGal, the numerical value of \mathcal{G} is chosen as 6.672 in the computations.

The goal of this inverse problem is to find out the values of z_o and R of the sphere with which the resulting gravity best fits n given gravity values G_i at point (x_i, y_i, z_i) . It will be assumed that ρ , x_o , and y_o are known, and hence this is a nonlinear inverse problem with the unknown model parameters $\mathbf{m} = (z_o, R)^T$. The synthetic data is generated using Eq. (3.82) with the following values: $x_o = y_o = 0$ km, $z_o = 7$ km, $x_i = 0$ km, $y_1 = -10$ km, $y_{i+1} - y_i = 1$ km for $i = 1, \dots, 20$, $z_i = 0$ km, $R = 5$ km, and $\rho = 0.25$ g/cm^3 . The mean of the square sum of the residuals, given by

$$\sigma^2(z_o, R) = \frac{1}{n} \sum_{i=1}^n [G_i - g(x_i, y_i, z_i)]^2, \quad (3.83)$$

plays the role of the objective function to be minimized and is also used for measuring of the data misfits σ . From a physical point of view, R cannot be larger than z_o , but for the analysis that follows,

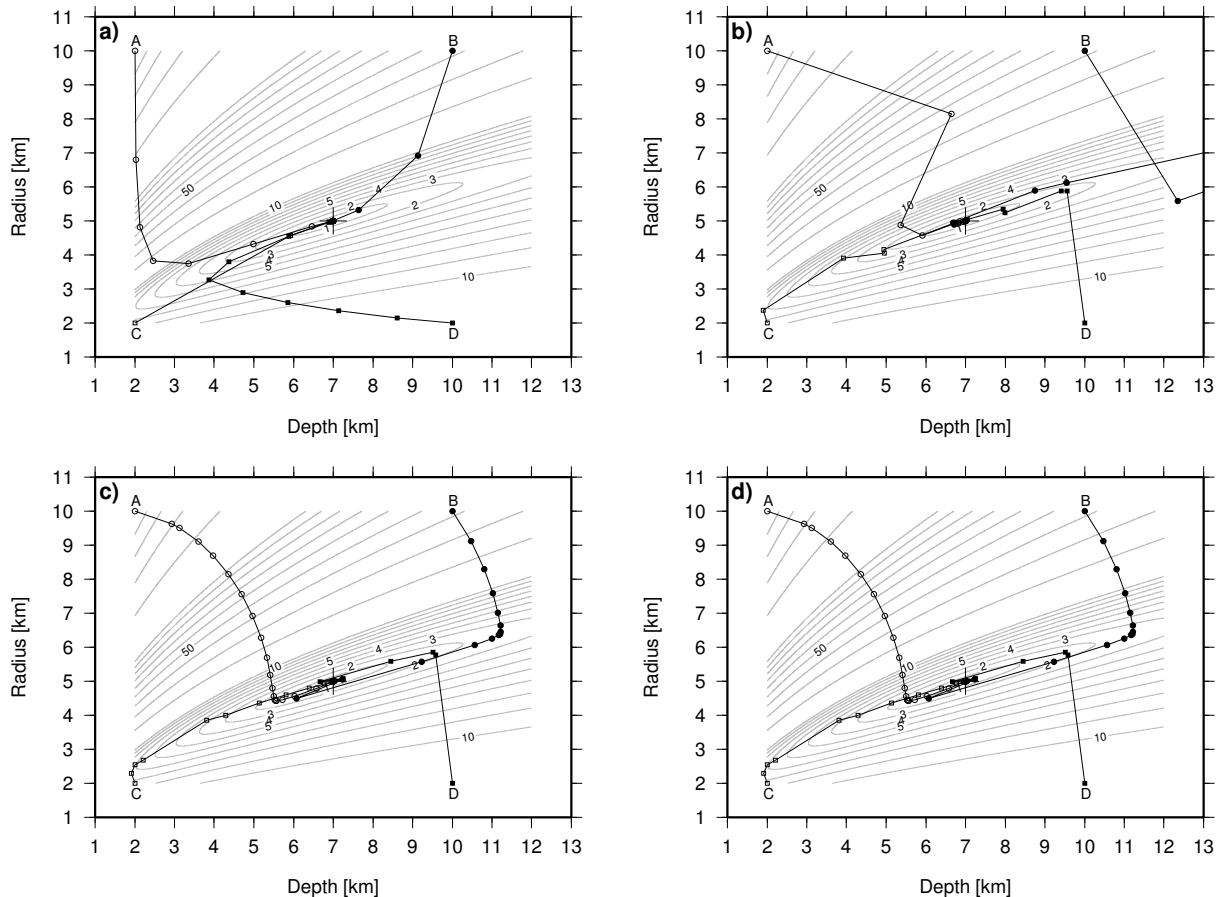


Figure 3.5: Contour lines of the data misfits σ and the paths followed by the estimated model points (z_o^ℓ, R^ℓ) at iteration ℓ for the algorithm: **a)** LM; **b)** NLCG; **c)** L-BFGS; **d)** L-BFGS-B. The points labeled as A, B, C, and D are the initial model points with the values of (2, 10), (10, 10), (2, 2), and (10, 2) for the inversion. The large cross is centered at the true model point (7, 5), which is at the minimum of the data misfit with the value of 0 mGal.

we will only be concerned with the mathematical aspects of the problem. For the sake of simplicity, the model parameters are assumed to be known in the range of $2 \leq z_o \leq 12$ and $2 \leq R \leq 10$. In order to investigate the behavior of the algorithms depending on the chosen initial model points, four points in the form of (z_o^0, R^0) are used: A (2, 10), B (10, 10), C (2, 2), and D (10, 2).

Fig. 3.5 shows the contour lines of the data misfits $\sigma(z_o, R)$ and the paths followed by the estimated model points (z_o^ℓ, R^ℓ) at iteration ℓ for each algorithm. The fact that, solving the inverse problem is equivalent to find a path in the (z_o, R) plane that connects an initial model point (z_o^0, R^0) and the target point (z_o^T, R^T) with the minimum of σ , must be kept in mind. In this example, $(z_o^T, R^T) = (7, 5)$, and $\sigma = 0$ at the target point. From this figure, it can be seen that the target model point can be found successfully by all algorithms starting from four different initial points. This indicates the effectiveness of the used algorithms. However, their paths are quite different. This is mainly caused by different approaches for finding the search direction in each algorithm. Since the L-BFGS and L-BFGS-B methods use the same approach (i.e., the limited-memory BFGS update of the inverse Hessian and the line search algorithm proposed by Moré and Thuente (1994)), as well as the inverse problem is unconstrained, the resulting paths are the same (see Figs 3.5c and 3.5d).

In addition, the data misfits in terms of the number of iterations for the four different initial model points are shown in Fig. 3.6. The curves for the L-BFGS method coincide with the ones for the L-BFGS-B method exactly. Besides the case of using the initial model point D, the LM method

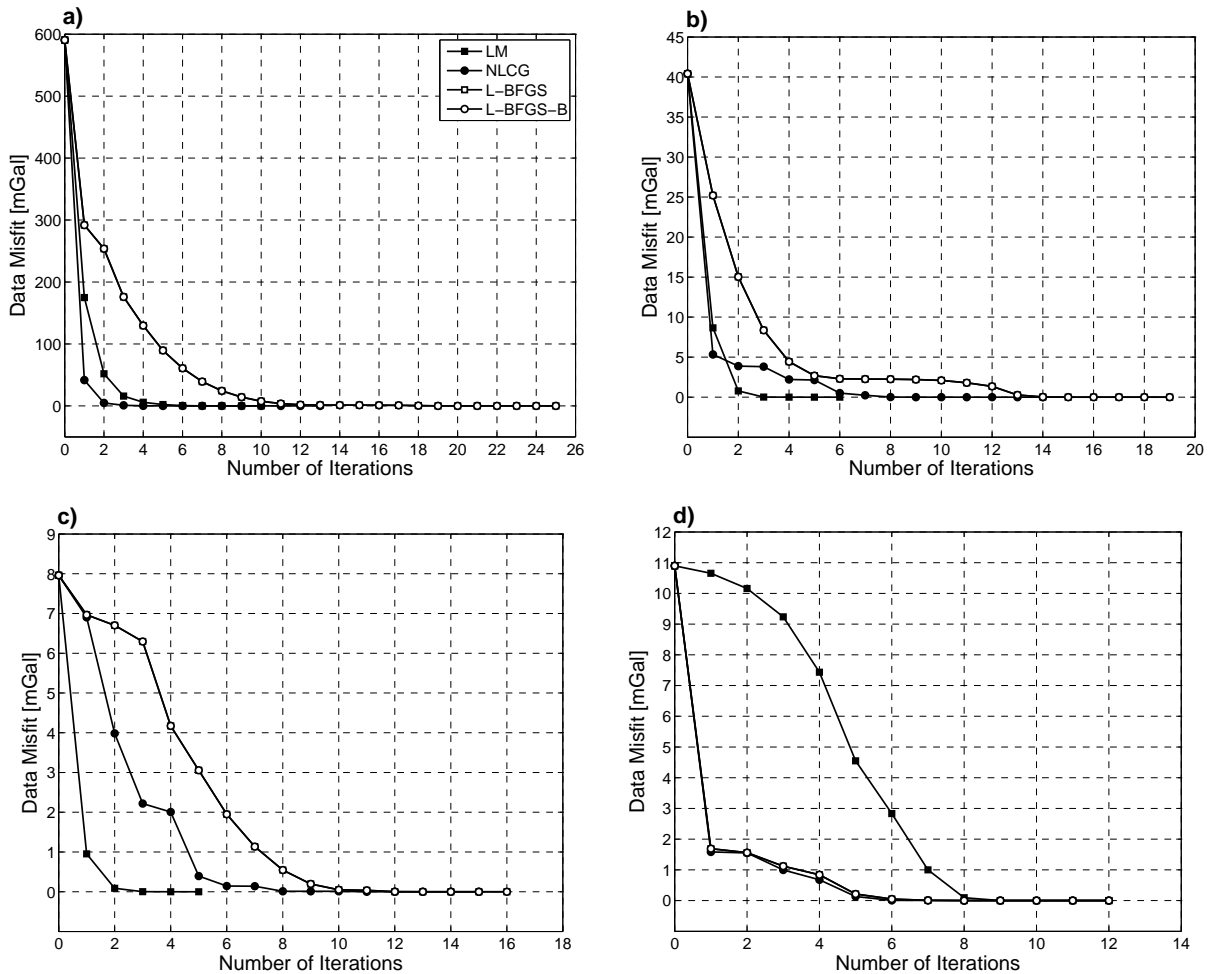


Figure 3.6: Data misfits in terms of the number of iterations for the initial model point: **a)** A (2, 10); **b)** B (10, 10); **c)** C (2, 2); **d)** D (10, 2).

converges rapidly within the smallest number of iterations, and then the NLCG method follows. The main reason can be attributed to the large descents of the objective function at the first several iterations for the LM method, in particular the first iteration in which the Hessian is computed based on Eq. (3.66b) with the given Jacobian matrix, while the Hessians for NLCG, L-BFGS, and L-BFGS-B are the identity matrices. The different behavior of the first iteration between NLCG and L-BFGS/L-BFGS-B is due to the differently implemented line search algorithms in the chosen software. For the case of using the initial point D, the required number of iterations is larger for the LM method than the other three methods. This may be due to the singularity of the Hessian computed by Eq. (3.66b). Pujol (2007) showed that the Gauss-Newton method fails to find the target point in this case. Instead, the trust region based LM method solves this problem by employing a regularization parameter and a regularization matrix, see Eqs (3.71) and (3.72), resulting in smaller search directions in the iterations, especially in the first iteration (see Figs 3.5 and 3.6).

The above discussion is only based on the simple example. At least, we can say that the performance of the four algorithms is quite similar when solving an unconstrained nonlinear problem. Often, the LM method can provide a faster convergence than the other three methods (see the cases of the model points A, B, and C); however, a slower convergence can be observed in the case of the model point D, indicating the higher dependence of the LM method on the chosen initial model point. If the nonlinear problem is bound constrained, of course, the dedicated L-BFGS-B method should outperform the other three methods. A related numerical comparison between the four algorithms for regional gravity field modeling will be carried out in the next chapter.

3.4 Point mass method with fixed positions

3.4.1 Mathematical model

In this method, the point mass RBFs are located on the nodes of one or more predefined grids. This means that the 3D positions of all point mass RBFs are known. Thus, only the magnitudes have to be estimated. Assuming that there are I observed linear functionals $l_i = L_i T$ and K point mass RBFs, the system of the observation equations is given as

$$\begin{cases} l(\phi_1, \lambda_1, r_1) - e_1 = \sum_{k=1}^K \beta_k D_l B^{\text{PM}}(\mathbf{r}_1, \mathbf{r}'_k) \\ l(\phi_2, \lambda_2, r_2) - e_2 = \sum_{k=1}^K \beta_k D_l B^{\text{PM}}(\mathbf{r}_2, \mathbf{r}'_k) \\ \vdots \\ l(\phi_I, \lambda_I, r_I) - e_I = \sum_{k=1}^K \beta_k D_l B^{\text{PM}}(\mathbf{r}_I, \mathbf{r}'_k) \end{cases} \quad \text{with } I \geq K \geq 1 \quad (3.84)$$

in accordance with Eq. (3.6). Due to the known position vectors \mathbf{r}_i for the observations and \mathbf{r}'_k for the RBFs, the observations l_i are linear functionals of the unknown magnitudes β_k , thus Eq. (3.84) can be expressed as a matrix-vector product

$$\mathbf{l} - \mathbf{e} = \mathbf{A}\mathbf{x}, \quad (3.85a)$$

where $\mathbf{l} = (l_1, l_2, \dots, l_I)^T$ is the $I \times 1$ vector of observations, $\mathbf{e} = (e_1, e_2, \dots, e_I)^T$ is the vector containing the random observation errors, and $\mathbf{x} = (\beta_1, \beta_2, \dots, \beta_K)^T$ is the $K \times 1$ vector of unknown magnitudes. The $I \times K$ design matrix \mathbf{A} consists of the point mass RBFs evaluated at the observation points \mathbf{r}_i for $i \in \{1, 2, \dots, I\}$, resulting in

$$\mathbf{A} = \begin{pmatrix} D_l B^{\text{PM}}(\mathbf{r}_1, \mathbf{r}'_1) & D_l B^{\text{PM}}(\mathbf{r}_1, \mathbf{r}'_2) & \cdots & D_l B^{\text{PM}}(\mathbf{r}_1, \mathbf{r}'_K) \\ D_l B^{\text{PM}}(\mathbf{r}_2, \mathbf{r}'_1) & D_l B^{\text{PM}}(\mathbf{r}_2, \mathbf{r}'_2) & \cdots & D_l B^{\text{PM}}(\mathbf{r}_2, \mathbf{r}'_K) \\ \vdots & \vdots & \ddots & \vdots \\ D_l B^{\text{PM}}(\mathbf{r}_I, \mathbf{r}'_1) & D_l B^{\text{PM}}(\mathbf{r}_I, \mathbf{r}'_2) & \cdots & D_l B^{\text{PM}}(\mathbf{r}_I, \mathbf{r}'_K) \end{pmatrix}. \quad (3.85b)$$

In the framework of the Gauss-Markov model, the unknown magnitude vector \mathbf{x} can be estimated by the linear least-squares procedures described in Section 3.3.3.

In addition to the observation equation system given by Eqs (3.84) and (3.85), $(n' + 1)^2$ additional equations, which play the role of constraints (see also Eq. (3.11)), are sometimes taken into account for estimating the magnitudes, especially in the case when the full point mass RBFs are used, but the input data are bandlimited. In this case, a combined observation equation system is obtained according to

$$\begin{pmatrix} 1 \\ 0 \end{pmatrix} - \begin{pmatrix} \mathbf{e} \\ \mathbf{e}' \end{pmatrix} = \begin{pmatrix} \mathbf{A} \\ \mathbf{C} \end{pmatrix} \mathbf{x}, \quad (3.86)$$

where \mathbf{C} is the $(n' + 1)^2 \times K$ design matrix and $\mathbf{C}\mathbf{x} = 0$ is the matrix-vector product of Eq. (3.11). Similar to the process of Tikhonov regularization described in Section 3.3.4, the least-squares solution of Eq. (3.86) can be obtained by solving the following normal equation

$$\left(\underbrace{\mathbf{A}^T \mathbf{P}_e \mathbf{A}}_{\mathbf{N}_1} + \lambda \underbrace{\mathbf{C}^T \mathbf{P}_{e'} \mathbf{C}}_{\mathbf{N}_2} \right) \mathbf{x} = \underbrace{\mathbf{A}^T \mathbf{P}_e \mathbf{l}}_{\mathbf{y}}, \quad (3.87)$$

where λ is a scaling factor, which is determined empirically in this thesis: let m_1 and m_2 be the mean value of the diagonal elements of \mathbf{N}_1 and \mathbf{N}_2 , respectively. The scaling factor is then defined as the ratio between m_1 and m_2 , yielding $\lambda = m_1/m_2$. Defining $\bar{\mathbf{N}} = \mathbf{N}_1 + \lambda \mathbf{N}_2$, Eq. (3.87) can be rewritten as

$$\bar{\mathbf{N}}\mathbf{x} = \mathbf{y}. \quad (3.88)$$

If $\bar{\mathbf{N}}$ is singular, the standard Tikhonov regularization will be applied to solve the above normal equation, resulting in

$$\hat{\mathbf{x}}_\alpha = \left(\bar{\mathbf{N}} + \alpha \mathbf{I} \right)^{-1} \mathbf{y}. \quad (3.89)$$

In the following, we call the solution considering the constraints the constrained solution, and the one obtained without using the constraints the unconstrained solution. In addition, the point mass method with fixed positions is abbreviated as PM-FIX in the remaining of this thesis.

3.4.2 Grid setup

Besides the estimation step of this method, another vital step is to design the grids by choosing proper grid factors (see Fig. 3.3 or Section 2.7.4 for a more detailed discussion). In this context, only the geographic grid is used, and the grid extent, grid spacing, as well as grid depth will be determined sequentially. The total number of grid points (i.e., total number of point mass RBFs) must not exceed the number of observations. It is dependent on the selected grid extent and grid spacing. Klees et al. (2008) and Wittwer (2009) found empirically that choosing a grid with an amount of RBFs equals to $1/4 - 1/3$ of the number of observations is advisable. However, in the case of oversampling of the observations, such a grid may be too dense. Often, to avoid possible over-parameterization, the grid spacing is preferred to be chosen in such a way that all signals in the areas with smooth features

can be modeled. Then, further steps can be carried out for representing rough features, such as the local refinement used in Klees and Wittwer (2007), Klees et al. (2008), and Wittwer (2009) or adding more grids. No explicit strategy to define the optimal grid spacing can be given as it is affected by the data distribution, signal variation, as well as spatial bandwidths of the RBFs. In practice, a proper grid spacing is usually chosen by experimenting with various candidates and comparing the obtained solutions. After defining the grid factors associated with the horizontal positions of the point mass RBFs, the grid depth is to be fixed. Because of the high correlation between the grid depth and the grid spacing, some attempts have been made to give the relationship between them. For example, Needham (1970) suggested that the depth-spacing ratio should be at least 0.8; however, Vermeer (1995) proposed a ratio of 2, and furthermore, the ratios of about 1 were used for the geoid computations in Ihde et al. (1998) and Tenzer et al. (2009).

In this thesis, we use an empirical and a heuristic approach for the grid depth determination. The principle of this empirical approach is the same as the one for finding the proper regularization parameter as described in Section 3.3.5. The only change is that the variable of the function becomes the grid depth d below the reference sphere. Given n depth candidates, our goal is to find the one with which the value of the function $RMS(d)$ in the form

$$RMS(d) = \sqrt{\frac{1}{N} \|\mathbf{B}\hat{\mathbf{x}}_d - \mathbf{q}\|^2} \quad (3.90)$$

is minimal. For the notations of the other variables in the above equation, see Eq. (3.46). It should be noted that the linear problem for estimating $\hat{\mathbf{x}}_d$ may be ill-posed. In this case, Tikhonov regularization should be applied, even though this will make the computation procedure more complicated. The successful application of this approach for finding a proper grid depth in local gravity field modeling can be found in Tenzer and Klees (2008).

The second approach is based on the GCV technique, which is frequently used for finding the proper regularization parameter (see also Section 3.3.5). Considering Eq. (3.50), the GCV function to be minimized in this case is given by

$$GCV(d) = \frac{I \|\mathbf{A}_d \hat{\mathbf{x}}_d - \mathbf{1}\|_{\mathbf{P}_e}^2}{[I - \text{tr}(\mathbf{Q}^d)]^2} \quad (3.91a)$$

with

$$\mathbf{Q}^d = \mathbf{A}_d \left(\mathbf{A}_d^T \mathbf{P}_e \mathbf{A}_d \right)^{-1} \mathbf{A}_d^T \mathbf{P}_e \quad (3.91b)$$

for the case that the linear problem for estimating $\hat{\mathbf{x}}_d$ is well-posed, or

$$\mathbf{Q}^d = \mathbf{A}_d \left(\mathbf{A}_d^T \mathbf{P}_e \mathbf{A}_d + \alpha_d \mathbf{R}_d \right)^{-1} \mathbf{A}_d^T \mathbf{P}_e \quad (3.91c)$$

for the case of ill-posedness. \mathbf{A}_d , α_d , and \mathbf{R}_d in Eq. (3.91) are the design matrix, the regularization parameter, and the regularization matrix associated with the grid depth d , respectively.

3.4.3 Grid formation

In this section, the issue of grid formation for PM-FIX will be discussed. It can be subdivided into two groups: (1) a single-grid formation and (2) a multi-grid formation. Fig. 3.7 shows two examples of the point mass RBF locations for the cases of a single-grid formation and a two-grid formation. In the first case, only one grid at the chosen depth is used for the modeling (see Fig. 3.7a). Such a formation is simple and quite suitable for regularly distributed observations. One main drawback of this formation is that it is not data-adaptive due to the same spatial bandwidths for all point mass

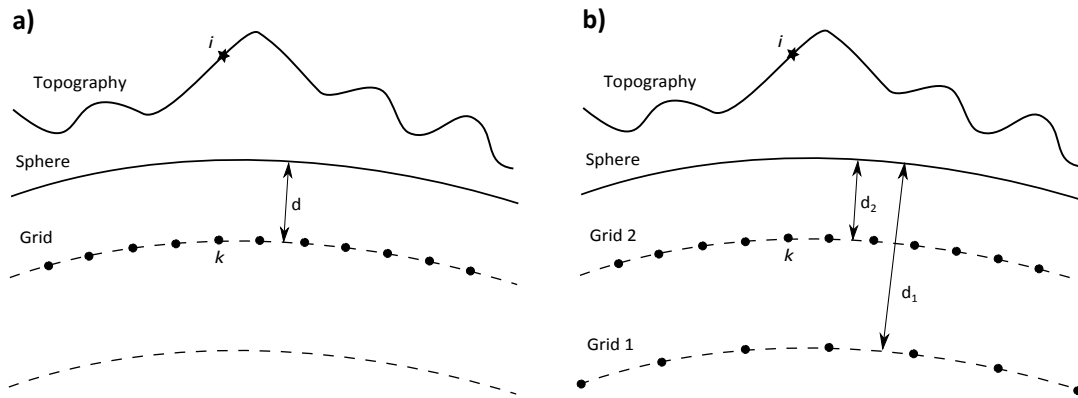


Figure 3.7: Illustration of the point mass RBF locations in the case of **a)** a single-grid formation; **b)** a two-grid formation.

RBFs. This makes it less suitable for the case of irregularly distributed data as RBFs with the same density are in the areas with dense and sparse data. A possible way to circumvent the drawback of the single-grid formation is to set up two or more grids at different depths. In this case, the point mass RBFs at different depths seem to be suitable for approximating different signal frequencies. This can also be interpreted from a geophysical point of view. The anomalous features with small scales but high frequencies are usually caused by anomalous masses near the Earth's surface, such as coal and metal deposits or oil and gas reservoirs, whereas large-scale and low-frequency features are mainly caused by anomalous masses in the deep Earth, such as the Moho undulations and mantle convection. Often, the deep grid should have a larger grid extent and grid spacing, and the shallower one has a smaller extent and spacing. Regarding the issue of numerical instabilities, it is possible to choose the extents of the grids at different depths as being similar to the data area in practical applications. If the result obtained by using only one grid is sufficiently satisfactory, no more grids are needed. Otherwise, two schemes can be utilized to set up the grid formation. In the first scheme, all grids with different grid factors are defined at one time. In the second scheme, the grids are arranged sequentially from the deepest to the shallowest. In this thesis, we employ the second scheme for the numerical tests in Chapter 4, as the approaches described above for finding a proper grid depth can be easily implemented in this case.

In the light of the above discussion, the general procedures of PM-FIX with the use of a single-grid and a multi-grid formation are described as follows:

Single-grid formation

- ① Define the grid extent according to the extents of data area and model area. If the data area is larger than the model area, set the grid extent to be similar to the data area. If the model area is the same as the data area, the grid extent is usually preferred to be larger than the data area; however, the larger the grid extent is, the more severe the numerical instabilities become.
- ② Give a set of grid spacings as candidates. For each candidate, solve a linear equation system, which is constructed by the point mass RBFs on the grid at a proper depth derived from the empirical or the GCV approach.
- ③ Assess the quality of the solutions by comparing the predicted values to the observed values on a set of control points. The solution with the smallest RMS (or STD) error is regarded as the final solution.

To reduce the computation complexity, only one grid spacing is usually used in ②.

Multi-grid formation

- ① For Grid 1. Define Grid 1 with a given grid extent and grid spacing. Determine the grid depth by the empirical or the GCV approach, and then solve the linear equation system constructed by the point mass RBFs on the nodes of Grid 1 and the initial input data. Subtract the contributions of the estimated point mass RBFs from the initial input data, resulting in the residuals that will be used as input for Grid 2.
- ② For Grid i ($i \geq 2$). If the given input residuals are sufficiently small by satisfying a predefined criterion, go to ④. Otherwise, define Grid i with a smaller grid spacing than Grid $i - 1$. Note that the extent of Grid i can either be the same or smaller than Grid $i - 1$. Determine the grid depth by the empirical or the GCV approach, but with the constraint that Grid i must be shallower than Grid $i - 1$. Solve the linear equation system constructed by the point mass RBFs on the nodes of Grid i and the input residuals, and then subtract the contributions of the estimated point mass RBFs from the input, resulting in new residuals that will be used as input for the next grid.
- ③ Let $i = i + 1$ and go to ②.
- ④ Solve the new linear equation system constructed by all point mass RBFs located on the chosen grids and the initial input data, yielding the final solution.

Each new grid is added manually. Often, two or three grids are sufficient for practical applications.

3.5 Point mass method with free positions

3.5.1 Mathematical model

Contrary to the point mass method with fixed positions introduced in Section 3.4, “free positions” means that the 3D positions of the point mass RBFs are completely or incompletely unknown within the computation process. As a consequence, the positions of the point mass RBFs have to be determined along with the magnitudes. Thus, the nonlinear problem with more than one unknown parameters for each point mass RBF needs to be solved. In the following description, the point mass method with free positions is abbreviated as PM-FRE.

Suppose again that I linear functionals $l_i = L_i T$ are observed, and K point mass RBFs are used to fit the observations. The system of the observation equations is the same as Eq. (3.84), leading to a matrix-vector notation

$$\mathbf{l} - \mathbf{e} = F(\mathbf{m}). \quad (3.92)$$

The notations of vectors \mathbf{l} and \mathbf{e} can be seen in Eq. (3.85a), \mathbf{m} is the model parameter vector with the length of M , containing unknown magnitudes and positions, and F is the forward modeling operator. The expression of $F(\mathbf{m})$ in the point mass method can be simply taken from the right-hand side of Eq. (3.6) for any linear functional of the disturbing potential. If the positions of the point mass RBFs are known, then $F(\mathbf{m})$ is equivalent to the term $\mathbf{A}\mathbf{x}$ in Eq. (3.85a).

The nonlinear equation system given by Eq. (3.92) is solved iteratively based on an initial guess of the model parameter vector. For more details about solving a nonlinear system, we refer to Section 3.3.6. According to the descriptions of the iteration algorithms in Section 3.3.6, the computation of the Jacobian matrix of the residual vector in iteration ℓ for updating $\mathbf{m}_{\ell+1}$ is necessary. Defining the residual vector $\mathbf{R}(\mathbf{m}_\ell) = \mathbf{l} - F(\mathbf{m}_\ell)$, the corresponding Jacobian matrix $\mathbf{J}(\mathbf{m}_\ell)$ can be expressed by

the following equations on the basis of Eq. (3.63):

$$\mathbf{J}(\mathbf{m}_\ell) = \begin{pmatrix} \mathbf{J}_{11}^\ell & \mathbf{J}_{12}^\ell & \cdots & \mathbf{J}_{1K}^\ell \\ \mathbf{J}_{21}^\ell & \mathbf{J}_{22}^\ell & \cdots & \mathbf{J}_{2K}^\ell \\ \vdots & \vdots & \ddots & \vdots \\ \mathbf{J}_{I1}^\ell & \mathbf{J}_{I2}^\ell & \cdots & \mathbf{J}_{IK}^\ell \end{pmatrix} \quad (3.93a)$$

with

$$\mathbf{J}_{ik}^\ell = \left(\frac{\partial \mathbf{R}^i(\mathbf{m})}{\partial \beta_k} \Big|_{\mathbf{m}=\mathbf{m}_\ell} \quad \frac{\partial \mathbf{R}^i(\mathbf{m})}{\partial r_k} \Big|_{\mathbf{m}=\mathbf{m}_\ell} \quad \frac{\partial \mathbf{R}^i(\mathbf{m})}{\partial \phi_k} \Big|_{\mathbf{m}=\mathbf{m}_\ell} \quad \frac{\partial \mathbf{R}^i(\mathbf{m})}{\partial \lambda_k} \Big|_{\mathbf{m}=\mathbf{m}_\ell} \right), \quad (3.93b)$$

$$\mathbf{m}_\ell = \left(\beta_1^\ell, r_1^\ell, \phi_1^\ell, \lambda_1^\ell, \dots, \beta_K^\ell, r_K^\ell, \phi_K^\ell, \lambda_K^\ell \right)^\top, \quad (3.93c)$$

for the case where the magnitude, radial distance, latitude, and longitude for each point mass RBF are to be estimated, and the Jacobian matrix $\mathbf{J}(\mathbf{m}_\ell)$ has a dimension of $I \times M$ with $M = 4 \times K$. Or, with

$$\mathbf{J}_{ik}^\ell = \left(\frac{\partial \mathbf{R}^i(\mathbf{m})}{\partial \beta_k} \Big|_{\mathbf{m}=\mathbf{m}_\ell} \quad \frac{\partial \mathbf{R}^i(\mathbf{m})}{\partial r_k} \Big|_{\mathbf{m}=\mathbf{m}_\ell} \right), \quad (3.93d)$$

$$\mathbf{m}_\ell = \left(\beta_1^\ell, r_1^\ell, \dots, \beta_K^\ell, r_K^\ell \right)^\top, \quad (3.93e)$$

for the case where only the magnitude and radial distance for each point mass RBF are to be estimated, and the Jacobian matrix $\mathbf{J}(\mathbf{m}_\ell)$ has a dimension of $I \times M$ with $M = 2 \times K$. The subscripts i and k satisfy $i = 1, \dots, I$ and $k = 1, \dots, K$. Herein, only the case with $I \geq M$ is considered. We call the first case the all-direction optimization and the second case the radial-direction optimization. In the light of Eq. (3.6), the four elements in Eq. (3.93b) are formulated as follows:

$$\frac{\partial \mathbf{R}^i(\mathbf{m})}{\partial \beta_k} = \frac{\partial \left[l_i - \sum_{k'=1}^K \beta_{k'} D_l B^{\text{PM}}(\mathbf{r}_i, \mathbf{r}_{k'}) \right]}{\partial \beta_k} = -D_l B^{\text{PM}}(\mathbf{r}_i, \mathbf{r}_k), \quad (3.94a)$$

$$\frac{\partial \mathbf{R}^i(\mathbf{m})}{\partial r_k} = \frac{\partial \left[l_i - \sum_{k'=1}^K \beta_{k'} D_l B^{\text{PM}}(\mathbf{r}_i, \mathbf{r}_{k'}) \right]}{\partial r_k} = -\beta_k \frac{\partial}{\partial r_k} D_l B^{\text{PM}}(\mathbf{r}_i, \mathbf{r}_k), \quad (3.94b)$$

$$\frac{\partial \mathbf{R}^i(\mathbf{m})}{\partial \phi_k} = \frac{\partial \left[l_i - \sum_{k'=1}^K \beta_{k'} D_l B^{\text{PM}}(\mathbf{r}_i, \mathbf{r}_{k'}) \right]}{\partial \phi_k} = -\beta_k \frac{\partial}{\partial \phi_k} D_l B^{\text{PM}}(\mathbf{r}_i, \mathbf{r}_k), \quad (3.94c)$$

$$\frac{\partial \mathbf{R}^i(\mathbf{m})}{\partial \lambda_k} = \frac{\partial \left[l_i - \sum_{k'=1}^K \beta_{k'} D_l B^{\text{PM}}(\mathbf{r}_i, \mathbf{r}_{k'}) \right]}{\partial \lambda_k} = -\beta_k \frac{\partial}{\partial \lambda_k} D_l B^{\text{PM}}(\mathbf{r}_i, \mathbf{r}_k). \quad (3.94d)$$

When using gravity anomalies for the modeling, i.e., $D_l B^{\text{PM}}(\mathbf{r}_i, \mathbf{r}_k) \rightarrow D_{\Delta g} B^{\text{PM}}(\mathbf{r}_i, \mathbf{r}_k)$, see also Eq. (3.5a), Eqs (3.94a)–(3.94d) are then reformulated as

$$\frac{\partial \mathbf{R}^i(\mathbf{m})}{\partial \beta_k} = A1 + \sum_{n=0}^{N_{\min}-1} \frac{n-1}{r_k r_i} \left(\frac{r_k}{r_i} \right)^{n+1} P_n(\cos \psi_{ik}) \quad (3.95a)$$

with

$$\mathcal{A}1 = \frac{2}{\ell_{ik} r_i} - \frac{r_i - r_k \cos \psi_{ik}}{\ell_{ik}^3},$$

$$\frac{\partial \mathbf{R}^i(\mathbf{m})}{\partial r_k} = \mathcal{A}2 + \beta_k \sum_{n=0}^{N_{\min}-1} \frac{n(n-1)}{r_k^2 r_i} \left(\frac{r_k}{r_i}\right)^{n+1} P_n(\cos \psi_{ik}) \quad (3.95b)$$

with

$$\mathcal{A}2 = \beta_k \left[\frac{3r_i r_k (1 - \cos^2 \psi_{ik})}{\ell_{ik}^5} - \frac{2r_k}{r_i \ell_{ik}^3} \right],$$

$$\frac{\partial \mathbf{R}^i(\mathbf{m})}{\partial \phi_k} = \mathcal{A}3 + \beta_k \sum_{n=0}^{N_{\min}-1} \frac{n-1}{r_k r_i} \left(\frac{r_k}{r_i}\right)^{n+1} \frac{\partial P_n(\cos \psi_{ik})}{\partial \cos \psi_{ik}} \frac{\partial \cos \psi_{ik}}{\partial \phi_k} \quad (3.95c)$$

with

$$\mathcal{A}3 = \beta_k \left\{ \frac{3(r_k^3 - r_i r_k^2 \cos \psi_{ik})}{\ell_{ik}^5} [\sin \phi_i \cos \phi_k - \cos \phi_i \sin \phi_k \cos(\lambda_i - \lambda_k)] \right\}, \quad \text{and}$$

$$\frac{\partial \mathbf{R}^i(\mathbf{m})}{\partial \lambda_k} = \mathcal{A}4 + \beta_k \sum_{n=0}^{N_{\min}-1} \frac{n-1}{r_k r_i} \left(\frac{r_k}{r_i}\right)^{n+1} \frac{\partial P_n(\cos \psi_{ik})}{\partial \cos \psi_{ik}} \frac{\partial \cos \psi_{ik}}{\partial \lambda_k} \quad (3.95d)$$

with

$$\mathcal{A}4 = \beta_k \left\{ \frac{3(r_k^3 - r_i r_k^2 \cos \psi_{ik})}{\ell_{ik}^5} [\cos \phi_i \cos \phi_k \sin(\lambda_i - \lambda_k)] \right\}.$$

From the above equations, it can be seen that the computation of the elements in the Jacobian matrix is fast in the case of $N_{\min} = 0$, as only the analytical terms (i.e., $\mathcal{A}1 - \mathcal{A}4$) are taken into account. If N_{\min} is much larger than 0, the computation will become much slower as time-consuming summations of the series expansions are required. For other observed gravity field quantities, such as the gravity disturbance and the geoid height/height anomaly, the expressions of the elements in the corresponding Jacobian matrix can be derived in a similar way with the help of the following auxiliary formulas:

$$\frac{\partial \cos \psi_{ik}}{\partial \phi_k} = \sin \phi_i \cos \phi_k - \cos \phi_i \sin \phi_k \cos(\lambda_i - \lambda_k), \quad (3.96a)$$

$$\frac{\partial \cos \psi_{ik}}{\partial \lambda_k} = \cos \phi_i \cos \phi_k \sin(\lambda_i - \lambda_k), \quad (3.96b)$$

$$\frac{\partial}{\partial \phi_k} \left(\frac{1}{\ell_{ik}} \right) = \frac{r_i r_k}{\ell_{ik}^3} \frac{\partial \cos \psi_{ik}}{\partial \phi_k}, \quad (3.96c)$$

$$\frac{\partial}{\partial \lambda_k} \left(\frac{1}{\ell_{ik}} \right) = \frac{r_i r_k}{\ell_{ik}^3} \frac{\partial \cos \psi_{ik}}{\partial \lambda_k}. \quad (3.96d)$$

3.5.2 Two-step point mass method and relevant model factors

In practice, there are usually two strategies to determine the magnitudes and positions of the point mass RBFs. The first is that a set of point mass RBFs with an initial guess of their magnitudes and positions are given; then these parameters are updated iteratively. In this case, the crucial issue is how to choose the number of used point mass RBFs and their initial positions properly. This is a hard task, and no explicit rules can be given. Although, the larger the number of used point mass RBFs is, the better fit of the data can be obtained, it nevertheless raises the risk of over-parameterization as well as numerical instabilities. Therefore, this strategy will not be considered in this thesis. In the second strategy, the point mass RBFs are searched for one by one with a simultaneous determination of the magnitude and position for each RBF within an iterative nonlinear approach (e.g., Barthelmes, 1986; Lehmann, 1993; Claessens et al., 2001). Compared to the first strategy, the advantages of the second strategy are that: (1) the number, magnitudes, and positions of the RBFs can be determined automatically based on the data distribution and accuracy as well as signal variations, making the resulting point mass model adaptive to the data; (2) the solution of a medium- or large-scale nonlinear equation system is avoided (e.g., thousands or ten thousands of model parameters), and instead, a series of small-scale nonlinear equation systems has to be solved (e.g., tens or hundreds of model parameters). The issue of computational complexity and numerical instabilities for a small-scale nonlinear equation system is insignificant, and hence the regularization term in the objective function given by Eq. (3.61) is not taken into consideration in the numerical computations in this thesis. However, the cost of the automatic selection of the point mass RBFs for the modeling is that several model factors should be defined properly by the user, which will be discussed later. Often, when the search and optimization of the point mass RBFs are finished, the resulting magnitudes and positions for all searched RBFs can be regarded as the final solution. To improve the solution, we propose to do a further adjustment of the magnitudes for all selected point mass RBFs, while keeping the obtained positions fixed. This leads to the two-step point mass method.

In the following, PM-FRE is implemented based on the two-step concept. It can be briefly described as follows: In the first step, a search process, originating from the idea in Barthelmes (1986), is developed to search for and optimize the point mass RBFs one by one by a chosen iteration algorithm. After stopping the search process, a number of point mass RBFs with estimated magnitudes and positions are obtained. These point mass RBFs are considered as being located at reasonable positions. Then the point mass RBF positions are held fixed and their magnitudes are readjusted by solving a linear equation system in the least-squares sense, where Tikhonov regularization may be applied to solve the ill-posedness caused by large point mass RBF depths, RBFs located in close proximity, or data gaps. From another perspective, the two-step method can be regarded as a modification of PM-FIX, in which the first step aims at determining the number and positions of the point mass RBFs, and their final magnitudes are estimated in the second step. Similar to PM-FIX, in the second step of PM-FRE, the magnitudes of the point mass RBFs can be estimated by using only the full/reduced point mass RBFs (i.e., unconstrained solution) in the least-squares adjustment or by using the full RBFs while considering the constraints (i.e., constrained solution) in the least-squares adjustment.

Fig. 3.8 shows the detailed computation procedure of the two-step method for practical applications. The total number K of point mass RBFs depends on the chosen stop criterion for the search process. This issue will be discussed in detail later. The theoretical explanation about why we place the newly searched point mass RBF below the observation point with the maximum absolute residual value can be found in, e.g., Barthelmes (1986), p. 48 – 49 and Claessens et al. (2001), p. 6 – 7.

As can be seen from Fig. 3.8, in order to reach a good solution with small errors, several model factors need to be chosen appropriately before starting the first step of the two-step method. In the context of this thesis, the model factors that will be discussed are:

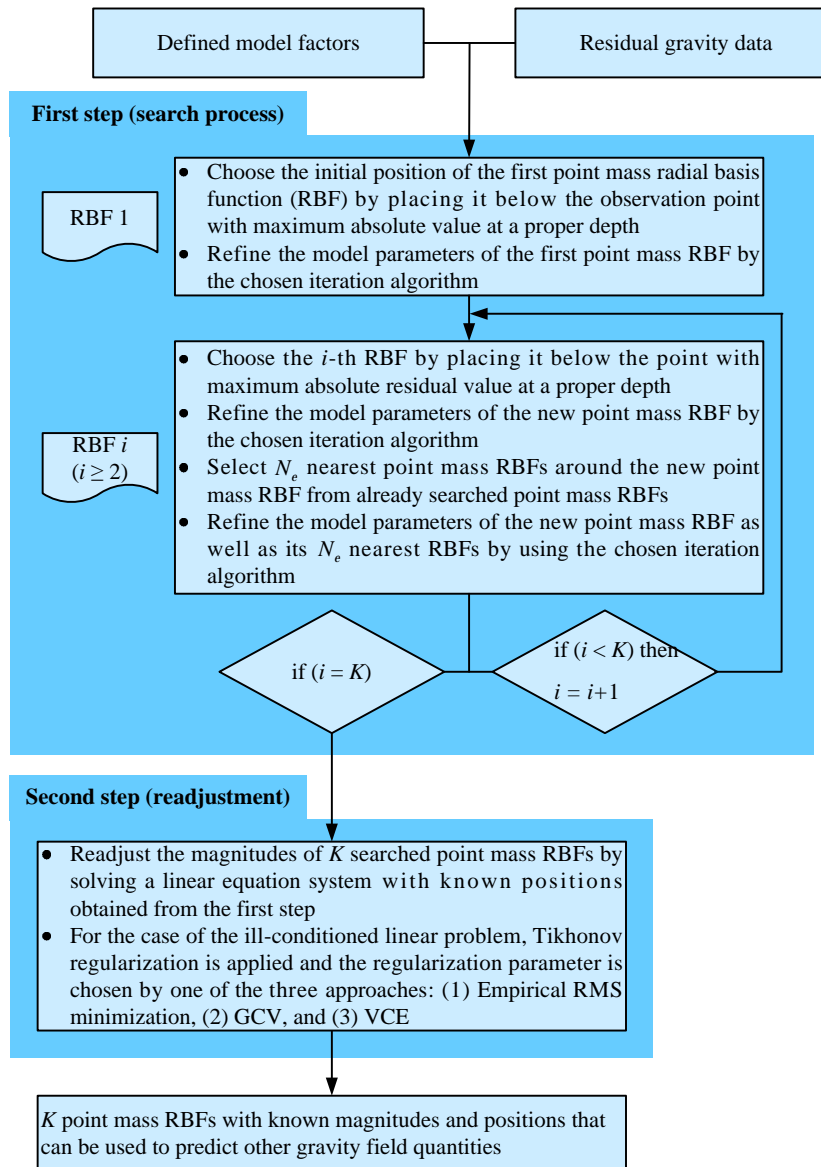


Figure 3.8: Computation procedure of the two-step method. The mentioned “maximum absolute residual value” is described as $\max |\sqrt{\mathbf{P}_e} [1 - F(\mathbf{m}')] |$ with \mathbf{m}' the model parameters for all previously selected point mass RBFs and \mathbf{P}_e the diagonal weight matrix for the input data.

- The initial depths and depth limits for the point mass RBFs: The depths of the point mass RBFs are directly related to their spatial bandwidths, playing a crucial role on the performance of the point mass RBFs in regional gravity field modeling. On the one hand, the point mass RBFs should not be located too deep (i.e., too large spatial bandwidths), as the input data for regional gravity field modeling are residuals with the removal of the long-wavelength components derived from a global geopotential model. The deeper the point mass RBFs are, the less orthogonal the basis functions become (e.g., Claessens et al., 2001). In addition, these deep point mass RBFs will also cause serious numerical instabilities, and represent only smooth signals. On the other hand, since the very-short-wavelength components computed by a DTM are also subtracted from the original input data, the point mass RBFs should not be too shallow either (i.e., too small spatial bandwidths). Otherwise, the fit of the data to the model can be achieved in terms of small RMS errors, but the fit of independent control values may become worse. Accordingly, it is necessary to limit the chosen RBFs in a layer with upper and lower bounds to guarantee the quality of the approximation. This means that we should introduce appropriate depth

constraints to the nonlinear problems to be solved for finding the point mass RBFs in the first step. In the context of this thesis, we employ simple bound constraints on the depths, and the L-BFGS-B algorithm is consequently a suitable choice. However, the other three iteration algorithms (i.e., LM, NLCG, and L-BFGS) introduced in Section 3.3.6 are also implemented in the first step. A numerical comparison between the four algorithms will be carried out in Chapter 4. Before choosing the depth limits, the initial depth for each newly found point mass RBF should be fixed first. It may be chosen based on the data spacing or the correlation length of the empirical covariance function derived from the observations. When the initial depth is fixed, the upper depth limit should be shallower than it, while the lower depth limit should be deeper. More numerical comparisons about the depth limits can be found in Chapter 4.

- The total number K of point mass RBFs: The required number of point mass RBFs for a good representation of regional gravity field depends on the data variability, data distribution, and targeted level for data misfit. More point mass RBFs are needed in an area with rough gravity field features while fewer RBFs are sufficient for representing smooth features. The addition of each new point mass RBF may decrease the data misfit, but it also reduces the redundancy. In the two-step point mass method, the total number of point mass RBFs is determined by one of the following three stop criteria for the search process: (1) a predefined data misfit; (2) the trend of the reduction of the data misfit in terms of the number of RBFs; and (3) a predefined number of point mass RBFs. Often, we prefer the first one, and then the second one follows. The target data misfit is usually determined based on the accuracy of the input data. If the accuracy of the input data is unknown, the target data misfit should be chosen carefully. If it is too small, we may also fit the errors in the data. Sometimes, the decreasing of the data misfit becomes very slow when the number of searched point mass RBFs is larger than a specific number N . In this case, the search process can stop at reaching N point mass RBFs according to the second criterion. Compared to the first two criteria, the last one is more empirical. No direct relation between the number of observations and the number of RBFs can be found. Klees et al. (2008) gave the empirical criterion that the number of RBFs is usually less than 25% of the number of data points. However, this ratio may change in different research areas.
- The spectral bandwidths of the point mass RBFs (i.e., the choice of N_{\min}): In the framework of the RCR technique, when using the full point mass RBFs (i.e., $N_{\min} = 0$), the errors caused by different spectral bandwidths of the input residuals and the RBFs are significant in the solutions of the gravity field quantities that are in the long-wavelength domain (e.g., height anomalies, geoid heights, disturbing potentials). In this case, the use of reduced point mass RBFs (i.e., $N_{\min} > 0$) will reduce the errors and provide better solutions. Related numerical comparisons will be carried out in Chapter 4. However, for the solutions of the gravity field quantities that are in the short-wavelength domain (e.g., gravity anomalies, gravity disturbances), the spectral bandwidths of the RBFs have minor effects on them. Related numerical investigations will also be given in Chapter 4. It has to be noted that, too much computation time is needed when using the reduced point mass RBFs in the first step of PM-FRE without obtaining significantly improved results, the full RBFs are employed for finding the point mass RBFs in the search process. The choice of the spectral bandwidths of the point mass RBFs is only considered in the second step for the readjustment of the magnitudes of all selected RBFs. In this case, the use of reduced point mass RBFs can be regarded as a modification of the spatial bandwidths of the RBFs obtained from the first step. In addition, the solution scheme of using the full RBFs and considering the constraints in the least-squares adjustment in the second step of PM-FRE (i.e., constrained solution, see also Section 3.4.1) will also be investigated.
- The optimization direction: Besides the magnitude of each new point mass RBF, the position

can be optimized in all directions or only in a radial direction (i.e., depth). Regarding the optimization in all directions in the test case using real gravity data, usually some point mass RBFs tend to move into the gaps to minimize the data misfit, and if the upper depth limit is too shallow, the estimated magnitudes for these RBFs may become too large and lead to unreasonable small-scale local features. In addition, the all-direction optimization may relocate the point mass RBFs near the edge of the data area far away from the initial locations, resulting in serious numerical instabilities. Hence, additional horizontal constraints must be added. Such circumstances can be avoided by using the radial-direction optimization, which is more simple and stable. Related numerical tests will be given in Chapter 4.

- The iteration limit N_{it} for each new point mass RBF: The magnitude and position for each new point mass RBF are estimated iteratively in the first step. The required number of iterations for finding the local minimum for each RBF is different. For the sake of simplicity, an iteration limit N_{it} is usually defined for all searched point mass RBFs. Sometimes, we divide the point mass RBFs to be sought into several groups. For each group, there is an iteration limit. Often, the larger the N_{it} is, the longer the computation time is. A numerical test by using different N_{it} will be carried out in Chapter 4.
- The number N_ϵ of the nearest point mass RBFs: Ideally, for each new point mass RBF, the magnitudes and positions of this and all other searched point mass RBFs should be recomputed. However, this is a very time-consuming process. Barthelmes (1986) showed that it was sufficient to recompute only a certain number N_ϵ of the nearest point mass RBFs together with the new one when the RBFs are nearly orthogonal. The value of N_ϵ was increased when the RBFs were not sufficiently orthogonal. For the sake of simplicity, the same N_ϵ is often used for each new point mass RBF. A related numerical comparison will also be given in Chapter 4.

3.5.3 Point mass search model

According to the descriptions and discussion in the previous section, the first step of PM-FRE is of most importance as it provides the positions of the point mass RBFs for a further readjustment of their magnitudes in the second step. To avoid an over-parameterization and extremely local gravity field features caused by too shallow point mass RBFs and to represent useful local features as much as possible, the depth of each point mass RBF should have an upper and a lower limit. As a consequence, the depth limits of the point mass RBFs are considered in the first step for finding the basis functions. In this thesis, some assumptions are made to simplify the point mass search model in the first step, resulting in two slightly different models labeled as SMA and SMB. They are briefly described as follows, with corresponding illustrations shown in Fig. 3.9:

- SMA: In this point mass search model, we assume that all point mass RBFs to be selected have the same upper and lower depth limits, as well as the same initial depths. It means that all searched point mass RBFs are located in a layer with a defined upper and lower bound. The initial depth for the RBFs is chosen between the two bounds (see Fig. 3.9a). Obviously, the key point is how to choose the bounds and the initial depth. An empirical rule for dealing with this issue will be derived from the numerical tests in Chapter 4. In this model, the same iteration limit N_{it} and the same number N_ϵ of the nearest point mass RBFs are used for each new point mass RBF.
- SMB: In this model, the single layer used in SMA is replaced by several layers. The lower bound of the deepest layer is the same as the lower bound of the single layer in SMA, while the upper bound of the shallowest layer corresponds to the upper bound of the single layer in SMA. The point mass RBFs are found in the deepest layer first. After reaching a specified number of point

mass RBFs, the RBFs are found in the second deepest layer. Similar procedures are repeated until the search of the RBFs is finished. Often, the deepest layer only contains a small number of point mass RBFs, while most of the RBFs are located in the shallowest layer. Furthermore, the values of N_{it} and N_ε for the point mass RBFs in different layers can be different. Usually, larger N_{it} and N_ε are preferred for the RBFs in deep layers. Fig. 3.9b shows an example of the two-layer model.

In general, SMB can be considered as the extension of SMA, but is more complicated. In the following numerical tests in Chapter 4, SMA is used as the default point mass search model in PM-FRE.

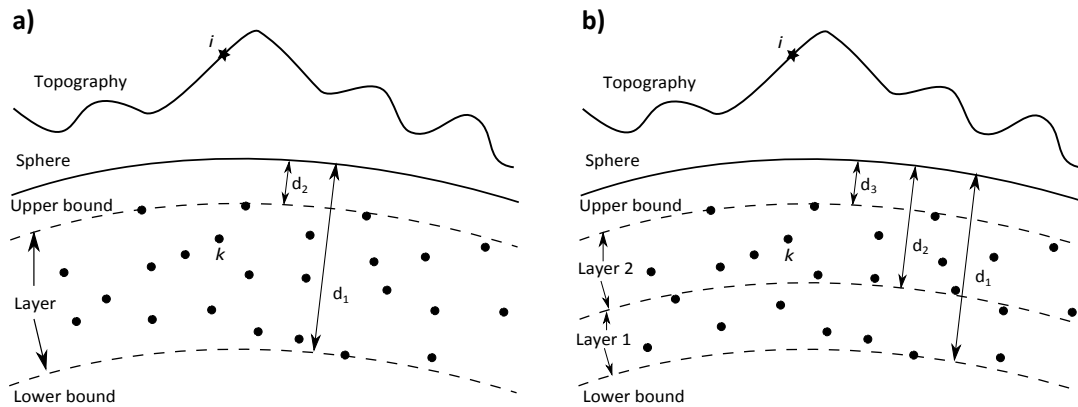


Figure 3.9: Illustration of the point mass search models: a) SMA and b) SMB with two layers.

4 Numerical results

In this chapter, we aim at testing the point mass method presented in Chapter 3 for regional gravity field modeling using synthetic and real data. Five numerical tests are carried out in different areas using different kinds of gravity field data. The goal of the first three tests is to find the “optimal” strategy for the proposed point mass method by investigating the effect on the solutions caused by various choices of relevant model factors, such as the design of the grid for PM-FIX and the determination of the depth limits for PM-FRE. In this context, “optimal” means that the selected strategy should provide the best result in terms of RMS error in the case where no systematic errors occur, or of STD error when systematic errors exist. This can be easily assessed by using synthetic data, as the predicted gravity field quantities can be compared to the true values. When using real data, the values at the control points are not error-free; they are known with low accuracy sometimes, or known with inhomogeneous distribution. In these cases, a good comparison can usually not be achieved. Alternatively, the solutions can be compared to the results computed by other regional approaches, such as the integral method and LSC. The remaining two numerical tests aim at verifying the applicability of the derived “optimal” strategy for the modeling. Often, real data are preferred in the relevant test cases as the final goal is for practical applications. However, test cases using synthetic data have the aforementioned advantages.

This chapter is composed of five sections. In each section, one or more test cases will be conducted. Various comparisons of the solutions, obtained by using different model setups, are carried out in Section 4.1. A synthetic data set with error-free gravity anomalies in the Central Alps area and a set of real gravity anomaly measurements in the New Mexico area are used as input. The results are validated at the given control points in each test area and also compared to the LSC results. In order to check the applicability of the point mass method for regional modeling based on other kinds of input data, the recovery of gravity anomalies in the North Atlantic region using a set of synthetic geoid heights is presented in Section 4.2. In addition, the performance of three approaches for finding the proper regularization parameter is compared. In Section 4.3, the region of interest is the same as in Section 4.2, but using two groups of synthetic geoid heights with different accuracies. To deal with such a case, an iterative procedure based on VCE is proposed and applied. In Section 4.4, the point mass method, followed by the derived “optimal” strategy, is applied to the tests with a set of synthetic terrestrial and airborne gravity disturbances provided by the Joint Study Group (JGS0.3) of International Association of Geodesy (IAG). Finally, a case study using a large number of real gravity anomaly measurements in the Auvergne area is addressed. In addition, the combination of gravity and GPS/leveling data is also discussed.

4.1 Tests with a small set of synthetic and real gravity data

In this section, various comparisons of the gravity solutions computed by PM-FIX and PM-FRE are presented. For PM-FIX, the focus is on the choices of the grid extent, grid spacing, grid depth, grid formation, and spectral bandwidths of the point mass RBFs (i.e., the value of N_{\min}). For PM-FRE, the choices of the nonlinear iteration algorithm, initial depth and depth limits, total number K of point mass RBFs, spectral bandwidths of the RBFs, optimization direction, iteration limit N_{it} for each new RBF as well as number N_e of the nearest RBFs are taken into consideration. Also the solutions obtained by using two search models (i.e., SMA and SMB, see Section 3.5.3) are compared. For both PM-FIX and PM-FRE, the solutions obtained with and without considering the constraints in the least-squares adjustment (see Section 3.4.1) are analyzed. Two data sets in two different research

areas are used for all investigations.

4.1.1 Description of the data sets

The first data set contains 4753 regular gravity anomalies simulated from the EGM2008 model from degree 361 up to 2160. The research area is chosen to be the Central Alps (CA) with the extension of 7°E to 15°E and 45°N to 49°N . The height for each observation is derived from the DTM2006.0 terrain model (Pavlis et al., 2007), and all observations are error-free. The statistics of this data set is: mean = -0.486 mGal; RMS = 16.809 mGal; min = -99.128 mGal; max = $+62.917$ mGal. In addition, 4608 independent control points with true values, located at half-way between the observations, are used to assess the quality of the modeled gravity and height anomalies. The location of all points and the topography of the research area are illustrated in Fig. 4.1. For the sake of simplicity, this test case is specified as the CA test case in the following.

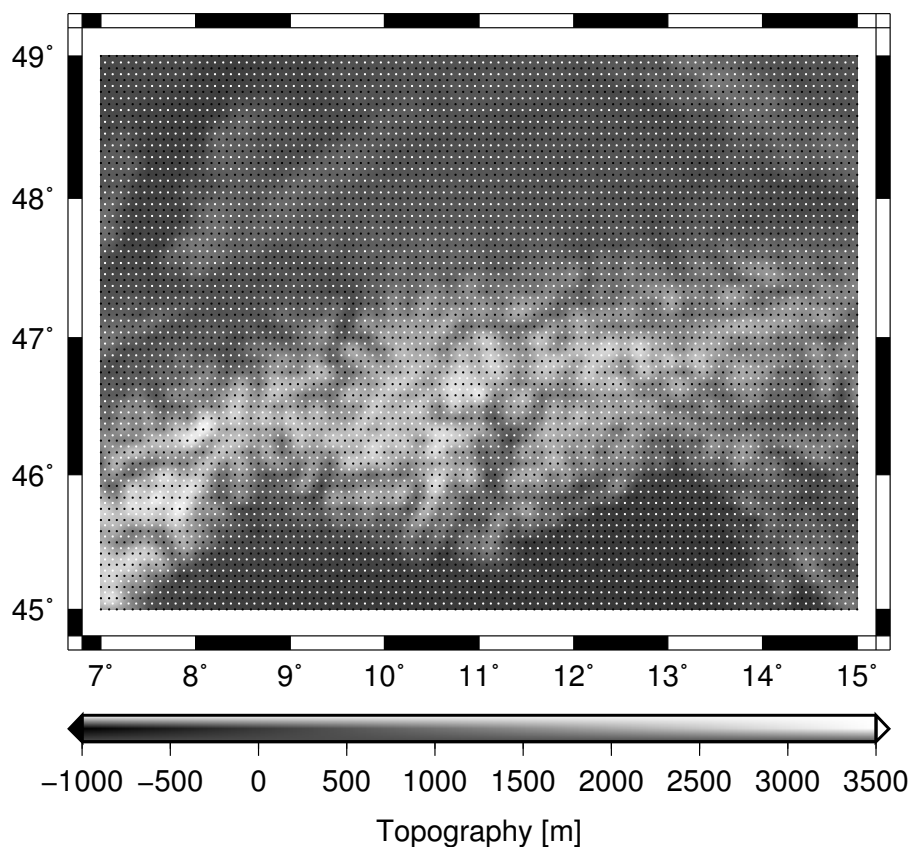


Figure 4.1: Location of observations (Δg , black dots) and control points (Δg and ζ , white dots) for the CA test case; the background shows the topography of the research area taken from the DTM2006.0 terrain model.

The second data set consists of 2767 real gravity anomaly measurements in the area of New Mexico (NM), USA, with the extent of -107.85°E to -105.15°E and 31.65°N to 34.85°N . The accuracy of the observations is expected to be about 2 mGal (Kearsley et al., 1985). Using the RCR technique, the residual gravity anomalies, which are obtained by removing the long-wavelength contributions computed from the EGM2008 model complete to degree and order (d/o) 360 and the short-wavelength signals by the RTM approach from the original input data, are used for the modeling. The statistics of the residuals is: mean = -0.453 mGal; RMS = 12.808 mGal; min = -40.724 mGal; max = $+42.622$ mGal. Moreover, 153 independent gravity anomaly measurements and 20 geometric height anomalies derived from the GPS/leveling data are used as control points. Fig. 4.2 shows the location

of all points. For the sake of simplicity, this test case is specified as the NM test case in the following.

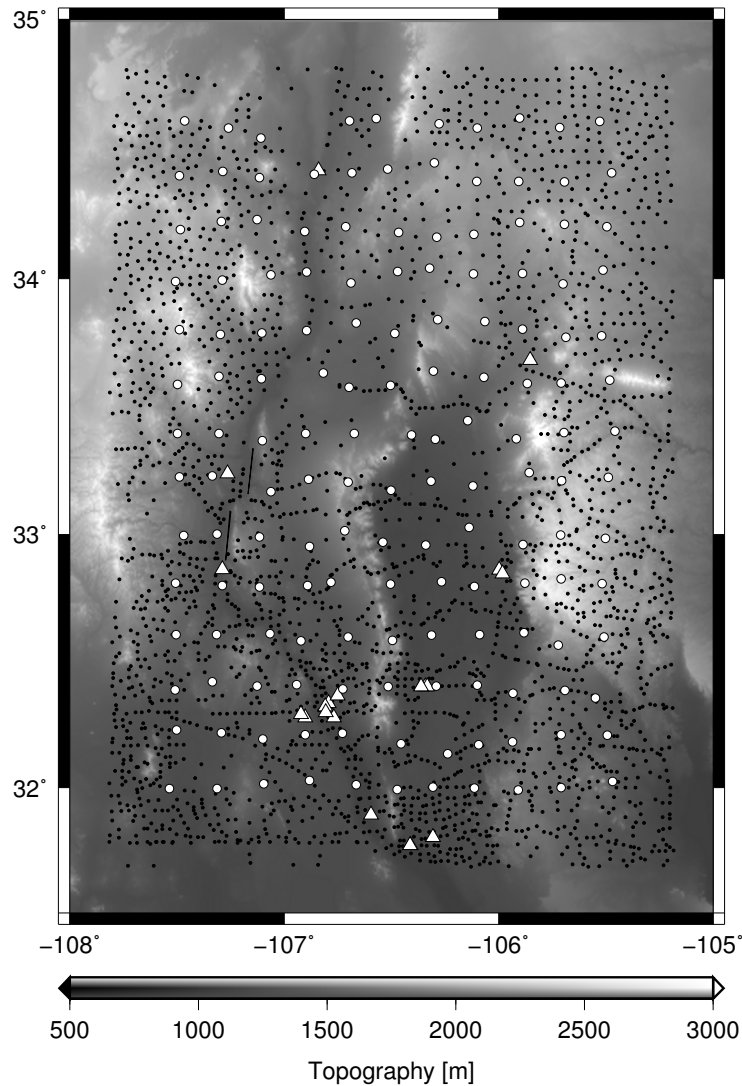


Figure 4.2: Location of 2767 Δg measurements (*black dots*), 153 Δg control points (*white circles*), and 20 GPS/leveling stations (*white triangles*) for the NM test case; the background shows the topography of the research area.

4.1.2 Analysis of the results computed by PM-FIX

4.1.2.1 Effect of the grid extent, grid spacing, grid depth, and spectral bandwidths of the point mass RBFs

The CA test case

To investigate the effect of the grid extent, the other three model factors (i.e., grid spacing, grid depth, and spectral bandwidths of the point mass RBFs) are fixed, while varying the grid extent. The basic grid is chosen to be the one, of which the boundary coincides with the data area (i.e., 7°E to 15°E, 45°N to 49°N). Suppose that the extent of the basic grid is defined by $(\lambda_1, \lambda_2, \phi_1, \phi_2)$ with $\lambda_1, \lambda_2, \phi_1, \phi_2$ being the minimal and maximal longitudes as well as the minimal and maximal latitudes, a new grid with the extent of $(\lambda_1 - \Delta_\lambda, \lambda_2 + \Delta_\lambda, \phi_1 - \Delta_\phi, \phi_2 + \Delta_\phi)$ can be obtained by specifying the area extensions along the longitude Δ_λ and the latitude Δ_ϕ . In our test cases, we assume that $\Delta_\lambda = \Delta_\phi = \Delta$. Following this way, six additional grids are selected for comparison. A positive Δ means that the obtained grid has a larger extent than the basic grid, and the grid associated with

$\Delta < 0$ is smaller than the basic grid. Furthermore, two grid depths and the RBFs with two values of N_{\min} are considered to study the effect of the grid extent in different scenarios. The model setup for this test case is described in Table 4.1.

Table 4.1: Model setup for investigating the effect of different area extensions Δ on the regional solution in the CA and the NM test case.

Model factors	CA test case	NM test case
Area extension Δ	$-30'$, $-20'$, $-10'$, $0'$, $10'$, $20'$, $30'$	-0.5° , -0.4° , -0.3° , -0.2° , -0.1° , 0.0° , 0.1° , 0.2° , 0.3° , 0.4° , 0.5°
Grid spacing	$10' \times 10'$	$6' \times 6'$
Grid depth [km]	① 20 ② 40	① 10 ② 20
Spectral bandwidths of the RBFs	① Full, $N_{\min} = 0$ ② Reduced, $N_{\min} = 301$	① Full, $N_{\min} = 0$ ② Reduced, $N_{\min} = 201$

Fig. 4.3 shows the condition number of the normal matrix as a function of the area extension Δ . The values of the condition numbers are similar for $\Delta \leq 0$, but become larger in the case of $\Delta > 0$. Due to the very large condition numbers for $\Delta = 20$ and 30 , Tikhonov regularization is employed for obtaining stable solutions, in which the regularization parameters are determined empirically by comparing to 4608 true gravity anomalies at the control points.

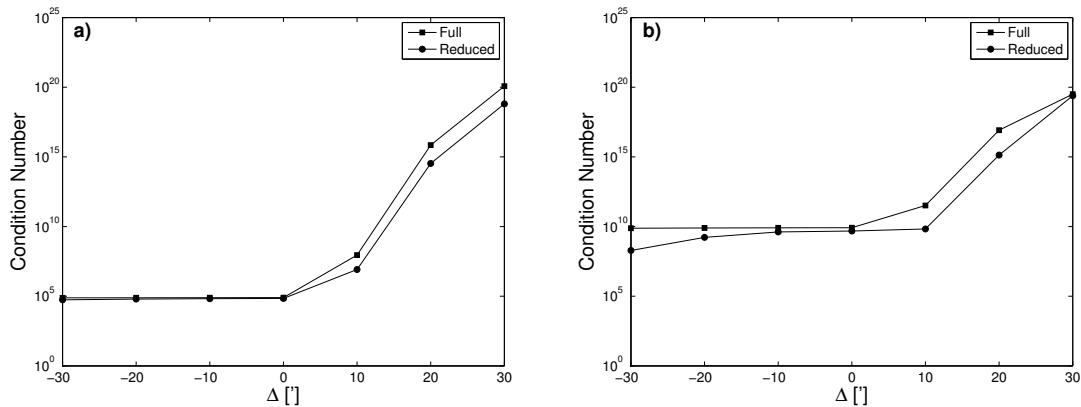


Figure 4.3: Condition number as a function of the area extension Δ for the CA test case: **a)** grid depth of 20 km; **b)** grid depth of 40 km.

The RMS errors of the model gravity and height anomalies at the control points are given in Tables 4.2 and 4.3. From each table, it can be seen that the gravity anomaly error decreases with increasing grid extent. This can be attributed to the increasing number of point mass RBFs for regional modeling. The RMS error for the height anomaly solution does not behave like the gravity anomaly error. It appears to be very sensitive to the chosen grid extent, especially for the case of $\Delta > 0$. For example, the height anomaly solutions are unacceptable when $\Delta = 20'$ and $30'$. The best height anomaly solution in terms of the smallest RMS error is obtained when using the basic

Table 4.2: RMS gravity anomaly (Δg) [mGal] errors and height anomaly (ζ) errors [m] for different Δ in units of arc-minutes. The chosen grid is located at the depth of 20 km with a spacing of $10' \times 10'$. The solutions in the first four lines correspond to the full point mass RBFs and the ones in the second four lines for the reduced RBFs. The symbol \times means the RMS error of ζ is larger than 1 m. The values marked by $*$ correspond to the control points in the inner area of 7.5°E to 14.5°E , 45.5°E to 48.5°N .

Δ	$-30'$	$-20'$	$-10'$	$0'$	$10'$	$20'$	$30'$
Δg	8.325	7.021	5.946	5.543	5.456	4.639	4.008
Δg^*	6.668	6.331	6.233	6.207	6.193	4.867	2.875
ζ	0.134	0.089	0.053	0.063	0.255	\times	\times
ζ^*	0.109	0.074	0.046	0.049	0.197	\times	\times
Δg	7.891	6.850	5.879	5.539	5.444	5.420	5.434
Δg^*	6.646	6.363	6.229	6.203	6.179	6.171	6.169
ζ	0.064	0.050	0.031	0.026	0.049	0.741	0.149
ζ^*	0.038	0.034	0.029	0.028	0.028	0.060	0.035

Table 4.3: The same as in Table 4.2, but for the case that the chosen grid is located at the depth of 40 km.

Δ	$-30'$	$-20'$	$-10'$	$0'$	$10'$	$20'$	$30'$
Δg	7.620	6.536	5.762	5.408	5.216	4.211	2.491
Δg^*	6.702	6.376	6.146	6.041	5.956	3.526	1.955
ζ	0.089	0.059	0.134	0.228	\times	\times	\times
ζ^*	0.063	0.040	0.118	0.198	\times	\times	\times
Δg	7.266	6.404	5.698	5.389	5.221	5.203	5.199
Δg^*	6.589	6.332	6.113	6.029	5.973	5.968	5.968
ζ	0.055	0.039	0.029	0.028	0.070	0.500	0.589
ζ^*	0.035	0.031	0.028	0.028	0.027	0.042	0.047

grid (i.e., $\Delta = 0'$). By means of using different spectral bandwidths of the point mass RBFs, we also find that much better height anomaly solutions are obtained when using the reduced RBFs (i.e., $N_{\min} = 301$). When not considering the used spectral bandwidths of the RBFs and the selected grid depth, the basic grid proves to be the best choice among the seven candidates in this test case.

In the following, the grid extent is fixed to be the same as the data area (i.e., the above-mentioned basic grid). Various choices of grid spacing, grid depth, and spectral bandwidths of the point mass RBFs are compared numerically. The model setup is described in Table 4.4. Four grids with different spacings will be used. In each case, the shallowest grid depth is chosen to be close to or smaller than the grid spacing, and the deepest depth is about 3 – 4 times of the grid spacing. For the sake of simplicity, no Tikhonov regularization is taken into consideration, even though the condition numbers are very large in some cases of deep grids. Fig. 4.4 shows the RMS errors of the solutions at the control points as a function of (1) the grid depth and (2) the spectral bandwidths of the point mass

Table 4.4: Model setup for investigating the effect of grid spacing, grid depth, and spectral bandwidths of the point mass RBFs. The step of varying the grid depth is 5 km for the CA test case; for the NM test case, it is 10 km for Cases ① – ③, and 20 km for Case ④.

Model factors	CA test case	NM test case
Grid extent	7.0°E to 15.0°E 45.0°N to 49.0°N	−107.90°E to −105.10°E 31.65°N to 34.85°N
Grid spacing & Grid depth [km]	① 6′ × 6′ & 5 – 50 ② 10′ × 10′ & 5 – 80 ③ 15′ × 15′ & 5 – 100 ④ 20′ × 20′ & 5 – 120	① 5.25′ × 6′ & 10 – 50 ② 6′ × 6′ & 10 – 50 ③ 12′ × 12′ & 10 – 80 ④ 24′ × 24′ & 20 – 140
Spectral bandwidths of the RBFs	$N_{\min} = 0, 51, 101, 151, 201, 251, 301, 351$	

RBFs for different grid spacings. Since the number of point mass RBFs is directly related to the grid spacing, the effect of grid spacing can be regarded as being equivalent to the effect of the number of point mass RBFs. In this test, the RMS error of the solution for the grid spacing of 6′ × 6′ is much smaller than the ones for the other three grid spacings, resulting in a gravity anomaly solution with an error of about 1.5 – 1.6 mGal and a height anomaly solution with an error less than 0.02 m if the grid depth and N_{\min} are chosen properly (see Figs 4.4a and 4.4e). However, the resulting number of point mass RBFs (3321 points) is also much larger, increasing the computational burden and the risk of over-parameterization. Thus, it may arise the question how dense a grid should be. This depends on the data distribution, the signal variation, and so on. Usually, we may choose the grid spacing based on the error of the input data if it is available. If the chosen grid spacing yields a data misfit being smaller or close to the data error, it can be regarded as the one we want. When the data error is unknown or using synthetic error-free data, we may define a target data misfit instead, although this process seems to be more empirical.

Comparing the solutions for different grid spacings shows that the RMS gravity anomaly error decreases from about 11 – 12 mGal for the 20′ × 20′ grid to about 1 – 2 mGal for the 6′ × 6′ grid, and the RMS height anomaly error decreases from about 0.08 – 0.10 m to less than 0.02 m. It shows that the gravity anomaly solution is more sensitive to the number of used point mass RBFs than the height anomaly solution. As an example, the 6′ × 6′ and 10′ × 10′ grids are capable of providing a height anomaly solution with an accuracy of about 0.03 m, but the accuracy of the gravity anomaly solution is about 1 – 2 mGal for the former grid and 5 – 6 mGal for the latter grid (see Figs 4.4a–4.4b and 4.4e–4.4f). Therefore, more point mass RBFs (i.e., a smaller grid spacing) are needed for the good representations of both gravity and height anomalies than for a good height anomaly solution only.

Besides grid spacing, the grid depth and the spectral bandwidths of the point mass RBFs also play important roles for obtaining a good solution. For a further investigation, several profiles extracted from Figs 4.4b and 4.4f (i.e., the 10′ × 10′ grid) are illustrated in Figs 4.5 and 4.6.

From Fig. 4.5a it is clear that the RMS error of gravity anomaly solution decreases with increasing grid depth at first (about 10 to 20 km), and then become quite stable (about 20 to 70 km), and finally increase dramatically (larger than 70 km) for the first three values of N_{\min} . For $N_{\min} = 351$, the gravity anomaly solution is still acceptable even if the grid depth is deeper than 70 km, indicating that the larger the N_{\min} is, the deeper the grid is allowed to be. Fig. 4.6a shows that the RMS

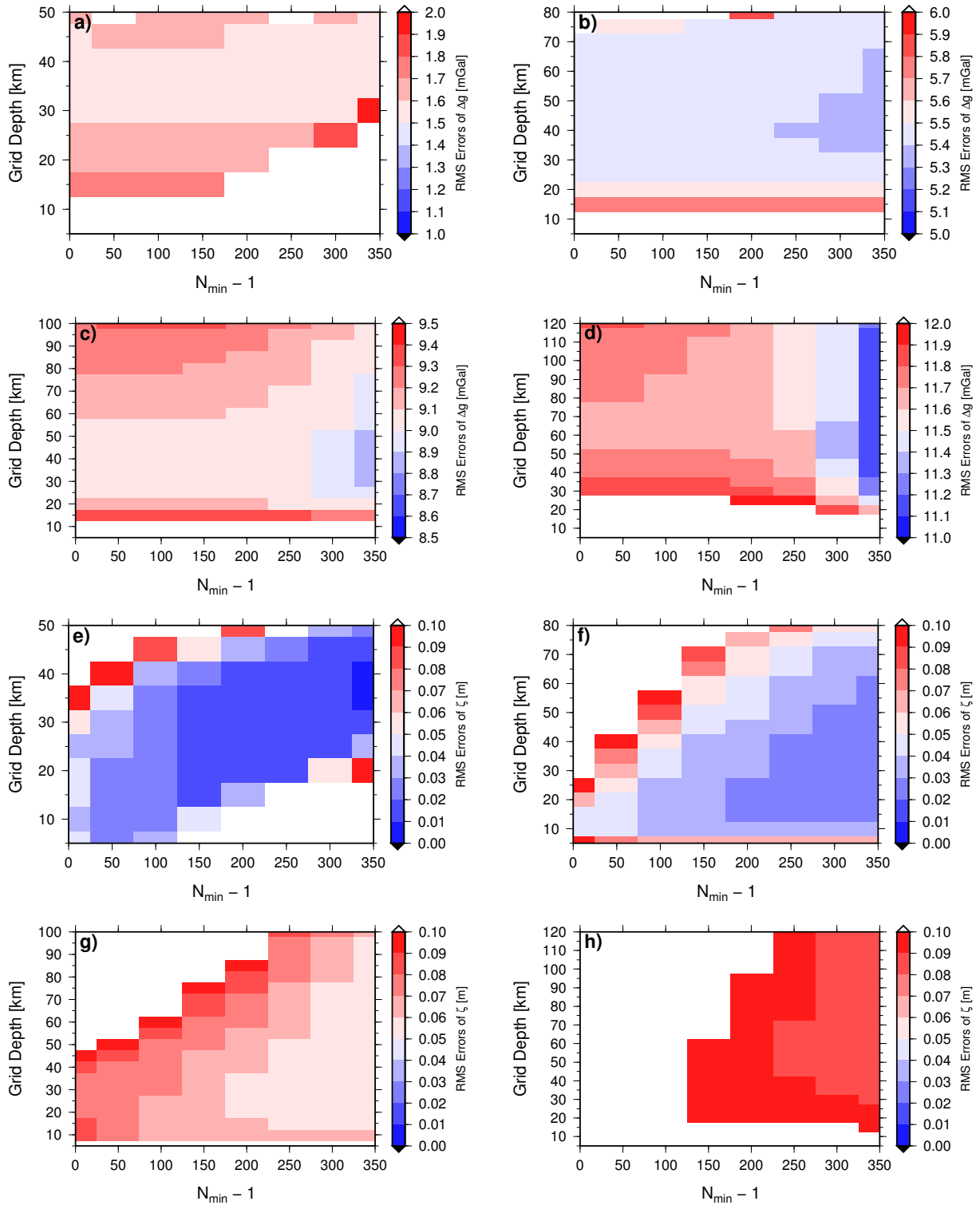


Figure 4.4: RMS errors of Δg at 4608 control points for the CA test case as a function of (1) grid depth and (2) spectral bandwidths of the point mass RBFs associated with different grid spacings: **a)** $6' \times 6'$; **b)** $10' \times 10'$; **c)** $15' \times 15'$; **d)** $20' \times 20'$; **e), f), g), and h)** are the same as **a), b), c), and d)**, but for the RMS errors of ζ at 4608 control points.

gravity anomaly error is about 5.4 – 5.5 mGal for $N_{\min} \in [251, 351]$ in the case of the grid depth of 80 km; however, the error becomes much larger for smaller values of N_{\min} (see the cyan line) due to too large spatial bandwidths of the RBFs. From both Figs 4.5a and 4.6a, one can conclude that the

gravity anomaly solutions are nearly independent on the chosen spectral bandwidths of the RBFs if the grid depth is selected properly, leading to similar solutions.

The RMS height anomaly errors shown in Figs 4.5b and 4.6b exhibit differently in comparison to the gravity anomaly errors. For each grid depth in Fig. 4.6b, the larger the N_{\min} is, the less the error becomes. Comparing the error lines in the same figure, it also shows that the shallower the grid depth is, the less dependent on N_{\min} the solution is. The use of reduced point mass RBFs is beneficial for improving the height anomaly solution, but the grid depth must also be chosen carefully (see Fig. 4.5b). The range of the grid depth for a stable height anomaly solution is about 20 – 60 km for $N_{\min} = 351$, but it becomes narrower when N_{\min} is smaller (e.g., about 15 – 35 km for $N_{\min} = 201$ in Fig. 4.5b). It shows that the choice of a large N_{\min} can also make the height anomaly solution be less sensitive to the grid depth.

Considering the grid spacing ($10' \times 10'$) as well as the depth range for a stable gravity (20 – 70 km) and height anomaly solution (20 – 60 km), it appears that the grid depth, which is about 1 – 3 times of the grid spacing (about 20 – 60 km) is an appropriate choice. This empirical relation is also suitable for the grid spacings of $15' \times 15'$ (about 25 – 75 km) and $20' \times 20'$ (about 40 – 120 km), but not for the $6' \times 6'$ grid (see Fig. 4.4).

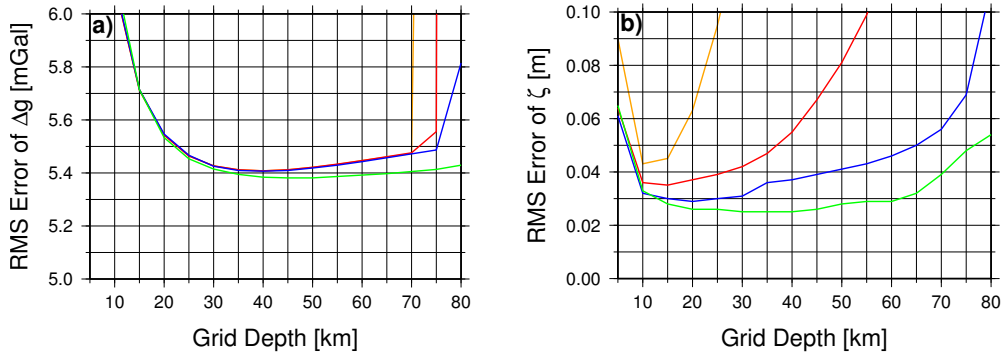


Figure 4.5: RMS errors of a) Δg and b) ζ as a function of grid depth associated with different spectral bandwidths of the point mass RBFs in the case of $10' \times 10'$ grid spacing. *Orange:* $N_{\min} = 0$; *red:* $N_{\min} = 101$; *blue:* $N_{\min} = 201$; *green:* $N_{\min} = 351$.

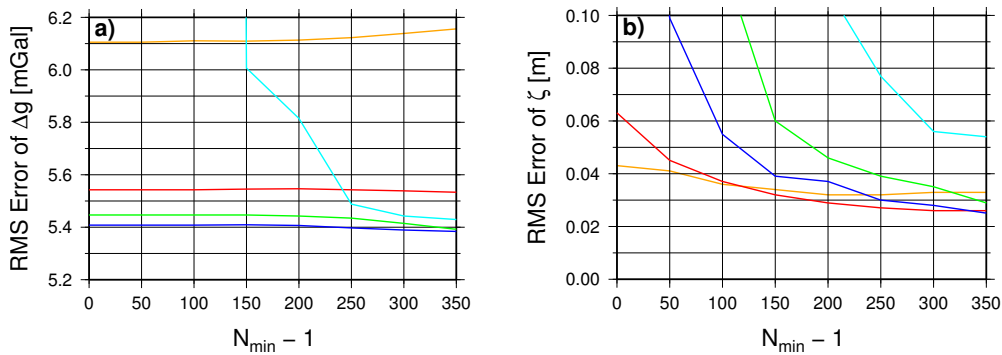


Figure 4.6: RMS errors of a) Δg and b) ζ as a function of $N_{\min} - 1$ associated with different grid depths in the case of $10' \times 10'$ grid spacing. *Orange:* 10 km; *red:* 20 km; *blue:* 40 km; *green:* 60 km; *cyan:* 80 km.

The NM test case

Similar procedures as used in the CA test case are applied in this test case. Because of the scattered data points, the basic grid is chosen such that its extent is close to the data area as much as possible,

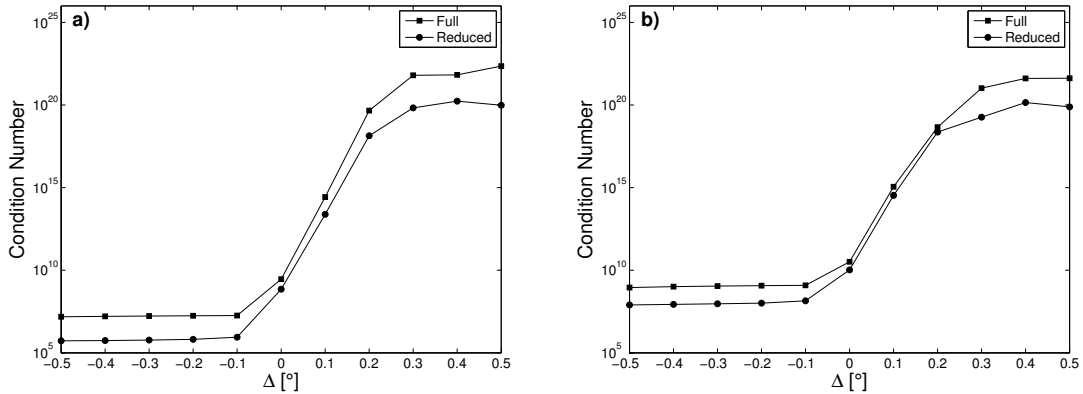


Figure 4.7: The same as in Fig. 4.3, but for the NM test case: **a)** grid depth of 10 km; **b)** grid depth of 20 km.

resulting in the extent of -107.90°E to -105.10°E , 31.65°N to 34.85°N . The related model setup for investigating the effect of the grid extent in this test case can also be found in Table 4.1.

The condition number of the normal matrix for various values of Δ is illustrated in Fig. 4.7. It shows an increasing ill-conditionedness for large positive values of Δ again. Combining the results from the CA test case, more effort must be taken to deal with the numerical instabilities in the case that the chosen grid is much larger than the data area.

Table 4.5: RMS errors of Δg [mGal] and STD errors of ζ [m] for different Δ in units of arc-degrees. The chosen grid is located at the depth of 10 km with a spacing of $6' \times 6'$. The solutions in the first two lines correspond to the full point mass RBFs and the ones in the second two lines for the reduced RBFs.

Δ	-0.5°	-0.4°	-0.3°	-0.2°	-0.1°	0.0°	0.1°	0.2°	0.3°	0.4°	0.5°
Δg	6.289	5.521	4.075	4.060	3.710	3.726	3.726	3.726	3.726	3.726	3.726
ζ	0.069	0.059	0.055	0.045	0.040	0.043	0.045	0.047	0.048	0.048	0.049
Δg	6.507	5.424	4.583	4.271	3.800	3.774	3.754	3.751	3.750	3.749	3.747
ζ	0.086	0.078	0.063	0.036	0.028	0.027	0.030	0.030	0.030	0.030	0.030

Table 4.6: The same as in Table 4.5, but for the case that the chosen grid is located at the depth of 20 km.

Δ	-0.5°	-0.4°	-0.3°	-0.2°	-0.1°	0.0°	0.1°	0.2°	0.3°	0.4°	0.5°
Δg	6.517	5.020	4.644	4.096	3.905	3.957	3.953	3.951	3.951	3.951	3.950
ζ	0.060	0.058	0.054	0.047	0.044	0.101	0.145	0.240	0.363	0.490	0.602
Δg	6.122	5.099	4.755	4.131	3.914	3.950	3.950	3.952	3.952	3.952	3.952
ζ	0.257	0.254	0.041	0.027	0.030	0.030	0.045	0.048	0.044	0.041	0.041

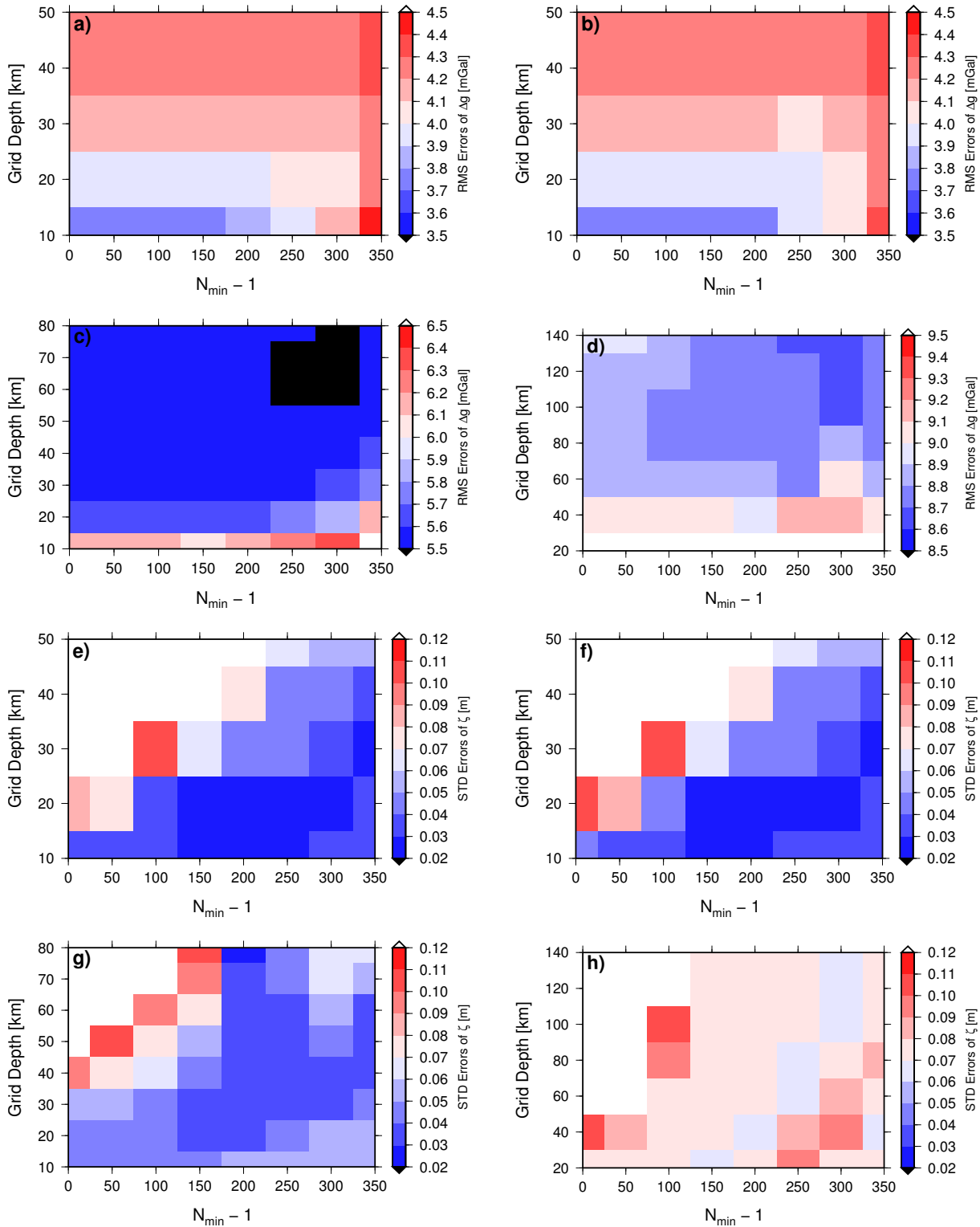


Figure 4.8: RMS errors of Δg at 153 control points for the NM test case as a function of (1) grid depth and (2) spectral bandwidths of the point mass RBFs associated with different grid spacings: **a)** $5.25' \times 6'$; **b)** $6' \times 6'$; **c)** $12' \times 12'$; **d)** $24' \times 24'$; **e)**, **f)**, **g)**, and **h)** are the same as **a)**, **b)**, **c)**, and **d)**, but for the STD errors of ζ at 20 GPS/leveling points.

Tikhonov regularization is employed for all computations in this test case. The statistics of the differences between the predicted and observed values at the control points are given in Tables 4.5 and

4.6. Due to the systematic inconsistency between the modeled and the GPS/leveling-derived height anomalies, a good height anomaly solution is interpreted as the one with a small STD error. Both tables show similar information as given by the CA test case. However, some differences can still be found. The gravity anomaly error decreases with increasing Δ , but it does not become smaller for $\Delta > 0.1^\circ$. The height anomaly solution becomes less sensitive to the grid extent in this test case. The resulting STD height anomaly errors remain at a similar level when the grid being larger than the data area, especially in the case that the reduced RBFs are used. The different performance of the height anomaly solutions in the CA and NM test cases may be due to the fact that there are lots of control points near the border of the data area in the CA test case, whereas only few control points can be found close to the border area in the NM test case (see Figs 4.1 and 4.2). In order to further investigate this issue, the comparison is repeated at the control points within the area of 7.5°E to 14.5°E , 45.5°N to 48.5°N in the CA test case. The results are also presented in Tables 4.2 and 4.3, from which it can be seen that without the control points near the borders, the errors appear to be less affected by the chosen grid, in particular in the case of using reduced RBFs. It indicates that the use of a grid larger than the data area has a negative effect on the prediction points near the edge of data area. Therefore, if the model area is similar to the data area, the selected grid should be close to the data area. If the model area is smaller than the data area, it is proper to choose a grid being either close to or larger than the data area. In the following, the grid extent is preferred to be close to the data area when using PM-FIX.

The test for investigating the effect of the other three model factors is based on the model setup given in Table 4.4. The related results are shown in Fig. 4.8. The information contained in Fig. 4.8 is similar to the one as given by Fig. 4.4. The empirical relation between the range of appropriate grid depth and the grid spacing is still satisfying. For the $5' \times 5'$ and $6' \times 6'$ grids, the estimated depth range is about 10 – 30 km, while the result observed from Figs 4.8a–4.8b and 4.8e–4.8f is about 10 – 20 km. In a similar way, the estimated and observed grid depth ranges for the other two grid spacings are given as follows: about 20 – 60 km and 30 – 60 km for the $12' \times 12'$ grid; about 40 – 120 km and 60 – 120 km for the $24' \times 24'$ grid. For the choice of N_{\min} , there is a small difference. In the CA test case, we find that $N_{\min} = 351$, which is close to the maximum degree $n_{\max} = 360$ of the reference field, is the best choice. The best value is smaller (about 150–250) in this test case, the main reason is the existence of long-wavelength errors in the input residuals.

4.1.2.2 Determination of the grid depth

In this test, our goal is to investigate the performance of the empirical and the GCV approach for finding the “optimal” grid depth. The result derived from the empirical approach is considered as the reference. Two grid spacings are selected in each test area for comparison. According to the findings from Section 4.1.2.1, the grid depth candidates are in the range between 1 and 3 times of the grid spacing. The details of the model setup are given in Table 4.7.

Table 4.7: Model setup for investigating the performance of the empirical and the GCV approach for finding the “optimal” grid depth. The search step of 2 km for grid depth is used for both test cases. The used grid extents are the same as the ones in Table 4.4, and the full point mass RBFs are used for related computations.

Model factors	CA test case	NM test case
Grid spacing & Grid depth candidates [km]	① $6' \times 6'$ & 10 – 30 ② $10' \times 10'$ & 18 – 54	① $6' \times 6'$ & 10 – 30 ② $12' \times 12'$ & 20 – 60

Figs 4.9 and 4.10 show the results computed by the two approaches for both test areas. As follows from the comparison of the empirical and the GCV approach, both provide similar results. In the CA test case, the “optimal” depths derived from the two approaches are about 30 km for the $6' \times 6'$ grid, and about 40 km for the $10' \times 10'$ grid. In the NM test case, the results computed from the two approaches are different when using the $6' \times 6'$ grid, resulting in the “optimal” depth of about 10 km for the empirical approach and 24 km for the GCV approach. The reason for the two different results is not clear. It might be caused by the different regularization parameters determined by the two approaches for each grid depth candidate (see also Section 3.4.2). When the grid spacing becomes larger (i.e., $12' \times 12'$), the resulting “optimal” depths are the same again, with the values of about 55 km.

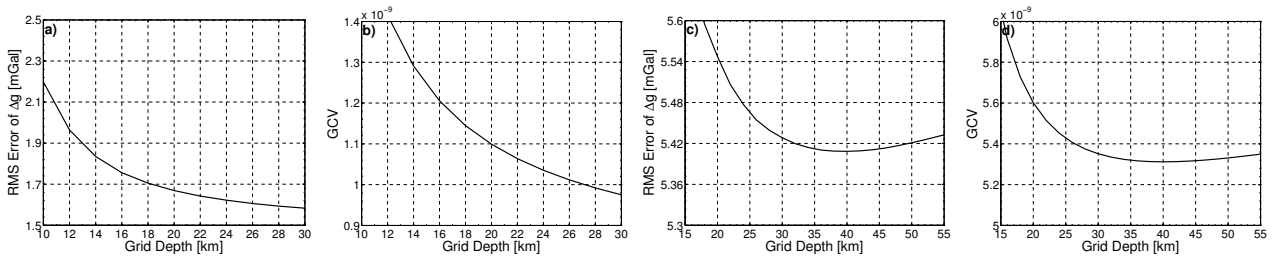


Figure 4.9: The choice of the “optimal” grid depth for the CA test case: **a)** the empirical approach for the $6' \times 6'$ grid; **b)** the same as in **a)**, but for the GCV approach; **c)** the empirical approach for the $10' \times 10'$ grid; **d)** the same as in **c)**, but for the GCV approach.

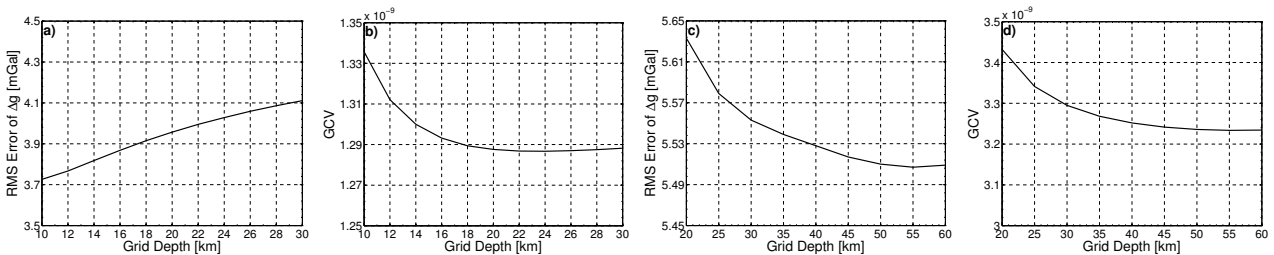


Figure 4.10: The choice of the “optimal” grid depth for the NM test case: **a)** the empirical approach for the $6' \times 6'$ grid; **b)** the same as in **a)**, but for the GCV approach; **c)** the empirical approach for the $12' \times 12'$ grid; **d)** the same as in **c)**, but for the GCV approach.

Through the above comparisons, the performance of the GCV approach is verified by the empirical approach. Nearly the same “optimal” depths can be obtained when large grid spacings are used (i.e., $10' \times 10'$ and $12' \times 12'$ for the CA and the NM test case respectively). Although the results may deviate from each other when using a small grid spacing (i.e., $6' \times 6'$ for the NM test case), the GCV technique can still be considered as a suitable tool for finding the “optimal” grid depth for regional gravity field modeling.

4.1.2.3 Comparison of unconstrained and constrained solutions

With the use of PM-FIX, the magnitudes of the point mass RBFs are to be estimated by solving a linear equation system in the least-squares sense after fixing the grid. As discussed in Section 3.2, two schemes are proposed to improve the solutions in the case where the input data are residuals. The first scheme is based on the modification of the point mass RBFs, resulting in the reduced RBFs (i.e., $N_{\min} > 0$). It proved to be capable of providing significantly improved height anomaly solutions in the previous numerical tests while keeping the quality of gravity anomaly solutions nearly the

same as before. In the following, the performance of the second scheme, in which the full RBFs are used for constructing the linear equation system and additional constraints are taken into account in the least-squares adjustment, will be studied by comparing the solutions (constrained) to the ones (unconstrained) obtained without considering the constraints in the adjustment. Only the full RBFs are used for computing the constrained solutions while either the full or the reduced RBFs are allowed for calculating the unconstrained solutions. The model setup for this study is given in Table 4.8.

Table 4.8: Model setup for comparing the unconstrained and constrained solutions for the CA and NM test cases. The used grid extents are the same as the ones in Table 4.4.

Model factors	CA test case	NM test case
Grid spacing	$10' \times 10'$	$6' \times 6'$
Grid depth [km]	40	20
Spectral bandwidths of the RBFs for unconstrained solution	① $N_{\min} = 0$ ② $N_{\min} = 301$	① $N_{\min} = 0$ ② $N_{\min} = 201$
Values of n' for constrained solution (see Eq. (3.11))	1, 50, 100, 150, 200, 250, 300	1, 50, 100, 150, 200

Table 4.9: RMS errors of Δg [mGal] and ζ [m] associated with the unconstrained and constrained solutions for the CA test case.

	Unconstrained solution		Constrained solution						
	$N_{\min} = 0$	$N_{\min} = 301$	$n' = 1$	50	100	150	200	250	300
Δg	5.408	5.389	5.410	5.418	5.427	5.430	5.432	5.433	5.435
ζ	0.228	0.028	0.106	0.057	0.042	0.040	0.038	0.038	0.037

Table 4.10: RMS errors of Δg [mGal] and STD errors of ζ [m] associated with the unconstrained and constrained solutions for the NM test case.

	Unconstrained solution		Constrained solution				
	$N_{\min} = 0$	$N_{\min} = 201$	$n' = 1$	50	100	150	200
Δg	3.957	3.950	3.955	3.946	3.938	3.945	3.946
ζ	0.101	0.030	0.068	0.035	0.029	0.028	0.027

The statistics of gravity and height anomaly errors associated with different solutions are summarized in Tables 4.9 and 4.10. It follows that adding constraints in the adjustment has minor effect on the gravity anomaly solutions, resulting in similar RMS errors with a value of about 5.40 mGal for the CA test case and about 3.95 mGal for the NM test case. The height anomaly solutions benefit from the consideration of constraints, resulting in much smaller RMS errors in comparison to the unconstrained solutions with $N_{\min} = 0$. In both test cases, the RMS errors of the constrained height anomaly solutions decrease with increasing values of n' , but do not become smaller when $n' > 150$ for the CA test case and $n' \geq 100$ for the NM test case. Regarding the maximum degree $n_{\max} = 360$ of the reference field used in both test cases, the choice of n' with a value being about half of n_{\max} or even smaller can provide a solution with a small error.

For a further investigation, the square roots of the degree variances based on the equivalent Stokes coefficients, which are transformed from the estimated point mass RBFs (see Eqs (3.7) and (3.8)), are shown in Figs 4.11 and 4.12. In the case of using full point mass RBFs, the long-wavelength components of the constrained solutions (the lines except the black and brown ones) are suppressed in comparison to the unconstrained solutions (the brown lines), in particular for the height anomaly solutions. This should be the reason for the significant enhancement of the height anomaly solutions as the height anomalies are in the long-wavelength domain. Due to the short-wavelength domain of gravity anomalies, all gravity anomaly solutions are at nearly the same level as shown in Tables 4.9 and 4.10. The use of reduced point mass RBFs acts as a high-pass filter in the frequency domain, and the value of $N_{\min} - 1$ defines the cut-off frequency. As a consequence, improved height anomaly solutions are guaranteed. Note that there are significant deviations between the degree variances for

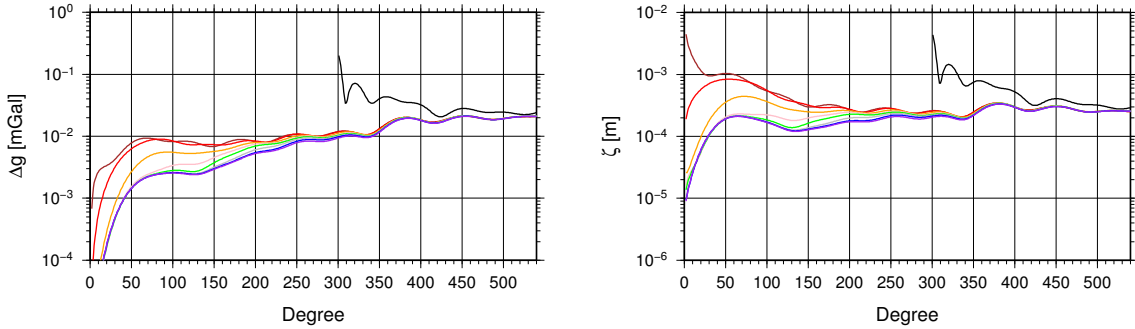


Figure 4.11: Square roots of the degree variances in terms of Δg (*left*) and ζ (*right*) associated with the unconstrained and constrained solutions for the CA test case. *Black:* $N_{\min} = 301$; *brown:* $N_{\min} = 0$; *red:* $n' = 1$; *orange:* $n' = 50$; *pink:* $n' = 100$; *green:* $n' = 150$; *gray:* $n' = 200$; *blue:* $n' = 250$; *purple:* $n' = 300$.

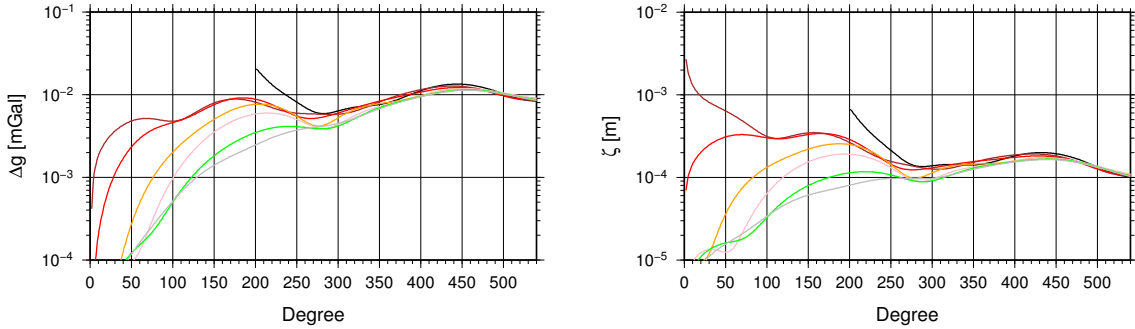


Figure 4.12: The same as in Fig. 4.11, but for the NM test case. *Black:* $N_{\min} = 201$; *brown:* $N_{\min} = 0$; *red:* $n' = 1$; *orange:* $n' = 50$; *pink:* $n' = 100$; *green:* $n' = 150$; *gray:* $n' = 200$.

the unconstrained solutions using reduced RBFs (the black lines) and for the constrained solutions. It should be the reason for the solutions with different accuracies as presented in Tables 4.9 and 4.10.

4.1.2.4 Conclusions

According to the above numerical comparisons, it appears that the “optimal” solution can only be obtained when all model factors are chosen properly, but it is hard to be achieved in practice. Alternatively, we propose to implement PM-FIX based on the following procedure, in which the model factors are determined one by one:

- ① The grid extent is recommended to be similar to the data area.
- ② The grid spacing is chosen as follows: if the grid at a depth, which is about 2 times of the grid spacing, can yield a data misfit smaller than a predefined value, this grid spacing will be used for the modeling. In practice, some changes can be made accordingly.
- ③ The “optimal” grid depth will be determined by the empirical or the GCV approach (see Section 3.4.2), in which the search interval of the grid depth candidates is between 1 and 3 times of the chosen grid spacing such that the resulting grid depth is neither too shallow nor too deep.
- ④ After fixing the grid, there are two schemes to estimate the magnitudes of the point mass RBFs. In the first case, the reduced point mass RBFs are usually recommended, and their magnitudes are estimated in least-squares adjustment. In the second case, the full RBFs are employed, and their magnitudes are computed by solving a linear equation system in the least-squares sense with the constraints.

The first three steps in the above computation procedure aim at determining the grid, in which the full point mass RBFs are used for all related computations. The above procedure is not only suitable for the case of single-grid formation, but also for the case of multi-grid formation (see Section 3.4.3).

4.1.3 Analysis of the results computed by PM-FRE

In this section, a series of numerical comparisons will be carried out by using PM-FRE based on the above two gravity data sets. In order to facilitate the discussion on the results in the following, the solutions computed by the full and reduced point mass RBFs are labeled as S1 and S2 and the solutions corresponding to the all- and radial-direction optimization are labeled as 4P and 2P. Consequently, the notation S1+2P indicates that the solution is computed by using the full RBFs and the radial-direction optimization. It is worth mentioning that, in all numerical computations in Section 4.1 with the use of PM-FRE, no regularization is used in the second step for the CA test case, but Tikhonov regularization is applied for the NM test case, where the regularization parameter is determined by an empirical approach by minimizing the RMS of the differences between the predicted and observed gravity anomalies at 153 control points.

4.1.3.1 Comparison of LM, NLCG, L-BFGS, and L-BFGS-B

The aim of the numerical tests in this section is to compare the performance of four iteration algorithms (i.e., LM, NLCG, L-BFGS, and L-BFGS-B, see also Section 3.3.6) for regional gravity field modeling. All of them are implemented in the first step of PM-FRE for searching for the point mass RBFs. In each test area, the solutions based on different choices of N_{\min} and the optimization direction are briefly discussed. Furthermore, the results are also compared to the LSC solutions, which are considered as the references.

As discussed in Section 3.5, the point mass RBFs are limited in a layer with upper and lower bounds. Thus, the nonlinear problem to be solved in the first step of PM-FRE is bound-constrained. Besides the L-BFGS-B algorithm, the other three are unconstrained algorithms. It arises the problem how to implement these unconstrained algorithms to solve the bound-constrained problem. To circumvent this problem, a simple approach is utilized:

Assuming that the model parameter vector \mathbf{m}_ℓ is obtained at iteration ℓ . If any parameter $m_i \in \mathbf{m}_\ell$ is out of the bounds (e.g., depth limits or horizontal limits), then let $\mathbf{m}_\ell = \mathbf{m}_{\ell-1}$ and terminate the iteration process.

Accordingly, the results associated with different iteration algorithms are illustrated in Figs 4.13 and 4.14, and the related model setup for the modeling is given in Table 4.11. The empirical and analytical covariance functions derived from the input residuals are shown in Fig. 4.15. The latter ones are used for the modeling within LSC, which is implemented by the **GRAVSOFT** package (Tscherning et al., 1992). The discussion on the results is given as follows.

In the CA test case (see Fig. 4.13), the solutions associated with L-BFGS-B algorithm are the best among all solutions and close to the LSC solution (see the black dashed lines in Fig. 4.13). The performance of L-BFGS and NLCG is similar, while LM delivers the worst solution. This might be due to the fact that LM usually generates larger search directions than NLCG and L-BFGS at the first several iterations (see also the numerical comparisons in Section 3.3.6), and hence it is of a high risk that the model parameters estimated by LM exceed the defined limits of model parameters (e.g., depth limits) within a few iterations, resulting in a worse fit of the data to the model than NLCG and L-BFGS. Since the input data are error-free, and the control values are true in this test case, the

Table 4.11: Model setup for the numerical tests in Section 4.1.3.1.

Model factors	CA test case	NM test case
Spectral bandwidths of the RBFs	① Full, $N_{\min} = 0$ (S1) ② Reduced, $N_{\min} = 201$ (S2)	① Full, $N_{\min} = 0$ (S1) ② Reduced, $N_{\min} = 101$ (S2)
Optimization direction		① Radial-direction (2P) ② All-direction (4P)
Initial depth [km]	15	13
Depth limits [km]	13 – 20	11 – 20
Horizontal limits for 4P	7.0°E to 15.0°E 45.0°N to 49.0°N	–107.85°E to –105.15°E 31.65°N to 34.85°N
Number N_ε of the nearest point mass RBFs		10
Total number K of point mass RBFs	1500	1000
Iteration limit N_{it} for each new point mass RBF		20

smallest RMS, STD, and RANGE of the results associated with L-BFGS-B indicate that L-BFGS-B is a better choice than the other three algorithms.

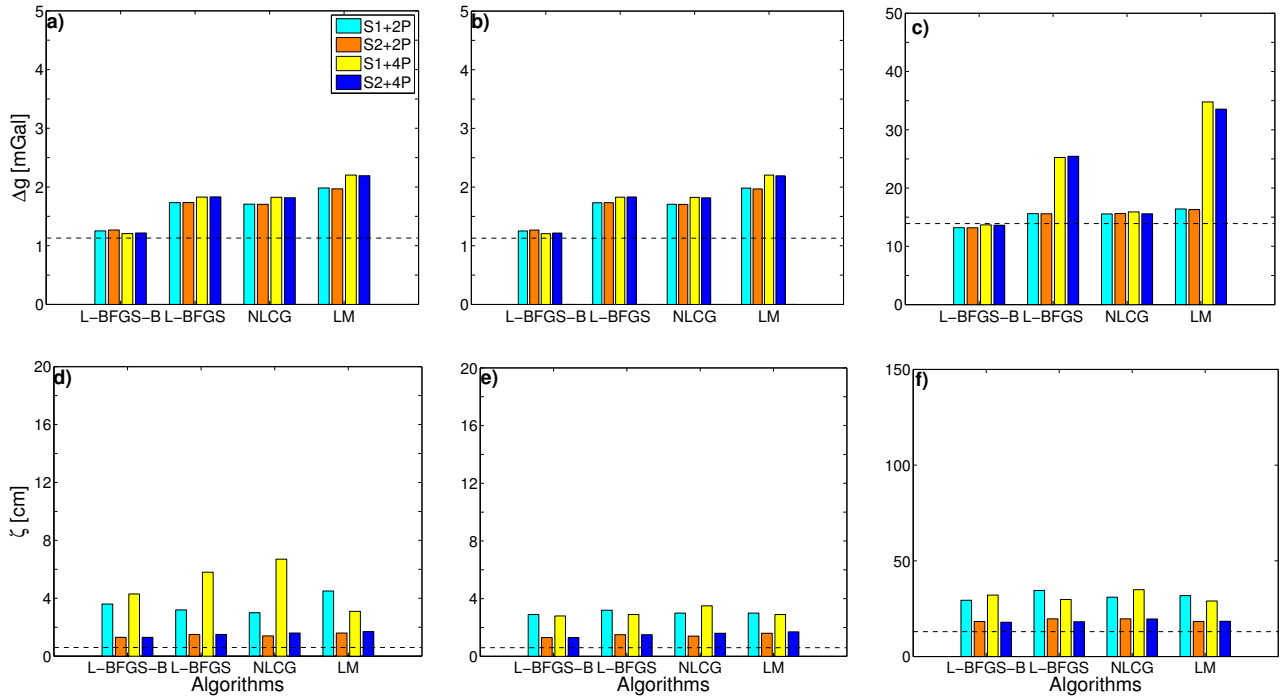


Figure 4.13: CA test case: **a)** RMS, **b)** STD, and **c)** RANGE of the differences between predicted and observed (true) values for Δg at control points associated with different iteration algorithms; **d)**, **e)**, and **f)** the same for ζ . The least-squares collocation results are shown as dashed lines.

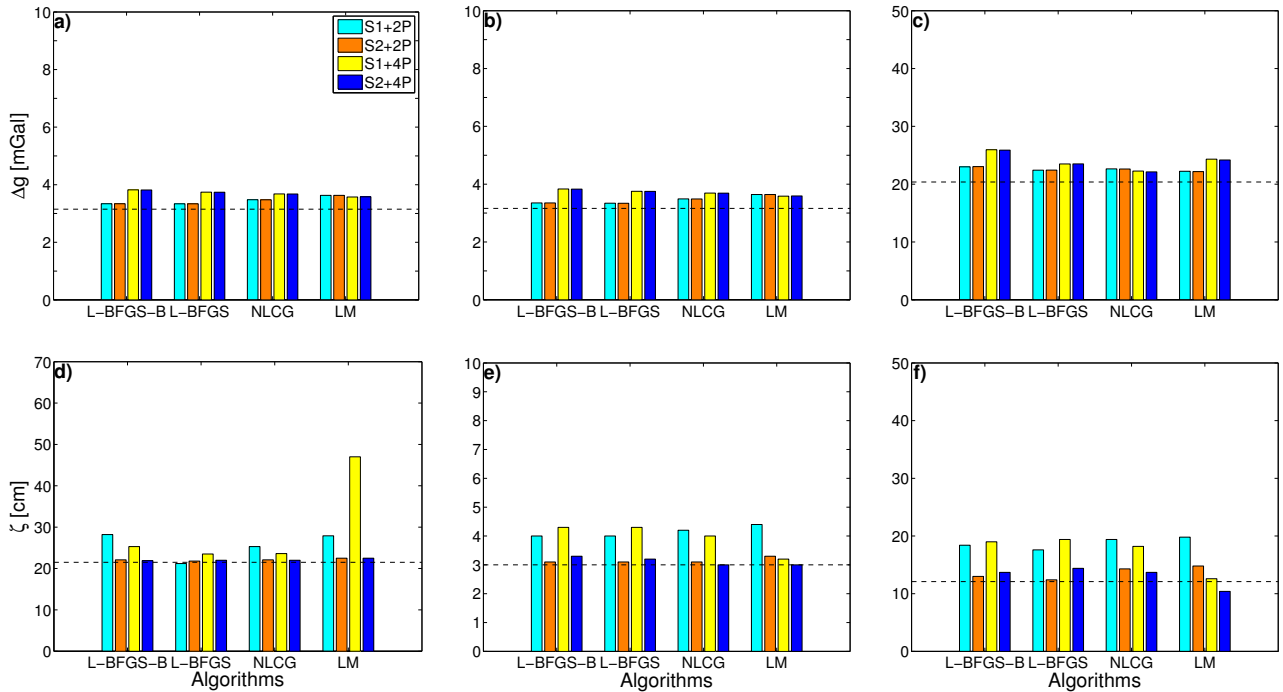


Figure 4.14: The same as in Fig. 4.13, but for the NM test case.

In the NM test case (see Fig. 4.14), the differences between the solutions derived from the four algorithms are not as evident as those in the CA test case. The gravity anomaly solutions associated with L-BFGS-B and L-BFGS look very similar. They are better than the ones associated with NLCG and LM in the case of using radial-direction optimization (i.e., 2P) and are slightly worse in the case of using all-direction optimization (i.e., 4P). In general, the 2P gravity anomaly solutions are better than the 4P solutions and close to the LSC solution in this test case. Similar height anomaly solutions are obtained by all algorithms. When using reduced point mass RBFs (i.e., S2), the height anomaly solutions are close to the LSC solution. More discussion on the issue about the optimization direction and the spectral bandwidths of the point mass RBFs will be given in the numerical tests in Section 4.1.3.2.

Although many other similar numerical tests with the use of different data sets in different test areas can be conducted to further test the four algorithms, we believe that our two numerical tests are sufficient to provide us some useful information. Accordingly, the better performance of L-BFGS-B than the other three algorithms enable us to implement it in PM-FRE for all remaining tests in this thesis.

4.1.3.2 Investigation on the effect of four important model factors

In the numerical tests presented in Section 4.1.3.1, we have compared the performance of four iteration algorithms for regional gravity field modeling. In this section, we will mainly focus on the effect on the solutions caused by the following four important model factors: (1) the initial depths and depth limits, (2) the total number K of point mass RBFs, (3) the spectral bandwidths of the point mass RBFs, and (4) the optimization direction. Related studies can also be found in Lin et al. (2014).

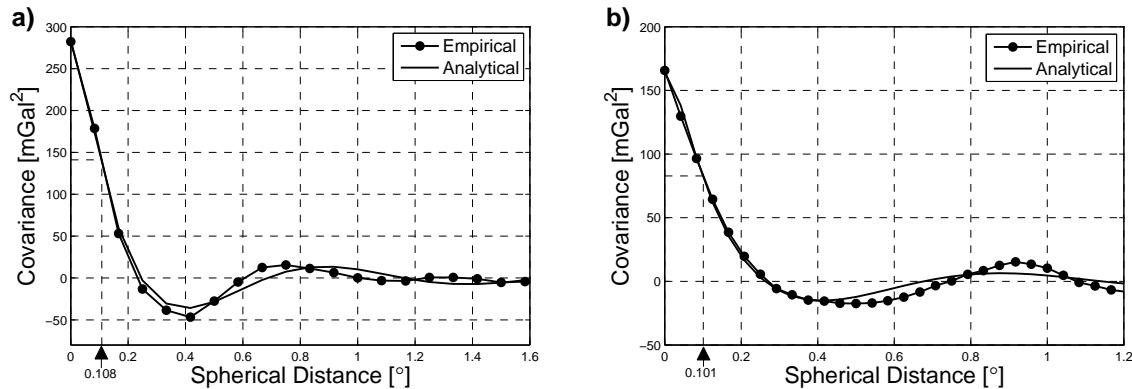


Figure 4.15: Empirical and analytical covariance functions of the observations for **a)** the CA and **b)** the NM test case. The corresponding correlation lengths of the empirical covariance functions are 0.108° and 0.101° , respectively.

Several scenarios are considered to study the sensitivity of the gravity field solutions with respect to the four model factors (see also Section 3.5.2). As shown in Hauck and Lelgemann (1985), the Krarup reproducing kernel defines the potential of one point mass RBF located below the observation point at a depth given by the Kelvin transformation at the Bjerhammar sphere, and if the number of point mass RBFs equals the number of observations, the point mass method can be considered as being equivalent to least-squares collocation with a covariance function defined by the Krarup kernel (Barthelmes, 1989). In regional gravity field modeling by collocation, the covariance function is always chosen to fit the empirical covariance function of the observations. Therefore, it seems to be quite reasonable to choose the initial depth of the point mass RBFs with the help of the empirical covariance function. The idea is to set the initial depth equal to the depth of the point mass RBF

Table 4.12: Model setup used for the numerical test cases in Section 4.1.3.2. The other model factors are the same as the ones in Table 4.11.

Model factors	CA test case	NM test case
Depth limits [km]	① 5 – 20	① 3 – 20
	② 9 – 20	② 6 – 20
	③ 13 – 20	③ 11 – 20
	④ 13 – 50	④ 11 – 30
Total number K of point mass RBFs	① 1100	① 700
	② 1500	② 1000

for which the corresponding half-width $\xi_{0.5}$ (i.e., spatial bandwidth of the RBF, see the definition in Section 2.7.4) and the correlation length ξ_e of the empirical covariance function match. Once ξ_e is known, it is easy to derive the initial depth iteratively.

According to Fig. 4.15, the correlation lengths of the empirical covariance functions are 0.108° and 0.101° for the CA and NM data sets. As a result, the estimates of the initial depths are about 15 and 13 km, respectively. Furthermore, the effect of four different sets of depth limits will be studied for each test area. The lower depth limits for the first three cases (see Table 4.12) are based on a simple formula $D = R/(n - 1)$ given in Bowin (1983), where D means the depth, R denotes the mean Earth radius, and n stands for the spherical harmonic degree. Based on the maximum degree of the chosen reference field ($n_{\max} = 360$), this results in a lower depth limit of about 20 km. In addition to this, also a deeper limit is chosen for each test area to study the corresponding impact on the results (see Case ④ in Table 4.12). Regarding the upper depth limit, practical investigations showed that this value is not expected to be smaller than the average data spacing as otherwise strong local unrealistic (erratic) features will show up. Based on these considerations, the upper depth limits are chosen to be equal to or larger than the average data spacing. Nevertheless, a shallower upper depth limit is also selected for each test area for comparison purposes (see Case ① in Table 4.12). In each test area, the point mass RBFs with two different N_{\min} are used for the modeling. The model setup is summarized in Table 4.12.

In each test case, the search process is terminated by finding a certain number of point mass RBFs. The main results based on two different total numbers K of point mass RBFs are shown in Figs 4.16 and 4.17 for the CA test case while corresponding results for the NM test case are displayed in Figs 4.18 and 4.19. These figures show the statistics (RMS, STD, and RANGE) of the differences between predicted and observed (or true) values at the control points for the different model setups listed in Table 4.12. Figs 4.20 and 4.21 show the RMS of the differences between the predictions and observations (data misfit) as well as the RMS of the differences between the predicted and observed (or true) values at the gravity anomaly control points (RMS difference) as a function of the number of point mass RBFs; both figures are based on the reduced point mass RBFs, and similar results are obtained when using the full RBFs (not shown here).

In addition, Table 4.13 gives the detailed statistics of the differences between the predicted values computed from PM-FRE as well as LSC and the true values at the control points for the CA test case, while Table 4.14 presents the statistics of the differences with respect to the observed values at the control points for the NM test case. The main findings are summarized as follows.

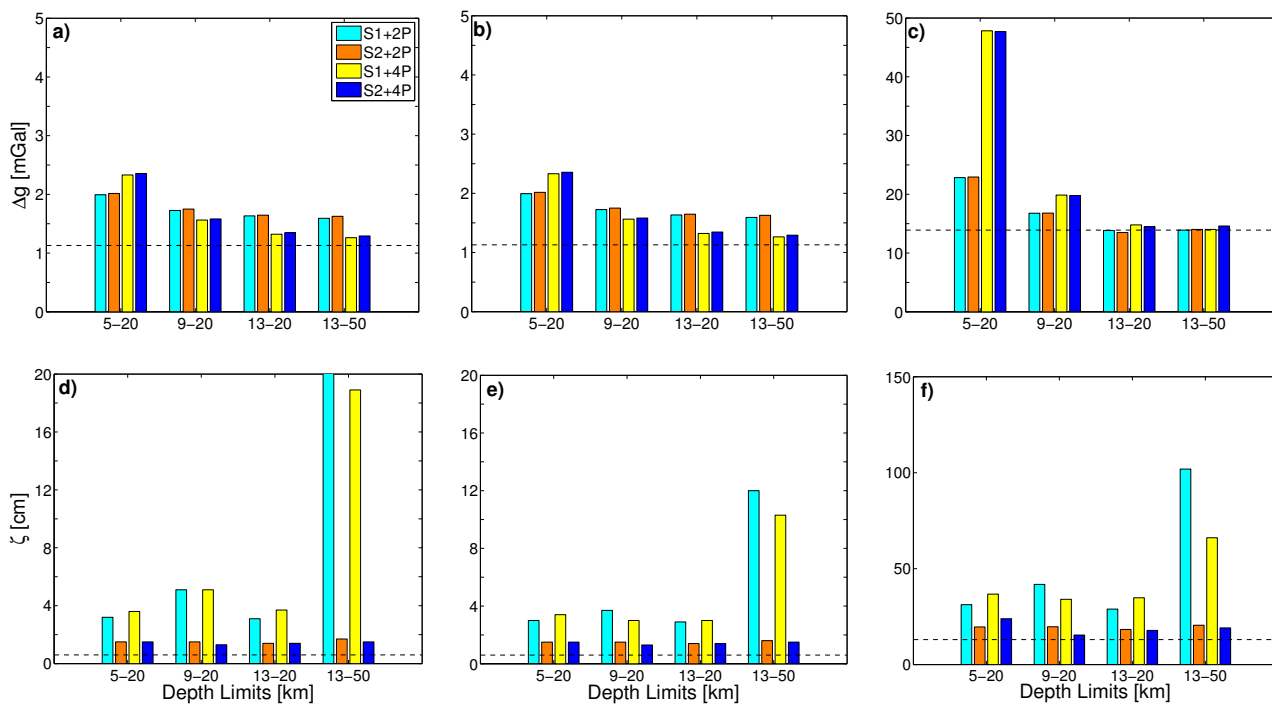


Figure 4.16: CA test case: **a)** RMS, **b)** STD, and **c)** RANGE of the differences between predicted and observed (true) values for Δg at control points associated with different model setups; **d)**, **e)**, and **f)** the same for ζ . 1100 point mass RBFs are selected for the modeling, and the related least-squares collocation results are shown as dashed lines.

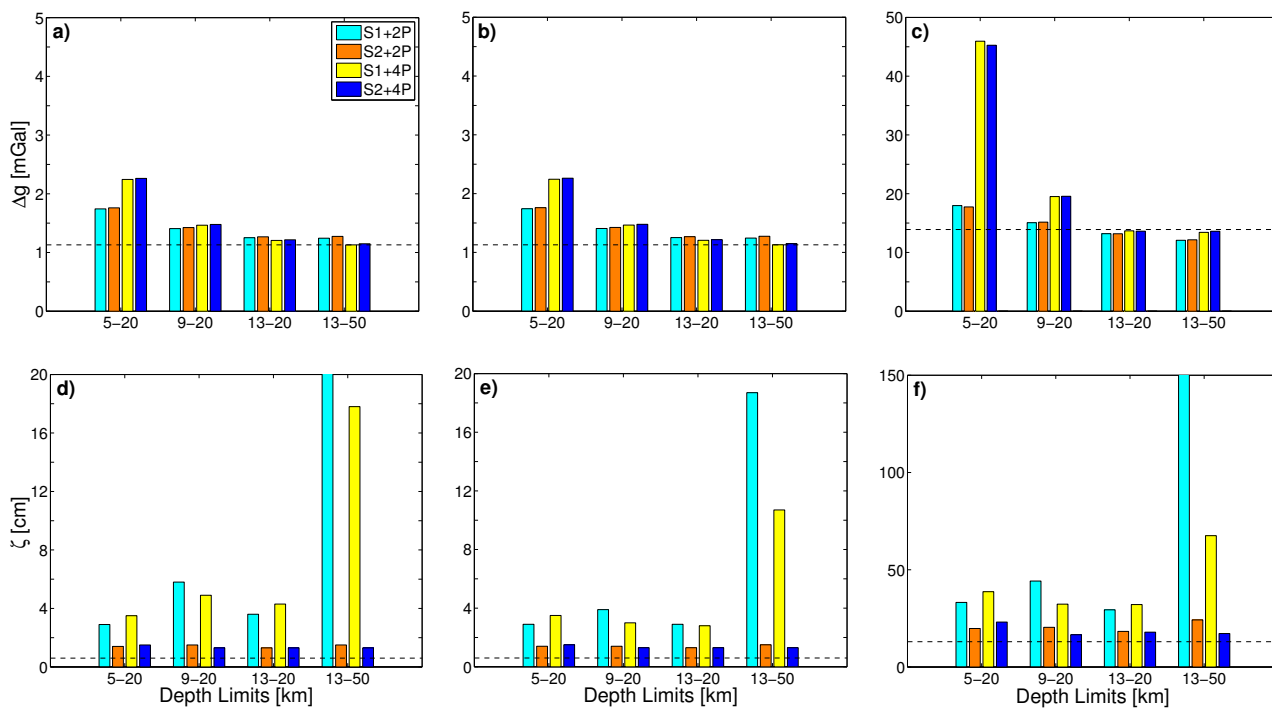


Figure 4.17: The same as in Fig. 4.16, but for 1500 point mass RBFs selected for the modeling.

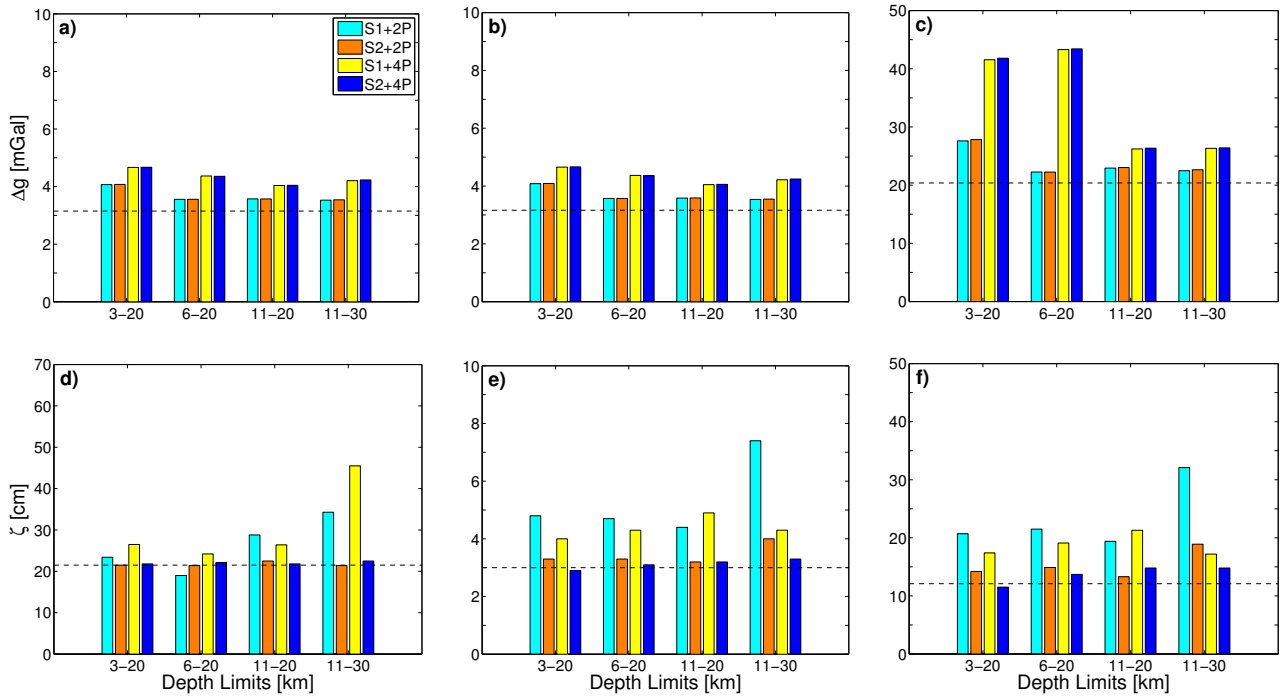


Figure 4.18: The same as in Fig. 4.16, but for the NM test case. 700 point mass RBFs are selected for the modeling.

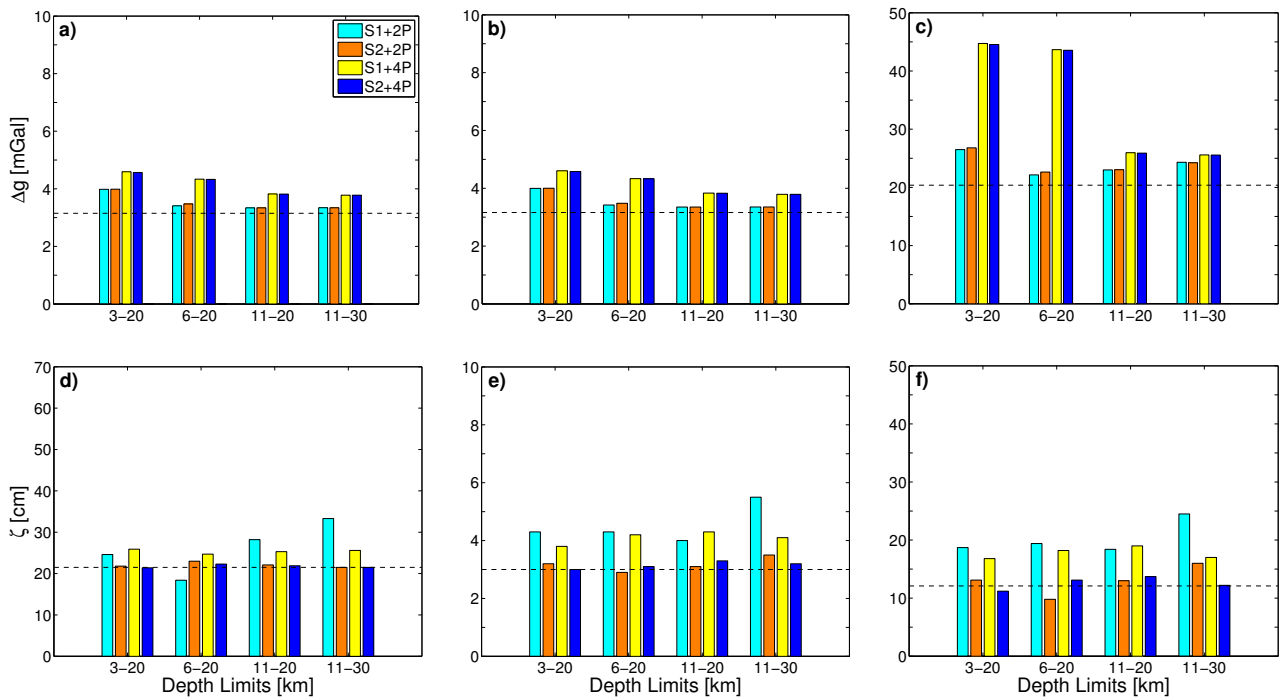


Figure 4.19: The same as in Fig. 4.18, but for 1000 point mass RBFs selected for the modeling.

The effect of the depth limits on the solutions

From Figs 4.16–4.19 (see the bar charts for different depth limits) it is obvious that a proper choice of depth limits is crucial to guarantee a high-quality solution with small errors in comparison to the control point values. Comparing the solutions with the same lower depth limits but different upper depth limits (i.e., the first three cases of the depth limits in Table 4.12), it can be seen that the gravity anomaly solutions are quite worse for a too shallow upper depth limit (i.e., 5 and 3 km for the CA and NM test cases), resulting in large RMS, STD, and RANGE of the differences. This can be attributed to the point mass RBFs located at or close to the upper depth limit, which produce some artificial high-frequency signals in the voids between the RBFs, as the spatial bandwidths of these point mass RBFs are too small. When the upper depth limit is deeper (i.e., 9 and 13 km for the CA test case; 6 and 11 km for the NM test case), the gravity anomaly solutions become much better with smaller errors when comparing to the values at the control points. No evident differences can be found between the height anomaly solutions for three different upper depth limits. Since the height anomalies are in the long-wavelength domain, the change of the upper depth limit has only minor effect on them. Now, for constant upper depth limits but different lower depth limits (Cases ③ and ④ for depth limits in Table 4.12), contrary to the previous investigation, the gravity anomaly solutions are nearly unaffected by using different lower depth limits, but the predicted height anomalies are distorted by some deep point mass RBFs. In the case of the depth limits of 13 – 50 km for the CA test case, the full RBFs located at deep depths, resulting in too large spatial bandwidths, lead to large RMS, STD, and RANGE of the height anomaly differences (see Figs 4.16 and 4.17). According to the above comparisons, the quality of gravity anomaly solutions is sensitive to the chosen upper depth limit, while the height anomaly solutions are mostly affected by the lower depth limit. Therefore, the depth limits must be chosen carefully based on the observations to be fitted. Shallower point mass RBFs are required for fitting high-frequency gravity signals and deeper RBFs for fitting long-wavelength height anomalies.

The solutions related to the upper depth limit of 13 km for the CA test case and 11 km for the NM test case are quite good and close to the corresponding LSC results. As a result, an upper depth limit of about 85% of the initial depth, which is derived from the approach based on the correlation length of the empirical covariance function, is a proper choice. The lower depth limits obtained from a simple formula given in Bowin (1983) prove to be appropriate (e.g., 20 km) in our test cases, but deeper limits are also suitable (e.g., 50 and 30 km). No explicit rules can be given for the optimal choice of depth limits. Usually, the selected upper depth limit is not expected to be smaller than the average data spacing (i.e., 9 and 6 km for the CA and NM test cases, respectively), while the lower depth limit is preferred to be smaller than the highest resolution of the chosen reference field (i.e., about 55 km for $n_{\max} = 360$ in both test cases).

The effect of the total number K of point mass RBFs on the solutions

Comparing Fig. 4.16 to 4.17 (i.e., 1100 and 1500 point mass RBFs for the CA test case) as well as Fig. 4.18 to 4.19 (i.e., 700 and 1000 point mass RBFs for the NM test case), the gravity anomaly solutions are obviously improved when more point mass RBFs are used, but improvements of the height anomalies are not evident. From Figs 4.20 and 4.21, the data misfit and RMS differences decrease rapidly in the beginning, but very slowly when more and more point mass RBFs are included. If the number of point mass RBFs is about 30% – 35% of the number of observations (i.e., 1500 vs. 4753 for the CA test case, 1000 vs. 2767 for the NM test case), the obtained solutions are close to the LSC results. The required number of point mass RBFs for a good approximation may also depend on the signal variation. However, it is not evident in the selected two test cases. In general, the use of a large number of point mass RBFs can represent high-frequency signals well, but also increase the numerical complexity and may cause an over-parameterization in the area with smooth features.

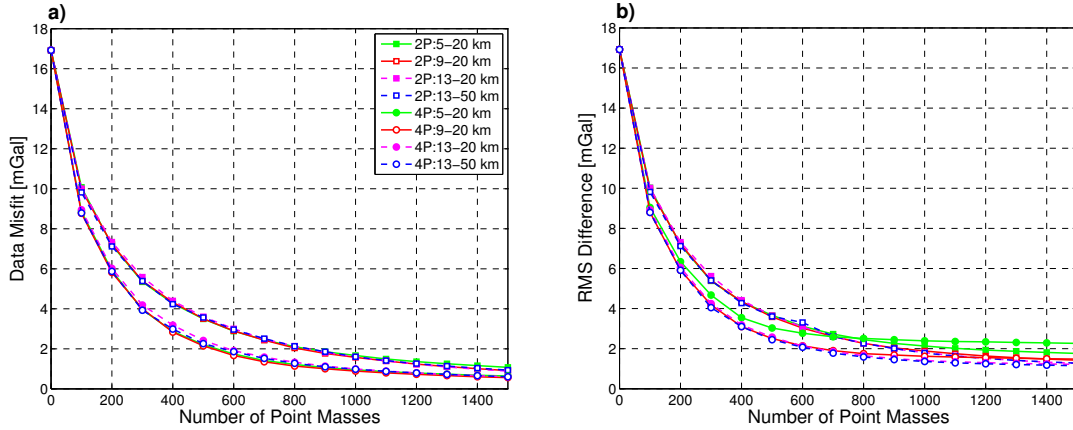


Figure 4.20: CA test case: **a)** data misfit and **b)** RMS difference at 4608 Δg control points with respect to different numbers of selected point mass RBFs associated with different depth limits and optimization directions. All results are computed by using reduced RBFs.

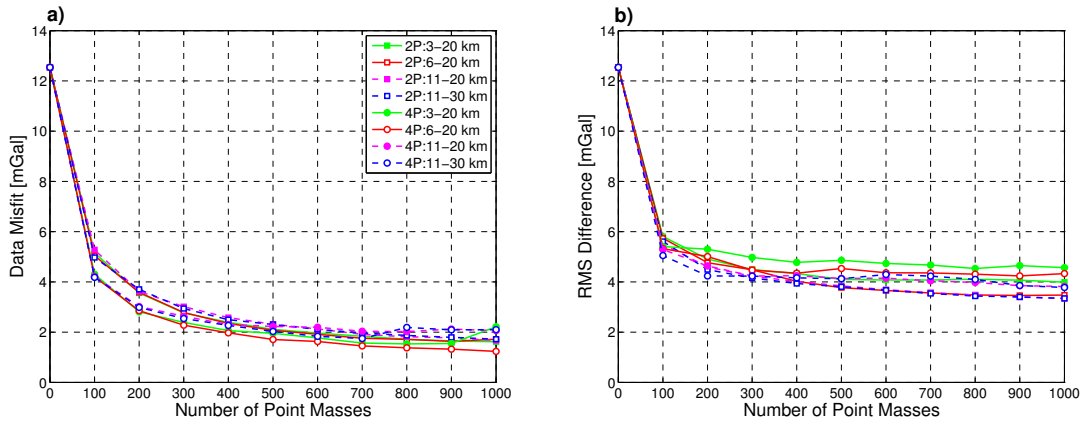


Figure 4.21: The same as in Fig. 4.20, but for the NM test case and 153 Δg control points in **b)**.

The effect of the spectral bandwidths of the point mass RBFs on the solutions

Significant differences between the S1 (i.e., full point mass RBFs) and S2 (i.e., reduced RBFs) gravity anomaly solutions are not seen in Figs 4.16–4.19 and Tables 4.13–4.14. For the height anomaly solutions, the situation is completely different, as the S2 solutions are significantly improved compared to the S1 solutions. Since the observations are residual gravity anomalies in our test cases, the errors caused by different spectral bandwidths between the full point mass RBFs and the input residuals are evident in the height anomaly solutions, resulting in large biases. Therefore, the reduced RBFs are recommended for quasigeoid modeling when only gravity anomalies are used as input data. However, also the S2 height anomaly solutions are slightly worse than the corresponding LSC solutions in our test cases. This may be due to edge effects caused by the limited data coverage. Usually, a simple way to reduce edge effects is to make the data area larger than the model area.

The effect of the optimization direction on the solutions

In the CA test case (see Figs 4.16, 4.17, 4.20, as well as Table 4.13), in which the grid data are used as input, the 4P solutions (i.e., all-direction optimization) perform better than the corresponding 2P solutions (i.e., radial-direction optimization) in approximating the gravity anomalies (except for the case with depth limits of 5 – 20 km). These improvements may be attributed to the optimization in

Table 4.13: Statistics of the differences between predicted values from PM-FRE as well as least-squares collocation and the true (simulated) values at the control points for the CA test case, i.e., 4608 Δg [mGal] and 4608 ζ [m] control points, respectively. The depth limits are 13–50 km, and the number of point mass RBFs is 1500 for the respective solutions.

	Δg					ζ				
	Mean	STD	RMS	Min	Max	Mean	STD	RMS	Min	Max
LSC	-0.049	1.129	1.130	-8.830	5.078	0.0	0.006	0.006	-0.053	0.077
S1+2P	-0.027	1.244	1.244	-7.243	4.827	0.403	0.187	0.444	-0.166	1.435
S2+2P	-0.011	1.274	1.274	-6.944	5.212	0.0	0.015	0.015	-0.120	0.122
S1+4P	-0.008	1.130	1.130	-4.903	8.519	0.142	0.107	0.178	-0.312	0.363
S2+4P	-0.002	1.149	1.149	-5.054	8.560	0.0	0.013	0.013	-0.077	0.095

Table 4.14: The same as in Table 4.13, but for the NM test case with 153 Δg [mGal] and 20 ζ [m] (GPS/leveling) control points (observed). The depth limits are 11–20 km, and the number of point mass RBFs is 1000 for the respective solutions.

	Δg					ζ				
	Mean	STD	RMS	Min	Max	Mean	STD	RMS	Min	Max
LSC	0.025	3.161	3.151	-8.444	11.926	0.213	0.030	0.215	0.155	0.276
S1+2P	0.039	3.351	3.340	-9.826	13.174	0.279	0.040	0.282	0.184	0.368
S2+2P	0.013	3.351	3.340	-9.909	13.131	0.218	0.031	0.221	0.141	0.271
S1+4P	0.050	3.833	3.821	-10.546	15.415	0.250	0.043	0.253	0.158	0.348
S2+4P	0.030	3.830	3.818	-10.505	15.384	0.216	0.033	0.219	0.141	0.278

the horizontal direction, leading to a more reasonable horizontal distribution of the point mass RBFs. For the height anomaly approximation both approaches in connection with the reduced RBFs give very similar results. Only the reduced point mass RBFs are utilized here as the negative effects caused by using the full RBFs on the height anomaly solutions are significant (see the discussion in the last paragraph). Furthermore, the results also indicate that the all-direction optimization (4P) is more sensitive to the chosen upper depth limit than the radial-direction optimization (2P). For the case of the depth limits of 5–20 km, the 4P gravity anomaly solutions are worse than the 2P solutions.

Similar comparisons are conducted in the NM test case (see Figs 4.18, 4.19, 4.21, as well as Table 4.14). Regarding again the 4P and 2P cases, the height anomaly solutions perform similarly, but larger discrepancies can be seen in the 4P gravity anomaly solutions. It is caused by the gaps of the input data. The optimization in horizontal direction moves some point mass RBFs into the gaps for a good fit of the data, resulting in shallow RBFs with large magnitudes that can produce unrealistic high-frequency signals. Consequently, the existence of data gaps is a critical issue for the all-direction optimization (4P), while good results can be obtained with the radial-direction optimization (2P) for both test areas with regular and irregular input data.

4.1.3.3 Comparison of different iteration limits N_{it} and different numbers N_ε of the nearest point mass RBFs

In this section, the effect on the solutions caused by another two model factors used in the first step of PM-FRE, i.e., (1) the iteration limit N_{it} for each new point mass RBF and (2) the number N_ε of the nearest RBFs, are numerically investigated. The used model factors are given in Table 4.15. When varying the iteration limit N_{it} , the number N_ε is fixed to be 10 for both test cases. Similarly, $N_{it} = 20$ is chosen when analyzing the effect of different choices of N_ε . The corresponding numerical results are presented in Tables 4.16 and 4.17.

Table 4.16 shows the errors for different iteration limits N_{it} while fixing N_ε to be 10. In the CA test case, as expected, the gravity anomaly solutions are slightly improved with increasing values of N_{it} . The RMS errors of the height anomaly solutions are close to each other. In the NM test case, an increase of N_{it} does not lead to a decrease of the RMS errors of the gravity anomaly solutions. The choice of $N_{it} = 5$ provides a smaller RMS error of the gravity anomaly solution than the cases of $N_{it} = 10, 20$, and 30 . A possible reason is due to the over-fitting of the model to the data and the irregular data distribution. This can also explain why the gravity anomaly RMS error for $N_{it} = 50$ is smaller than the case of $N_{it} = 100$. However, the differences between the RMS errors of the gravity anomaly solutions are small, ranging from about 3.25 mGal to 3.42 mGal. The STD errors of the height anomaly solutions are in the range of 0.034 m to 0.037 m, meaning that they are not sensitive to the choice of N_{it} .

Table 4.17 gives the errors for different N_ε with fixed $N_{it} = 20$. Similar to the case of varying N_{it} and fixed N_ε , the larger the N_ε is, the smaller the RMS error for the gravity anomaly solution is in the CA test case. In the NM test case, the RMS errors of the gravity anomalies decrease with increasing N_ε at first, but remain nearly the same when $N_\varepsilon \geq 20$ with values between 3.26 mGal and 3.36 mGal. In both test cases, the height anomaly solutions show the insensitivity to N_ε .

According to the above studies, we find that the choice of $N_{it} = 20$ and $N_\varepsilon = 10$ for the search process in the first step is usually satisfactory for providing a set of point mass RBFs at proper positions. This choice is used as default in the following computations when using PM-FRE.

Table 4.15: Model setup used for the numerical tests in Section 4.1.3.3.

Model factor	CA test case	NM test case
Spectral bandwidths of the RBFs	Reduced, $N_{\min} = 201$	Reduced, $N_{\min} = 101$
Optimization direction		Radial-direction
Initial depth [km]	15	13
Depth limits [km]	13 – 50	11 – 30
Number N_ε of the nearest point mass RBFs		5, 10, 20, 30, 40, 50
Total number K of point mass RBFs	1500	1000
Iteration limit N_{it} for each new point mass RBF		5, 10, 20, 30, 50, 100

Table 4.16: *First two lines:* RMS errors of Δg [mGal] and ζ [m] associated with different values of N_{it} for the CA test case. *Second two lines:* RMS Δg errors and STD ζ errors for the NM test case. Note that $N_\varepsilon = 10$ in this test.

N_{it}	5	10	20	30	50	100
Δg	1.381	1.313	1.274	1.266	1.245	1.237
ζ	0.015	0.015	0.015	0.015	0.016	0.016
Δg	3.303	3.419	3.419	3.397	3.246	3.276
ζ	0.034	0.035	0.035	0.036	0.037	0.037

Table 4.17: *First two lines:* RMS errors of Δg [mGal] and ζ [m] associated with different values of N_ε for the CA test case. *Second two lines:* RMS Δg errors and STD ζ errors for the NM test case. Note that $N_{it} = 20$ in this test.

N_ε	5	10	20	30	40	50
Δg	1.383	1.274	1.256	1.241	1.229	1.220
ζ	0.015	0.015	0.015	0.015	0.018	0.016
Δg	3.547	3.419	3.278	3.362	3.317	3.257
ζ	0.031	0.035	0.031	0.033	0.033	0.032

4.1.3.4 Comparison of unconstrained and constrained solutions

In Section 4.1.2.3, we showed that using additional constraints for solving the linear equation system constructed by full point mass RBFs provides similar solutions as the unconstrained solutions computed by using reduced RBFs in PM-FIX. Here, similar procedures are applied in the second step of PM-FRE with the known positions of the RBFs derived from the first step. Most of the used model factors are given in Table 4.15 while letting $N_{it} = 20$ and $N_\varepsilon = 10$. Five constrained solutions using different values of n' are computed. Tables 4.18 and 4.19 present the RMS (or STD) errors of the solutions. Comparing the constrained solutions to the unconstrained solutions with the use of reduced RBFs (i.e., $N_{\min} > 0$) in each test case, a good agreement between the constrained solution with $n' \in [N_{\min}/2, N_{\min}]$ (e.g., $n' \in [100, 200]$ for the CA test case and $n' \in [50, 100]$ for the NM test case) and the unconstrained solution is obtained, whereas the latter is slightly better than the former.

Figs 4.22 and 4.23 show the related square roots of the degree variances in terms of gravity and height anomaly for the CA and the NM test case, respectively. It can be seen that the degree variances for the unconstrained and constrained solutions coincide quite well. Considering the significant deviations between the degree variances (unconstrained solutions with reduced RBFs vs. constrained solutions) in the case of PM-FIX (see Section 4.1.2.3), the similar degree variances shown here may be attributed to the fact that the positions of the point mass RBFs obtained from the first step of PM-FRE are more reasonable than the grid points used in PM-FIX.

Table 4.18: RMS errors of Δg [mGal] and ζ [m] associated with the unconstrained and constrained solutions for the CA test case.

	Unconstrained solution		Constrained solution				
	$N_{\min} = 0$	$N_{\min} = 201$	$n' = 1$	50	100	150	200
Δg	1.244	1.274	1.256	1.282	1.314	1.328	1.338
ζ	0.444	0.015	0.061	0.035	0.023	0.019	0.018

Table 4.19: RMS errors of Δg [mGal] and STD errors of ζ [m] associated with the unconstrained and constrained solutions for the NM test case.

	Unconstrained solution		Constrained solution				
	$N_{\min} = 0$	$N_{\min} = 101$	$n' = 1$	50	100	150	200
Δg	3.418	3.419	3.415	3.419	3.424	3.432	3.440
ζ	0.052	0.035	0.048	0.033	0.033	0.032	0.029

4.1.3.5 Conclusions

The effect of several model factors on regional gravity field modeling using PM-FRE is studied numerically in two different test areas with synthetic and real data. The L-BFGS-B algorithm is demonstrated to be a suitable tool for solving the bound-constrained nonlinear least-squares problem in the first step of the entire procedure. However, the quality of the final solutions is highly dependent on the choice of various model factors, and although an improper choice may still lead to a satisfactory data misfit, large errors can result in the final solutions when comparing them with independent data. The numerical results lead to the following conclusions:

- The determination of the initial depth and depth limits is of highest importance. They must be chosen very carefully to avoid unreliable solutions. Testing of different initial depths and related depth limits leads to the following empirical rule: the initial depth is derived from the empirical covariance function of the observations, and the upper depth limit is preferred to be about 0.8 – 0.9 times of this value, while being larger than the average data spacing. The lower depth can be selected by a simple formula given in Bowin (1983) or being deeper, but it should be less than the highest resolution of the chosen reference gravity field.
- To get a good fit of the data in the selected two test cases, the data distribution has an impact on the necessary number of point mass RBFs, but the data variability plays only a minor role. An efficient way for choosing the number of point mass RBFs is to terminate the search process in the first step by satisfying a defined data misfit. However, in many cases, the number of point mass RBFs is chosen by the user through numerical comparisons.
- Reduced point mass RBFs are recommended for geoid/quasigeoid modeling when using gravity anomalies as input. The value of N_{\min} for the reduced RBFs can be equal to or less than the maximum degree n_{\max} of the chosen reference gravity field. When only using the full RBFs,

the consideration of additional constraints with a proper value of $n' < n_{\max}$ in the least-squares adjustment can also provide accurate gravity and height anomaly solutions.

- If the depth limits are appropriate, the all-direction optimization performs slightly better than the radial-direction optimization in the CA test case with error-free data at the grid points. However, the all-direction option is very sensitive to the upper depth limit as well as to the data distribution, and large errors occur in corresponding solutions for the NM test case with data gaps. The radial-direction option is more reliable and simple.
- The large values of the iteration limit N_{it} and the number N_ε of the nearest RBFs are usually not necessary for PM-FRE. Often, the choice of $N_{it} = 20$ and $N_\varepsilon = 10$ is sufficient for regional modeling within PM-FRE.

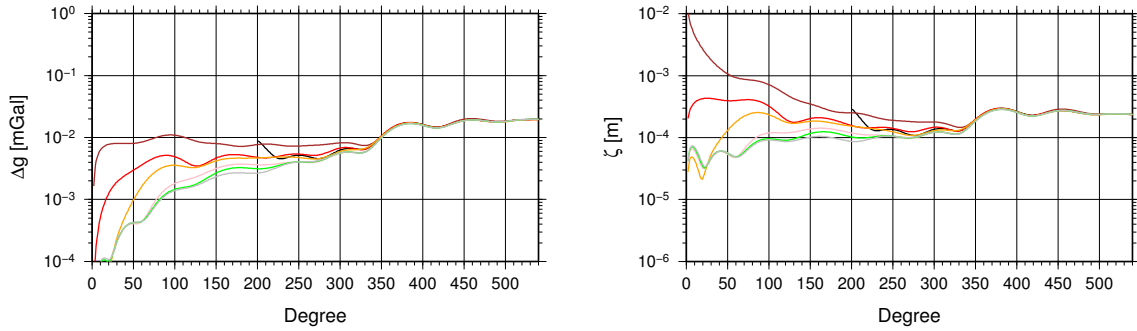


Figure 4.22: Square roots of the degree variances in terms of Δg (left) and ζ (right) associated with the unconstrained and constrained solutions for the CA test case. *Black:* $N_{\min} = 201$; *brown:* $N_{\min} = 0$; *red:* $n' = 1$; *orange:* $n' = 50$; *pink:* $n' = 100$; *green:* $n' = 150$; *gray:* $n' = 200$.

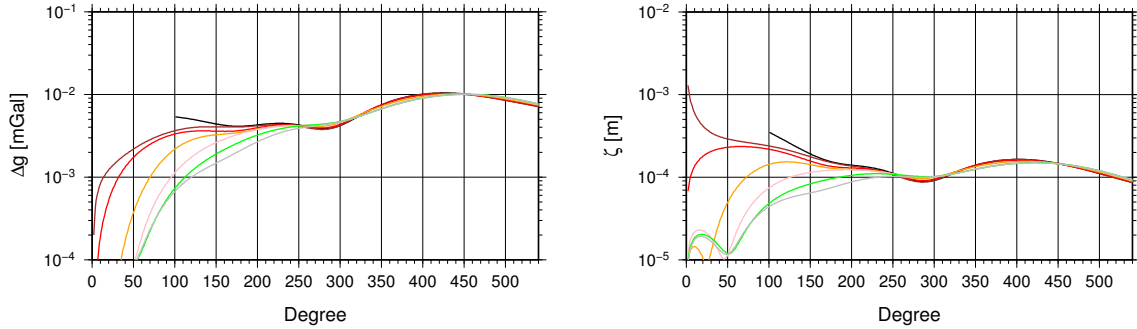


Figure 4.23: The same as in Fig. 4.22, but for the NM test case. *Black:* $N_{\min} = 101$; *brown:* $N_{\min} = 0$; *red:* $n' = 1$; *orange:* $n' = 50$; *pink:* $n' = 100$; *green:* $n' = 150$; *gray:* $n' = 200$.

4.1.4 A comparison between PM-FIX and PM-FRE

In this section, the performance of PM-FIX and PM-FRE for regional gravity field modeling using the above two data sets is compared. PM-FIX is based on the computation procedure described in Section 4.1.2.4, and the solutions associated with a single-grid formation and a two-grid formation are labeled as FIX-S and FIX-T. Similarly, FRE-A and FRE-B denote the solutions, which are computed by using PM-FRE with the point mass search model SMA and SMB (see Section 3.5.3). For each test case, the target data misfit is defined to determine the grid in PM-FIX, as well as the number of point mass RBFs in PM-FRE. For PM-FIX, all grids have the same extents as the ones in Table 4.4. The reduced point mass RBFs with $N_{\min} = 301$ and 201 are used for the final adjustment of

Table 4.20: Statistics of Δg [mGal] and ζ [m] errors at the control points associated with different solutions for the CA test case. The value in the parentheses means the number of used point mass RBFs.

Solutions	Δg					ζ				
	Mean	STD	RMS	Min	Max	Mean	STD	RMS	Min	Max
FIX-S (3321)	-0.008	1.598	1.598	-10.249	7.249	0.000	0.011	0.011	-0.106	0.088
FIX-T (3226)	-0.016	0.954	0.954	-7.465	5.575	0.001	0.027	0.027	-0.336	0.370
FRE-A (1498)	-0.036	1.317	1.317	-7.464	4.629	0.000	0.011	0.011	-0.077	0.095
FRE-B (1996)	-0.012	1.131	1.131	-6.486	4.846	0.000	0.012	0.012	-0.189	0.129

Table 4.21: The same as in Table 4.20, but for the NM test case.

Solutions	Δg					ζ				
	Mean	STD	RMS	Min	Max	Mean	STD	RMS	Min	Max
FIX-S (1189)	0.029	3.888	3.875	-9.743	14.551	0.241	0.028	0.243	0.195	0.298
FIX-T (1344)	0.119	3.953	3.942	-9.033	14.077	0.241	0.026	0.242	0.193	0.289
FRE-A (713)	-0.046	3.746	3.734	-9.516	14.023	0.243	0.026	0.244	0.199	0.287
FRE-B (876)	0.211	3.703	3.697	-11.542	14.929	0.241	0.027	0.242	0.194	0.286

the magnitudes for the CA and the NM test case, respectively. The details of the comparisons are discussed in the following.

Model setup for the CA test case

Since the input gravity data are error-free in this test case, no information can be referred to set the target data misfit. Considering the RMS of the input residuals (about 16.9 mGal), the target data misfit is defined as 1 mGal. For FIX-S, a $6' \times 6'$ grid (here, the first $6'$ means the grid spacing along the parallel and the second $6'$ means the grid spacing along the meridian) is selected for the computation. Although the resulting data misfit associated with the grid depth of 20 km (about 2 times of the grid spacing) is about 1.557 mGal, being larger than the target value of 1 mGal (see Step ② of the computation procedure in Section 4.1.2.4), a smaller grid spacing is not preferred. Otherwise, the number of point mass RBFs will be too large. The “optimal” depth is then chosen to be 30 km by using the GCV technique (see also Fig. 4.9b). For FIX-T, a coarse $15' \times 15'$ grid at the GCV derived “optimal” depth of 33 km is used to represent the smooth features of the research area. The resulting residuals will then be used for choosing a dense grid. Similar to the procedures for the single-grid formation, a dense $7.5' \times 6'$ grid at the “optimal” depth of 30 km is used. In this case, Tikhonov regularization is applied due to the numerical instabilities caused by the two grids at different depths. No regularization is applied for the other three solutions. FRE-A is mainly based on the model setup in Table 4.15 with $N_{it} = 20$ and $N_e = 10$. The first step is terminated by satisfying a data misfit smaller than 1 mGal, resulting in 1498 point mass RBFs. For FRE-B, two layers are defined for the

modeling. The depth limits of Layer 1 are 30 – 50 km, in which the initial depth for each new point mass RBF is 33 km. Only 100 RBFs are allowed to be in this layer. The other model factors for Layer 1 are $N_{it} = 50$ and $N_\varepsilon = 20$. For Layer 2, the corresponding model factors are 13 – 30 km (depth limits), 15 km (initial depth), $N_{it} = 20$, and $N_\varepsilon = 10$. In this layer, the point mass RBFs are searched for until the target data misfit is reached. A total number of 1996 RBFs are selected for FRE-B.

Model setup for the NM test case

In this test case, the target data misfit is set to be 2 mGal based on the input data error mentioned in Section 4.1.1. For FIX-S, a $6' \times 4.8'$ grid is selected for the computation. The resulting data misfit associated with the grid depth of 20 km (about 2 times of the grid spacing) is about 2.079 mGal and the “optimal” depth derived from the GCV technique is 18 km. For FIX-T, a coarse $12' \times 12'$ grid at the “optimal” depth of 55 km and a dense $5.25' \times 6'$ grid at the depth of 20 km are used for the modeling. Again, FRE-A is computed by using the model factors in Table 4.15 with $N_{it} = 20$ and $N_\varepsilon = 10$. For FRE-B, also two layers are used. The model factors for Layer 1 are 20 – 30 km (depth limits), 23 km (initial depth), $N_{it} = 50$, $N_\varepsilon = 20$, and only 100 RBFs are allowed to be in this layer. Similarly, the model factors for Layer 2 are 11 – 20 km, 13 km, $N_{it} = 20$, and $N_\varepsilon = 10$.

Results and discussion

Four solutions are computed based on the previously described model setup in each test area. The statistics of the gravity and height anomaly errors at the control points are given in Tables 4.20 and 4.21. They show that the solutions of PM-FRE (i.e., FRE-A and FRE-B) are better than the solutions of PM-FIX (i.e., FIX-S and FIX-T). In addition, the used number of point mass RBFs in PM-FRE is also much smaller. Comparing FIX-T to FIX-S, the use of two grids does not provide a better solution, i.e., with a smaller RMS (or STD) error, in our two test cases, but also raises the computational complexity. The best gravity anomaly solution of FIX-T in the CA test case benefits from the use of a large number of point mass RBFs as well as the gridded input data. However, too many deep RBFs (561 RBFs at the depth of 33 km) weaken the height anomaly solution. Although the number of used point mass RBFs is the largest for FIX-T in the NM test case, the corresponding gravity anomaly solution is the poorest. As the data points are irregularly distributed, over-parameterization can be caused when using too many point mass RBFs. Thus, a multi-grid formation should be carefully used. The two solutions of PM-FRE are quite similar. The used number of RBFs for FRE-B is larger than the number for FRE-A. It is due to the different point mass search models. Comparing to SMA, the point mass RBFs are searched for and restricted to the deepest layer first within SMB, then to the shallower layers. This leads to a slower decreasing of the data misfit with respect to the number of RBFs. Therefore, a larger number of point mass RBFs are needed to achieve the same target data misfit. As a result, the gravity anomaly solution for FRE-B is slightly better than for FRE-A, but the height anomaly solutions are similar. It also can be expected that with the use of the same number of point mass RBFs, the gravity anomaly solution for FRE-B should be a little worse than for FRE-A, whereas the height anomaly solutions are still similar.

4.1.5 Summary and conclusions

The developed point mass methods (i.e., PM-FIX and PM-FRE) can provide accurate results when applied to a synthetic and a real data set. A set of model factors for both methods must be defined properly. From the numerical studies in this section, it was obvious that PM-FRE outperforms PM-FIX for regional gravity field computations (see Section 4.1.4). Hence, only PM-FRE will be applied for the numerical tests in the following. Based on various comparisons, several conclusions can be drawn, and choices of model factors can be made. This leads to the “optimal” strategy for PM-FRE:

- For the point mass search model in PM-FRE, either SMA or SMB can be applied for the regional modeling. Without notification, SMA is used as the default search model. Numerous tests show that SMA performs slightly better than SMB, and the former is also much simpler. No matter which search model is used, the initial depth and depth limits are determined based on the empirical rule described in Section 4.1.3.5.
- For the optimization direction, the radial-direction optimization is applied as it is much more stable and reliable than the all-direction optimization, in particular in the case of using real data. However, if the chosen depth limits are improper, unrealistic predictions also exist, especially in the data gaps. The L-BFGS-B algorithm is used for solving the nonlinear least-squares problem with bound constraints on the depths (or radial distances) of the point mass RBFs.
- The above two items are relevant for finding the point mass RBFs in the first step of PM-FRE, in which the full RBFs are used for all computations. In the second step, we usually recommend using the reduced RBFs for the readjustment of the magnitudes of all selected RBFs. The use of reduced RBFs can also be explained as a further modification of the spatial bandwidths of the RBFs, which are originated from the first step. An alternative scheme is to use the full RBFs while considering the constraints in the adjustment.
- The empirical approach works well for finding the proper regularization parameter α in the second step of PM-FRE for the NM test case; however, it is not well suited for the case with a large number of unknowns or the case with no or inhomogeneous control values. Therefore, some heuristic approaches for choosing a proper α need to be incorporated in PM-FRE.

Part of the “optimal” strategy will be further completed by the following numerical tests.

4.2 Tests with a set of synthetic geoid heights with the same accuracy

In Section 4.1, we demonstrated the applicability of the developed point mass methods, in particular PM-FRE, for regional gravity field modeling using observed gravity anomalies. It arises the question whether the method can also deal with other kinds of input gravity field quantities. In the following, three numerical test cases using synthetic geoid heights with different noise levels are considered in one test area to test PM-FRE by comparing the results to corresponding LSC solutions (Lin et al., 2015). Another goal of these test cases is to compare the performance of three approaches as described in Section 3.3.5 for choosing the proper regularization parameter.

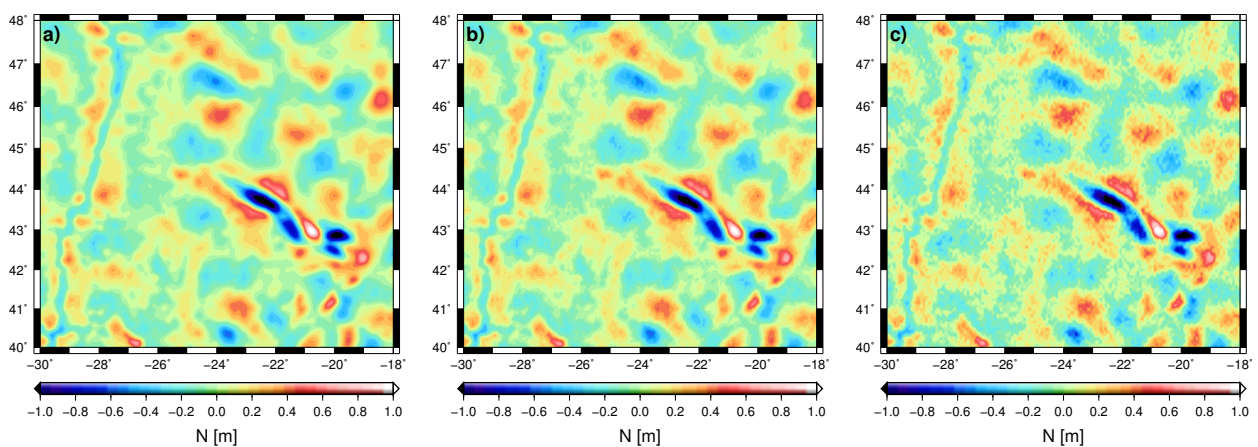


Figure 4.24: Simulated residual geoid heights over the test area: **a)** error-free data; **b)** noisy data, where white noise with a standard deviation of 0.02 m is added; **c)** noisy data, where white noise with a standard deviation of 0.05 m is added.

4.2.1 Description of the data sets

The test area is situated in the North Atlantic Ocean with an extent from -30°E to -18°E and 40°N to 48°N . The data set (a) consists of 14065 residual geoid heights (error-free), which are computed by the EGM2008 model up to d/o 2160 with the removal of the long-wavelength contributions from the GOCO03S model (Mayer-Gürr et al., 2012) up to d/o 250. The input residuals are located at grid points with a resolution of $5'$ and the height for each point is 0 m. Data sets (b) and (c) are obtained by adding white noise with an STD of 0.02 m and 0.05 m to data set (a). All three data sets are illustrated in Fig. 4.24. In addition, 11305 residual gravity anomalies located at grid points with true values are used as control points to assess the modeled gravity anomalies in each test case. The grids for the control points coincide with the ones for the observations but have a smaller extent. As the test area is in the ocean area, the test cases can be considered as analogue to gravity anomaly recovery from the altimeter data.

4.2.2 Model setup

Before the computation using PM-FRE, several model factors (e.g., initial depth, depth limits, etc.) have to be chosen properly. The empirical rule derived from the numerical tests in Section 4.1.3.5 for choosing the initial depth and depth limits is applied here. Accordingly, the upper depth limit should be larger than the average data spacing (e.g., about 9 km in our test cases), and the lower depth limit should be smaller than the highest resolution of the reference gravity field (e.g., about 80 km in our test cases). Fig. 4.25 shows the empirical covariance function and the fitted analytical Tscherning-Rapp covariance function model (e.g., Tscherning and Rapp, 1974) for data set (a), the latter one being used in LSC. The covariance functions for the other two data sets are not shown here as they look similar to the ones for data set (a). As a result, the correlation lengths are about 0.240° , 0.238° , and 0.227° for the three data sets, resulting in an initial depth of about 15.5 km for all test cases. The chosen upper depth limit is about 0.9 times of the initial depth, and the lower depth limit is computed from Bowin's formula using $R = 6371$ km and $n = 250$, resulting in a point mass layer with the upper depth of 14 km and the lower depth of 25 km. Fig. 4.26 shows the histograms of the depths for the searched point mass RBFs in each test case. Most of the point mass RBFs are located around the depth limits (about 80% – 90%). The point mass RBFs around the lower depth limit contribute to the long-wavelength signals while the short-wavelength signals are mostly represented

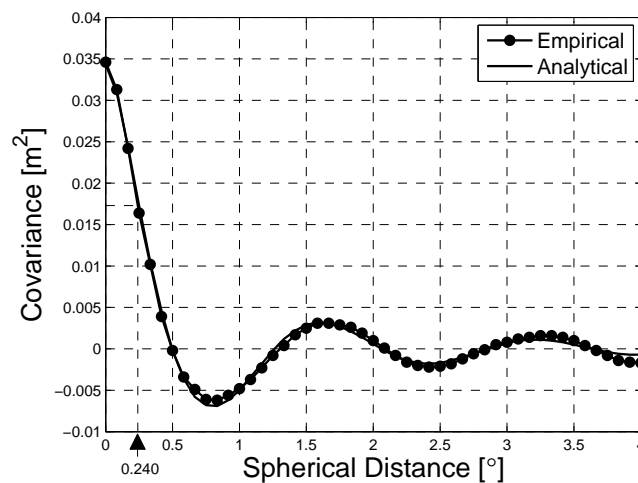


Figure 4.25: Empirical covariance function and the fitted analytical Tscherning-Rapp covariance function model for data set (a). The value of 0.240° means the correlation length of the empirical covariance function.

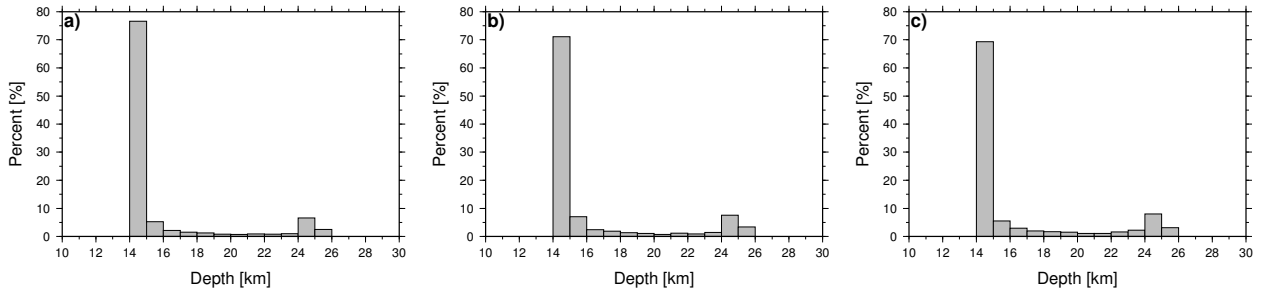


Figure 4.26: Histogram of the depths for the searched point mass RBFs in the test case **a)** with data set (a); **b)** with data set (b); **c)** with data set (c).

Table 4.22: Model setup used in the numerical tests in Section 4.2.

Spectral bandwidths of the RBFs	① Full, $N_{\min} = 0$ ② Reduced, $N_{\min} = 101$
Optimization direction	Radial-direction
Initial depth [km]	15.5
Depth limits [km]	14 – 25
Number N_{ε} of the nearest point mass RBFs	10
Total number K of point mass RBFs	3000
Iteration limit N_{it} for each new point mass RBF	20

by the RBFs close to the upper depth limit. To investigate the effect of the spectral bandwidths of the point mass RBFs when using the geoid heights as input, the full RBFs and the reduced RBFs with $N_{\min} = 101$ are compared. Most model factors used for the following computations are given in Table 4.22.

4.2.3 Determination of the regularization parameter

No regularization is applied in the second step of PM-FRE for the test case with data set (a) while Tikhonov regularization with an identity regularization matrix is applied in the other two test cases. The regularization parameters determined by the three approaches (i.e., empirical approach, GCV, and VCE) are given in Table 4.23. Obviously, the chosen parameters are nearly the same with the use of the full and reduced point mass RBFs for each approach in each test case. When the input data contain larger errors (e.g., test case (c)), a larger regularization parameter is chosen to reduce the effect of errors in the solutions. In addition, the regularization parameters α of the regularized LSC (see also Section 2.6) for test cases (b) and (c) are determined by Eq. (2.50), resulting in the values of 6.25 and 4.0, respectively.

Table 4.23: Regularization parameters obtained by three approaches associated with the full and reduced point mass RBFs for test cases (b) and (c).

Method	Test case (b)		Test case (c)	
	Full	Reduced	Full	Reduced
Empirical	3.981×10^{-13}	3.981×10^{-13}	2.512×10^{-12}	2.512×10^{-12}
GCV	1.000×10^{-14}	1.000×10^{-14}	1.000×10^{-13}	1.000×10^{-13}
VCE	2.261×10^{-13}	2.267×10^{-13}	1.311×10^{-12}	1.307×10^{-12}

4.2.4 Results and discussion

The solutions computed by PM-FRE, as well as the LSC solutions are validated by a set of control points with true values for each test case. The statistics of the modeled gravity anomaly errors are listed in Tables 4.24–4.26. It can be seen that, when the input data are error-free (see Table 4.24), the solutions of PM-FRE without regularization are close to the standard LSC solutions with an accuracy of about 1 mGal. When the input data are noisy (see Tables 4.25 and 4.26), the application of Tikhonov regularization in PM-FRE improves the solutions marginally in test case (b), i.e., with an accuracy from about 2.7 mGal to 2.5 mGal, but significant improvements can be achieved in test case (c), i.e., with an accuracy from about 5.8 mGal to 3.9 mGal. The standard LSC solutions are severely affected by the data noise (see Tables 4.25 and 4.26), indicating that the amount of smoothing defined by the noise covariance matrix \mathbf{C}_{ee} is not enough (see Eq. (2.45)). Better results can be obtained by introducing a regularization parameter $\alpha > 1$ (i.e., 6.25 and 4.0) into the regularized LSC (see Eq. (2.47)).

The performance of the three approaches for choosing a proper regularization parameter in PM-FRE is different. The regularization parameters determined by the empirical approach are the most proper among the three approaches according to the numerical results, and the ones associated with the other two approaches are smaller, meaning that the effect caused by the data noise in the solutions are larger. Furthermore, the VCE determined regularization parameters are much closer to the ones determined by the empirical approach than the GCV determined regularization parameters, resulting in better solutions (see Tables 4.23, 4.25, and 4.26). The square roots of the variance components of data sets (b) and (c) estimated by VCE are about 0.0197 and 0.0490 m, which are slightly smaller than the known data noise (i.e., 0.02 and 0.05 m), indicating that the noise in both data sets is slightly underestimated. This is the reason why the VCE determined regularization parameters are smaller than the ones derived from the empirical approach.

The use of full and reduced point mass RBFs gives similar gravity anomaly solutions in the three test cases. Comparing to the results in Section 4.1, the reason is that the modeled gravity field quantities are gravity anomalies, which are in the short-wavelength domain. The main contributions to these gravity field quantities are from the observations in the near zone. With the increase of the distance to the prediction points, the contributions of the observations decrease rapidly. Although the full point mass RBFs are always nonzero, the far zone contributions to the gravity anomalies are still negligible. Therefore, the choice of the spectral bandwidths of the point mass RBFs for regional gravity field modeling also depends on the kind of modeled gravity field quantities. If the gravity field quantities to be modeled are in the short-wavelength domain, the full point mass RBFs also work fine.

Table 4.24: Statistics of the modeled Δg errors [mGal] at 11305 control points for test case (a). The first and second lines of the solutions computed by PM-FRE correspond to the full and reduced point mass RBFs, respectively.

Method	Mean	STD	RMS	Min	Max
No regularization	-0.051	1.154	1.155	-5.396	5.472
	0.004	1.164	1.164	-5.382	5.525
Standard LSC	-0.498	0.869	1.019	-4.352	2.917

Table 4.25: The same as in Table 4.24, but for test case (b).

Method	Mean	STD	RMS	Min	Max
No regularization	-0.025	2.738	2.738	-18.649	12.760
	0.006	2.740	2.740	-19.070	12.738
Empirical	-0.027	2.481	2.481	-13.921	11.826
	0.009	2.480	2.480	-13.948	11.591
GCV	-0.039	2.675	2.675	-13.759	11.874
	0.006	2.674	2.674	-13.587	11.780
VCE	-0.031	2.492	2.492	-13.325	12.101
	0.008	2.491	2.491	-13.350	11.820
Standard LSC	-0.197	5.074	5.078	-22.375	19.196
Regularized LSC	-0.055	2.420	2.421	-10.343	9.936

Table 4.26: The same as in Table 4.24, but for test case (c).

Method	Mean	STD	RMS	Min	Max
No regularization	-0.028	5.839	5.839	-34.933	32.801
	0.012	5.840	5.840	-34.955	32.949
Empirical	-0.012	3.909	3.908	-16.886	22.329
	0.019	3.911	3.911	-16.721	22.393
GCV	-0.033	5.022	5.022	-21.940	24.289
	0.013	5.024	5.024	-21.974	24.247
VCE	-0.017	3.986	3.986	-16.395	19.138
	0.017	3.989	3.989	-16.205	19.238
Standard LSC	-0.047	5.568	5.568	-21.451	22.113
Regularized LSC	-0.005	3.596	3.596	-16.902	18.750

4.2.5 Conclusions

The performance of PM-FRE using the RCR technique has been demonstrated by three numerical test cases for gravity anomaly recovery from simulated geoid heights with different noise levels. If the model setup for PM-FRE is proper and the input data are error-free, the solutions can be achieved close to the LSC solutions. The implementation of Tikhonov regularization in the second step of PM-FRE guarantees stable solutions if ill-posedness exists. By comparing three approaches for choosing a proper regularization parameter in our test cases, the empirical approach proves to be the best, and then VCE follows. However, the empirical approach is hard to be applied in practical applications with a large amount of unknowns or in the absence of control points. Then VCE is an alternative approach. Furthermore, it also provides the variance components of the input data, which can be interpreted as a posteriori information of the data. As a consequence, VCE is preferred to find the proper regularization parameter in the following numerical tests using PM-FRE.

Although GCV gives the worst regularization parameters in our test cases, it does not mean it could not provide better regularization parameters in other applications. The solutions of the standard LSC are found to suffer from the data noise. Therefore, a regularization parameter $\alpha > 1$ is required to further reduce the effect of the data noise in the solutions, resulting in the best results for test cases (b) and (c). The regularized LSC could be a complement to the standard LSC; however, it will not be further discussed as it is out of the scope of this thesis.

4.3 Tests with a set of synthetic geoid heights with different accuracies

This numerical test is a continuation of the test cases presented in Section 4.2. The main goal now is to investigate the performance of PM-FRE for dealing with the case of two data groups with the same data type but different accuracies. The main focus is on the first step of PM-FRE for searching for the point mass RBFs. In the case of a single data type with the same accuracy, each new point mass RBF is searched for by placing it below the observation point with $\max |\sqrt{\mathbf{P}_e} [\mathbf{1} - F(\mathbf{m}')]|$, in which $\mathbf{P}_e = \mathbf{I}$ (see also Fig. 3.8). However, \mathbf{P}_e should be a non-identity diagonal matrix in the case of a single data type with different accuracies. Two issues will be discussed. One is that, if the accuracy of two input data sets is known, whether the use of a related diagonal weight matrix \mathbf{P}_e for finding the point mass RBFs in the first step can help to improve the solution. If the answer is positive, what to do if the data accuracy is unknown. In this case, the key question is how to properly get the weight matrix \mathbf{P}_e . To solve this problem, an iterative procedure is proposed based on VCE as it can provide a posteriori information on the input data sets. This procedure is outlined as follows:

- ① Iteration 1: The weight matrix $\mathbf{P}_e = \mathbf{I}$ is used for the computations in the first step of PM-FRE. After obtaining the positions of all selected point mass RBFs, the second step of PM-FRE is implemented by using VCE, with which the variance component for each data group can be obtained.
- ② Iteration i ($i \geq 2$): A new non-identity diagonal weight matrix \mathbf{P}_e , which is derived from the variance components provided in Iteration $i - 1$, is used for the modeling, resulting in a new set of variance components. If the new variance components are close to the old ones, then stop the whole procedure, and the current solution is regarded as the final solution. Otherwise, let $i = i + 1$ and repeat ②.

With the use of a non-identity diagonal weight matrix in the search process, more point mass RBFs are to be located below the data points with higher accuracy. In the following, simple tests using two groups of synthetic geoid heights will be conducted to discuss the above two issues.

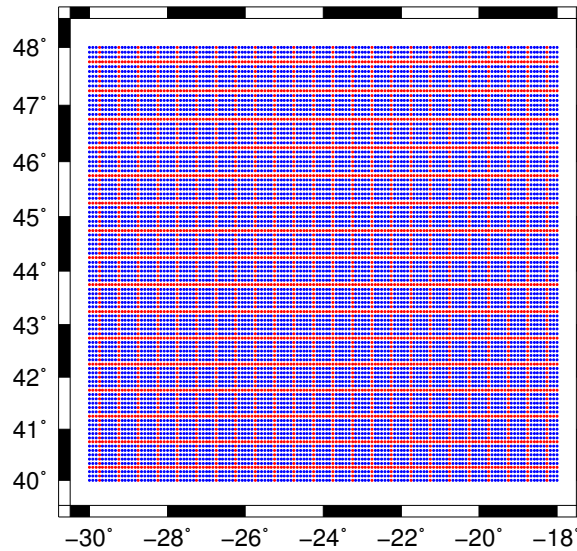


Figure 4.27: Distribution of 9801 data points (*blue*) for group (1) and 4264 points (*red*) for group (2).

4.3.1 Data description

The original synthetic data set is based on the data set (a) used in Section 4.2. The only difference is that the total 14065 data points are divided into two groups: (1) a group with 9801 data points, contaminated by white noise with an STD of 0.02 m and (2) a group of 4264 data points with an accuracy of 0.05 m. Fig. 4.27 shows the point distribution of the two data groups. As can be seen, each data group has a homogeneous distribution. For the other information about the input data, we refer to the description in Section 4.2.1.

4.3.2 Solutions of PM-FRE

The model factors used in this numerical test are almost the same as the ones in Table 4.22 except that only the full point mass RBFs are used. To compare the solution of using an identity weight matrix for finding the point mass RBFs in the first step and to assess the proposed iterative procedure in assuming that the accuracy of the two data sets is unknown, the solution computed by using the diagonal weight matrix derived from the exact accuracy of the two data sets is taken as reference. The statistics of the modeled gravity anomaly errors for the reference solution and the solutions within the first three iterations are given in Table 4.27. It should be noted that the identity weight matrix is employed in the solution of the first iteration. The results show that: (1) the use of exact

Table 4.27: Statistics of the modeled Δg errors [mGal] at 11305 control points associated with different solutions.

Solution	Mean	STD	RMS	Min	Max
Reference	-0.030	2.728	2.728	-12.830	14.021
Iteration 1	-0.024	2.994	2.994	-14.747	18.332
Iteration 2	-0.021	2.751	2.751	-12.020	14.580
Iteration 3	-0.024	2.726	2.726	-12.732	13.136

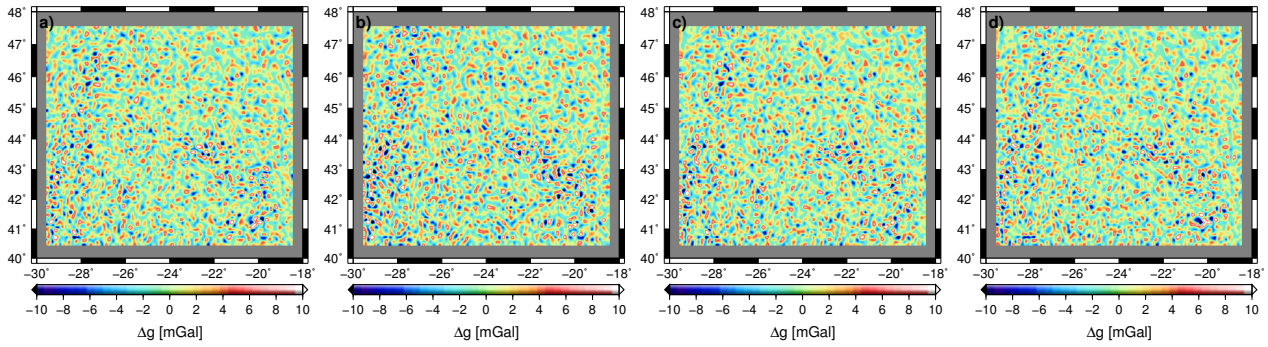


Figure 4.28: Errors of the modeled Δg at 11305 control points associated with different solutions; **a)** Reference; **b)** Iteration 1; **c)** Iteration 2; **d)** Iteration 3.

Table 4.28: Square roots of estimated variance components [m] for the two data groups associated with different solutions.

	True	Reference	Iteration 1	Iteration 2	Iteration 3
group (1)	0.0200	0.0199	0.0219	0.0202	0.0200
group (2)	0.0500	0.0493	0.0472	0.0487	0.0491

data weights in the search process improves the gravity anomaly solutions. A reduction of the RMS error of about 0.3 mGal in comparison to the case of using an identity weight matrix is observed (see ‘Reference’ and ‘Iteration 1’ in Table 4.27); (2) the solution similar to the one using the exact weight matrix can be obtained within three iterations, the resulting RMS error is about 2.73 mGal. Fig. 4.28 shows the gravity anomaly errors at the control points for different solutions. The residuals become slightly smoother from the solutions of Iteration 1 to Iteration 3 (see Figs 4.28b–4.28d), and similar error patterns can be observed between the solution of Iteration 3 (see Fig. 4.28d) and the reference solution (see Fig. 4.28a). From another aspect, the feasibility of the proposed iterative procedure for dealing with a single data type with different accuracies can also be demonstrated by the square roots of estimated variance components, which are presented in Table 4.28. The estimated variance components of the two data groups related to the reference solution and the solution of Iteration 3 are very close to the true values.

4.3.3 Conclusions

A simple iterative procedure is proposed and demonstrated to be capable of providing reasonable solutions in the case when two (or more) data groups with the same data type but different accuracies are used as input. It mainly benefits from the VCE technique, which can deliver the variance component of each data group to help for the modification of the search process in the first step of PM-FRE. In this test, the iterative solution obtained within three iterations seems to be sufficient. However, more iterations could also be carried out but requiring more computation time.

4.4 Tests with synthetic terrestrial and airborne gravity disturbances

4.4.1 Data description

Recently, a set of synthetic gravity field observations representing data from terrestrial, airborne, and satellite sensors are provided by the Joint Study Group (JSG0.3) of IAG for the comparison of current methodologies in regional gravity field modeling in two test regions. One is in Europe (EU) and the other is in South America (SA). This benchmark data set is publicly available (<http://jsg03.dgfi.badw.de>) and free for all interested researchers to test and validate their modeling approaches. In this section, terrestrial gravity disturbances with a fine $5' \times 5'$ grid and airborne gravity disturbances are used for testing the point mass method PM-FRE. Both data sets are simulated from the EGM2008 model up to d/o 2190 by adding white noise with a standard deviation of 0.01 mGal to the error-free terrestrial data and a standard deviation of 1 mGal to the airborne data. All results are compared with validation data sets (i.e., disturbing potentials T synthesized from the EGM2008 model up to d/o 2190) on geographic grids on the surface of the topography. The validation data grids have the same grid spacing as the terrestrial observation grids, but are shifted for half the spacing. Two flight campaigns are available in the EU test area, we only choose the one over the Adriatic Sea (i.e., flight_A) as it mostly overlaps the test region. The location of the data points is shown in Fig. 4.29. For more details about the data sets, we refer to the information given on the above-mentioned website.

With the RCR technique, the residuals obtained by removing the long-wavelength components computed from the EGM2008 model up to d/o 250 are used as input for the modeling. No topography reduction is applied due to the synthetic data. The statistics of the global model-derived and residual gravity disturbances δg in the two test areas are summarized in Table 4.29. As can be seen, rough residual gravity field features are presented in both test areas.

4.4.2 Solution of PM-FRE using terrestrial data only

The initial depth of the point mass RBFs are chosen to be 19.0 km for the EU test case and 14.0 km for the SA test case on the basis of the empirical covariance functions of the observations. According

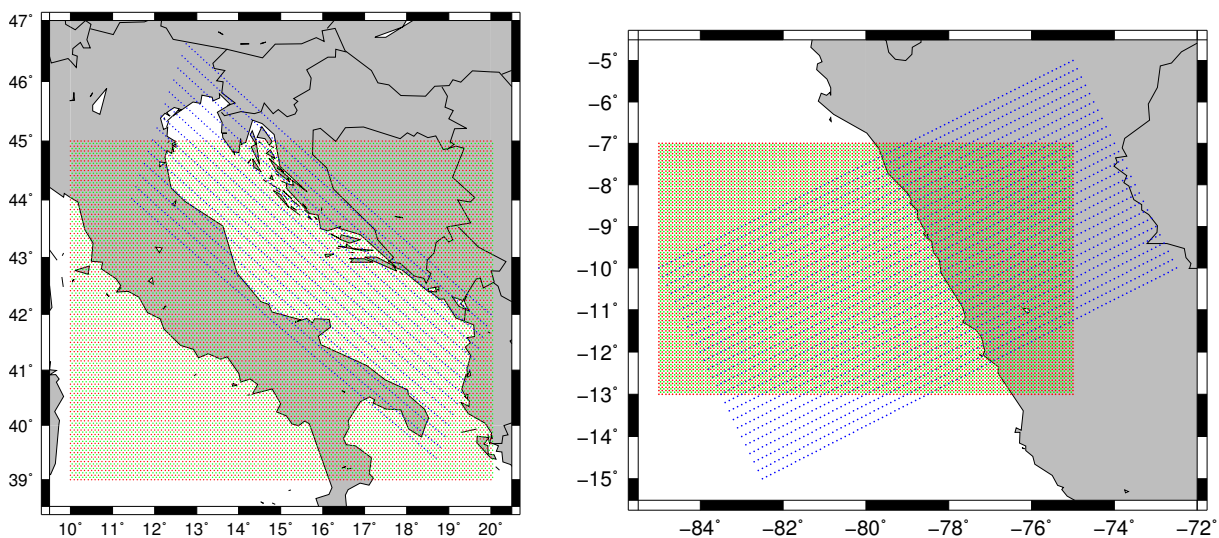


Figure 4.29: Distribution of the input terrestrial (*red*, 8833 points for both EU and SA), airborne (*blue*, 1484 points for EU and 2626 points for SA) gravity disturbances (δg), and of the terrestrial disturbing potentials (T) (*green*, 8712 points for EU and 8640 points for SA) for the validation in the study areas of Europe (*left*) and South America (*right*).

Table 4.29: Statistics of global model-derived terrestrial δg_{ter}^M , airborne gravity disturbances δg_{air}^M , and residual terrestrial δg_{ter}^R , airborne gravity disturbances δg_{air}^R [mGal].

Area	Obs	Mean	STD	RMS	Min	Max
EU	δg_{ter}^M	-25.130	41.661	48.652	-148.592	102.796
	δg_{ter}^R	0.498	25.186	25.189	-133.343	102.485
	δg_{air}^M	-11.611	36.767	38.545	-99.767	67.928
	δg_{air}^R	0.002	20.065	20.059	-83.103	64.464
SA	δg_{ter}^M	-7.005	62.379	62.773	-183.091	137.120
	δg_{ter}^R	1.332	34.621	34.645	-188.716	217.019
	δg_{air}^M	-5.662	54.138	54.423	-176.741	123.109
	δg_{air}^R	-0.297	24.269	24.266	-143.996	130.880

to the empirical rule described in Section 4.1.3.5, the upper depth limit is not shallower than 9 km and the lower depth limit is not deeper than 80 km for both test cases. Here, the upper depth limit is chosen to be about 0.8 times of the initial depth and the lower depth limit is about 2 times of the initial depth. The resulting upper and lower depth limits are 15.0 km and 35.0 km for the EU test case, and 11.0 km and 30.0 km for the SA test case.

4.4.2.1 Number of point mass RBFs

Principally, we could determine the number of RBFs by achieving the target data misfit of 0.01 mGal that is derived from the accuracy of the terrestrial data. In practice, this target misfit can not be achieved even if the number of selected RBFs is the same as the number of data points. Alternatively,

Table 4.30: RMS of the fit to observed δg [mGal] and true T [m^2/s^2] for different numbers of point mass RBFs.

Number	EU		SA	
	δg	T	δg	T
500	9.820	0.879	12.057	1.555
1000	6.616	0.548	7.080	0.835
1500	4.888	0.432	4.727	0.504
2000	3.656	0.371	3.332	0.332
2500	2.917	0.336	2.621	0.280
3000	2.381	0.318	2.228	0.260
3500	1.948	0.303	1.965	0.251
4000	1.639	0.292	1.840	0.245

Table 4.31: RMS of the fit to observed δg [mGal] and true T [m²/s²] for different values of N_{\min} .

N_{\min}	EU		SA	
	δg	T	δg	T
0	2.273	4.788	1.872	1.447
51	2.288	0.900	1.875	0.942
101	2.297	0.552	1.907	0.443
151	2.347	0.361	1.928	0.296
201	2.381	0.318	1.965	0.251
251	2.579	0.292	2.198	0.282
261	3.160	0.488	2.910	0.488

the search process is terminated by finding a predefined number of RBFs. For all comparisons, $N_{\min} = 201$ is used and VCE is applied for choosing proper regularization parameter. The RMS of the fit to the observations (i.e., terrestrial gravity disturbances δg) and validation points (i.e., ground true disturbing potentials T) for different numbers of point mass RBFs are given in Table 4.30. When increasing the number of used point mass RBFs, the fit to both the observed gravity disturbances and true disturbing potentials becomes better. The best fit to the disturbing potentials is found with the use of 4000 RBFs, leading to the RMS error of 0.292 m²/s² for the EU test area and 0.245 m²/s² for the SA test area. Furthermore, we also find that the decrease of the RMS errors becomes quite slow when the number of RBFs reaches 3000. As a result, 3000 point mass RBFs will be used in the EU test case and 3500 RBFs in the SA test case.

4.4.2.2 Spectral bandwidths of the point mass RBFs

In Section 4.4.2.1, the number of point mass RBFs in the modeling has been fixed through numerical comparisons. In the following, we are going to select a proper N_{\min} with which a good fit to the disturbing potentials at validation points can be achieved. Seven candidates have been tested, and the related RMS of the fit is presented in Table 4.31. As expected, the use of $N_{\min} = 0$ provides the worst fit to the disturbing potentials due to the long-wavelength domain of the disturbing potential. With increasing of N_{\min} , the fit to the disturbing potentials becomes better; however, the fit to the terrestrial gravity disturbances becomes poorer. The best fit of the disturbing potentials is obtained when $N_{\min} = 251$ for the EU test case and $N_{\min} = 201$ for the SA test case. Therefore, the optimal N_{\min} is chosen as 251 for the EU test case and 201 for the SA test case.

4.4.2.3 Comparison of PM-FRE and LSC

The goal of this section is to compare PM-FRE and LSC for the modeling of disturbing potential using terrestrial gravity disturbances. According to the findings in Sections 4.4.2.1 and 4.4.2.2, the model factors for PM-FRE is summarized in Table 4.32. The LSC approach is implemented by the **GRAVSOFT** package (Tscherning et al., 1992).

The statistics of the differences between the modeled and true disturbing potentials T at the control points are presented in Table 4.33. The disturbing potential errors at the control points are also illustrated in Fig. 4.30. In both test cases, both methods provide comparable results in terms of RMS

Table 4.32: Model setup used for the numerical tests in Section 4.4.2.3.

Model factors	EU test case	SA test case
Spectral bandwidths of the RBFs	$N_{\min} = 251$	$N_{\min} = 201$
Optimization direction	Radial-direction	
Initial depth [km]	19.0	14.0
Depth limits [km]	15.0 – 35.0	11.0 – 30.0
Number N_{ε} of the nearest point mass RBFs	10	
Total number K of point mass RBFs	3000	3500
Iteration limit N_{it} for each new point mass RBF	20	

Table 4.33: Statistics of the residual disturbing potentials T [m^2/s^2] at the control points computed from two methods for the two test cases.

Method	EU					SA				
	Mean	STD	RMS	Min	Max	Mean	STD	RMS	Min	Max
PM-FRE	-0.010	0.292	0.292	-3.068	2.664	0.003	0.251	0.251	-2.763	2.235
LSC	-0.002	0.367	0.367	-3.027	4.335	-0.017	0.253	0.254	-3.510	1.767

errors of the disturbing potentials at ground. PM-FRE allows a better approximation than LSC. In the EU test case, the main differences between PM-FRE and LSC are in the edge of the research area (Figs 4.30a and 4.30b), and larger errors can be found for the latter. In the SA test case, the main differences appear in the coastal area and inland (Figs 4.30c and 4.30d).

4.4.3 Solution of PM-FRE using both terrestrial and airborne data

In Section 4.4.2, we have discussed the results computed by PM-FRE using terrestrial data only and also compared the results to LSC. A better performance of PM-FRE can be found. Therefore, only this approach is applied to the modeling using both terrestrial and airborne data in this section.

In each test case, three solutions are computed based on different schemes for finding the point mass RBFs in the first step. The three solutions are specified as follows:

- EU-I: In this solution, only the terrestrial δg are used for finding the point mass RBFs in the first step; however, both terrestrial and airborne δg are used for the readjustment in the second step.

- EU-II: Both terrestrial and airborne δg are used for the modeling. The point mass RBFs are searched for with the use of exact data weights.
- EU-III: The same as EU-II, but using the iterative procedure to generate the data weights for finding the point mass RBFs in the first step. The solution after three iterations is presented.
- SA-I, SA-II, and SA-III are the same as EU-I, EU-II, and EU-III, but for the South America test case.

For all solutions, VCE is applied to determine the proper regularization parameter as well as the weights for the two data sets in the second step of PM-FRE. For the solutions in the EU test case, the number of point mass RBFs is specified as 3000, which is the same as the case in Section 4.4.2. Similarly, 3500 point mass RBFs are to be selected for the modeling in the SA test case. Since both terrestrial and airborne data are used for finding the point mass RBFs in EU/SA-II and EU/SA-III, the initial depths derived from the empirical covariance functions of both data sets are a little different from the ones in Section 4.4.2, yielding the value of 20.0 km for the EU test case and 14.5 km for the SA test case. Accordingly, we choose the depth limits of 15.0 – 40.0 km for the EU test case and 11.0 – 40.0 km for the SA test case. Comparing to the depth limits in Section 4.4.2, the upper depth limit remains the same but with a deeper lower depth limit in each test case. The reason is that we believe that the short-wavelength signals can be fully provided by the terrestrial data, and hence the upper depth limits are the same as the ones used in Section 4.4.2, which proved to be able to provide good solutions. The choice of deeper lower depth limits is that we expect that the adding of airborne data can provide more regional information, which can be well represented by deeper RBFs.

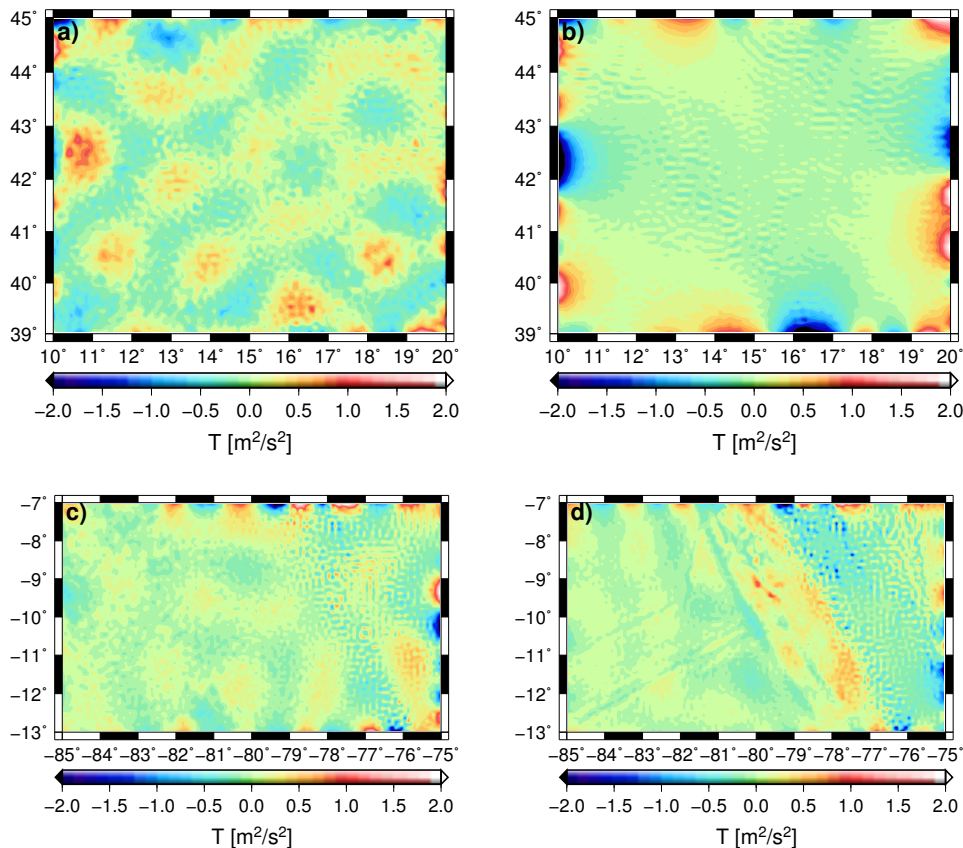


Figure 4.30: Errors of the modeled disturbing potentials associated with two regional methods at 8712 control points for the EU test case: a) PM-FRE; b) LSC; and at 8640 control points for the SA test case: c) PM-FRE; d) LSC.

Table 4.34: RMS of the fit to observed terrestrial δg^T and airborne δg^A [mGal], as well as to true T [m²/s²] for different solutions.

Solution	EU			SA		
	δg^T	δg^A	T	δg^T	δg^A	T
I	2.584	6.304	0.288	1.970	8.060	0.241
II	2.838	4.907	0.307	2.297	4.705	0.210
III	2.819	1.389	0.292	2.367	1.026	0.199

Table 4.34 gives the RMS of the fit to the observations and the validation values for different solutions. Comparing to the solutions in Table 4.33 (see PM-FRE), almost no improvements of the combined solutions can be found in the EU test case while slightly better solutions are obtained in the SA test case. The main reason can be attributed to the fact that the terrestrial data points are homogeneously distributed over the test region and the airborne data area overlaps the terrestrial data area very much (see Fig. 4.29). In the EU test case, the use of two data sets in the search process (EU-II and EU-III) provides a slightly poorer fit to the disturbing potentials than using terrestrial data only (EU-I). In the SA test case, SA-II and SA-III have better fit to the disturbing potentials than SA-I. From the RMS of the fit to the observations we may get some useful information to explain why the combined solutions behave differently. For the first solution, the chosen point mass model fits to the terrestrial data quite well, but much poorer to the airborne data. It is because all point mass RBFs are selected based on the terrestrial data. The combined solutions are mostly dominated by the terrestrial data, yielding the RMS fit to the disturbing potentials close to the ones in Table 4.33. Because of the use of both data sets in the search process for the second and third solutions, the fit to the airborne data is much better than the first solution, but worse to the terrestrial data. The best fit to the airborne data is provided by the third solution using the iterative procedure. The reason is that the accuracy of both data sets is assumed to be the same in Iteration 1 and the airborne data are smoother than the terrestrial data. As a consequence, a better fit to the airborne data is achieved by using VCE, resulting in a smaller variance component for the airborne data. And hence, a larger weight is assigned to the airborne data in the following iterations. Finally, a good fit to the airborne data is achieved. In general, the combined disturbing potential solution with an RMS error of about 0.3 m²/s² can be calculated using PM-FRE for the EU test case and about 0.2 m²/s² for the SA test case. The disturbing potential errors at the control points are illustrated in Fig. 4.31. In each test case, the error patterns for the three solutions look quite similar. Comparing to the error patterns in Figs 4.30a and 4.30c, the adding of airborne data does not help to improve the disturbing potential solution in the EU test case as also shown in Table 4.34. The errors in the edge area are slightly reduced in the SA test case, especially in the northeast corner (Fig. 4.30c vs. Figs 4.31d–4.31f). It is because some point mass RBFs are selected around this corner due to the availability of airborne data points (see also Fig. 4.29).

4.4.4 Conclusions

In this section, the point mass method PM-FRE has been applied to model the disturbing potential at ground using synthetic terrestrial and airborne gravity disturbances in two test areas, Europe and South America, both with rough gravity field features. The method PM-FRE is implemented based on the “optimal” strategy given in Section 4.1.5, in which VCE is used for choosing the proper reg-

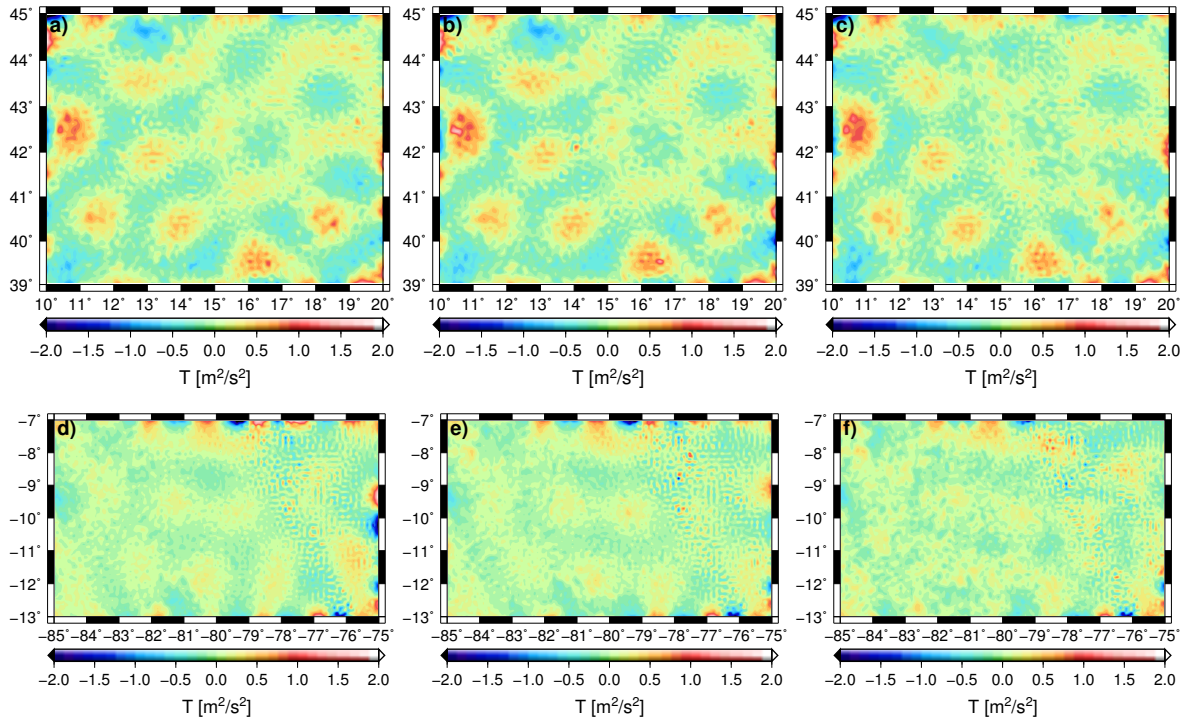


Figure 4.31: Errors of the modeled disturbing potentials at 8712 control points for the EU test case and 8640 control points for the SA test case; a) EU-I; b) EU-II; c) EU-III; d) SA-I; e) SA-II; f) SA-III.

ularization parameter and combining different data sets in the second step. When using terrestrial data only as input, a comparison between PM-FRE and LSC is carried out. The numerical results show the better performance of PM-FRE than LSC. The RMS error of the modeled disturbing potential at ground is about $0.3 \text{ m}^2/\text{s}^2$ for the EU test case, and about $0.25 \text{ m}^2/\text{s}^2$ for the SA test case. Furthermore, an iterative procedure based on VCE is applied for finding the point mass RBFs using both terrestrial and airborne gravity disturbances. Three solutions, which use different schemes for finding the point mass RBFs in the first step, are computed and analyzed in each test case. A good agreement between them can be obtained, with the RMS error of about $0.3 \text{ m}^2/\text{s}^2$ for the EU test case and about $0.2 \text{ m}^2/\text{s}^2$ for the SA test case.

In the case of several data groups with the same data type but different accuracies (assuming each data group corresponds to one accuracy), two cases will be encountered: (1) the number of the data points for one group is much larger than the total number of the other groups and (2) each group has a similar number of data points. In the first case, we recommend using only the group with the largest number of data points for searching for the point mass RBFs in the first step, then all data groups are used for the combination in the second step with the help of VCE. In the second case, it is necessary to use all data points for the regional modeling (in both first and second step of PM-FRE). The iterative procedure based on VCE can be applied, with which the point mass RBFs can be selected based on data accuracy. It is also worth mentioning that, when using several data groups with different data types and one group possesses most of the data points, the same process as in the above-mentioned Case (1) can be applied. For quasigeoid modeling by using gravity and GPS/leveling data, the input data are always dominated by the gravity anomalies. Therefore, in most cases, only the gravity anomalies are used for finding the point mass RBFs in the first step. Then, the two different kinds of gravity field quantities are combined in the second step.

4.5 Tests with a large-scale real data set in the Auvergne area

Finally, we apply PM-FRE to a large-scale real gravity data set over the Auvergne area. The modeled gravity and height anomalies are compared with independently observed values with high accuracy. The combination of gravity and GPS/leveling data is also discussed.

4.5.1 Data and preprocessing

The Auvergne data set was provided in 2008 by the Institut Géographique National (IGN), France. The gravity data are used as a “ground truth” example for testing geoid computation methods (Duquenne, 2007). There are about 244000 gravity data (Δg) points from the Bureau Gravimétrique International (BGI), covering an area with the extent of -1°E to 7°E and 43°N to 49°N ; a DTM based on 3'' Shuttle Radar Topography Mission (SRTM) height data (version 3) covering a somewhat larger area (-2°E to 8°E , 42°N to 50°N); and a set of 75 GPS/leveling points.

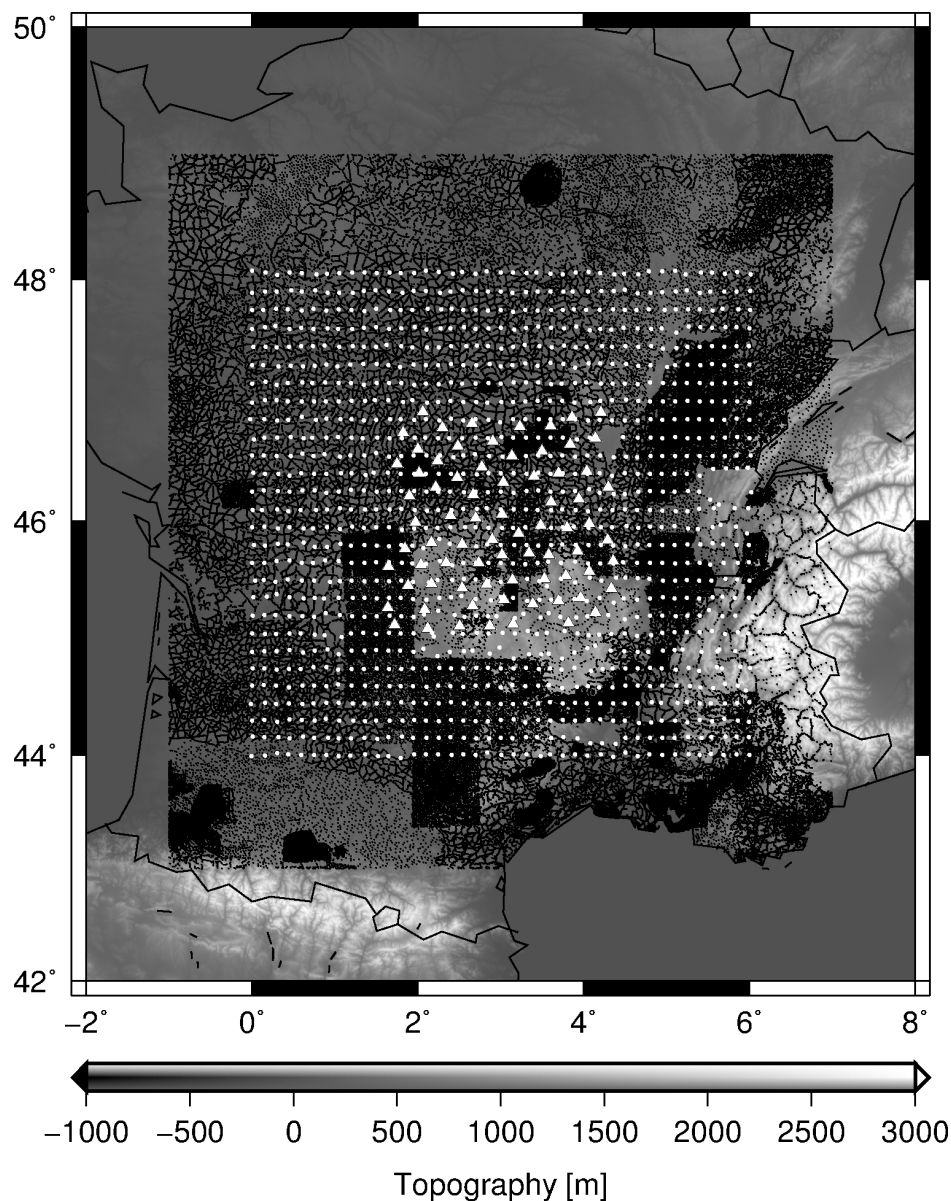


Figure 4.32: Location of 242809 Δg observations (*black dots*), 1145 Δg control points (*white circles*), and 75 GPS/leveling points (*white triangles*) in the Auvergne area, France. The background shows the topography of the test area.

The distribution of the gravity data is quite homogeneous, except in the most mountainous areas and in a few isolated regions (south of Auvergne, see Fig. 4.32). Although the gravity data are checked by BGI, some points obviously are still wrong. After deleting these erroneous points, 243954 points are used for the modeling in this numerical test, in which 242809 points are selected as input, and the remaining 1145 points are taken as control points to assess the modeled gravity anomalies (see Fig. 4.32). The accuracy of the gravity anomalies is evaluated as 0.25–0.75 mGal. But in the case of using residual anomalies it can be worse, up to 1 or 2 mGal (Duquenne, 2007). Considering the accuracy of about 2 cm for the precise leveling measurements and about 2–3 cm for the ellipsoidal heights (Duquenne, 2007), an accuracy of about 2.8–3.6 cm for the GPS/leveling-derived height anomalies can be attained through error propagation with the assumption that the errors are uncorrelated. For a more detailed description of the Auvergne data set, we refer to Duquenne (2007).

In practical computations, the long-wavelength contributions of the gravity field, which are modeled by the EGM2008 model up to d/o 360, and the topographic corrections, which are integrated up to a radius of 10 km for the dense $3'' \times 3''$ DTM and 200 km for the coarse $30'' \times 30''$ DTM with respect to the reference $30' \times 30'$ DTM, are removed from the original input data. The residuals are used to compute (1) the predictions at the control points and (2) a $1' \times 1'$ grid (0°E to 6°E , 44°N to 48°N) of gravity anomalies and height anomalies (i.e., a gravity anomaly model and a quasigeoid model). Table 4.35 summarizes the statistics of the gravity anomalies (Δg : free-air, Δg_{EGM08} : from EGM2008, Δg_{RTM} : from RTM, Δg_{res1} : $\Delta g - \Delta g_{EGM08}$, Δg_{res2} : $\Delta g_{res1} - \Delta g_{RTM}$) and height anomalies (ζ : original, ζ_{EGM08} : from EGM2008, ζ_{RTM} : from RTM, ζ_{res1} : $\zeta - \zeta_{EGM08}$, ζ_{res2} : $\zeta_{res1} - \zeta_{RTM}$).

4.5.2 Gravimetric solutions

The computation procedure is the same as in the previous numerical tests. The employed point mass search model is SMA. First, the initial depth of the point mass RBFs is derived from the empirical covariance function of the input gravity residuals, resulting in the value of 16 km. Second, the depth limits are determined based on the empirical rule described in Section 4.1.3.5. Accordingly, the shallowest upper depth limit is limited to 2 km, and the deepest lower depth limit is set to 55 km. Here, the upper and lower depth limits are chosen to be about 0.875 and 3 times of the initial depth,

Table 4.35: Statistics of the gravity anomalies [mGal] and height anomalies [m].

	Mean	STD	RMS	Min	Max
Δg	3.066	20.697	20.922	-127.459	177.841
Δg_{EGM08}	7.788	18.686	20.244	-45.761	125.033
Δg_{res1}	-4.722	16.276	16.947	-206.735	91.440
Δg_{RTM}	-6.115	15.327	16.502	-179.018	90.691
Δg_{res2}	1.394	9.544	9.645	-49.426	72.054
ζ	49.550	1.473	49.571	46.774	52.147
ζ_{EGM08}	49.659	1.466	49.680	47.049	52.455
ζ_{res1}	-0.109	0.172	0.203	-0.537	0.272
ζ_{RTM}	0.083	0.197	0.212	-0.247	0.562
ζ_{res2}	-0.192	0.185	0.266	-0.605	0.108

Table 4.36: Model setup used for the numerical tests in the Auvergne area.

Spectral bandwidths of the RBFs	① $N_{\min} = 51$ (unconstrained solution) ② $N_{\min} = 0$ and $n' = 40$ (constrained solution)
Optimization direction	Radial-direction
Initial depth [km]	16
Depth limits [km]	14 – 50
Number N_ε of the nearest point mass RBFs	10
Total number K of point mass RBFs	10000
Iteration limit N_{it} for each new point mass RBF	20

resulting in the values of 14 km and 50 km, respectively. Third, the spectral bandwidths of the RBFs are chosen. For the unconstrained solutions, $N_{\min} = 51$ is selected after various tests. For the constrained solutions, the full point mass RBFs are employed while n' is chosen to be 40 (see Eq. (3.11)). Fourth, as the accuracy of the input gravity residuals is assumed to be about 1–2 mGal, the searching for the point mass RBFs is set to be terminated after reaching the target data misfit of 1 mGal. If the target data misfit can not be achieved with a maximum number of 10000 point mass RBFs, then the search process is stopped. The reason why the number of RBFs is limited to 10000 is that the data fit to the input data is very close to the target data misfit. In this case, the data misfit is 1.136 mGal for 10000 RBFs and 1.044 mGal for 20000 RBFs. Obviously, the former choice is better when considering the numerical complexity. Tikhonov regularization is applied for all computations in the second step of PM-FRE, and the regularization parameter is determined by VCE. The detailed model setup is given in Table 4.36.

On the basis of the above model setup, 10000 point mass RBFs are found and positioned in the defined single layer. The depth histogram and the horizontal distribution of these point mass RBFs are shown in Fig. 4.33. Most of the searched RBFs are located around the upper depth limit while only a small part of them are near the lower depth limit. This is because a large amount of shallow point mass RBFs are needed to represent the high-frequency gravity field signals, while only a small number of deep RBFs are required for approximating the long-wavelength signals. The horizontal distribution of the RBFs shows a high correlation to the topography, or equivalently, to the roughness of the gravity field. In the areas with rough features (i.e., rough topography), the point mass RBFs are dense, whereas the RBFs are sparsely distributed in the areas with smooth features (i.e., flat topography).

With the use of the point mass RBFs with known positions, two solutions are computed in the second step of PM-FRE, i.e., the unconstrained solution and the constrained solution. Both are validated by comparing to the observed values at the control points, and the statistics of the differences are presented in Table 4.37. The RMS of the gravity anomaly errors is about 1.2 mGal for both solutions, where the unconstrained solution is slightly better than the constrained one. From the gravity anomaly errors illustrated in Fig. 4.34, a good agreement between the two solutions can be seen except for the

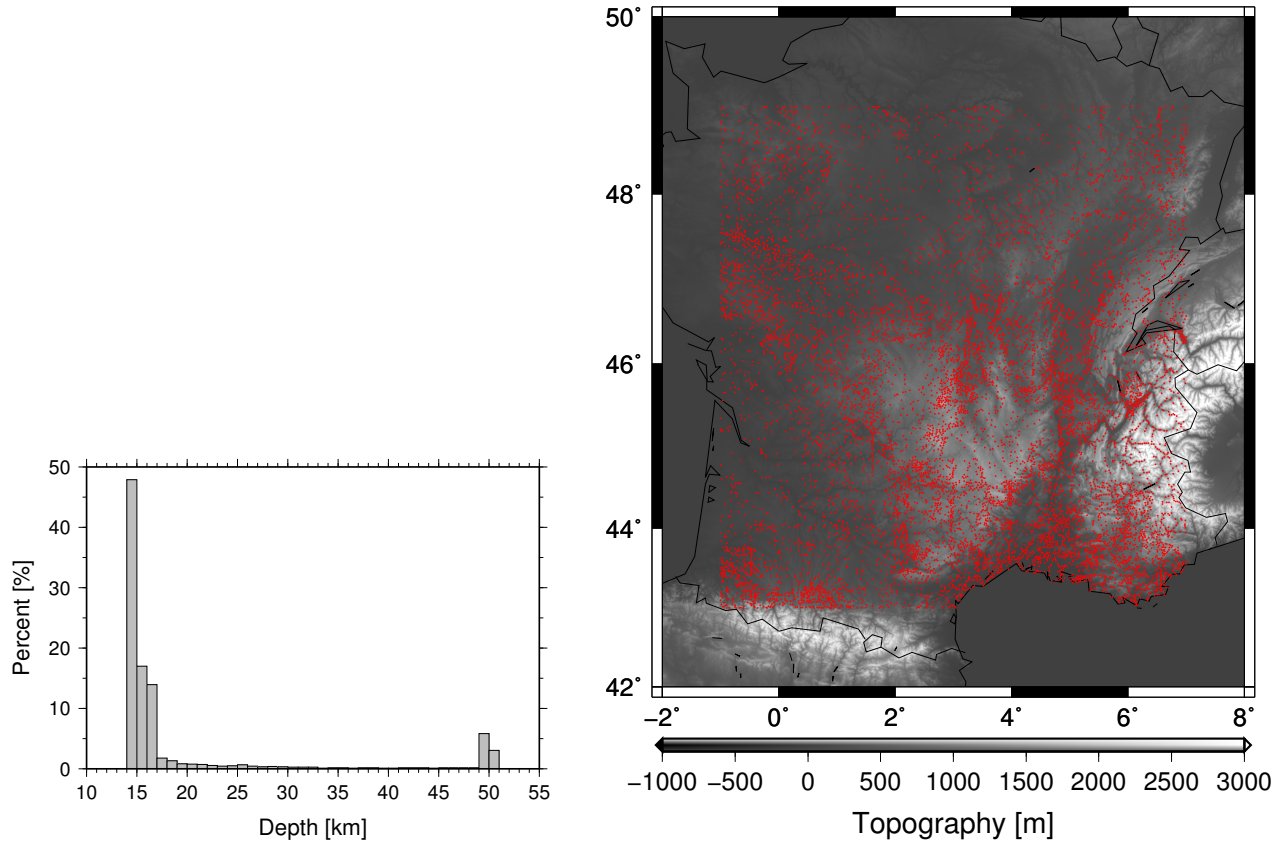


Figure 4.33: Depth histogram (*left*) and horizontal distribution (*right*) for 10000 searched point mass RBFs.

points located near the center of (3°E , 45°N), where only a small number of gravity observations are available (see Fig. 4.32). The largest errors for the two solutions are observed at the same points, which are located in the Alps area around the point of (5.5°E , 45°N). The STD of the height anomaly errors is about 0.035 m for the two solutions, and close to the results presented in Ågren et al. (2009). A mean difference of -0.182m for the unconstrained solution and -0.165m for the constrained solution are observed, indicating the inconsistency between the gravimetric and GPS/leveling-derived height anomalies. Due to the biases, the height anomaly errors at the GPS/leveling points with the removal of the mean errors are shown in Fig. 4.35 so that some useful information is visible. It clearly shows that most height anomaly errors are in the range between -0.1m and 0.1m if the biases are

Table 4.37: Statistics of the differences between the predicted and observed values at the control points, i.e., 1145 observed gravity anomalies [mGal] and 75 GPS/leveling-derived height anomalies [m], for unconstrained (*first two lines*) and constrained solutions (*second two lines*).

	Mean	STD	RMS	Min	Max
Δg	0.048	1.190	1.191	-6.625	17.412
ζ	-0.182	0.034	0.185	-0.255	-0.069
Δg	0.078	1.239	1.241	-6.802	17.589
ζ	-0.165	0.035	0.169	-0.247	-0.070

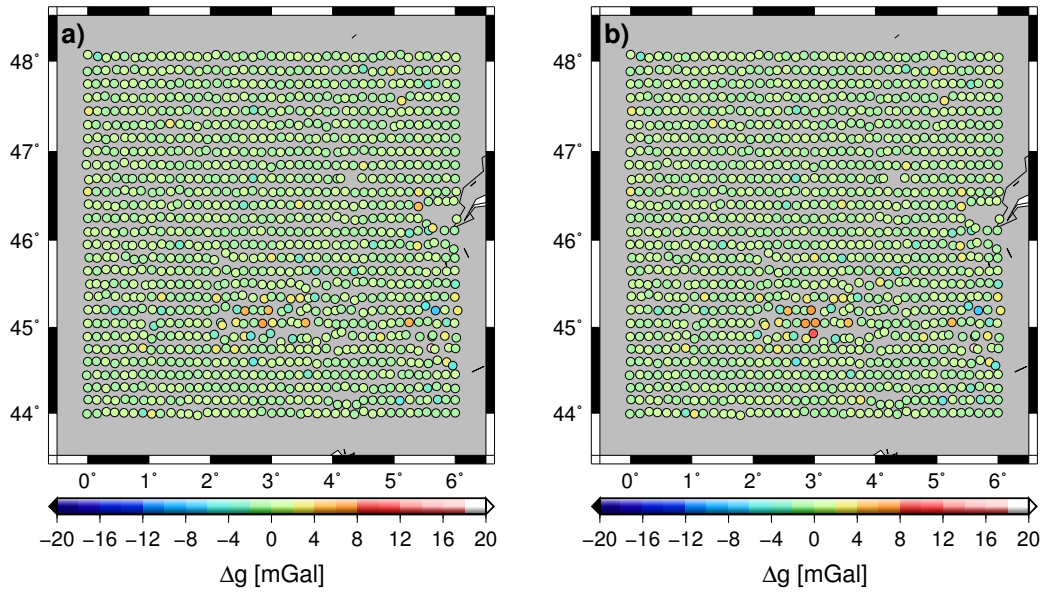


Figure 4.34: Gravity anomaly errors at 1145 control points associated with **a)** the unconstrained solution and **b)** the constrained solution.

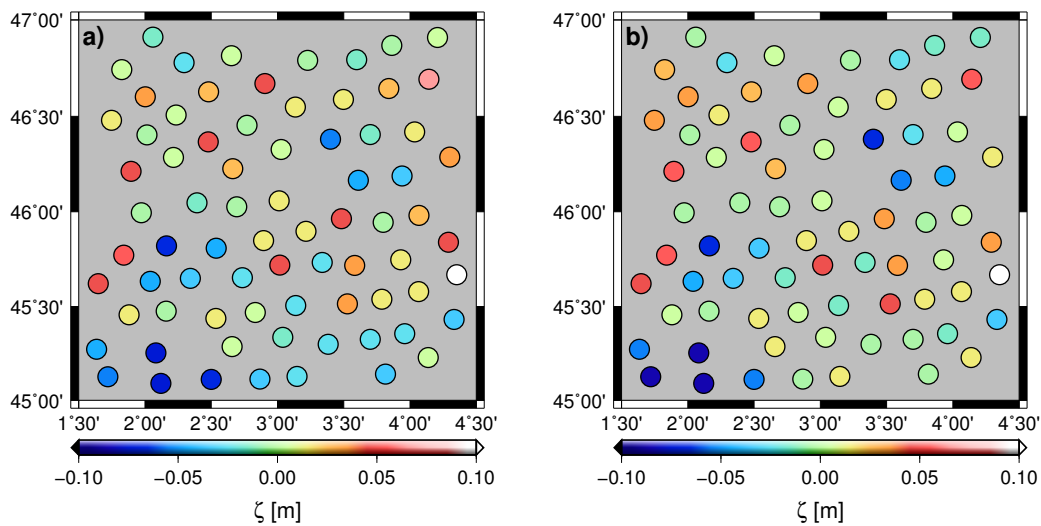


Figure 4.35: Height anomaly errors at 75 GPS/leveling points associated with **a)** the unconstrained solution with the removal of the mean of -0.182 m and **b)** the constrained solution with the removal of the mean of -0.165 m.

removed. The largest errors for both solutions are at the same points, located in the southeast of the region covered by the GPS/leveling points. Comparing the error distribution for both gravity and height anomalies (Figs 4.34 and 4.35) to the input data locations in Fig. 4.32, large errors can be seen in the area with sparse observations, indicating the importance of using homogeneous input data to compute high-quality regional gravity field models.

Based on the estimated point mass RBFs, a $1' \times 1'$ grid of gravity anomalies and height anomalies on the Earth's surface associated with the two solutions are computed and shown in Fig. 4.36, so are the differences between them. The differences between the two gravity anomaly models are very small with values in the range between -2 mGal and 2 mGal in most areas. Differences with values larger than 8 mGal can be observed in two places due to the lack of gravity observations (see also Fig. 4.32). It is obvious that one of the two solutions provides worse predictions in the gaps of the input data points. According to the comparisons at the control points, the gravity anomaly model

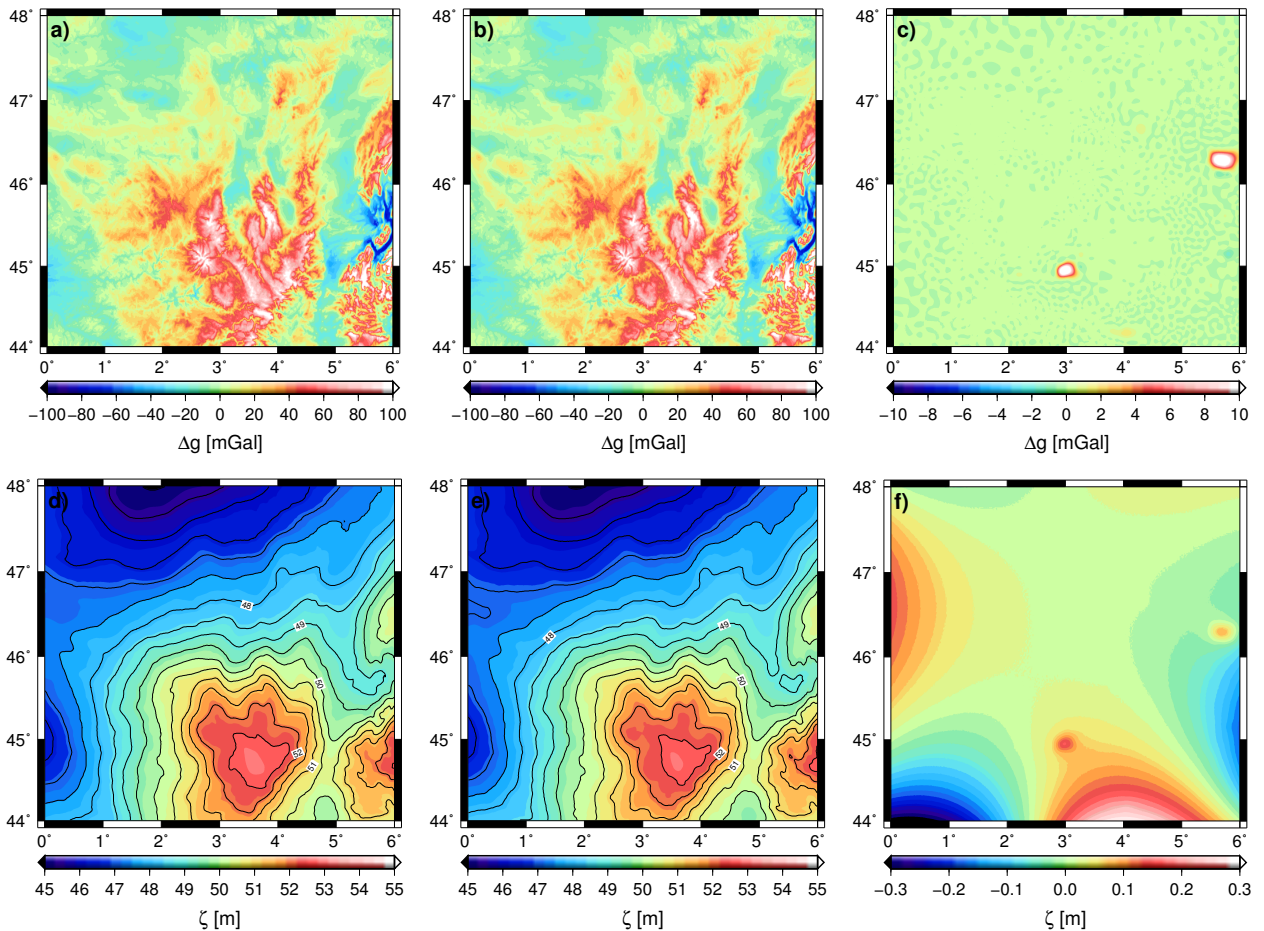


Figure 4.36: Gravimetric gravity anomaly models with a resolution of $1' \times 1'$ for **a)** the unconstrained solution; **b)** the constrained solution; **c)** the differences between **a)** and **b)**; **d)**, **e)**, and **f)** the same, but for the gravimetric quasigeoid models.

associated with the unconstrained solution is regarded as the better one (Fig. 4.36a). As expected, significant height anomaly differences are found in the same two places in Fig. 4.36f. Besides the two small-scale height anomaly differences with large values, large-scale differences reaching up to ± 30 cm are observed in the border area from Fig. 4.36f. It might be caused by the different computation schemes, i.e., the reduced RBFs without constraints and the full RBFs with constraints.

4.5.3 Combined solutions

According to the results of Section 4.5.2, the unconstrained solutions perform slightly better than the constrained solutions. Therefore, only the former will be considered in the following. In Section 4.5.2, we observed systematic differences in the order of more than one decimeter when comparing the gravimetric height anomalies to the geometric values derived from the GPS/leveling data. Many approaches have been developed so far for the combination of gravity and GPS/leveling data. The commonly applied approach is the corrector-surface approach (e.g., Milbert, 1995; Denker et al., 2000; Nahavandchi and Soltanpour, 2006; Soltanpour et al., 2006), in which the gravimetric quasigeoid model is fitted to the GPS/leveling quasigeoid heights by adding a “corrector surface” that is modeled based on the differences between gravimetric and geometric height anomalies. Another popular technique to approximate the differences is LSC (e.g., Denker et al., 2000; Darbeheshti and Featherstone, 2010). Alternatively, the combination can also be realized by the integrated processing of all available data using least-squares techniques (e.g., Ihde et al., 1998; Denker et al., 2000) or LSC.

In addition, the data combination is written as the solution of a Cauchy boundary value problem for the Laplace equation, which allows to remove the non-uniqueness of the problem of local gravity field modeling using terrestrial gravity data only (Prutkin and Klees, 2008). This approach is further modified for the combination of a gravimetric quasigeoid with GPS/leveling data in the presence of noise with correlations and/or spatially varying noise variances (Klees and Prutkin, 2010). Although many approaches are available for the combination of GPS/leveling and gravity data, we will not pay too much attention to this issue in this thesis, only the corrector-surface approach and the integrated processing of the GPS/leveling and gravity data will be discussed in this section.

4.5.3.1 Method I

In this method, an empirical corrector surface, which incorporates systematic errors from ellipsoidal, leveling, and geoidal sources, is constructed to relate the gravimetric quasigeoid model to the model derived from the GPS/leveling data. Modeling of such a corrector surface begins by forming residuals in the form of (Denker et al., 2000)

$$\zeta_{GPS} - \zeta_{model} = (h_{GPS} - H^N) - \zeta_{model} = l = t + s + n, \quad (4.1)$$

where ζ_{GPS} is the geometric height anomaly, computed as the difference between the ellipsoidal height h_{GPS} and the leveled normal height H^N , ζ_{model} is the gravimetric height anomaly, and l are the raw residuals, which are considered as a trend t , signal s , and noise n component in a least-squares collocation model.

The trend component t is modeled in the form of

$$t = \cos \phi \cos \lambda \Delta X + \cos \phi \sin \lambda \Delta Y + \sin \phi \Delta Z \quad (4.2)$$

with the geodetic latitude ϕ and longitude λ , and the 3-parameter datum shift ΔX , ΔY , and ΔZ .

After computing the trend parameters, an empirical covariance function of the detrended residuals (i.e., $l - t$) is computed and modeled by a simple mathematical function. Here, a second-order Markov covariance model is employed, which has the form

$$Cov(d) = C_0 \left(1 + \frac{d}{\alpha} \right) e^{-\frac{d}{\alpha}}, \quad (4.3)$$

in which d is the distance, C_0 is the signal variance, and α is a parameter that describes the characteristic length of the covariance function. When the signal and error covariance models are fixed, the signal component at an arbitrary point P can be predicted by the formula

$$\hat{s} = \mathbf{c}_P^T (\mathbf{C} + \mathbf{D})^{-1} (\mathbf{l} - \mathbf{t}), \quad (4.4)$$

where \hat{s} is the predicted signal in point P , \mathbf{C} is a matrix containing the signal covariances between the observations, \mathbf{D} is the noise covariance matrix, and \mathbf{c}_P is the vector consisting of the signal covariances between the predicted signal and the observations.

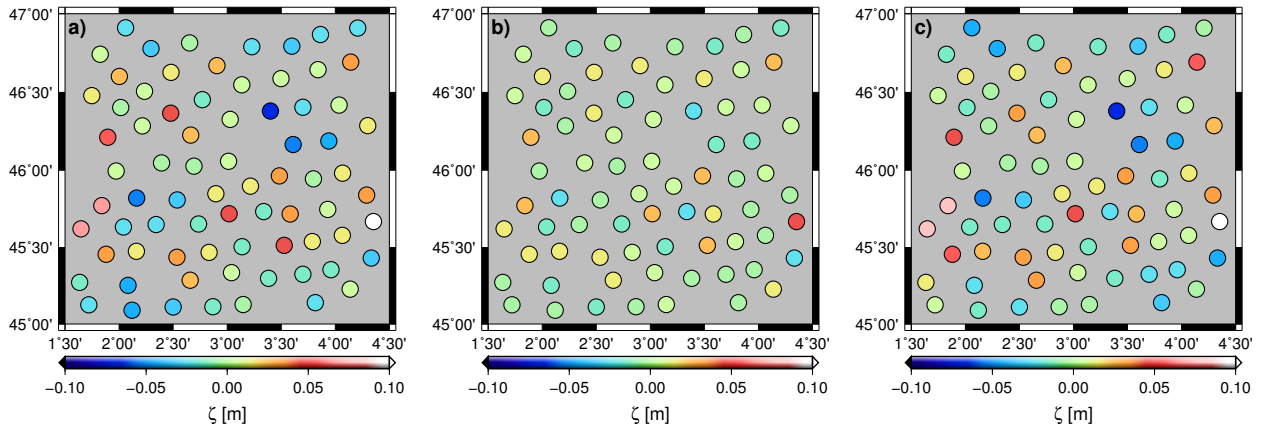
Finally, the corrected quasigeoid model is obtained by adding the predicted signal and the trend component to the gravimetric quasigeoid model, yielding

$$\zeta_{model}^c = \zeta_{model} + \underbrace{t + \hat{s}}_{\text{corrector surface}}. \quad (4.5)$$

With the use of the available 75 GPS/leveling points, the empirical corrector surface is computed by the collocation approach. In order to discuss the benefit from each model component, the statistics of the discrepancies between the observed and three modeled quasigeoid undulations at the 75

Table 4.38: Statistics of the differences between the observed and three modeled height anomalies [m] at 75 GPS/leveling points for Method I.

	Mean	STD	RMS	Min	Max
$\zeta_{GPS} - \zeta_{model}$	-0.182	0.034	0.185	-0.255	-0.069
$\zeta_{GPS} - (\zeta_{model} + t)$	0.000	0.032	0.031	-0.067	0.106
$\zeta_{GPS} - (\zeta_{model} + t + s)$	0.000	0.013	0.013	-0.026	0.043

**Figure 4.37:** Height anomaly errors at 75 GPS/leveling points for **a)** $\zeta_{GPS} - (\zeta_{model} + t)$; **b)** $\zeta_{GPS} - (\zeta_{model} + t + s)$; **c)** the directly combined solution using the full point mass RBFs.

GPS/leveling points are presented in Table 4.38. The residuals $\zeta_{GPS} - \zeta_{model}$ show a mean value of -0.182 m and an RMS of 0.185 m (see also Table 4.37), exhibiting a constant bias at the level of 18.2 cm. The residuals $\zeta_{GPS} - (\zeta_{model} + t)$ and $\zeta_{GPS} - (\zeta_{model} + t + s)$ have zero means with RMS values of 0.031 m and 0.013 m, respectively. Obviously, the quasigeoid after trend and signal corrections shows a big improvement in accuracy. This proves the efficiency of the procedure. Figs 4.37a and 4.37b show the error distribution for $\zeta_{GPS} - (\zeta_{model} + t)$ and $\zeta_{GPS} - (\zeta_{model} + t + s)$, from which it can be seen that the errors are much smaller for the latter one than the former one. The largest errors for both models are located in the southeast corner of the area covered by the GPS/leveling points, in which only a small number of gravity observations are available. The other errors are all in the range from -0.10 m to 0.10 m.

4.5.3.2 Method II

In this method, the gravity and GPS/leveling data are directly combined in the estimation process by using PM-FRE. Since the number of GPS/leveling points is much smaller than the number of gravity anomaly observations (75 vs. 242809), it is sufficient to use only the gravity anomalies for finding the point mass RBFs in the first step of PM-FRE. Therefore, the first step of PM-FRE is the same as the one used in Section 4.5.2 (i.e., the same number of point mass RBFs at the same positions). In the second step, the gravity anomalies and GPS/leveling-derived height anomalies are introduced as inputs for the final adjustment of the magnitudes, where VCE is applied for the proper weighting of the two data groups as well as for the proper determination of the regularization parameter. As the two data sets are different kinds of gravity field quantities, the choice of $N_{\min} = 51$ that works fine in the case of using gravity anomalies as inputs does not hold in this case. Therefore, two choices of $N_{\min} = 0$

Table 4.39: Statistics of the differences between the predicted and observed values at the control points, i.e., 1145 gravity anomalies [mGal] and 75 GPS/leveling-derived height anomalies [m], for two choices of N_{\min} .

N_{\min}	Solution	Mean	STD	RMS	Min	Max
0	Δg	0.047	1.191	1.191	-6.601	17.373
	ζ	0.000	0.031	0.031	-0.066	0.096
51	Δg	0.051	1.190	1.190	-6.620	17.413
	ζ	-0.175	0.034	0.179	-0.246	-0.058

and 51 are compared. The statistics of the differences at the control points for the two solutions is given in Table 4.39. From this table, we find that adding of GPS/leveling data has no contribution to the gravity anomaly solutions, leading to a similar RMS fit as in Table 4.37. For the height anomaly solutions, only the case of using $N_{\min} = 0$ is affected by considering additional GPS/leveling data. The corresponding mean difference reduces to zero, and a smaller STD of 0.031 m is obtained. The case of $N_{\min} = 51$ provides a combined height anomaly solution similar to the gravimetric solution, meaning that the GPS/leveling data have almost no contribution to the combined height anomaly solution. It could be expected that the reduced point mass RBFs (i.e., $N_{\min} = 51$) are less sensitive to long-wavelength signals and the GPS/leveling quasigeoid heights are in the long-wavelength domain in comparison to the short-wavelength domain of the ground gravity data. Alternatively, the use of full point mass RBFs (i.e., $N_{\min} = 0$) can take the GPS/leveling data into account as they are more sensitive to the long-wavelength signals than the reduced RBFs. The square roots of the variance components for the gravity data estimated by VCE are 0.829 mGal for the two choices of N_{\min} due to the large amount of gravity anomaly observations. The square roots for the GPS/leveling data are 0.033 m and 0.179 m corresponding to $N_{\min} = 0$ and 51, respectively. According to the definition of the weight in Koch and Kusche (2002), the larger the variance component is, the smaller the weight is and the smaller is the contribution of the related data set to the solution. The use of full RBFs attains a smaller variance component for the GPS/leveling data, leading to a better fit. The height anomaly error distribution associated with $N_{\min} = 0$ is illustrated in Fig. 4.37c.

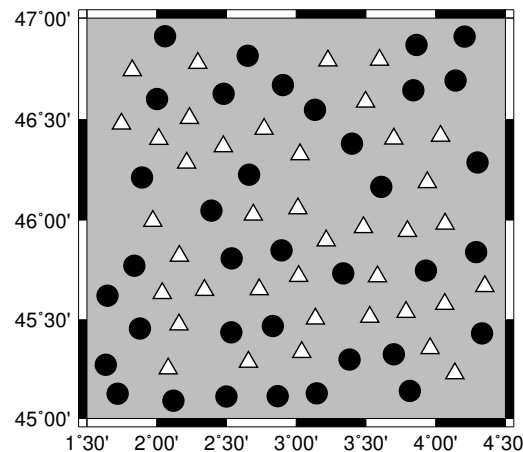


Figure 4.38: Location of 36 GPS/leveling points for the development of the combined solutions (*black circles*) and 39 points for the external validation (*white triangles*).

4.5.3.3 Comparison and discussion

Previously, the combined height anomaly solutions are validated by the GPS/leveling data, which is also used for the modeling. A good quality test of the used combination procedures is to compare the combined height anomaly solutions with an independent GPS/leveling data set. Therefore, the available 75 GPS/leveling points are divided into two groups: (1) 36 points for the development of the combined solutions and (2) 39 points for the external validation. The location of the two data groups is shown in Fig. 4.38.

According to previous analysis, the spectral bandwidth of $N_{\min} = 51$ is employed for the combined modeling when using Method I, and $N_{\min} = 0$ for Method II. For the sake of simplicity, the combined height anomaly solutions computed by Method I considering 75 GPS/leveling points are denoted as I_{75} , and I_{36} means that only 36 GPS/leveling points are used for the modeling. Similarly, II_{75} and II_{36} have the same meaning but for Method II.

The statistics of the differences at the GPS/leveling points for all combined solutions are summarized in Table 4.40. This table shows an evident increase of RMS difference at the independent validation points (i.e., 39 GPS/leveling points) for I_{36} (i.e., from 1.2 cm to 3.5 cm) and a slight increase for II_{36} (i.e., from 3.1 cm to 3.2 cm), but all results are still very satisfactory, leading to RMS errors of 0.035 m and 0.032 m, respectively. The spatial distribution of the differences is shown in Fig. 4.39. All differences are in the range between -0.10 m and 0.10 m except for one point with the largest error in the southeast corner of the area covered by GPS/leveling data.

Table 4.40: Statistics of the differences [m] at GPS/leveling points for different combined solutions.

Solution		Mean	STD	RMS	Min	Max
I_{75}	(75)	0.000	0.013	0.013	-0.026	0.043
II_{75}	(75)	0.000	0.031	0.031	-0.066	0.096
I_{36}	(36)	0.000	0.012	0.012	-0.024	0.025
	(39)	-0.001	0.036	0.035	-0.077	0.103
II_{36}	(36)	0.001	0.032	0.031	-0.067	0.064
	(39)	-0.001	0.033	0.032	-0.062	0.111

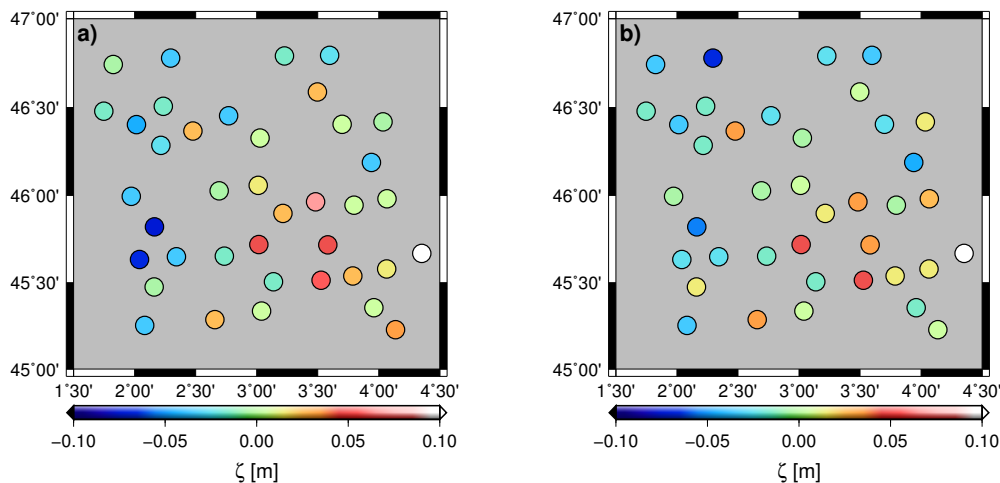


Figure 4.39: Height anomaly errors at 39 independent GPS/leveling points associated with a) I_{36} and b) II_{36} .

The quasigeoid models with a resolution of $1' \times 1'$ for the above four combined solutions, as well as the internal comparison between them, are shown in Fig. 4.40. The use of different combination methods causes small undulations in the area covered by the GPS/leveling points, but yields large differences in the four corners of the research area (see Figs 4.40a–4.40c and 4.40d–4.40f). The differences between the models computed by using different numbers of GPS/leveling points (i.e., 75 vs. 36 points) show a trend increasing from northwest to southeast in the case of Method II (see Figs 4.40b, 4.40e, and 4.40h). In addition to the trend, some signal differences caused by adding more GPS/leveling points can be observed in the case of Method I (see Figs 4.40a, 4.40d, and 4.40g). This

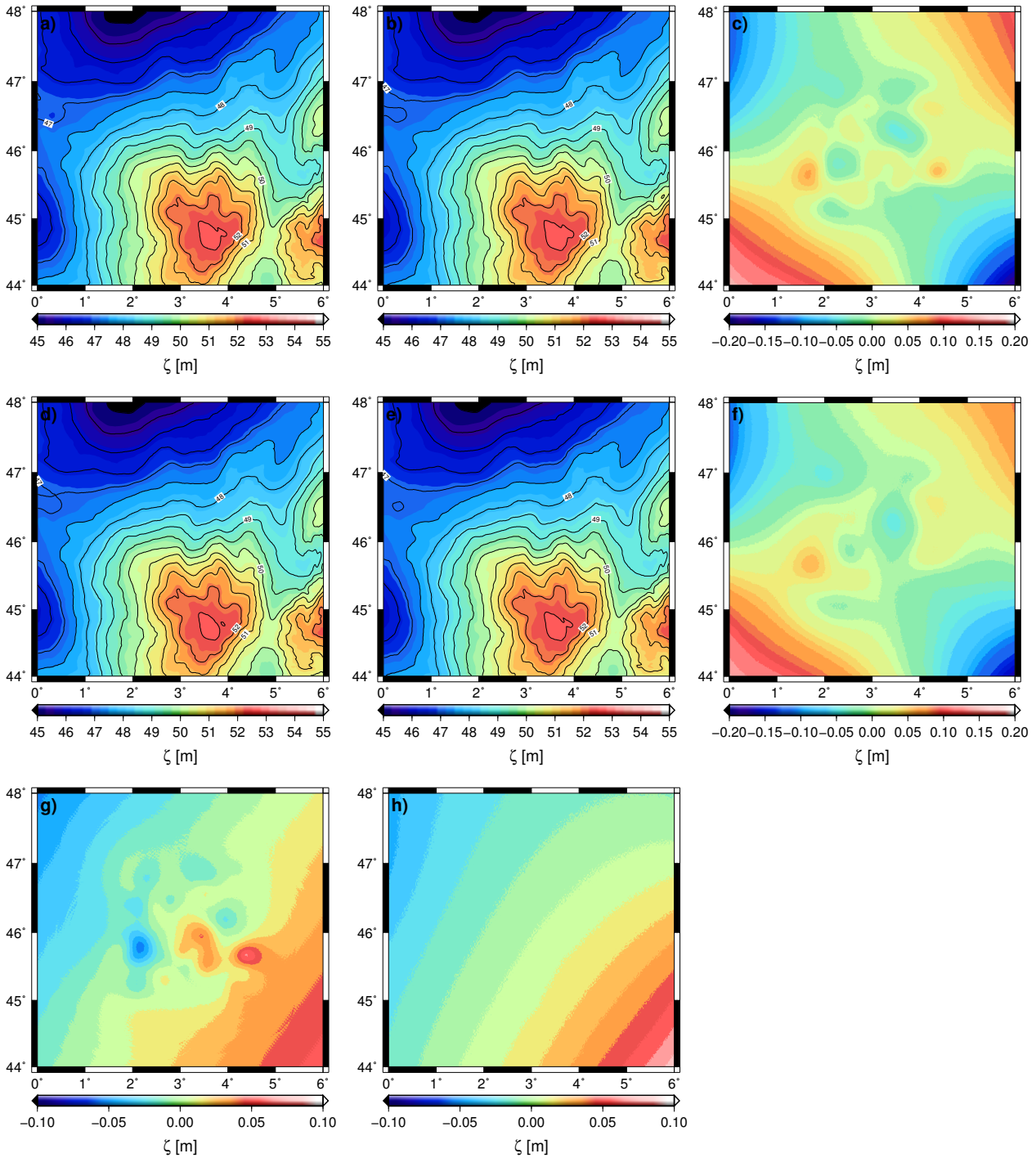


Figure 4.40: Combined $1' \times 1'$ quasigeoid models for a) I_{75} ; b) II_{75} ; c) $I_{75} - II_{75}$; d) I_{36} ; e) II_{36} ; f) $I_{36} - II_{36}$; g) $I_{75} - I_{36}$; h) $II_{75} - II_{36}$.

indicates that the combined models computed by Method I are more dependent on the amount of GPS/leveling points used for the combination than the ones computed from Method II.

Finally, the differences between the four combined quasigeoid models and the previously determined gravimetric model (see Fig. 4.36d) are illustrated in Fig. 4.41 (the difference associated with Method I is also called the corrector surface). For the models computed by Method I, the use of different numbers of GPS/leveling points for the modeling can lead to different corrector surfaces (see Figs 4.41a and 4.41b). The models computed by Method II again are less dependent on the number of used GPS/leveling points, leading to similar differences (see Figs 4.41c and 4.41d).

4.5.4 Conclusions

In this section, the proposed point mass method PM-FRE based on the RCR technique was successfully applied for a real case in the Auvergne area with moderate topography. When only using gravity anomalies as input, two solutions are computed and compared at given control points. The RMS of

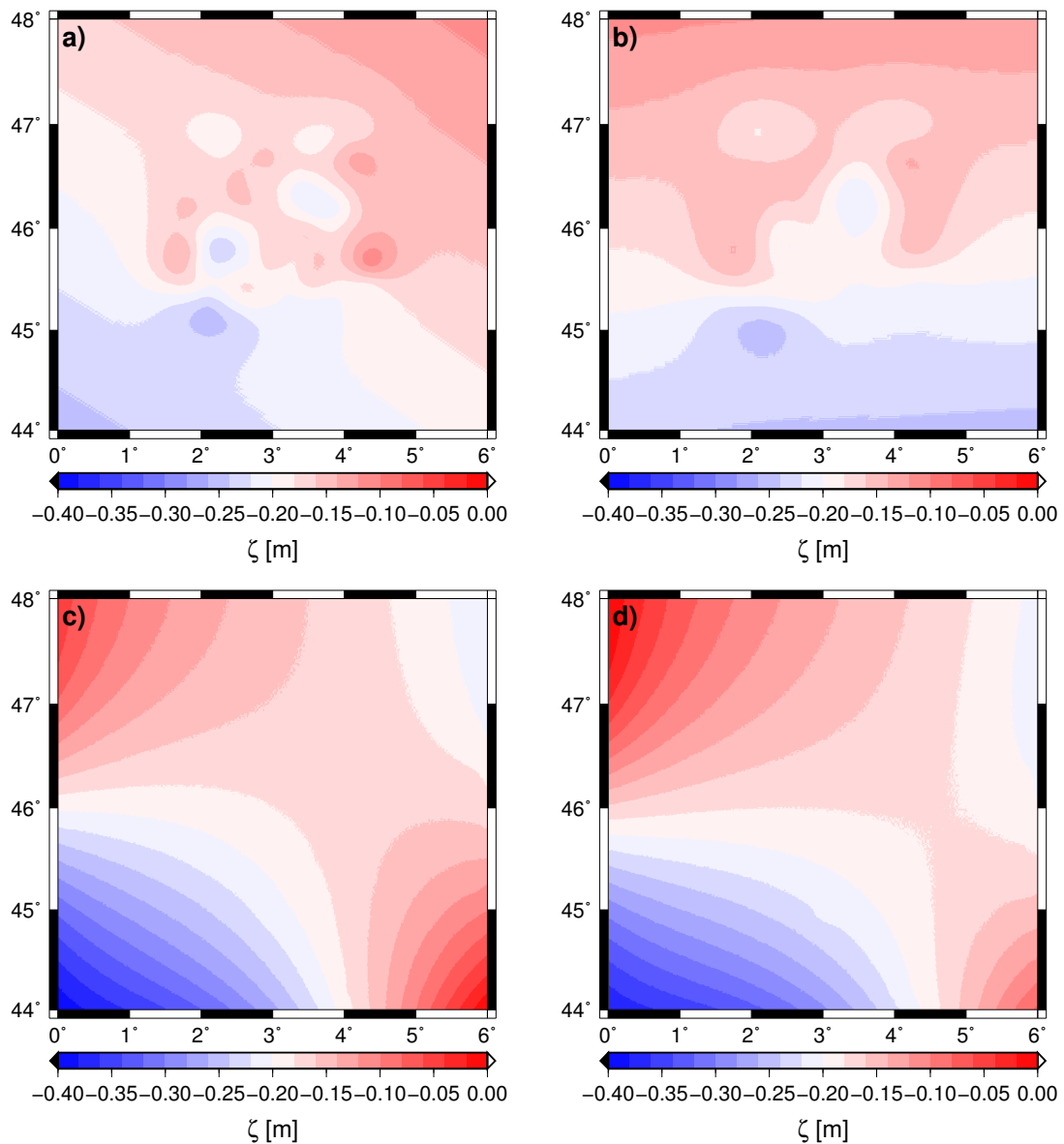


Figure 4.41: Differences between the gravimetric quasigeoid model (Fig. 4.36d) and the combined quasigeoid models associated with **a)** I_{75} ; **b)** I_{36} ; **c)** II_{75} ; **d)** II_{36} .

gravity anomaly differences is about 1.2 mGal for both solutions. The STD of the height anomaly differences is about 0.035 m for the two solutions. The results are comparable to the ones computed by various methods published by Duquenne (2007), Ågren et al. (2009), Forsberg (2010), Valtý et al. (2012), and Yildiz et al. (2012). The mean difference of -0.182 m and -0.165 m is obtained in the unconstrained solution and constrained solution respectively, indicating the inconsistency between the gravimetric and GPS/leveling-derived height anomalies. To overcome this problem, two approaches based on entirely different concepts are used to combine the gravity and GPS/leveling data. In the first approach, an empirical corrector surface is developed based on the height anomaly residuals at the GPS/leveling points, and then added to the gravimetric quasigeoid model, yielding a corrected model. In the second approach, the two data sets are directly combined in the weighted least-squares adjustment, in which the weight for each data set is determined by VCE. The combined gravity anomaly solution is nearly the same as the one computed by using only gravity anomaly observations, resulting in an RMS error of 1.19 mGal. For the two combined height anomaly solutions, the average RMS error at 39 independent GPS/leveling points is about 0.034 m. Comparing to the RMS error of 0.185 m of the gravimetric (unconstrained) solution, the improvements of the combined solutions are significant. But one has to note that, in the integrated processing of the gravity and GPS/leveling data, the use of reduced point mass RBFs (i.e., $N_{\min} = 51$) fails to combine the GPS/leveling data by using VCE. The reason is due to the insensitivity of the reduced RBFs to the GPS/leveling data that are in the long-wavelength domain. Instead, the full RBFs (i.e., $N_{\min} = 0$) with larger spatial bandwidths work fine. Furthermore, by inter-comparisons of the combined quasigeoid solutions as well as of the differences between the combined and gravimetric models we found that the combined model computed by Method II is less dependent on the number of GPS/leveling points used for the modeling than the combined model computed by Method I. Therefore, if only a small number of GPS/leveling points are available for the combination, Method II is preferred.

5 Summary and outlook

5.1 Summary

In this thesis, a parameterization method using radial basis functions was developed for regional gravity field modeling. It comprises (1) the design of the RBFs, including the choice of the spatial bandwidths and horizontal positions of the RBFs, and (2) the parameter determination. Moreover, the spatial bandwidths of the RBFs are determined by the type, spectral bandwidths, and radial distances of the RBFs.

Due to the availability of analytical expressions, the point mass RBFs were selected for representing the regional gravity field by fitting to different kinds of gravity data, leading to the so-called point mass method, which was applied together with the RCR technique. As a result, the input data were residuals with the low and very-high frequencies removed. To avoid errors caused by the mismatch of the spectral bandwidths between the RBFs and the input data, the point mass RBFs neglecting the low and very-high degree terms in the series expansions were preferred. Since the removal of the very-high degree terms had nearly no effect on the spatial bandwidths of the RBFs, only the terms from degree 0 to degree $N_{\min} - 1$ were set to be zero (see Eq. (3.6)), yielding the reduced point mass RBFs. Accordingly, the point mass RBFs containing all degree terms were called the full RBFs. Both RBFs were tested numerically.

For the determination of the positions of the point mass RBFs (i.e., radial distances and horizontal positions), two cases were examined. In the first case, the point mass RBFs were located at the grid points. This point mass method was named PM-FIX. The employed grid type was the geographic grid. Afterwards, several model factors for designing the grid had to be considered. They were the grid extent, grid spacing, and grid depth. Furthermore, the grid formation was also of importance for achieving a good approximation of the gravity field. All these factors were investigated numerically.

In the second case, the related point mass method was called PM-FRE, in which the number and the positions of the RBFs were completely or partly unknown. A search process was developed for finding the RBFs, in which the magnitudes and positions of the RBFs were estimated simultaneously by solving a series of small-scale nonlinear problems. This search process aimed at minimizing the residuals between the predicted and observed gravity values (i.e., data misfit). Before starting it, several model factors (e.g., initial depth and depth limits, optimization direction, etc.) had to be defined properly so that a good approximation can be guaranteed. They were all numerically investigated and discussed. Due to the depth limits on the selected point mass RBFs, the nonlinear problem to be solved in the search process was bound-constrained. Consequently, the choice of a suitable optimization algorithm was necessary. Among the four tested iteration algorithms (i.e., LM, NLCG, L-BFGS, and L-BFGS-B), the L-BFGS-B algorithm proved to be the most proper one. The search process was usually terminated by satisfying a defined data misfit, or by satisfying a given number of point mass RBFs, which is defined based on the number of observations or by testing different choices. Sometimes, the criterion for stopping the search process was realized by considering the data misfit as a function of the number of RBFs. In this case, if the data misfit decreased very slowly, the search can be stopped accordingly. After the search process, a set of point mass RBFs with known positions and magnitudes are obtained. Because the point mass RBFs were selected and estimated individually, a readjustment of the magnitudes of all found RBFs based on the whole input data was carried out while keeping the positions of the RBFs fixed. This led to the two-step approach of PM-FRE, which is one of the major innovations of this thesis.

No matter whether PM-FIX or PM-FRE was used, the final magnitudes of the point mass RBFs

were obtained by solving a linear equation system in the least-squares sense. In the case of ill-posedness, Tikhonov regularization was applied. Three approaches were compared for choosing the proper regularization parameter. Although the empirical approach provided the best solutions with the smallest errors when comparing to the independent data, the VCE technique proved to be more elegant. Besides its capability for the determination of the regularization parameter, it was also well suited for the data combination.

The applicability of this regional approach was demonstrated by analyzing the results of five numerical tests with synthetic and real data. The first numerical test aimed at investigating the effect of different choices of model factors on the solutions. As a result, a computation procedure of PM-FIX was proposed for practical applications. Regarding PM-FRE, an empirical rule was developed for choosing the initial depth and depth limits and the radial-direction optimization was preferred in the search process. In the second step, the reduced RBFs are highly recommended for the readjustment of the magnitudes, leading to an unconstrained solution. Alternatively, the use of full RBFs for constructing the linear equation system and the adding of the constraints in the adjustment are also able to provide good solutions, resulting in a constrained solution. The unconstrained solution performed slightly better than the constrained one, and also was easier to calculate. Therefore, the former was preferred. By means of numerical comparisons between PM-FIX and PM-FRE, the latter outperformed the former. Therefore, only PM-FRE was used in the remaining numerical tests. Through the second and the third tests, it was shown that PM-FRE can recover the gravity anomalies from the observed geoid heights, providing better solutions than LSC. We also found that the use of full RBFs works fine for computing the unconstrained solution, indicating that the choice of spectral bandwidths of the RBFs depends on the type of modeled gravity field quantities. If they were in the short-wavelength domain, the use of reduced RBFs is not necessary. In addition, an iterative procedure based on VCE was developed for dealing with the case of several data groups with the same data type but different accuracies. The numerical results confirmed the advantage of the iterative procedure. On the basis of the three numerical tests, the “optimal” strategy for PM-FRE was obtained. In the fourth numerical test, a set of synthetic terrestrial and airborne gravity disturbances were used for the regional modeling. When using terrestrial data only, the solution of PM-FRE was compared to the LSC solution, showing a smaller RMS error of the modeled disturbing potential at ground. When considering both terrestrial and airborne data, the solutions obtained by using different schemes for finding the point mass RBFs were compared and validated, exhibiting a good agreement between each other. In the last numerical test in the Auvergne area using a large number of real gravity observations, both gravity and height anomaly solutions were calculated with small RMS (or STD) errors by PM-FRE. Two combination approaches were successfully applied to eliminate the discrepancies between the gravimetric and GPS/leveling-derived height anomalies.

In general, it can be concluded that, a good representation of the gravity field over a particular research area can be achieved by using PM-FRE as was demonstrated by five numerical tests. In comparison to the traditional integral method, PM-FRE is expected to predict all gravity field quantities with the use of resulting point mass RBFs. In all numerical tests carried out in this thesis, PM-FRE provides good gravity and height anomaly solutions. Comparing to PM-FIX or a related parameterization method, in which the RBFs are at the nodes of defined grids, PM-FRE is able to adapt the spatial distribution of the RBFs to the given gravity field characteristics. As can be seen from the Auvergne test case, more point mass RBFs are selected in the regions with rough gravity field features and fewer RBFs in areas with smooth structures. The advantage of PM-FRE with respect to LSC is that a smaller number of unknowns has to be estimated either in the nonlinear problems in the first step or in the linear problem in the second step. As a consequence, PM-FRE can be applied to some large-scale test cases (e.g., Auvergne test case) with the use of personal computer, whereas LSC can not. However, some effort is required for finding the point mass RBFs in the first step of PM-FRE, as a series of small-scale nonlinear problems has to be solved. Regarding the linear problem

in the second step, the computational complexity of the entire process of PM-FRE is quite high.

5.2 Outlook

Despite the satisfactory results already obtained by PM-FRE in this thesis, more numerical tests using real data sets are recommended for further testing of this method. There is still potential for further improvements of the method. In the current version, the Tikhonov regularization matrix used in the second step is simply taken as the identity matrix. The solution accuracy of PM-FRE might be improved if the identity regularization matrix is replaced by a diagonal matrix, of which the diagonal elements are appropriately tailored according to the signal content in the areas around the point mass RBFs. The respective information can be obtained from the available digital terrain models or a priori gravity field solutions. Similar studies have been carried out by Eicker (2008) and Eicker et al. (2014).

In this thesis, the point mass RBFs to be selected in a layer have the same initial depths and depth limits when using either the point mass search model SMA or SMB. A more reasonable case would be that each point mass RBF has its own initial depth and depth limits, which could be determined based on the density of the data points or the signal content in the area around the RBF. Further investigations are necessary.

So far, we have tested the performance of PM-FRE for regional modeling in the case of using a single data type with the same accuracy or different accuracies. Here arises the question how to deal with the case of several data groups with different data types. If the number of data points for one data group is much larger than the others, the point mass RBFs can be searched for based on only this data group; such a case has been verified in the Auvergne test case for the combination of gravity and GPS/leveling data. Otherwise, the search process becomes more complicated. A possible scheme is that the search process is carried out individually based on each data group. Suppose that there are a set of marine gravity data and a set of altimetry data, the first set of point mass RBFs can be obtained based on only the marine gravity data, then similar procedures are repeated for generating the second set of point mass RBFs based on the altimetry data. Afterwards, all searched point mass RBFs are readjusted with the input of the two data sets in the weighted least-squares. The weight for each data group can be determined by VCE or manually fixed by the user based on available a priori information. This is subject to further work.

Although Tenzer and Klees (2008) demonstrated that similar gravity solutions can be obtained when using different types of RBFs (i.e., different shape coefficients) if the spatial bandwidths of the RBFs are chosen properly, it is also of interest to apply the concept of PM-FRE to other types of RBFs. The approach offers various possibilities for further applications due to its flexible and modular structure.

Bibliography

- Ågren J, Barzaghi R, Carrion D, Denker H, Grigoriadis VH, Kiamehr R, Sona G, Tscherning CC, Tziavos IN (2009) Different geoid computation methods applied on a test dataset: results and considerations. In: Hotine-Marussi Symposium, Rome, Italy, 6-12 July (poster)
- Alberts B (2009) Regional gravity field modeling using airborne gravimetry data. PhD Thesis, Nr. 70, Delft University of Technology, Delft, Netherlands
- Ameti P (2006) Downward continuation of Geopotential in Switzerland. PhD Thesis, TU Darmstadt, Darmstadt, Germany
- Antunes C, Pail R, Catalao J (2003) Point mass method applied to the regional gravimetric determination of the geoid. *Studia Geophysica et Geodaetica* 47:495–509
- Asnaashari A, Brossier R, Garambois S, Audebert F, Thore P, Virieux J (2013) Regularized seismic full waveform inversion with prior model information. *Geophysics* 78:R25–R36
- Barthelmes F (1986) Untersuchungen zur approximation des äußeren Schwerefeldes der Erde durch Punktmassen mit optimierten Positionen. Report Nr. 92, Veröffentlichungen des Zentralinstituts für Physik der Erde, Potsdam, Germany
- Barthelmes F (1989) Local gravity field approximation by point masses with optimized positions. Report Nr. 102(2), Veröffentlichungen des Zentralinstituts für Physik der Erde, Potsdam, Germany
- Bentel K, Schmidt M, Gerlach C (2013) Different radial basis functions and their applicability for regional gravity field representation on the sphere. *GEM-International Journal on Geomathematics* 4:67–96
- Bouman J (1998) Quality of regularization method. DEOS Report Nr. 98.2, Delft Institute for Earth-Orient Space Research, Delft University of Technology, Delft, Netherlands
- Bowin C (1983) Depth of principal mass anomalies contributing to the Earth's geoidal undulations and gravity anomalies. *Marine Geodesy* 7:61–100
- Brossier R, Operto S, Virieux J (2009) Seismic imaging of complex onshore structures by 2D elastic frequency-domain full-waveform inversion. *Geophysics* 74:WCC105–WCC118
- Byrd RH, Lu P, Nocedal J, Zhu C (1995) A limited memory algorithm for bound constrained optimization. *SIAM Journal on Scientific Computing* 16:1190–1208
- Chen WY (2006) A study of determination of Taiwan's local geoid by combination of GPS Leveling and gravity data with point masses. Master Thesis, National Cheng Kung University, Taiwan (in Chinese)
- Claessens SJ, Featherstone WE, Barthelmes F (2001) Experiences with point-mass gravity field modeling in the Perth Region, Western Australia. *Geomatics Research Australasia* 75:53–86
- Colombo O (1981) Numerical methods for harmonic analysis on the sphere. Technical Report 310, Department of Geodetic Science and Surveying, Ohio State University, Columbus, Ohio, USA
- Cordell L (1992) A scattered equivalent-source methods for interpolation and gridding of potential-field data in three dimensions. *Geophysics* 57:629–636
- Dampney CNG (1969) The equivalent source technique. *Geophysics* 34:39–53
- Darbeshti N, Featherstone WE (2010) Tuning a gravimetric quasigeoid to GPS-levelling by non-stationary least-squares collocation. *Journal of Geodesy* 84:419–431

- Denker H (1998) Evaluation and improvement of the EGG97 quasigeoid model for Europe by GPS and leveling data. In: Vermeer M, Adam J (eds.) Second continental workshop on the geoid in Europe, Proceedings of Rep. Finnish Geod. Inst., Masala, Finland, 98:53-61
- Denker H (2013) Regional gravity field modeling: Theory and Practical Results, In: Xu G (ed.) Science of Geodesy - II, Springer Verlag, Heidelberg, Germany, 185-291
- Denker H, Torge W, Wenzel G, Ihde J, Schirmer U (2000) Investigation of different methods for the combination of gravity and GPS/levelling data. In: Schwarz KP (ed.) Proceedings of Geodesy Beyond 2000: The Challenges of the First Decade, Springer Verlag, Berlin, Germany, 137-142
- Denker H, Barriot JP, Barzaghi R, Fairhead D, Forsberg R, Ihde J, Kenyeres A, Marti U, Sarrailh M, Tziavos IN (2009) The development of the European gravimetric geoid model EGG07. In: Sideris MG (ed.) Observing our changing earth, International Association of Geodesy Symposia, Springer-Verlag, Berlin, Heidelberg, Germany, 133:177-186
- Ding Y, Jia YF, Wang SY (2004) Identification of manning's roughness coefficients in shallow water flows. Journal of Hydraulic Engineering 130:501-510
- Ditmar P, Kusche J, Klees R (2003) Computation of spherical harmonic coefficients from gravity gradiometry data to be acquired by the GOCE satellite: regularization issues. Journal of Geodesy 77:465-477
- Drinkwater MR, Floberghagen R, Haagmans R, Muzi D, Popescu A (2003) GOCE: ESA's first Earth explorer core mission, In: Beutler et al (eds.) Earth Gravity Field from Space - from Sensors to Earth Sciences, Space Sciences Series of ISSI, vol 18, Kluwer, Dordrecht, 419-432
- Duquenne H (2007) A data set to test geoid computation methods. In: Proceeding of the 1st International Symposium of the International Gravity Field Service "Gravity field of the Earth", Harita Dergis, General Command of Mapping, Istanbul, Turkey, Specific Issue 18:61-65.
- Eicker A (2008) Gravity field refinement by radial basis functions from in-situ satellite data. PhD Thesis, University of Bonn, Bonn, Germany
- Eicker A, Schall J, Kusche J (2014) Regional gravity modelling from spaceborne data: case studies with GOCE. Geophysical Journal International 196:1431-1440
- Forsberg R (1984) A study of terrain reductions, density anomalies and geophysical inversion methods in gravity field modeling. OSU Report 355, Department of Geodetic Science and Surveying, Ohio State University, Columbus, Ohio, USA
- Forsberg R (2010) Geoid determination in the mountains using ultra-high resolution spherical harmonic models - the Auvergne case, In: Contadakis ME, Kaltsikis C, Spatalas S, Tokmakidis K, Tziavos I N (eds.) The apple of the knowledge, In Honor of Professor Emeritus Arabelos DN, Ziti Editions, Thessaloniki, Greece, 101-111
- Forsberg R, Tscherning CC (1981) The use of height data in gravity field approximation by collocation. Journal of Geophysical Research 86:7843-7854
- Forsberg R, Tscherning CC (1997) Topographic effects in gravity field modelling for BVP, In: Sanso F, Rummel R (eds.) Geodetic Boundary Value Problems in View of the One Centimeter Geoid, Lecture Notes in Earth Science, Springer Verlag, Heidelberg, Germany, 65:241-272
- Gilbert JC, Nocedal J (1992) Global convergence properties of conjugate gradient methods for optimization. SIAM Journal on Optimization 2:21-42
- Goad CC, Tscherning CC, Chin MM (1984) Gravity empirical covariance value for the continental United States. Journal of Geophysical Research 89:7962-7968
- Golub GH, van Loan C (1996) Matrix computations. Johns Hopkins University Press, Baltimore, MD, USA

- Golub GH, von Matt U (1997) Generalized cross-validation for large-scale problems. *Journal of Computational Graphical Statistics* 6:1–34
- Golub GH, Heath M, Wahba G (1979) Generalized cross-validation as a method for choosing a good ridge parameter. *Technometrics* 21:215–223
- Guitton A, Symes WW (2003) Robust inversion of seismic data using the Huber norm. *Geophysics* 68:1310–1319
- Haagmans R, Prijatna K, Omang O (2003) An alternative concept for validation of GOCE gradiometry results based on regional gravity. In: Tziavos IN (ed.) *Gravity and geoid 2002, 3rd meeting of the international gravity and geoid communication*, Ziti Editions, Thessaloniki, Greece, 281-286
- Hadamard J (1923) *Lectures on the Cauchy Problem in Linear Partial Differential Equations*. Yale University Press, New Haven
- Hansen PC (1987) The truncated SVD as a method for regularization. *BIT Numerical Mathematics* 27:534–553
- Hansen PC (1997) *Rank Deficient and Discrete Ill-Posed Problems*. SIAM, Philadelphia, USA
- Hansen PC (2008) *Regularization Tools, A Matlab package for analysis and solution of discrete ill-posed problems - Version 4.1 for Matlab 7.3*. Department of Informatics and Mathematical Modelling, Technical University of Denmark, Lyngby, Denmark
- Hardy RL, Göpfert WM (1975) Least squares prediction of gravity anomalies, geoid undulations, and deflections of the vertical with multiquadric harmonic functions. *Geophysical Research Letters* 2:423–426
- Hauck H, Lelgemann D (1985) Regional gravity field approximation with buried masses using least-norm collocation. *Manuscripta Geodaetica* 10:50–58
- Heck B (1997) Formulation and linearization of boundary value problems: from observables to a mathematical model, In: Sanso F, Rummel R (eds.) *Geodetic Boundary Value Problems in View of the One Centimeter Geoid*, Lecture Notes in Earth Science, Springer Verlag, Heidelberg, Germany, 65:121-160
- Heikkinen M (1981) Solving the shape of the Earth by using digital density models. Report 81:2, Finnish Geodetic Institute, Helsinki, Finland
- Heiskanen W, Moritz H (1967) *Physical Geodesy*. Freeman
- Hofmann B, Moritz H (2005) *Physical Geodesy*. Springer Wein New York
- Huang JL (2002) Computational methods for the discrete downward continuation of the Earth gravity and effects of lateral topographical mass density variation on gravity and the geoid. PhD Thesis, Department of Geodesy and Geomatics Engineering, University of New Brunswick, Canada
- Huang JL, Veronneau M (2013) Canadian gravimetric geoid model 2010. *Journal of Geodesy* 87:771–790
- Huang JL, Vanicek P, Pagiatakis S, Brink W (2001) Effect of topographical mass density variation on gravity and geoid in the Canadian Rocky Mountains. *Journal of Geodesy* 74:805–815
- Hutchinson MF (1990) A stochastic estimator of trace of the influence matrix for Laplacian smoothing splines. *Communications in Statistics - Simulation and Computation* 19:433–450
- Ilde J, Schirmer U, Stefani F, Töppe F (1998) Geoid modeling with point masses. In: *Proceedings of the second continental workshop on the Geoid in Europe*, Budapest, Hungary, 199-204
- Jekeli C (2009) Potential theory and static gravity field of the Earth, In: Herring T (vol ed.) *Treatise on geophysics*, vol. 3, Geodesy, Elsevier, Amsterdam, Netherland, 11-42
- Kaula W (1966) *Theory of Satellite Geodesy, Applications of Satellites to Geodesy*. Dover Publications, INC. Mineola, New York, USA

- Kearsley AHW, Sideris MG, Krynski J, Forsberg R, Schwarz KP (1985) White Sands Revisited - A comparison of techniques to predict deflections of the vertical. Report No. 30007, Division of Surveying Engineering, University of Calgary, Alberta, Canada
- Kern M (2004) A Comparison of Data Weighting Methods for the Combination of Satellite and Local Gravity Data. In: Sanso F (ed.) V Hotine-Marussi Symposium on mathematical geodesy, International Association of Geodesy Symposia, Springer Verlag, Berlin, Heidelberg, Germany, 127:137-144
- Klees R, Prutkin I (2010) The combination of GNSS-levelling data and gravimetric (quasi-) geoid heights in the presence of noise. *Journal of Geodesy* 84:731–749
- Klees R, Wittwer T (2007) A data-adaptive design of a spherical basis function network for gravity field modelling. In: Tregoning P, Rizos C (eds) *Dynamic Planet—monitoring and understanding a dynamic planet with geodetic and oceanographic tools*, IAG symposia, Springer Verlag, Berlin, Germany, 322-328
- Klees R, Tenzer R, Prutkin I, Wittwer T (2008) A data-driven approach to local gravity field modeling using spherical radial basis functions. *Journal of Geodesy* 82:457–471
- Knudsen P (1987) Estimation and modelling of the local empirical covariance function using gravity and satellite altimeter data. *Bulletin Geodesique* 61:145–160
- Koch K (1999) *Parameter Estimation and Hypothesis Testing in Linear Models*. Springer Verlag, Berlin Heidelberg New York
- Koch K, Kusche J (2002) Regularization of geopotential determination from satellite data by variance components. *Journal of Geodesy* 76:259–268
- Kotsakis C (2000) *Multiresolution Aspects of Linear Approximation Methods in Hilbert Spaces Using Gridded Data*. PhD Thesis, Department of Geomatics Engineering, University of Calgary, Canada
- Kotsakis C, Sideris MG (1999) The long road from deterministic collocation to multiresolution approximation. *Schriftenreihe der Institute des Studiengangs Geodäsie und Geoinformatik 1999.5*, Department of Geodesy and Geoinformatics, Stuttgart University, Stuttgart, Germany
- Krarpup T (1969) A contribution to the mathematical foundations of physical geodesy. Report 44, Danish Geodetic Institute, Copenhagen, Denmark
- Kusche J, Klees R (2002) Regularization of gravity field estimation from satellite gravity gradients. *Journal of Geodesy* 76:359–368
- Lehmann R (1993) The method of free-positioned point masses – geoid studies on the Gulf of Bothnia. *Bulletin Geodesique* 67:31–40
- Levenberg K (1944) A method for the solution of certain non-linear problems in least squares. *Quarterly of Applied Mathematics* 2:164–168
- Li JC (2012) The recent Chinese terrestrial digital height datum model: Gravimetric Quasi-Geoid CNGG2011. *Acta Geodaetica et Cartographica Sinica* 41:651–660 (in Chinese)
- Lin M, Denker H, Müller J (2014) Regional gravity field modeling using free-positioned point masses. *Studia Geophysica et Geodaetica* 58:207–226
- Lin M, Denker H, Müller J (2015) Regional gravity field modeling by radially optimized point masses: case studies with synthetic data. *International Association of Geodesy Symposia*, Springer Berlin Heidelberg, pp 1–7, doi:10.1007/1345_2015_92
- Liu D, Nocedal J (1989) On the limited memory BFGS method for large scale optimization. *Mathematical Programming* 45:503–528
- Marchenko AN (1998) *Parameterization of the Earth's Gravity Field: Point and Line Singularities*. Lviv Astronomical and Geodetic Society

- Marchenko AN, Tartachynska ZR (2003) Gravity anomalies in the Black sea area derived from the inversion of GEOSAT, TOPEX/POSEIDON and ERS-2 altimetry. *Bolletino di Geodesia e Scienze Affini* LXII:50–62
- Marchenko AN, Barthelmes F, Mayer U, Schwintzer P (2001) Regional geoid determination: an application to airborne gravity data in the Skagerrak. Scientific Technical Report No. 01/07, GFZ, Potsdam, Germany
- Marquardt D (1963) An algorithm for least-squares estimation of nonlinear parameters. *SIAM Journal on Applied Mathematics* 11:431–441
- Mayer-Gürr T, Rieser D, Höck E, Brockmann JM, Schuh W, Krasbutter I, Kusche J, Maier A, Krauss S, Hausleitner W, Baur O, Jäggi A, Meyer U, Prange L, Pail R, Fecher T, Gruber T (2012) The new combined satellite only model GOCO03s. In: International Symposium on Gravity, Geoid and Height Systems, Venice, Italy, October 9-12 (oral presentation)
- Milbert DG (1995) Improvement of a high resolution geoid height model in the United States by GPS height on NAVD 88 benchmarks. *New Geoids in the World*, IGeS bulletin no. 4, International Geoid Service, Milan, Italy, 13-36
- Mohr PJ, Taylor BN, Newell DB (2012) CODATA recommended values of the fundamental physical constants: 2010. *Reviews of Modern Physics* 84:1527–1605
- Molodenskii MS, Eremeev VF, Yurkina MI (1962) Methods for study of the external gravitational field and figure of the Earth. Translation of the Russian Book, Israel Program for Scientific Translations, Jerusalem
- Moré JJ (1978) The Levenberg-Marquardt algorithm: implementation and theory, In: Watson GA (ed.) *Numerical Analysis*, Lecture Notes in Mathematics Volume 630, Springer Verlag, Berlin, Heidelberg, Germany, 105-116
- Moré JJ, Thuente J (1994) Line search algorithms with guaranteed sufficient decrease. *ACM Transactions on Mathematical Software* 20:286–307
- Moré JJ, Garbow BS, Hillstom KE (1980) User guide for MINPACK-1. ANL-80-74, Argonne National Laboratory, USA
- Moritz H (1976) Integral formulas and collocation. *Manuscripta Geodaetica* 1:1–40
- Moritz H (1978) Least-squares collocation. *Reviews of Geophysics and Space Physics* 16:421–430
- Moritz H (1980) *Advanced physical geodesy*. Herbert Wichman, Karlsruhe
- Moritz H (2000) Geodetic reference system. *Journal of Geodesy* 74:128–133
- Naeimi M (2013) Inversion of satellite gravity data using spherical radial basis functions. PhD Thesis, Nr. 309, Institut für Erdmessung, Leibniz Universität Hannover, Hannover, Germany
- Nahavandchi H, Soltanpour A (2006) Improved determination of height using a conversion surface by combination gravimetric quasi-geoid/geoid and GPS-levelling height differences. *Studia Geophysica et Geodaetica* 50:165–180
- Needham PE (1970) The formation and evaluation of detailed geopotential models based on point masses. Report 149, Department of Geodetic Science and Surveying, Ohio State University, Columbus, Ohio, USA
- NIMA (1997) Department of defense world geodetic system 1984 - its definition and relationships with local geodetic datums. Technical Report NIMA TR8350.2, 3rd Edition, 4 July 1997, NIMA National Imagery and Mapping Agency, USA
- Nocedal J (1980) Updating quasi-newton matrices with limited storage. *Mathematics of Computation* 95:339–353
- Nocedal J (1992) Theory of algorithms for unconstrained optimization. *Acta Numerica* 1:199–242

- Nocedal J, Wright SJ (2006) Numerical Optimization. Springer, New York
- Panet I, Kuroishi Y, Holschneider M (2010) Wavelet modelling of the gravity field by domain decomposition methods: an example over Japan. *Geophysical Journal International* 184:203–219
- Pavlis NK, Factor JK, Holmes SA (2007) Terrain-related gravimetric quantities computed for the next EGM. In: *Proceeding of the 1st International Symposium of the International Gravity Field Service "Gravity field of the Earth"*, Harita Dergisi, General Command of Mapping, Istanbul, Turkey, Specific Issue 18:318-323
- Pavlis NK, Holmes S, Kenyon SC, Factor JK (2012) The development and evaluation of the Earth Gravitational Model 2008 (EGM2008). *Journal of Geophysical Research* 117:B04406, doi:10.1029/2011JB008916
- Prutkin I, Klees R (2008) On the non-uniqueness of local quasi-geoids computed from terrestrial gravity anomalies. *Journal of Geodesy* 82:147–156
- Pujol J (2007) The solution of nonlinear inverse problems and the Levenberg-Marquardt method. *Geophysics* 72:W1–W16
- Reilly JP, Herbrechtsmeier EH (1978) A systematic approach to modeling the geopotential with point mass anomalies. *Journal of Geophysical Research* 83:841–844
- Rummel R, Schwarz KP, Gerstl M (1979) Least squares collocation and regularization. *Bulletin Geodesique* 53:343–361
- Schmidt M, Fengler M, Mayer-Gürr T, Eicker A, Kusche J, Sanchez L, Han SC (2007) Regional gravity field modeling in terms of spherical base functions. *Journal of Geodesy* 81:17–38
- Sideris MG (1987) Spectral methods for the numerical solution of Molodensky's problem. UCSE Reports. No. 20024, Department of Surveying Engineering, University of Calgary, Canada
- Sideris MG (1994) Regional geoid determination, In: Vanicek P, Christou NT (eds.) *Geoid and its geophysical interpretations*, CRC Press, Inc, Boca Raton, FL, USA, 77-94
- Sjöberg LE (1980) Least squares combination of satellite harmonics and integral formulas in physical geodesy. *Gerlands Beiträge zur Geophysik* 89:371–377
- Sjöberg LE (1981) Least squares combination of satellite and terrestrial data in physical geodesy. *Annales de Geophysique* 37:25–30
- Sjöberg LE (2003) A general model for modifying Stokes' formula and its least-squares solution. *Journal of Geodesy* 77:459–464
- Soltanpour A, Nahavandchi H, Featherstone WE (2006) The use of second-generation wavelets to combine a gravimetric quasigeoid model with GPS-levelling data. *Journal of Geodesy* 80:82–93
- Sünkel H (1981) Point mass models and the anomalous gravitational field. Report 328, Department of Geodetic Science, Ohio State University, Columbus, USA
- Tenzer R, Klees R (2008) The choice of the spherical radial basis functions in local gravity field modeling. *Studia Geophysica et Geodaetica* 52:287–304
- Tenzer R, Klees R, Prutkin I, Wittwer T, Alberts B, Schirmer U, Ihde J, Liebsch G, Schäfer U (2009) Comparison of techniques for the computation of a height reference surface from gravity and GPS-Levelling data. In: Sideris MG (ed.) *Observing our Changing Earth*, International Association of Geodesy Symposia, Springer Verlag, Heidelberg, Germany, 133:263-273
- Tikhonov AN (1963) Solution of incorrectly formulated problems and the regularization method. *Soviet Mathematics - doklady* 4:1035–1038
- Torge W, Müller J (2012) *Geodesy*. Walter de Gruyter, Berlin/Boston

- Tscherning CC (1981) Comparison of some methods for the detailed representation of the Earth's gravity field. *Reviews of Geophysics* 19:213–221
- Tscherning CC (2013) Geoid Determination by 3D Least-Squares Collocation, In: Sanso F, Sideris MG (eds.) *Geoid Determination*, Lecture Notes in Earth System Sciences, Springer Verlag, Berlin, Heidelberg, Germany, 311–336
- Tscherning CC, Rapp RH (1974) Closed covariance expressions for gravity anomalies, geoid undulations and deflections of the vertical implied by anomaly degree variance models. OSU Report 208, Department of Geodetic Science and Surveying, Ohio State University, Columbus, Ohio, USA
- Tscherning CC, Forsberg R, Knudsen P (1992) The GRAVSOFT package for geoid determination. In: *Proc. of 1st Continental Workshop on the Geoid in Europe*, Research Institute of Geodesy, Topography and Cartography, Prague, 327–334
- Valty P, Duquenne H, Panet I (2012) Auvergne dataset: testing several geoid computation methods. In: Kenyon S, et al (eds.) *Geodesy for Planet Earth*, International Association of Geodesy Symposia, Springer Verlag, Heidelberg, Germany, 136:465–472
- Vermeer M (1983) A new SEASAT altimetric geoid for the Baltic. Report 83:4, Finnish Geodetic Institute, Helsinki, Finland
- Vermeer M (1984) Geoid studies on Finland and the Baltic. Report 84:3, Finnish Geodetic Institute, Helsinki, Finland
- Vermeer M (1995) Mass point geopotential modeling using fast spectral techniques: historical overview, toolbox description, numerical experiments. *Manuscripta Geodaetica* 20:362–378
- Wang YM, Saleh J, Li X, Roman DR (2012) The US Gravimetric Geoid of 2009 (USGG2009): model development and evaluation. *Journal of Geodesy* 86:165–180
- Wenzel HG (1981) Zur Geoidbestimmung durch Kombination von Schwereanomalien und einem Kugelfunktionsmodell mit Hilfe von Integralformeln. *ZfV* 106:102–111
- Wenzel HG (1982) Geoid computation by least squares spectral combination using integral formulas. In: *Proceedings of general meeting of IAG*, Tokyo, Japan, 438–453
- Wittwer T (2009) Regional gravity field modeling with radial basis functions. PhD Thesis, Nr. 72, Delft University of Technology, Delft, Netherlands
- Xu PL (1998) Truncated SVD methods for discrete ill-posed problems. *Geophysical Journal International* 179:182–200
- Yildiz H, Forsberg R, Ågren J, Tscherning CC, Sjöberg LE (2012) Comparison of remove-compute-restore and least squares modification of Stokes' formula techniques to quasi-geoid determination over the Auvergne test area. *Journal of Geodetic Science* 2:53–64
- Zhu C, Byrd RH, Lu P, Nocedal J (1997) Algorithm 778: L-BFGS-B: Fortran subroutines for large-scale bound-constrained optimization. *ACM Transactions on Mathematical Software* 23:550–560

Acknowledgement

This PhD thesis and the related research would not have been possible without the help of many people. First of all, I would like to express my gratitude to my supervisor, Prof. Dr.-Ing. Jürgen Müller, for providing me this opportunity to study in the Institut für Erdmessung (IfE) to pursue the PhD degree as well as for his help and support during more than four years of research. I also appreciate the freedom he gave me to choose the interested research topics.

I greatly appreciate the steady support from Dr.-Ing. Heiner Denker, who was always ready to help me to solve the encountered problems regardless of his busy schedule. He provided excellent guidance and constructive comments throughout the PhD study period. Special thanks go to Dr.-Ing. Ludger Timmen, Dr.-Ing. Tobias Kersten, Dipl.-Ing. Phillip Brieden, M.Sc. Hu Wu, and Dr. rer. nat. Kaiyang Qiu for giving me lots of help in both daily life and studies. Many thanks also go to my other colleagues in the IfE for giving me a feel of studying in my hometown. The China Scholarship Council (CSC) is gratefully acknowledged for the four-year financial support of my living and studying in Hannover, Germany.

Last but not least, I would like to say thanks to my parents and parents-in-law for their understanding and encouragements in the whole period. My wife, Feiyan Wang, was always there when I needed help, encouraging me and giving me confidence to go forward. We shared the successes and also faced the difficulties together.

Curriculum Vitae

Personal information

Name	Miao Lin
Date of birth	08.05.1985
Place of birth	Taizhou, Zhejiang
Nationality	China

Educational background

since 10.2010	PhD candidate supported by China Scholarship Council (CSC) at Institut für Erdmessung, Leibniz Universität Hannover, Hannover, Germany
09.2007–06.2010	Master of Science in geodesy, Central South University, Changsha, Hunan, China
09.2003–07.2007	Bachelor of Science in survey engineering, Central South University, Changsha, Hunan, China
09.2000–07.2003	Senior high school education at Luqiao Middle School, Taizhou, Zhejiang, China
09.1997–07.2000	Junior high school education at Pengjie Private Middle School, Taizhou, Zhejiang, China